UNIVERSIDADE DE LISBOA

FACULDADE DE CIÊNCIAS

DEPARTAMENTO DE ENGENHARIA GEOGRÁFICA, GEOFÍSICA E ENERGIA

DYNAMICS AND HYDROLOGY OF THE TAGUS ESTUARY:

RESULTS FROM *IN SITU* OBSERVATIONS

Filipe João Ricardo Correia dos Santos da Silva Neves

Doutoramento em Ciências Geofísicas e da Geoinformação

(Oceanografia)

2010

UNIVERSIDADE DE LISBOA

FACULDADE DE CIÊNCIAS

DEPARTAMENTO DE ENGENHARIA GEOGRÁFICA, GEOFÍSICA E ENERGIA

DYNAMICS AND HYDROLOGY OF THE TAGUS ESTUARY:

RESULTS FROM *IN SITU* OBSERVATIONS

Filipe João Ricardo Correia dos Santos da Silva Neves

Tese orientada pela Prof. Doutora Isabel Luísa S. A. Ambar

DOUTORAMENTO EM CIÊNCIAS GEOFÍSICAS E DA GEOINFORMAÇÃO

(OCEANOGRAFIA)

2010

Acknowledgements

Writing a Ph.D. thesis can be compared to a long and, most of the time, lonely journey. I could not have accomplished such a journey without the support and friendship of a great number of people.

I would like to start by thanking to Professor Isabel Ambar, who has been my supervisor since the beginning of my research and has been a great contributor to my development, both as a person and as a researcher. It would not have been possible to complete my Ph.D. degree without her valuable suggestions, always constructive critics and comments, important advice and friendship during the course of this study.

I would also like to thank to Professor Joaquim Dias for his valuable suggestions, especially on spectral and harmonic analysis, and to Dr. Nuno Serra for the support when I was investigating the possibility of setting up a numerical model for the Tagus Estuary. My sincere gratitude goes to the whole group of Physical Oceanography for providing me all the conditions to keep carrying out my investigation. The secretariat staff of the group is not forgotten, so I would like to thank them all, Ana, Beatriz and Mafalda, for helping me to keep motivated along the way.

I am indebted to Professor Cristina Catita, who has given me an enormous and valuable help during the digitalisation of the numerous tidal gauge charts. I would also like to thank Professor Carlos Antunes for providing tidal gauge data contemporary with the INTAGUS observational surveys.

A very special thanks must go to my friends and colleagues Alberto Azevedo, Nuno Prista, Rafael Mendes and Telmo Frias, for sharing my frustrations, as well as my victories, for making me see that sometimes, research does not need to be solitary and also for those great (and sometimes long) conversations during coffee time.

I would like to express my sincere and very special thanks to my family, namely my parents, my brother, my grandparents and my mother, father and brothers-in-law, for the unconditional support and encouragement to pursue my objectives.

Finally, no word is big enough to express my gratitude to my wife Alda and to my daughter Carolina, for being always there, for their everyday support, comprehension and love. Their presence in my life was fundamental in order to keep me on track and to keep my mental health during the hardest periods in the course of this work. To them I owe the achievement of my Ph.D. degree and to them I dedicate this thesis.

I acknowledge the following research projects, in the frame of which the observational data used in this study was obtained: “Hydrodynamics of Estuaries and Coastal Waters”, supported by the Junta Nacional de Investigação Científica e Tecnológica (JNICT), the Instituto Nacional de Investigação Científica (INIC) and the Bundesministerium für Forschung und Technologie, in the frame of the Portugal-Federal Republic of Germany bilateral cooperation; “Dynamical Response of the Tagus Estuary to the Forcing Mechanisms”, supported by JNICT and INIC; “ Integrated physical and biological study of the Tagus Estuary and adjacent coastal waters”, supported by Fundação para a Ciência e a Tecnologia (FCT). I also would like to thank to all the people involved in the observational data collection as well as to acknowledge the Instituto Geofísico do Infante Dom Luiz (IGIDL) for providing wind data contemporary with the INTAGUS observational surveys.

To conclude this long list of acknowledgements, I acknowledge the financial support provided by Fundação para a Ciência e a Tecnologia, via the grant SFRH/BD/13759/2003.

Abstract

The present study was carried out with the main objective of describing some aspects of the physical oceanography of the Tagus Estuary, in order to increase the understanding of its dynamics, namely in what concerns the propagation of the tide within the estuary, the thermohaline and circulation patterns and the role of the principal forcing mechanisms of the estuarine dynamics.

The study was based on the analysis of a comprehensive observational data set of the Tagus Estuary, obtained under different seasons and tidal conditions. This set includes hydrology and current profiles measured in sections along and across the estuary, repeated profiles at fixed positions and also time series obtained with self-recording equipment moored at several positions within the estuary. The data were complemented by contemporary records of water level, wind and river discharge.

The Tagus Estuary is a "mesotidal" estuary that fits the category of "coastal plain estuary". Concerning its stratification, the estuary can generally be classified as "partially mixed". However when neap tide conditions are combined with high river discharge, the Tagus Estuary can then be considered "stratified". The current meter data is compatible with a circulation pattern typical of a partially mixed estuary. Results show some features pointing to the existence of eddies, most probably generated by the action of the estuarine morphology on the flow. These structures seem to be affected by the wind and by the spring-neap cycle of the stratification. Saltiest bottom water flows along the deepest sites. At the inlet channel, saltier bottom water is found close to the southern margin, whereas fresher surface water is found close to the northern margin, not only in the inlet channel, but also in the inner bay.

As in most estuaries, the tide is clearly the main forcing mechanism of the Tagus Estuary dynamics. The semi-diurnal tide, the main source of variability, is modulated by the

fortnightly cycle, which strongly influences the stratification and, consequently, the circulation patterns. The tide propagates as a mixed progressive/standing wave, becoming essentially a standing wave in the interior region. An asymmetric behaviour, due to M_4, characterises the tide within the estuary, showing an ebb dominance, intensifying towards the interior. Depending on its amplitude ratio and phase relation with M_2, the shallow-water M_6 constituent can also play an important role on the asymmetry, leading to flood dominance.

The river discharge acts mainly in a seasonal time scale, influencing the stratification of the water column. The wind remote effects were evidenced by the significant lowering of the estuarine water temperature associated to the occurrence of wind-driven coastal upwelling. The effects of the air temperature proved to be mainly seasonal, influencing the surface water temperature. The coherency between the water level and the atmospheric pressure evidenced the inverse barometer effect.

This study contributed to clarify some aspects of the dynamics of the Tagus Estuary, namely the links between some features of the thermohaline and circulation patterns and the corresponding forcing mechanisms and also helped to clarify some aspects of the tidal asymmetry in the estuary.

Keywords: Tagus Estuary, tidal propagation, estuarine circulation, forcing mechanisms

Resumo

O Estuário do Tejo situa-se na costa Oeste de Portugal e é o maior estuário da Península Ibérica, ocupando uma área de aproximadamente 320 km^2, em que cerca de 40% corresponde a regiões intertidais. O estuário é composto por um canal relativamente estreito e profundo com cerca de 15 km de extensão e por uma região interior, mais larga e menos profunda, com cerca de 25 km de extensão. A região interior caracteriza-se por uma topografia de fundo complexa, com dois canais principais (Cala de Samora e Cala do Norte) e extensas regiões intertidais.

O presente trabalho teve como objectivo geral descrever alguns aspectos da oceanografia física do Estuário do Tejo, com base em observações *in situ*, no sentido de contribuir para uma melhor compreensão da sua dinâmica, nomeadamente a propagação da maré no estuário, os padrões termohalinos e de circulação e o papel dos principais mecanismos forçadores (a maré, o vento e a descarga do rio) da dinâmica estuarina.

O conjunto de dados observacionais usados neste trabalho inclui perfis de temperatura, salinidade e velocidade da corrente ao longo de secções longitudinais e transversais ao estuário, assim como perfis repetidos em posições fixas (com sondas de Condutividade, Temperatura, Pressão – CTD) e séries temporais obtidas com diverso equipamento de autoregisto (correntómetros e cadeias de termístores) em amarrações. Os dados foram obtidos no âmbito de campanhas observacionais realizadas em diferentes estações do ano e em diferentes fases do ciclo quinzenal de maré. Em Setembro de 1985 (TEJO85) realizaram-se perfis de hidrologia em condições de maré viva e obtiveram-se séries temporais de hidrologia e velocidade da corrente com cerca de um mês de duração. Em Fevereiro de 1988 (TEJO88/1) realizaram-se perfis de hidrologia em condições de maré morta. Durante os meses de Agosto de 1988 (TEJO88/2) e de Novembro de 1989 (TEJO89) obtiveram-se séries temporais de hidrologia e velocidade da corrente. Em Agosto de 2007 (INTAGUS07) e em Janeiro de 2008 (INTAGUS08) realizaram-se perfis de hidrologia e velocidade da corrente durante um ciclo quase completo de maré semi-diurna e em condições de maré viva

e de maré morta. Estes dados foram complementados com dados contemporâneos do nível da água medido com marégrafos instalados em vários locais das margens do Estuário do Tejo, velocidade e direcção do vento medidos numa estação meteorológica próxima do estuário, e descarga do rio em Almourol, a cerca de 130 km da sua foz.

Morfologicamente, o Estuário do Tejo é categorizado como um "estuário de planície costeira", classificando-se como "mesotidal" no que diz respeito à altura da maré (entre 2 e 4 m). Quanto à estratificação, pode ser classificado como "parcialmente misturado". Verificou-se que, em condições de maré morta conjugadas com uma elevada descarga do rio, o estuário pode ser classificado como "estratificado".

Os dados obtidos no Estuário do Tejo apontam para a existência de um padrão de circulação típico de um estuário parcialmente misturado (escoamento para jusante na camada superficial e para montante na camada profunda). Os resultados das observações indicam, em certos casos, a existência de vórtices, muito provavelmente gerados pelo efeito da morfologia do estuário sobre o escoamento. Estas estruturas mostraram ser afectadas pela acção do vento e/ou pelas variações de estratificação associadas ao ciclo quinzenal da maré. No que diz respeito à estrutura termohalina, a água mais salgada é encontrada junto ao fundo, sendo a salinidade tanto maior quanto maior a profundidade, como seria de esperar. Por outro lado, a água proveniente do rio ocupa a camada superficial, encontrando-se os valores mais baixos de salinidade geralmente mais próximos da margem norte ao longo de todo o estuário. Em particular, no canal de entrada do estuário, a água do mar, junto ao fundo, encontra-se mais perto da margem sul, enquanto a água proveniente do rio, na camada superficial, se encontra mais próxima da margem norte. Estas observações são compatíveis com o efeito a acção da força de Coriolis no escoamento.

Apesar de a morfologia do estuário (orientação da linha de costa e relevo do fundo) poder ser considerada um mecanismo forçador "estático", tem um papel activo na variabilidade espacial dos padrões de circulação residual observados e dos efeitos do atrito devido à proximidade de fronteiras laterais. Considerando a maré semi-diurna, o relevo do fundo é mesmo o principal factor de influência na direcção da corrente de maré.

A maré mostra-se claramente como sendo o principal mecanismo forçador da dinâmica no Estuário do Tejo, sendo a frequência semi-diurna a dominante em termos de variabilidade, como demonstrado pela análise harmónica e espectral das séries temporais de hidrologia e de velocidade da corrente. Esta frequência é modulada pelo ciclo quinzenal de maré, que exerce a sua acção na estratificação da coluna de água e, consequentemente, na circulação residual, através da variação da intensidade da mistura vertical turbulenta.

A maré propaga-se com um comportamento misto de onda progressiva/estacionária, verificando-se, no entanto, o aumento da contribuição estacionária em direcção ao interior. A propagação da maré no Estuário do Tejo revela a existência de uma assimetria, com a vazante geralmente mais curta e mais forte do que a enchente. Este domínio da enchente intensifica-se em direcção ao interior do estuário, associado à existência de extensas áreas intertidais nessa região. A assimetria é principalmente causada por acelerações advectivas não-lineares, as quais dão origem ao constituinte harmónico de águas pouco profundas M_4. O aumento da amplitude deste em direcção ao interior do estuário leva à intensificação do domínio da vazante. A montante de Cabo Ruivo observa-se um aumento significativo da amplitude do constituinte harmónico de águas pouco profundas M_6, a que parece corresponder uma mudança no sentido da assimetria da maré, com domínio da enchente. Uma experiência teórica mostrou que, dependendo da razão entre as amplitudes de M_2 e M_6 e da sua fase relativa, o constituinte M_6 poderá desempenhar um papel importante na assimetria, originando mesmo uma mudança de sentido.

A descarga do rio tem a sua acção principal numa escala de tempo sazonal, exercendo uma forte influência na salinidade da camada superficial do estuário e portanto na estratificação da coluna de água. Regimes de descarga do rio típicos de Inverno terão tendência para intensificar a estratificação no Estuário do Tejo.

As observações apenas mostraram os efeitos remotos do vento na estrutura termohalina do estuário, através da relação de alterações significativas da temperatura da água com a ocorrência de afloramento na região costeira adjacente, em consequência de episódios de

vento intenso de norte. Os dados mostraram ainda que a acção directa do vento no estuário é também relevante para a circulação residual.

O presente estudo contribuiu para clarificar alguns aspectos da dinâmica do Estuário do Tejo, nomeadamente a relação entre algumas características dos padrões termohalinos e de circulação e os respectivos mecanismos forçadores. Este trabalho permitiu também clarificar alguns aspectos da assimetria da maré no estuário.

Palavras-chave: Estuário do Tejo, mecanismos forçadores, propagação da maré, circulação estuarina

Contents

List of Figures

List of Tables

Chapter 1

Introduction

1.1 Motivation, objectives and work outline

For centuries, estuaries have been regions of extremely high importance to society. These regions are characterised by their high primary productivity, by their role as nurseries for some fish species and by providing sheltered anchorages and easy navigational access to the ocean. All these aspects lead to the establishment of populations and industries in the vicinity of estuaries which, due to the associated anthropogenic pressure, turn the estuaries into vulnerable systems.

The correct management and protection of such important natural resources require well supported decision making. Results generated by numerical models are then highly useful but their reliability depends on the adequacy of the numerical model to the domain's characteristics as well as to the physical processes to be simulated. The spatial and temporal time scales used in the numerical simulations must be appropriate to the phenomena that is to be studied and the physical processes not resolved by the model's space and time scales should be correctly parametrised. Thus, a correct knowledge of the estuarine physical processes like circulation and mixing, is fundamental for a proper use of numerical modelling as a support for a sustainable environmental management.

The Tagus Estuary (Fig. 1.1) is the most extensive Iberian Peninsula estuary and one of Europe's largest estuaries. Due to its great importance as a natural resource, the estuary's surroundings are characterised by both high population and industrial occupation.

Motivated by the need to preserve such resource and to start a rational management of the estuary, the Natural Reserve of the Tagus Estuary was created in 1976 (Decreto Lei n.° 565/76 de 19 de Julho, 1976). It comprises an area of about 32 km^2, located in the upstream region of the estuary (ICNB, 2007), as shown by the darker green shaded area in Fig. 1.2.

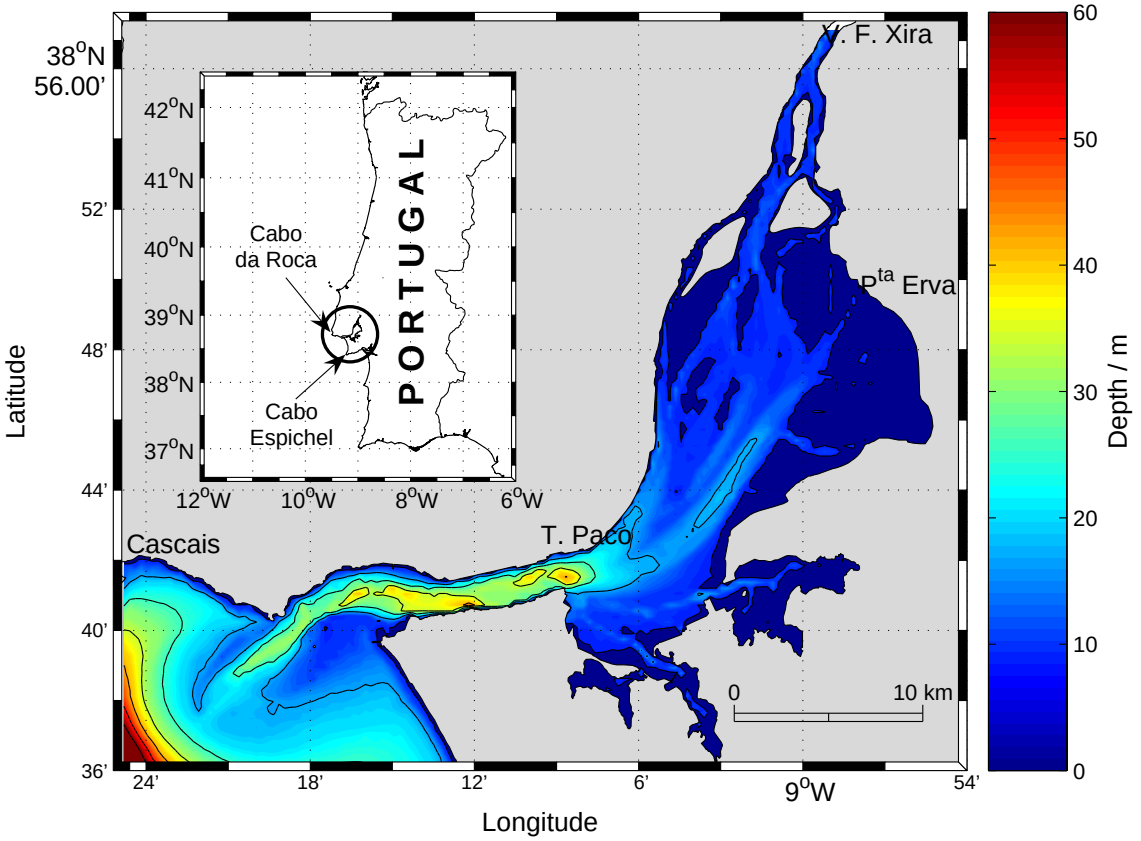

Figure 1.1 – Location of the Tagus Estuary at the Portuguese west coast (inset). Depths are relative to a datum positioned about 2 m below the mean sea level at Cascais. The dark blue area corresponds to intertidal flats and contours are drawn every 10 m between 0 and 60 m depth.

The Tagus Estuary has been widely studied, but there are still many aspects that need further clarification. The relation between the Tagus Estuary's circulation and its main forcing mechanisms (tide, wind and river discharge) can still be further investigated. Also

Figure 1.2 – Area covered by the Natural Reserve of the Tagus Estuary, shaded as darker green (ICNB, 2007).

some aspects of the tidal propagation within the estuary, mainly related to the tidal wave distortion as it propagates into the estuary's interior, need clarification. The present study is therefore justified by these main aspects that can be further investigated, together with the availability of a hydrology, current velocity and tidal data base obtained during a wide variety of conditions of the main forcing mechanisms, and with a good spatial coverage of the estuary.

The general objective of this study is to describe some aspects of the physical oceanography of the Tagus Estuary, which will help to increase the understanding of its dynamics and to improve the design of future monitoring programmes.

To achieve the main objective, some specific objectives are established for this study. Thus, it aims to increase the understanding of the propagation of the tide within the estuary, namely the evolution of the tidal harmonic constituents along the estuary, the study of tidal currents and their behaviour regarding tidal asymmetry, as well as the role of the shallow-water constituent M_6 in the tidal asymmetry. This study also aims to establish thermohaline and circulation patterns, based on the analysis of *in situ* data and, taking advantage from the

fact that these data were collected during a wide variety of conditions of the main forcing mechanisms (tide, wind and river discharge), it seeks to increase the understanding of their role on the Tagus Estuary's dynamics.

Concerning its structure, this dissertation is constituted by five chapters. Chapter 1 presents a brief overview of general aspects of estuarine physics and the characterisation of the study region. In Chapter 2, the observational data used in this work are presented. Chapter 3 is devoted to the tidal propagation within the estuary and Chapter 4 to the hydrographic conditions, stratification and analysis of the current velocity data, with the objective of establishing patterns of circulation for the Tagus Estuary in relation with the main forcing mechanisms. Finally, Chapter 5 presents an overview of the results, a summary of the conclusions and some suggestions for future work.

1.2 Definition and classification of estuaries

1.2.1 Definition

Defining an estuary is not a simple task, given the enormous variety of estuarine systems, each with its specific characteristics. Following Pritchard (1967), from a physical point of view, the definition of estuaries should point out to their characteristic salinity and density distributions, as well as to their circulation patterns and mixing processes; it should also refer the boundaries, which are partially responsible for the distribution of properties and the movement and mixing of waters.

Estuaries are commonly defined following Cameron and Pritchard (1963): 'An estuary is a semi-enclosed coastal body of water which has free connection to the open sea and within which sea water is measurably diluted with freshwater derived from land drainage'. However, this definition does not take into account tidal influence, being only valid for a tidally averaged situation. In this sense, Dyer (1997) suggests an adaptation to the definition presented above: 'An estuary is a semi-enclosed coastal body of water which has free connection to the open sea, extending into the river as far as the limit of tidal influence, and within which sea water is measurably diluted with freshwater derived from land drainage'.

1.2.2 Classification

According to Pritchard (1989), the earliest estuarine classification schemes were developed in order to establish a framework for organising the growing estuarine data base, associated to the rapid increase of estuarine research.

Estuarine classification can be either qualitative or quantitative and several different schemes are possible, depending on which aspects are focused (e.g. tides, geomorphology, salinity structure). In the next sections, some of the most used classification schemes are presented and shortly described.

Classification based on tidal range

Davies (1964) created a classification scheme based on the tidal range (surface level difference between consecutive high and low water in a tidal cycle) of an estuary. Thus, an estuary can be classified as *Microtidal* (tidal range lower than 2 m), *Mesotidal* (tidal range between 2 and 4 m), *Macrotidal* (tidal range between 4 and 6 m) or *Hypertidal* (tidal range greater than 6 m).

Classification based on geomorphology

Pritchard (1952) presented a classification scheme based on the geomorphology of estuaries, grouping them as (*i*) coastal plain estuaries; (*ii*) fjords; (*iii*) bar-built estuaries; and (*iv*) other estuaries.

(i) Coastal plain estuaries

These estuaries often have maximum depths of as much as 30 m and their width-depth ratio is usually large. The river flow per tidal cycle is generally small when compared with tidal prism (volume of water within the estuary between high and low tide). Coastal plain estuaries are essentially characteristic of temperate latitudes.

(ii) Fjords

Fjords are characterised by the existence of a shallow sill at their mouths and also at the intersection with other fjords. Inside the sills, maximum depths can reach up to 800 m.

Fjords have a small width-depth ratio and river flow per tidal cycle is often large in comparison with tidal prism. This type of estuaries is restricted to high latitudes in mountainous regions.

(iii) Bar-built estuaries

These are essentially coastal plain estuaries that have developed a bar across their mouths. These estuaries are generally only a few meters deep. River flow is large and seasonally variable. The mouth's position can undergo considerable variations from year to year. Bar-built estuaries are usually found in tropical areas or in areas with active coastal deposition of sediments.

(iv) Other estuaries

This group includes all the estuaries that do not fit in the former groups, namely the tectonically produced estuaries, formed by faulting, landslides or volcanic eruptions.

Classification based on salinity structure

Most estuaries that have been studied belong to the coastal plain category but, within this group, large differences in circulation patterns, stratification and mixing processes are evident. As a consequence, Pritchard (1955) and Cameron and Pritchard (1963) created a classification scheme based on stratification and characteristics of salinity distribution. Four main types of estuaries were defined: (*i*) highly stratified (salt wedge); (*ii*) highly stratified (fjords); (*iii*) partially mixed; and (*iv*) vertically homogeneous or well mixed. The last group can be subdivided into *laterally inhomogeneous* and *laterally homogeneous* estuaries.

This classification system deals with motion and salinity distributions in the longitudinal-vertical plane, both averaged over the tidal cycle. It is based essentially on qualitative criteria, and so its nature is mainly descriptive. However, transitions from one category to another are related with changes in quantitative descriptors such as river flow, tidal velocities, width and depth of the estuary (Pritchard, 1989).

(i) Highly stratified: salt wedge type

In salt wedge estuaries, river flow almost completely dominates the circulation. The salt water extends landwards as a wedge along the bottom of the estuary. The position of the salt wedge varies with the river flow and estuaries of this type are normally microtidal estuaries. From the head to the mouth, the structure of the flow changes from a thick upper layer flowing over a thin lower layer, to a thin surface layer flowing over a thick lower layer. Both fresh and salt water layers are almost homogeneous at each point of the estuary and have very little interaction between them. The interface between fresh and salty water corresponds to a strong velocity vertical shear which drives entrainment[1], the main mixing process for this category of estuaries. The current velocity vanishes at the top of the salt wedge.

(ii) Highly stratified: fjord type

Fjords are very similar to salt wedge estuaries. However, the vertical longitudinal salinity distribution of fjords is not characterised by a wedge but by a thin upper freshwater layer overlying a very deep, lower salt water layer. The thickness of the upper layer is almost constant from head to mouth and, in some fjords, is restricted to a depth equal to the depth of the sill (see description of fjords above in the classification on geomorphology). Over the sills, tidal current velocities can be larger than within the fjords and thus mixing can be stronger and, as a consequence, stratification is weaker.

(iii) Partially mixed estuaries

The river flow per tidal cycle of partially mixed estuaries is usually small compared with tidal prism, since most estuaries of this type are mesotidal. The mean flow vertical distribution shows a distinct two-layer system. Salinity increases towards the mouth at all depths, the upper layer being slightly fresher than the lower layer. In these estuaries, tidal range can change significantly between spring and neap tide. During spring tide, as turbulent exchanges of salt and freshwater increase, the vertical gravitational circulation is

[1]Process by which denser water is mixed into the overlying, less dense water through internal wave breaking at the interface between the two layers. The internal waves are generated by strong velocity vertical shear between the two layers.

intensified and, consequently, stratification decreases. On the other hand, high river flow causes the stratification to increase, resulting in the decrease of the intensity of the mean circulation. Estuaries of this type usually show a considerable variation of structure, being highly stratified near the head (tidal prism diminishes and river flow per tidal cycle becomes comparatively more important) and vertically homogeneous near the mouth (higher current velocities).

(iv) Vertically homogeneous or well mixed estuaries

The tidal range must be large enough relative to the water depth in order to mix completely the water column by turbulence. In this case, tidal flow is much larger than river flow, meaning that these estuaries are macrotidal. Vertically homogeneous estuaries may be subdivided into two categories: *(a)* laterally inhomogeneous and; *(b)* laterally homogeneous.

A vertically homogeneous estuary is laterally inhomogeneous if it is wide enough for the Coriolis force to give rise to a lateral variation of salinity. In the northern hemisphere, the seaward net flow (lower salinity water) occurs at all depths on the right-hand side (looking toward the sea) and the compensating landward flow (higher salinity water) on the left.

On the other hand, in a narrow vertically homogeneous estuary, sufficiently intense lateral shear can create laterally homogeneous conditions. Salinity increases toward the mouth and the mean flow is seawards throughout the cross-sections.

Quantitative classifications

Quantitative classification schemes were developed in order to establish boundaries between estuarine types. One of the most widely used and considered the best quantitative classification scheme is the Stratification-Circulation diagram, developed by Hansen and Rattray (1966). This scheme is based on two dimensionless parameters: a stratification parameter $\delta s/\langle s \rangle$, defined as the ratio between the surface to bottom difference in salinity (δs) and the average vertical or cross-sectional salinity ($\langle s \rangle$); and a circulation parameter u_s/u_f, the ratio between the net surface current (u_s) and the mean cross-sectional velocity

(u_f). The classification diagram was reconstructed (Fig. 1.3), showing the various types of estuaries defined by the authors of this scheme.

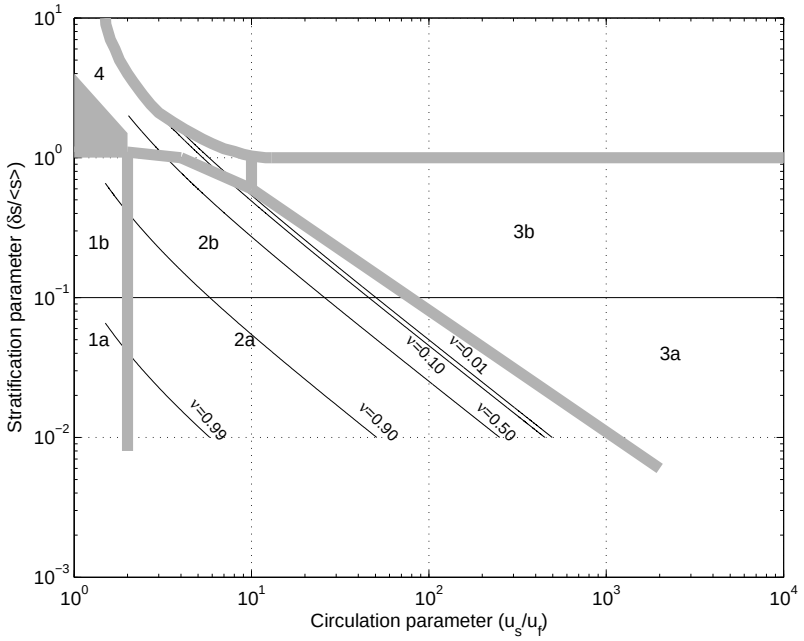

Figure 1.3 – Reconstruction of the Stratification-Circulation diagram, based on Hansen and Rattray (1966) estuarine classification, indicating the types of estuaries according to the stratification and circulation parameters. Contours of the diffusive upstream salt transport fraction (ν) are also represented.

An important parameter associated with this classification is ν, defined as the diffusive fraction of the total upstream salt transfer in a rectangular channel (Hansen and Rattray, 1966). The remaining upstream salt flux is due to advection, resulting from the gravitational convection in the estuary. The parameter ν can be written in terms of the stratification and circulation parameters as:

$$\nu = 1 - 0.20 \frac{u_s}{u_f} \frac{\delta s}{\langle s \rangle} \, . \tag{1.1}$$

Analysing equation (1.1), it becomes evident that weak stratification, small net surface current and large mean cross-sectional velocity are responsible for a small gravitational convection and, consequently, for a large contribution of diffusion to the total upstream salt flux. In the limit, when $\nu = 1$, the upstream salt flux is entirely due to diffusion. On the

other hand, large gravitational convection occurs for strong stratification, large net surface current and small mean cross-sectional velocity; as $\nu \rightarrow 0$, diffusion becomes negligible and the upstream salt transport is due almost entirely to advection. Advective and diffusive fluxes are both important in the horizontal salt balance for values of ν between 0.1 and 0.9.

The Stratification-Circulation diagram is subdivided as shown in Fig. 1.3, principally according to the field of the parameter ν. The main characteristics of each region of the diagram are described as follows. *Type 1* estuaries are characterised by seaward net flow at all depths; the mean cross-sectional velocity (u_f) is much higher than the net surface current (u_s). In this case, equation (1.1) shows that $\nu \rightarrow 1$, and the upstream salt flux is mainly due to diffusion. The difference between types *1a* and *1b* is essentially in the stratification; the type *1a* corresponds to well mixed estuaries (slight stratification) while in *1b* there is appreciable stratification.

In *Type 2* estuaries, the net flow reverses at depth and the circulation parameter is such that ν falls within the interval between 0.1 and 0.9. This means that both advection and diffusion have important contributions to the total upstream salt flux. An estuary of type *2a* is less stratified than an estuary of type *2b*.

In estuaries of *Type 3*, the salt transfer is primarily advective, which means that the net surface current is much higher than the mean-cross-sectional velocity. *Type 3b* estuaries have a lower layer so deep that the salinity gradient and the circulation do not extend to the bottom. Fjords are generally of type *3b* until mixed to a point that they assume the type *3a* characteristics of small stratification.

The *Type 4* estuaries essentially correspond to salt wedge estuaries and the stratification is greater than in the other types defined here.

According to Hansen and Rattray (1966), the uppermost boundary represented in the diagram corresponds to conditions of freshwater outflow over a stagnant saline layer. In addition, these authors state that the separation of the types of estuaries carry a certain degree of arbitrariness. According to them, the *a* and *b* separation of each type is only a matter of convenience for expressing the relative stratification of the estuaries and the transition between types 3 and 4 has little observational or theoretical basis.

Prandle (1985) has defined the stratification number (S_t) as a measure of the amount of energy lost by the tidal wave within the estuary relative to that used in the mixing of the

water column. The stratification number is therefore given by the equation:

$$S_t = \frac{0.85 k U_0 L}{(\Delta\rho/\rho)\, g h^2 u_f} , \tag{1.2}$$

where k is the friction coefficient, L the estuary length, U_0 the amplitude of tidal currents, h the water depth and u_f the depth mean current. Using *in situ* observations and flume tests data, this author established a relation between the stratification number and the stratification parameter, earlier defined as $\delta s/\langle s \rangle$. Thus, it was shown that the water column was *well mixed* for $\delta s/\langle s \rangle < 0.15$, *partially mixed* for $0.15 < \delta s/\langle s \rangle < 0.32$ and *stratified* for $\delta s/\langle s \rangle > 0.32$.

1.3 Estuarine circulation

1.3.1 Tide and river flow as forcing mechanisms

The classification scheme based on the salinity structure, developed by Pritchard (1955) and Cameron and Pritchard (1963), presented in Section 1.2.2, reflects the different relations between tidal currents and river flow.

The longitudinal density gradient extending from the river freshwater to the denser seawater is a main characteristic of many estuaries. This gradient drives the gravitational circulation, which is characterised by a bidirectional flow, regarded as the basic flow pattern in a partially mixed estuary (Pritchard, 1952). The bidirectional flow consists of a surface current flowing seaward and a landward near-bottom flow. This type of non-tidal circulation is responsible for inducing stratification, competing against turbulent mixing generated by tidal currents to determine the vertical structure of the estuarine water column. Stratification can therefore be weakened or strengthened by turbulent mixing which, in turn, is controlled by the intensity of tidal currents. As an example, one should expect weaker stratification during spring tide than during neap tide, as the tidal currents are generally more intense during spring tide, causing the intensification of turbulent mixing.

Considering a tidally averaged situation and a no-slip boundary condition, Officer (1976) derived the following equation for the profile of the vertical gravitational circulation:

$$u(\eta) = \frac{1}{48} \frac{\partial \rho}{\partial x} \frac{g h^3}{\rho N_z} \left(8\eta^3 - 9\eta^2 + 1\right) , \tag{1.3}$$

where $u(\eta)$ represents the vertical profile of the flow parallel to the horizontal density gradient, ρ is the density, g is the acceleration due to gravity, $\eta = z/h$ where z is the height above the bottom and h the total depth, and N_z is the coefficient of vertical eddy viscosity.

Assuming the constancy of the horizontal density gradient, equation (1.3) shows that the magnitude of the gravitational circulation is inversely dependent on the coefficient of vertical eddy viscosity, i.e., inversely dependent on turbulent mixing. The results reported by Ribeiro et al. (2004) are an example of how the spring-neap tidal variability of the turbulent mixing modulates the strength of the non-tidal residual circulation.

The forcing exerted by tide and river flow on estuarine gravitational circulation can therefore be an important control on the transport of buoyant material within an estuary and also between an estuary and the adjacent coastal ocean.

1.3.2 Wind stress as forcing mechanism

So far, only the effects of the tide and river flow on the estuarine circulation have been mentioned, but the wind can also exert an important influence on estuarine circulation and mixing, as the wind is the major cause of eddy flux of momentum across the air-water interface in coastal plain estuaries (Officer, 1976; Wang, 1979). Non-tidal variability in estuaries may be induced by the wind through a combination of remote and local effects. In what concerns the remote effects, winds on the coastal ocean adjacent to an estuary may produce sea level fluctuations at the mouth of that estuary, which propagate to its interior. Remotely generated surface wind waves can also travel into the estuary, contributing to the intensification of the vertical mixing, thus affecting the stratification and, consequently, the circulation.

As for the role of local wind, Officer (1976) presented a parabolic profile of wind induced flow, with surface and upper layer water flowing in the direction of the wind, a lower layer flowing in the opposite direction and no flow at the bottom. Kiley and Welch (1989) refer several studies that support the wind induced flow profile formulated by Officer (1976) (e.g. Weisberg (1976), Wang and Elliott (1978) and Wang (1979)). More recently, on a study about the long-term variability of the non-tidal circulation in Southampton Water, Ribeiro et al. (2004) reported the observation of pulses of increased gravitational circulation as being related to wind-driven mixing, especially when the wind direction was along

the main axis of the estuary.

Wind can also generate surface waves inside an estuary, which will affect the water column structure through the variation of the intensity of vertical mixing, as already referred.

1.3.3 Characteristic time scales

The forcing conditions of an estuary change over a broad spectrum of time scales. Large wind-driven velocity fluctuations at several time scales (2-3 days for local wind forcing and more than 10 days for non-local wind forcing) on non-tidal circulation in Chesapeake Bay were reported by Wang (1979). Also river flow rates are known to vary by an order of magnitude or more just over a few days due to storms, snow melt and dam releases (MacCready, 1999).

The strength of the non-tidal residual circulation can be modulated by the spring-neap tidal variability of the turbulent mixing due to tidal currents, as reported by Ribeiro et al. (2004).

At longer time scales, seasonal variations in river flow are reflected by the salinity distribution. For example, the increase of the river flow during winter, will tend to intensify the vertical gradients of density, thus reducing vertical mixing and, as a consequence, intensifying the gravitational circulation.

The estuarine circulation therefore results from complex interactions of several forcing mechanisms – the principal being the tide, river flow and wind stress – over a wide range of time scales.

1.4 The Tagus Estuary

1.4.1 Geographical location and morphological characteristics

Situated in the Portuguese west coast, covering an area of about 320 km^2 and with a mean volume of 1.8 km^3 (Freire et al., 2006), the Tagus Estuary is the Iberian Peninsula largest estuary. Its mouth opens to a large bay in the adjacent coastal ocean, between Cape of Roca and Cape Espichel. The salt water region of the estuary, defined by Lemos (1965)

as the region where tidal currents always reverse in the slack water[2], reaches up to Vila Franca de Xira, 50 km upstream from the mouth. As for the tidal amplitude, it vanishes in the vicinity of Muge, about 80 km upstream from the mouth.

The estuary is composed of a deep, narrow inlet channel (known as "Corredor") and a shallow, broad inner bay (known as "Mar da Palha") – see Fig. 1.1. The inlet channel, being 15-km long, 2-km wide and reaching depths of about 40 m in some places, constitutes the deepest part of the estuary. The inner bay, about 25-km long and 15-km wide, is the shallowest part of the estuary and has complex bottom topography with narrow channels, tidal flat areas and small islands. Tidal flats, corresponding to about 40% of the estuary's total area, are known to have an important role in Tagus Estuary's hydrodynamics by modifying the shape of the tidal wave (Fortunato et al., 1999; Fortunato and Oliveira, 2005). The estuary is also characterised by the existence of sand beaches, both in the inlet channel (northern margin) and in the inner bay (southern margin) (Freire et al., 2006).

1.4.2 Research programmes and projects

The Tagus Estuary has been widely studied over the last century. The first important study, as cited by Rodrigues da Silva (2003), was the one carried out by Baldaque da Silva (1893), motivated by the need to assure the easy and safe navigability within the estuary. The first integrated study on this estuary was performed by Arantes e Oliveira (1941), who analysed the hydrodynamic and salinity distribution processes and the water quality in the Tagus Estuary. These two studies are worth mentioning due to their historical importance.

During the seventies, several other studies had been done on the dynamics and salinity distribution of the Tagus Estuary, e.g. the observational campaigns carried out from 1972 to 1975 by the Lisbon Harbour Administration (APL, formerly AGPL) (Alves, 1983). Another important study worth mentioning is the tidal observational program carried out by the Hydrographic Institute of the Portuguese Navy (IH) during 1972. This program was designed to gather the necessary information to build and calibrate a scale model of the Tagus Estuary. The resulting data base is referred as the most complete tidal data base of the Tagus Estuary (Rodrigues da Silva, 2003) and, besides its primary objective, it has been

[2]State of a tidal current when its speed is near zero.

used on several studies about tidal propagation and water level evolution within the estuary (e.g. Fortunato et al., 1999; Canas et al., 2009).

In the eighties, a multidisciplinary project named "Environmental Study of the Tagus Estuary" comprised several observational campaigns, carried out during 1980 and 1982, and was aimed to produce the necessary knowledge to the long-term planning and management of water quality in the estuary (DGQA, 1986). It comprised studies on: hydrodynamics, showing the applicability of a bi-dimensional numerical model to simulate the tidal propagation within the estuary (Rodrigues et al., 1986) and the applicability of a physical model to understand the hydrodynamics of the Tagus Estuary (Elias, 1986); studies on biology, like the one carried out by Costa (1986), which showed the importance of the estuary as a nursery for some fish species with economic importance; or studies on pollution, like the one by Lima et al. (1986), in which the impact of the pollution caused by mercury in the estuary is assessed.

These and several other projects have been carried out on the Tagus Estuary, using *in situ* measurements, physical and numerical modelling or remote detection, which resulted on publications about morphodynamics (e.g. Freire et al., 2006), pollution (e.g. Andreae et al., 1983; Figueres et al., 1985), suspended sediments (e.g. Vale and Sundby, 1987; Portela and Neves, 1994b), hydrodynamics (e.g. Alves, 1983; Portela and Neves, 1994a; Portela and Neves, 1996), circulation and tidal propagation (e.g. Ambar and Backhaus, 1983; Fortunato et al., 1997; Fortunato et al., 1999), wind effects and surface waves (e.g. Freire and Andrade, 1999; Oliveira, 2000; Rusu et al., 2009), monitoring and operational modelling (e.g. Anjos et al., 2003; Fernandes et al., 2004), estuary's plume (e.g. Valente and da Silva, 2009; Vaz et al., 2009), phytoplankton (e.g. Gameiro et al., 2007) and fisheries (e.g. Costa et al., 2007).

1.4.3 Tidal propagation

Tides in Tagus Estuary are mainly semi-diurnal. The tidal range within the estuary varies from 0.8 m (neap tide) to 4.0 m (spring tide) (Fortunato et al., 1997) and increases towards the estuary's interior (Oliveira, 1993; Portela and Neves, 1994b), as the result of a small resonance effect. The tidal prism ranges from 0.75 to 1.0 km^3, as reported by Portela and Neves (1996) and Oliveira (1993). Using a physical model of the Tagus

Estuary, Elias (1986) computed tidal prisms for some cross-sections of the estuary, using a high spring tide, with a range of 3.26 m. This author reported tidal prisms of 1.3 km^3 at the mouth, 0.07 km^3 at Vila Franca de Xira and a total tidal prism for the smaller freshwater contributors of about 9% of the value estimated for the mouth. These estimates included a constant freshwater inflow of 100 $m^3\ s^{-1}$.

When analysing the numerical model results of introducing an artificial barrier on the mouth of the estuary, Oliveira (1993) noticed a tidal prism increase when the entrance of the estuary was partially closed. This author attributed this effect to the enhancement of the resonance within the estuary, since the introduction of the barrier would be equivalent to extending the length of the estuary (considering the estuary as a rectangular basin), thus increasing its natural period of oscillation.

The tidal wave is reported as progressive and at spring tide the high water can be delayed by as much as two hours between Lisboa and Vila Franca de Xira (Vale and Sundby, 1987). Tidal currents invert their sense during slack water and this effect is felt up to Vila Franca de Xira. Further upstream, the flood current is progressively weaker and shorter until is no longer felt (Lemos, 1965). As reported by Portela and Neves (1994a), tidal currents near the surface can exceed 1.5 m s^{-1} during spring tide in the inlet channel. Numerical model results show different flow patterns at the mouth in ebb compared with flood conditions (Fortunato et al., 1997).

Dias (1993) and Fortunato et al. (1999) noticed that ebbs are shorter than floods within the estuary. These latter authors showed, through a numerical model experience, that the removal of tidal flats would reduce the energy transfer from the astronomical to the non-linear constituents, thus affecting the resonance period of the estuary. Without tidal flats, the average difference in duration between ebbs and floods would also change, from ebbs 43 minutes shorter than floods to ebbs about 5 minutes longer than floods. This experience showed the important role of the tidal flats on the hydrodynamics of the Tagus Estuary.

1.4.4 River discharge

The Tagus river is the main source of freshwater of the estuary. According to Macedo (2006), the Tagus river discharge regime became modulated since the fifties, due to the building of the most important dams of the Tagus hydrographic basin. This author pre-

sented a study on the Tagus river discharge during the period between 1974 and 2001 at Almourol – about 130 km upstream of the estuary's mouth –, which showed a mean annual river discharge of 331 m^3 s^{-1} and identified the year 1992 as a dry year and 1979 as a wet year.

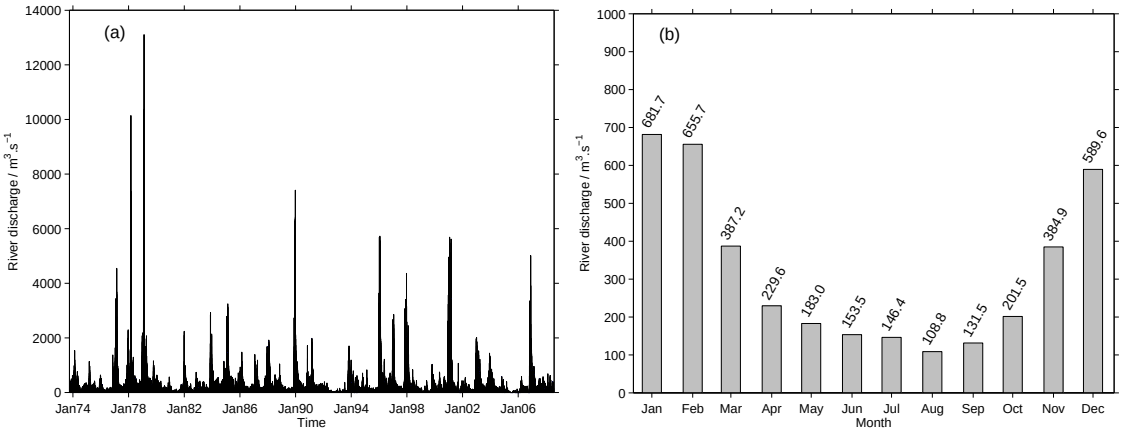

Figure 1.4 – River discharge (m^3 s^{-1}) at Almourol as (a) daily mean values for the period 10/1973 – 07/2008 and (b) monthly means weighted by the number of months with observations.

Our analysis of a 35 year-long (October 1973 – July 2008) time series of daily mean river flow values measured at Almourol, obtained from the Sistema Nacional de Informação de Recursos Hídricos (SNIRH) website, (http://snirh.pt/), shows that the main period of variability of the series corresponds to the seasonal cycle, despite the modulated character of the Tagus river discharge regime. In Fig. 1.4(a), presenting the analysed time series, the highest peaks are generally observed between December and February. In fact, for that period (10/1973 – 07/2008), the monthly mean values of river discharge (Fig. 1.4(b)), computed as means weighted by the number of days with observations, reach a minimum in August and a maximum in January. The annual mean values, weighted by the number of months with observations, range from 47 m^3 s^{-1} (in 2005) to 1318 m^3 s^{-1} (in 1979). The annual mean river discharge obtained for the entire series, is about 368 m^3 s^{-1}, corresponding to a river flow *per* tidal cycle of about 8.2×10^6 m^3.

Previous calculations of Lemos (1965), using monthly mean values obtained for a non-

specified period of 34 years, showed the occurrence of minimum river discharge in August (~47 m^3 s^{-1}) and maximum in February (~1234 m^3 s^{-1}). The monthly mean values are referred by the author as being collected before the building of dams that partly contributed to regularize the Tagus river flow. Nevertheless, these results are similar to the ones reported by Macedo (2006) and to those presented in this study (using a series from 1973 to 2008), which still evidence the seasonal cycle. Thus, the dams act mainly as low-pass filters, retaining the high-frequency variability.

Other freshwater inputs to the estuary, from the Sorraia and Trancão rivers, with average annual discharges of about 35 and 2.5 m^3 s^{-1}, respectively (as reported by Fortunato et al., 1999), are comparatively small and will be neglected in this work.

The influence of the river discharge seasonal variability is evidenced by several estimates for the water residence time within the Tagus Estuary. As an example, Martins et al. (1984) reported a residence time between 6 and 65 days, respectively for a river discharge between 2200 and 100 m^3 s^{-1}, and 23 days for a mean river discharge of 350 m^3 s^{-1}. Besides temporal variability, residence times have also strong spatial variability. This is shown by Braunschweig et al. (2003), by dividing the Tagus Estuary in ten regions and computing the respective residence times, assuming a constant river discharge. They concluded that the shallow inner bay region presents residence times > 20 days, the tidal flats in the south and southeast of the estuary have residence times < 10 days, as well as the inlet channel and the region close to the mouth. Thus, a global estimate of the residence time could be useful to classify an estuary in a general way or to give a picture of the estuary's transport, but it is an oversimplification (Oliveira and Baptista, 1997).

1.4.5 Wind, surface waves and storm surges

The wind effects on estuaries are commonly a combination of both local and remote effects (see Section 1.3.2). The wind regime in the Tagus Estuary region is mainly characterised by northerly winds, predominant during summer, and by southwesterly wind, mainly occurring during winter (Lemos, 1965). In a recent study, applying statistical analysis to an eleven-year period of meteorological data (1995-2005), Rusu et al. (2009) identified four dominant wind directions affecting the Tagus Estuary, North, South-Southwest, East-Northeast and North-Northwest, although no seasonality is referred. Concerning the

daily maximum, these authors identified North-Northeast and West-Southwest as the dominant directions in summer, whereas East-Northeast and West-Southwest were identified as the dominant directions during winter.

Northerly winds are responsible for the local generated waves in the estuary's shallow inner bay, which re-suspend, move and accumulate sand in the southern margin of the inner Tagus Estuary (Freire and Andrade, 1999). As for the swell coming from the ocean, it never propagates into the upstream part of the estuary, mainly due to the geographical orientation of the inlet channel (WSW-ENE, see Fig. 1.1) (Rusu et al., 2009). Still regarding swell coming from the ocean, small frequency waves are prevented from entering the inlet channel due to the sheltering effects of the submerged sand bars near the mouth of the estuary. However, the high frequency incoming waves are less susceptible to dissipate energy over the bars and can cause higher disturbances into the channel (Oliveira, 2000).

Significant elevations of the sea level generated by severe storms are known as storm surges (Pugh, 1987). Storm surges can be generated directly due to atmospheric pressure gradients or through the resulting wind forcing. In the west Iberian coast, due to its relatively narrow shelf, the determinant process is the atmospheric pressure forcing (Fanjul et al., 1998). Storm surges are reported to be frequent in the Tagus Estuary, causing important water level anomalies, which have been recorded in Lisbon and Cascais tidal gauge records (Canas et al., 2009). These authors showed that the large scale atmospheric pressure changes are important to explain the variability, for periods larger than 30 hours, of the detided water level at the mouth, inlet channel and mid-estuarine region of the Tagus Estuary.

1.4.6 Classification of the Tagus Estuary

According to the Pritchard's classification of estuaries by topography (see Section 1.2.2), the Tagus Estuary can be classified as a coastal plain estuary. Most of its morphological characteristics fits this category: its location in temperate latitudes, the maximum depth of ~45 m, its large width-depth ratio, the existence of intertidal flats, extensive mudflats and saltmarshes and the small river flow per tidal cycle (8.2×10^6 m^3) compared with the tidal prism (7.5×10^8 m^3). The one property that does not fit the coastal plain estuary category is its shape, which does not widen towards the mouth. On the other hand, Vale

and Sundby (1987) stated that the Tagus Estuary morphological characteristics are typical of tidal lagoons.

If the criteria to be used is the salinity structure, the Tagus Estuary fits best the partially mixed estuary category, as many other authors stated (Andreae et al., 1983; Dias, 1993; Portela and Neves, 1996; Fortunato et al., 1997), although showing a tendency to be vertically homogeneous during spring tide conditions. As seen above, the river flow is small compared to the tidal prism and tidal range changes significantly between neap and spring tide. During neap tides, residual currents were observed to be landward near the bottom and seaward near the surface (Vale and Sundby, 1987), corresponding to the basic flow pattern in a partially mixed estuary.

Taking in consideration the Stratification-Circulation diagram (see Fig. 1.3), results from Fiadeiro (1987), cited by Dias (1993), showed that the Tagus Estuary fits the type *2b*, equivalent to partially mixed (see Section 1.2.2). In this case, both diffusion and advection have important contributions to the total upstream salt flux. The results presented by Fiadeiro (1987) show a two layered residual flow, with upstream flow in the lower layer and downstream flow characterising the upper layer.

Chapter 2

Data presentation

The data used in the present dissertation is divided in two groups: an historical data set, obtained in the frame of two research projects during the late eighties; and a more recent set, obtained in the frame of a research project with a joint participation of the Physical Oceanography and Marine Botany groups from the Institute of Oceanography, Faculty of Sciences of the University of Lisbon (IOFCUL).

The present chapter is dedicated to the presentation of these two sets of data and the respective contemporary data of tide, wind and river discharge.

2.1 Historical campaigns

2.1.1 Hydrographic and current velocity data

The data set was obtained during four field surveys conducted by the Physical Oceanography group of IOFCUL respectively in September 1985 (TEJO85), in February 1988 (TEJO88/1), in August 1988 (TEJO88/2) and in November 1989 (TEJO89). The TEJO85 survey took place in the frame of the research project "Hydrodynamics of Estuaries and Coastal Waters", with the collaboration of the Institut für Meereskunde of the University of Hamburg. The TEJO88/1, TEJO88/2 and TEJO89 surveys were conducted in the frame of the research project "Dynamical Response of the Tagus Estuary to the Forcing Mechanisms". The dates and duration of each observational campaign are summarised in Fig. 2.1.

More specific information about the dates and duration of the observational campaigns can be found in Appendix A (Table A.1).

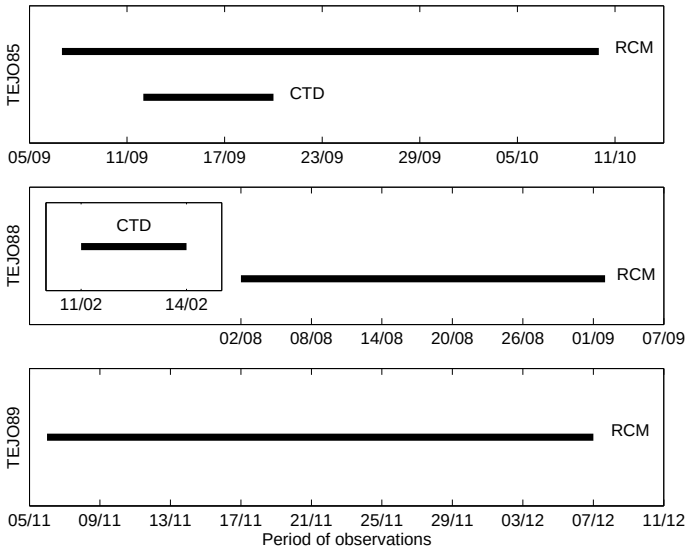

Figure 2.1 – Period of observations for the historical data set. (Top) Duration of the CTD (Conductivity-Temperature-Depth probe) and RCM (Recording Current Meter) observations during TEJO85. (Middle) Duration of the CTD observations during TEJO88/1 (inset) and current meter observations during TEJO88/2. (Bottom) Duration of the current meter observations during TEJO89.

The field experiment in September 1985 (TEJO85) included an extensive collection of hydrographic data on longitudinal (along the axis of the estuary) and transverse (across the estuary) sections complemented by repeated stations at several fixed sites in the estuary's interior (Fig. 2.2(a)). This survey was carried out during spring tide conditions. The data was collected from aboard the research launch "Vórtice" (from IOFCUL), the tug boat "Serra de Palmela" (from Lisbon Harbour Administration – APL), and from the anchored ships "Alfama", "Rodrigues Cabrilho" and "Ribeira Grande", using a Meerestechnik Elektronik CTD (Conductivity-Temperature-Depth probe) and a Montedoro-Whitney multiparameter probe. The collected data went through a calibration routine, described in a technical report (Ambar et al., 1989), being afterwards linearly interpolated to 2-dbar steps. This hydrographic data set consists of 173 CTD profiles, measured at 60 different

sites. Also in this survey, time series of currents and hydrographic data were obtained using Aanderaa RCM (Recording Current Meter) – model RCM-4S – suspended from the anchored ships (about 4 m depth) at three different sites in the estuary (sites A, B and C in Fig. 2.2(c)). The data was collected with a sampling interval of 10 minutes.

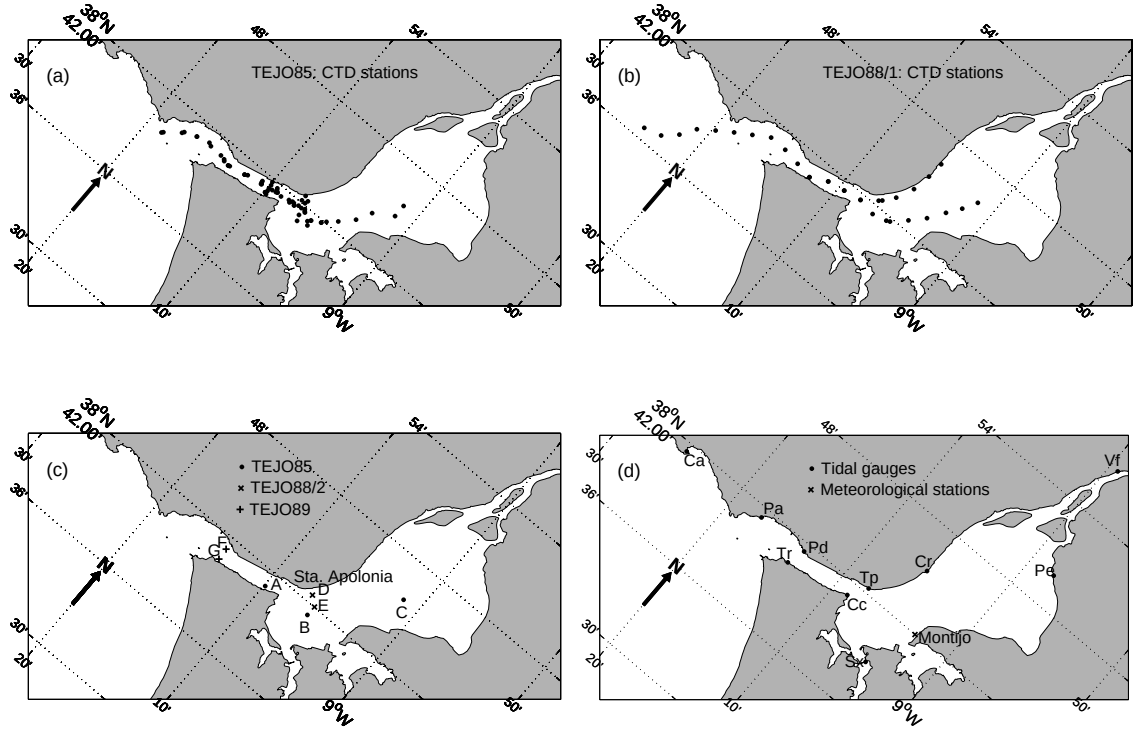

Figure 2.2 – Location of (a) TEJO85 CTD stations, (b) TEJO88/1 CTD stations, (c) current meters suspended from anchored ships during TEJO85 (A, B, C), moorings with current meters and thermistor chains during TEJO88/2 (D, E) and TEJO89 (F, G), (d) tidal gauges (Ca: Cascais, Pa: Paço de Arcos, Tr: Trafaria, Pd: Pedrouços, Cc: Cacilhas, Tp: Terreiro do Paço, Sx: Seixal, Cr: Cabo Ruivo, Pe: Ponta da Erva, Vf: Vila Franca de Xira) and Montijo meteorological station.

In February 1988, the hydrographic survey TEJO88/1 was conducted from aboard the research vessel "Mestre Costeiro" (from Fisheries Institute – IPIMAR), using a Meerestechnick Elektronik OTS-27 CTD probe, along the Tagus Estuary from the mouth to the interior's two main channels (Fig. 2.2(b)), both at high and low tide, in neap tide

conditions. The collected data, which consists in 70 CTD profiles obtained at 28 different sites, was validated and linearly interpolated to 1-dbar steps (Ambar, 1989).

In August 1988 (TEJO88/2), time series of current and hydrographic data were obtained using moored Aanderaa current meters (RCM-4S) and thermistor chains (TR-2) located at two sites within the estuary's interior. In each of these sites, three moorings were placed, one with a near-surface current meter, another with a near-bottom current meter and a third one with a thermistor chain extending through the whole water column (Fig. 2.3(a)). The RCM's sampling interval was 5 minutes, while the TRs recorded the data with a sampling interval of 10 minutes. These moorings were located in the transition between the inlet channel and the beginning of each of the main channels of the inner bay of the estuary (sites D and E in Fig. 2.2(c)).

In November 1989 (TEJO89), time series of current and hydrographic data were obtained using sets of moorings with Aanderaa current meters (RCM-7) and thermistor chains (TR-7) located at two sites near the estuary's mouth (sites F and G in Fig. 2.2(c)). Each set was constituted by three moorings, one with a near-surface current meter, another with mid-water and near-bottom current meters, and a third one with a thermistor chain extending through the whole water column (Fig. 2.3(b)). Many of these instruments were not retrieved due to damages caused by a severe storm and associated river runoff peak, which occurred soon after their deployment. Only the near-bottom and mid-water current meters were recovered. The RCM's sampling interval was 5 minutes.

Although all these field campaigns were designed to obtain current and hydrographic observations for different forcing conditions, the cases "summer/neap tide" and "winter/spring tide" are missing. The more recent observational campaigns, carried out in the frame of the project INTAGUS (presented in Section 2.2), were designed to fill this gap.

All the measured time series of temperature, salinity and current velocity (along and across-channel components), as well as the vertical distributions of temperature and salinity obtained during the campaigns are represented in Appendix B.

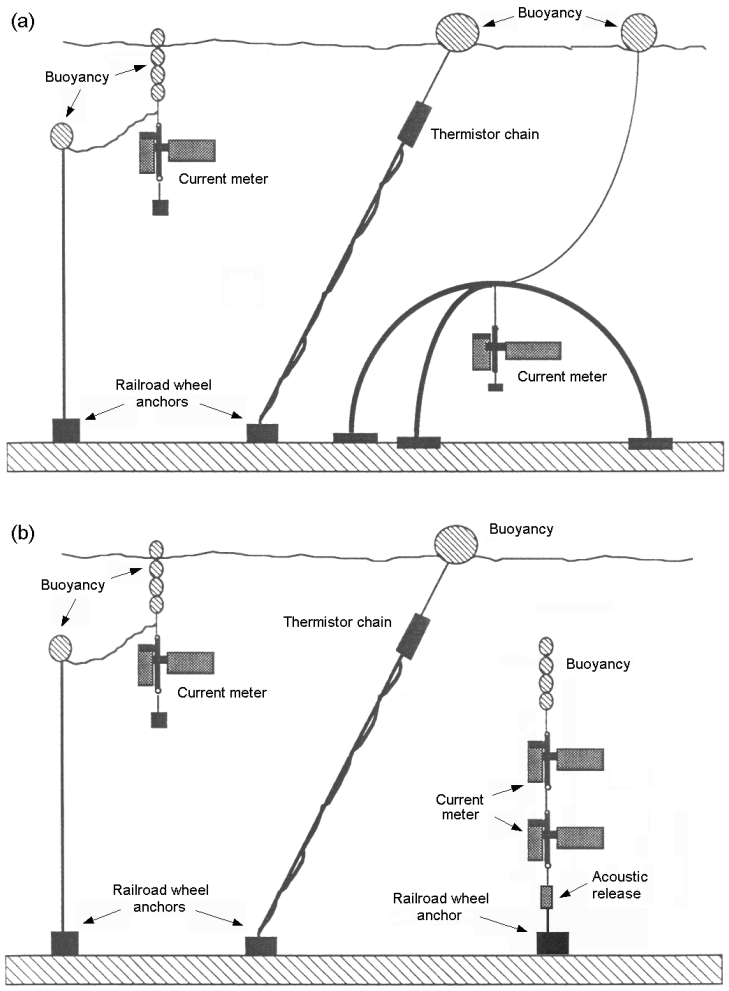

Figure 2.3 – Schematic representation of the moorings used in (a) TEJO88/2 and (b) TEJO89 campaigns.

Pre-processing of time series

The raw data obtained with the current meters and thermistor chains were submitted to pre-processing procedures, which included the following steps: conversion of instrument values to engineering units, removal of the out-of-water measurements, detection and removal of erroneous values with subsequent interpolation.

Before converting the raw data to engineering units, the number of records in each time series was compared with the expected number, given the data acquisition period and the

sampling frequency. This verification is needed since errors can arise due to recorder's clock problems or digital samples missing during the recording stage (Emery and Thomson, 2001).

After this verification, the instrument values were converted to physical units. In the case of the RCMs, raw data columns of temperature, conductivity, pressure, current direction and current speed were respectively converted to units of "°C", "mmho cm^{-1}", "kg cm^{-2}", "magnetic degrees" and "cm s^{-1}". As for the thermistor chains, the eleven columns (corresponding to the number of thermistors along the chain) of raw temperature were converted to units of "°C". At this point, the conductivity and temperature values at both ends of the time series allowed to identify and remove the out-of-water samples.

The derived quantities, like salinity or the current velocity components, were computed using the parameters directly measured. Namely, the salinity was computed from conductivity, temperature and pressure (using the Unesco (1983) algorithms) and the zonal and meridional velocity components from current speed and direction (corrected from the magnetic declination for the location and date of each campaign).

All the individual time series (pressure, salinity, temperature and current velocity components) were then visually analysed in order to identify any unexpected values. Two types of errors were identified in the data: (1) "spikes" caused, for example, by equipment failure or power surges (Emery and Thomson, 2001); and (2) major gaps with abnormal data, either due to biological fouling (affecting the conductivity cells and/or the movement of the current meter rotor), or other causes that prevented the free movement of the current meter vane. Some examples of these errors are shown in Fig. 2.4, representing the time series of the RCM E_b (TEJO88/2, near-bottom).

The majority of the identified "spikes" consisted in outliers of one or two consecutive samples which, depending on the sampling rate, corresponded to holes of 5-10 minutes or 10-20 minutes in the data. According to Emery and Thomson (2001), when a significant fraction (30-50%) of the signal of interest is lost or when the overall data gap is about 20-30%, major dificulties may arise regarding interpolation. As that was not the case, the gaps left by "spike" removal were filled through linear interpolation.

In the presence of data loss situations, where the data is clearly not valid beyond a certain record, like the ones shown in the conductivity and in the current direction time

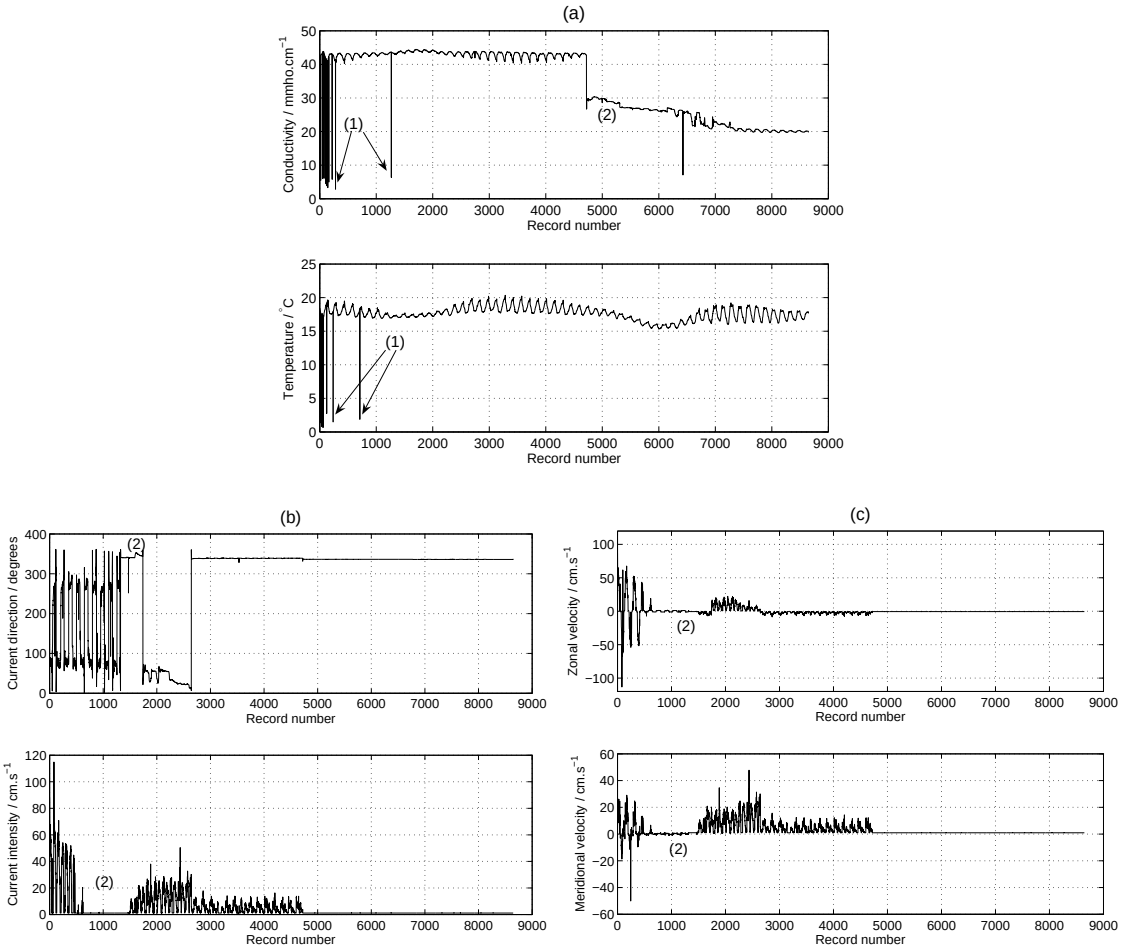

Figure 2.4 – Time series of (a) conductivity and temperature, (b) current direction and intensity and (c) zonal and meridional current velocity components, measured by the RCM E_b (TEJO88/2), after removing the out-of-water records. (1) – "Spikes"; (2) – Gaps with abnormal data.

series (Fig. 2.4), the non-valid data was simply discarded. The same procedure was applied on situations like the one shown in the current intensity time series (Fig. 2.4(b)), where the rotor of the RCM seems to have started working again after a period of inactivity. The data was discarded beyond the first stop, since there is no assurance that the rotor was completely free and working properly.

2.1.2 Water level, meteorological and river discharge data

The water level data contemporary with the above described campaigns, was provided by the Lisbon Harbour Administration (APL) at three different sites represented by the labels "Pa" (Paço de Arcos), "Tp" (Terreiro do Paço) and "Cr" (Cabo Ruivo) in Fig. 2.2(d). The data were provided in the form of tidal charts (represented in Appendix C) that were digitalised with a sampling period of five minutes. At Cascais, represented by the label "Ca" in Fig. 2.2(d), the water level records were obtained from the web site of the University of Hawaii Sea Level Center (http://ilikai.soest.hawaii.edu/uhslc/), with a sampling period of one hour.

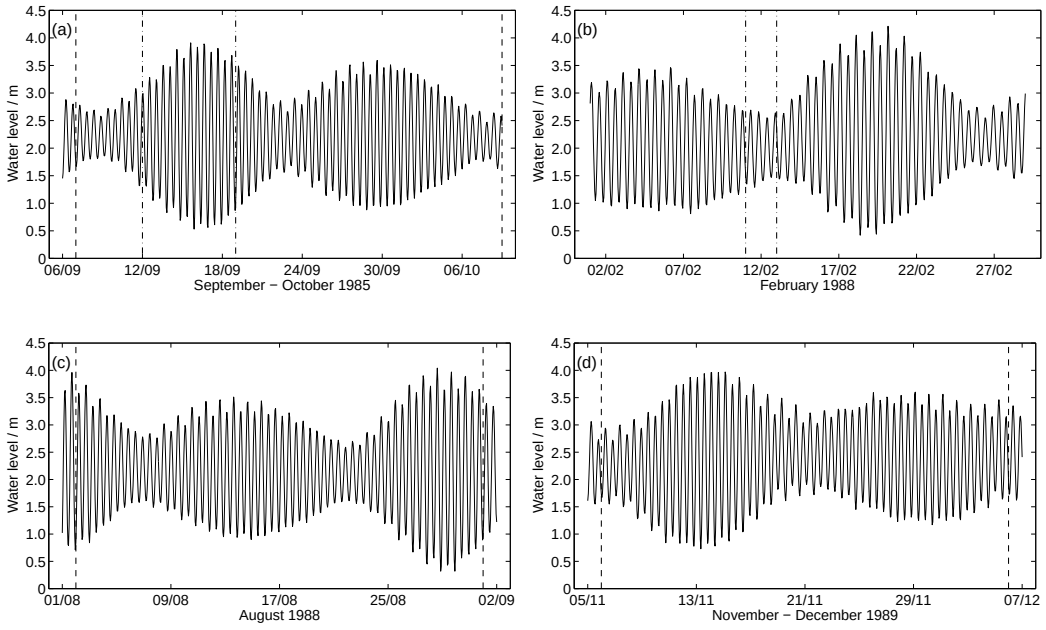

Figure 2.5 – Water level height at Cascais during (a) TEJO85, (b) TEJO88/1, (c) TEJO88/2 and (d) TEJO89 campaigns. The vertical lines mark the period of observations during RCM (dashed lines) and CTD (dot-dashed lines) surveys.

The tidal range – surface level difference between consecutive high and low water in a tidal cycle – was calculated for the periods of the observational campaigns, using the water level time series from Cascais, presented in Fig. 2.5. During TEJO85, the tidal range varied between 0.67 (corresponding to neap tide) and 3.38 m (corresponding to spring tide). The

CTD observations took place during the transition from neap to spring tide, when the tidal range reached 3.38 m. The period of the RCM campaign is delimited in Fig. 2.5(a) by dashed lines and the CTD campaign, by dot-dashed lines. The TEJO88/1 campaign took place during a neap tide peak (marked by dashed lines in Fig. 2.5(b)), with a tidal range of 1.08 m. During the RCM campaign TEJO88/2 the tidal range varied between 0.98 and 3.72 m (Fig. 2.5(c)). During the RCM campaign TEJO89 the tidal range varied between 1.02 and 3.18 m (Fig. 2.5(d)).

An additional water level database was also available and consists on one-year long records, with a sampling period of one hour, obtained at ten tidal gauges distributed along the estuary, in both margins (see Fig. 2.2(d) for locations). This one-year long water level database was used to study the tidal propagation within the Tagus Estuary (Chapter 3).

Meteorological data (surface air temperature, sea level pressure, wind velocity and direction) measured at Montijo during the campaigns were provided by the Portuguese Air Force (see Fig. 2.2(d) for location). These parameters were sampled every three hours during the day, generally from 6 to 18 o'clock.

The original records of wind had to be converted from meteorological convention (direction from which the wind blows) to oceanographic convention (direction towards which the wind blows). Then, the west-east and south-north wind velocity components were computed and interpolated to a regular sampling interval of 3 hours (equivalent to eight values per day). Fig. 2.6 represents the wind conditions during a period of about one month, within which the observational campaigns are included. This figure depicts the wind vectors with a six-hour time step (the dates of start and end of the campaigns are shown by vertical lines).

The sea-level pressure and air temperature series (represented in Fig. 2.7) were also interpolated to a regular sampling interval of 3 hours. The air temperature series clearly show the diurnal signal and, comparing the four periods of observations, it is also evident the variation of the mean air temperature between summer (roughly between 20 and 30 °C) and winter (roughly between 10 and 20 °C). As for sea-level pressure, larger variations are present during the winter campaigns (Figs. 2.7(b) and 2.7(d)).

Tagus river discharge data (time series of daily mean values), measured at Almourol (~130 km from the estuary's mouth), was obtained at the web site of Sistema Nacional

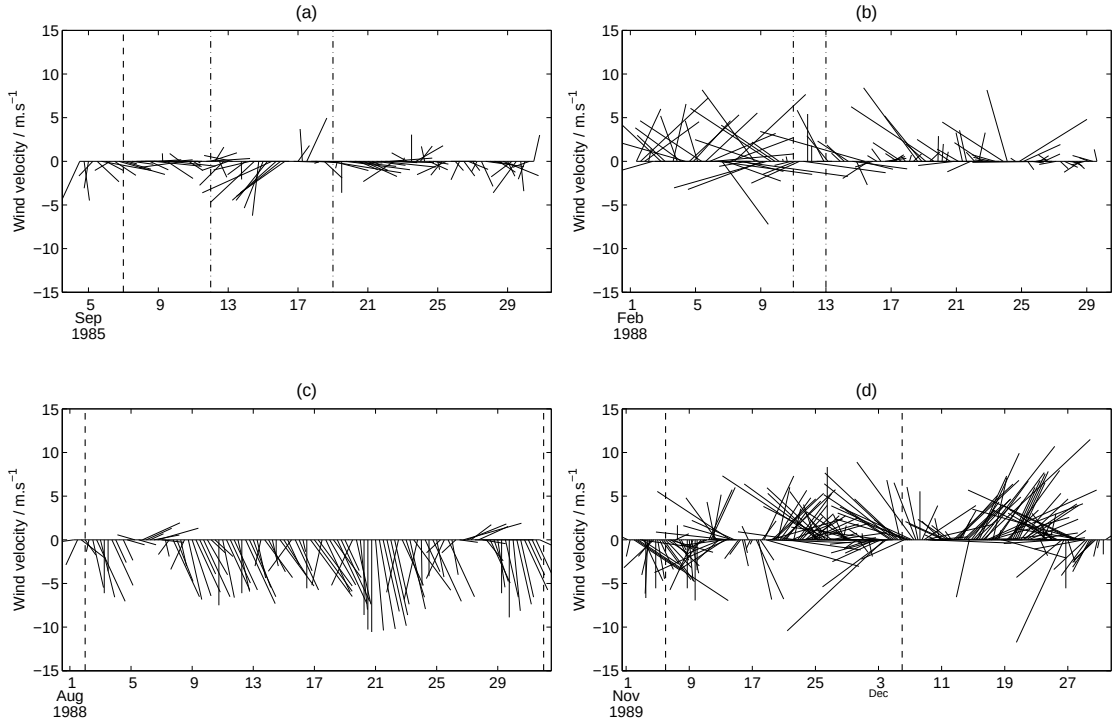

Figure 2.6 – Wind velocity and direction at Montijo during (a) TEJO85, (b) TEJO88/1, (c) TEJO88/2 and (d) TEJO89 campaigns. The vertical lines mark the period of observations during RCM (dashed lines) and CTD (dot-dashed lines) surveys.

de Informação de Recursos Hídricos (http://snirh.pt/). The data since October 1973 are available and the time series used in this study corresponds to the period between October 1973 and July 2008. This time series was used to calculate monthly mean values, which were used to characterise the freshwater input into the estuary during the observational campaigns (Fig. 2.8). The monthly mean river discharge was 184 m^3 s^{-1} during TEJO85 (September 1985), 1201 m^3 s^{-1} during TEJO88/1 (February 1988), 255 m^3 s^{-1} during TEJO88/2 (August 1988) and 611 m^3 s^{-1} during TEJO89 (November 1989).

Tables A.2 and A.3 in Appendix A gather more detailed information about the water level, meteorological and river discharge data, namely the start and end dates of the measurements used in this work and some characteristics of the sites where the data were collected.

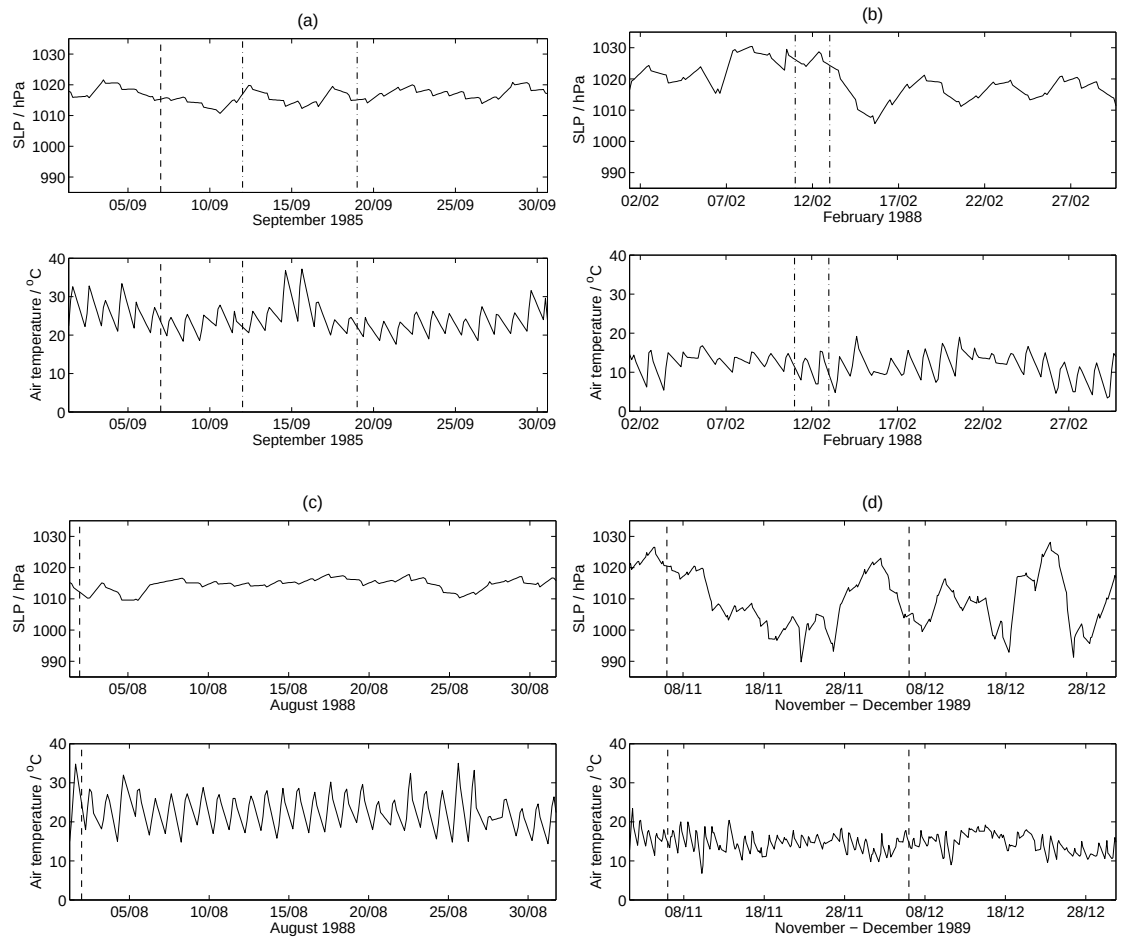

Figure 2.7 – Sea-level pressure (top) and air temperature (bottom) at Montijo during (a) TEJO85, (b) TEJO88/1, (c) TEJO88/2 and (d) TEJO89 campaigns. The vertical lines mark the period of observations during RCM (dashed lines) and CTD (dot-dashed lines) surveys.

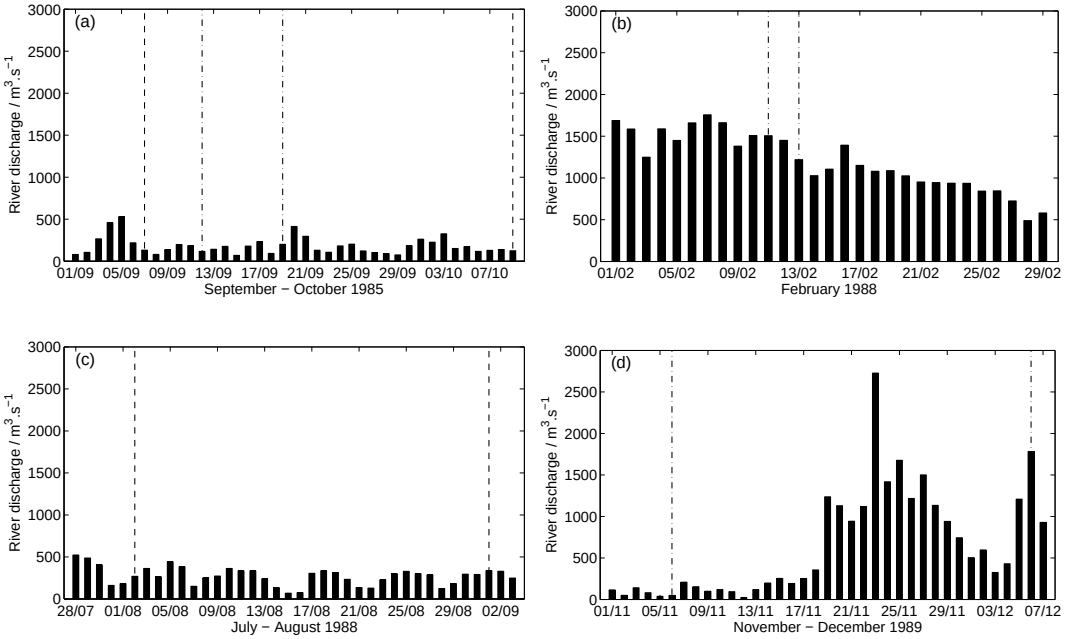

Figure 2.8 – Daily mean values of river flow during (a) TEJO85, (b) TEJO88/1, (c) TEJO88/2 and (d) TEJO89 campaigns. The vertical lines mark the period of observations during RCM (dashed lines) and CTD (dot-dashed lines) surveys.

2.2 INTAGUS campaigns

One of the main objectives of the research project INTAGUS – "Integrated physical and biological study of the Tagus Estuary and adjacent coastal ocean" – was to investigate the residual circulation in the inner region of the Tagus Estuary under realistic forcing conditions of the tide, wind and river discharge and its implications to the biological cycles as well as to the transport of contaminants.

Historical data sets collected in the Tagus Estuary were re-analysed, helping to design the observational strategy to be followed in the frame of this project. This re-analysis, the planning of the INTAGUS campaigns and their physical oceanography component were done as part of the present dissertation work.

2.2.1 Hydrographic and current velocity data

In the frame of the research project INTAGUS, two cross-sections were carried out in summer (22-23 August: INTAGUS07/1; 30-31 August 2007: INTAGUS07/2) and repeated in winter (10-11 January: INTAGUS08/1; 17-18 January 2008: INTAGUS08/2). The two cross-sections, one located at the deep, narrow inlet channel (section Channel – hereafter abbreviated as C) and another at the shallow, broad inner bay (section Bay – hereafter abbreviated as B) were sampled over an almost complete semi-diurnal tidal cycle during neap and spring tide peaks. Section C (5 stations) was occupied 9 times during neap and spring tide peaks in summer; in winter, this section was occupied 6 times during a spring tide peak and 7 times during a neap tide peak. Section B (7 stations in summer and 6 stations in winter) was occupied 8 times during the neap and spring tide peaks in summer and 7 times during the neap and spring tide peaks in winter. Each cross-section took about 50 to 60 minutes to complete. The location of the sections and the respective stations are represented in Fig. 2.9.

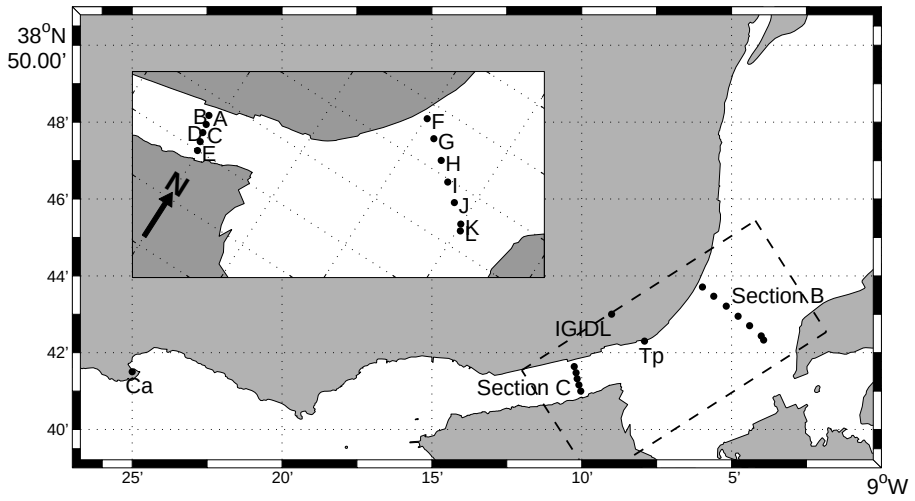

Figure 2.9 – Location of the CTD and current meter stations along sections Channel (C) and Bay (B) during the INTAGUS surveys, meteorological station at Lisboa (IGIDL) and tidal stations of Cascais (Ca) and Terreiro do Paço (Tp). Inset – Detailed view of the cross-sections C and B, corresponding to the area delimited by the dashed lines in the main figure. During the winter campaign, the station "L" at section B was not occupied.

During each survey, conducted from aboard a fishing boat, hydrographic and current velocity profiles were obtained, totalling 202 stations in summer and 149 stations in winter. The hydrographic data was measured using a Falmouth Scientific CTD probe (NXIC-CTD-ADC) and the current velocity was measured using an Aanderaa Doppler current sensor (DCS4100). The CTD probe and the current meter sensor were coupled as shown in Fig. 2.10. During the observational campaigns, the data measured by the CTD were stored in an internal memory, being downloaded at the end of each day, whereas the data acquired by the current sensor was sent to a data reading unit, from which it was sent directly to a computer aboard.

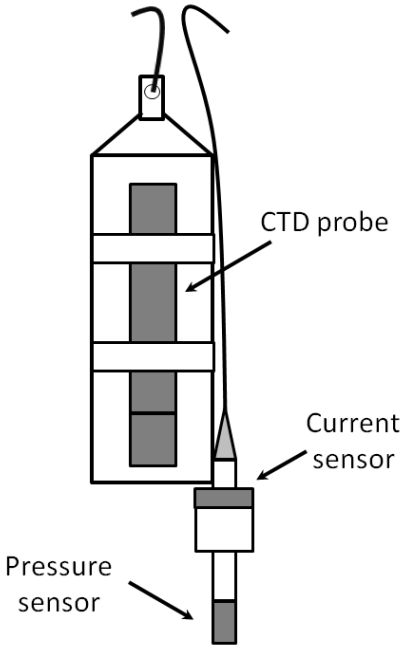

Figure 2.10 – Schematic representation of the coupling between the CTD probe and the current and pressure sensors used in the INTAGUS campaigns.

Due to logistical constraints, measurements were performed only during daylight. Their situation relative to the semi-diurnal tidal cycle is shown by the Fig. 2.11. For this reason, it was not possible to sample a complete semi-diurnal tidal cycle and the sampling periods in summer are longer than in winter.

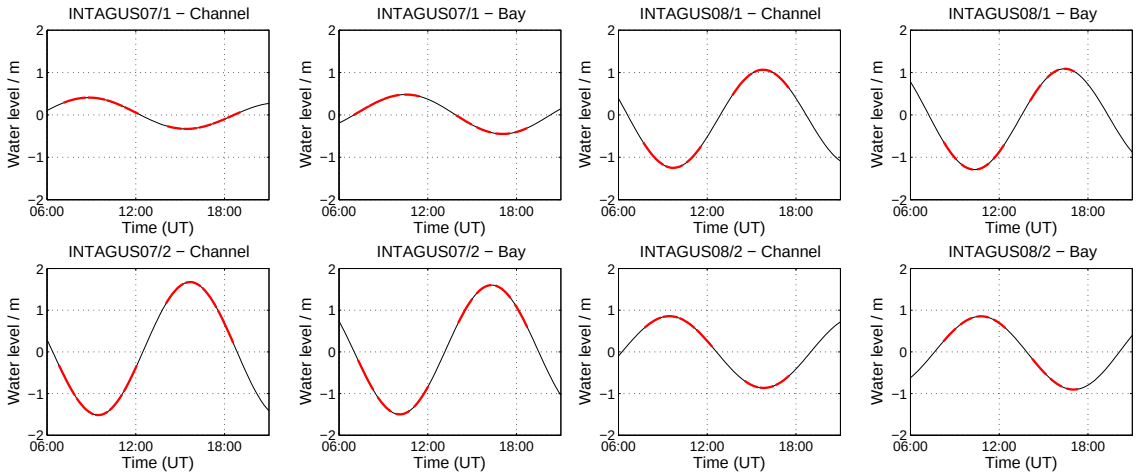

Figure 2.11 – Observations in the cross-sections during the INTAGUS campaigns and their situation (thick red lines) relative to the semi-diurnal tidal cycle.

Pre-processing of CTD and current velocity data

At the beginning of each station, the coupled CTD and DCS (Fig. 2.10) were lowered just below the water surface, with all the sensors submerged, for a period of about 1 minute, in order to bring the sensors to water temperature equilibrium.

The CTD was programmed to sample at 10 Hz. Given a descending velocity of about 1 m s^{-1} during a profile, this would provide about ten samples *per* meter. Conductivity (mmho cm^{-1}), temperature (°C) and pressure (dbar) were directly measured, whereas time, salinity (PSS-78) and sound velocity (m s^{-1}) were internally computed by the CTD.

Pressure measurement can be affected by a drift of the zero, by hysteresis or by temperature changes (Unesco, 1988), so a correction routine was applied to each profile, averaging the pressure measured in the instants before the beginning of a profile (out of the water) and removing the resulting value from the in-water pressure measurements. Having the pressure offset corrected, the out-of-water ($p < 0.5$ dbar) samples were removed and the up and downcasts were separated. The data were then linearly interpolated to 0.5-dbar steps, starting at the 1 dbar level.

In what concerns the Doppler current sensor (DCS), its sampling frequency was of 1 Hz, measuring the current speed (cm s^{-1}) and direction (magnetic degrees) and also the

temperature (°C). These measurements were transmitted in real-time during the profiles and stored in a computer aboard. The downcast was the one selected for further use, so the sensors were stopped approximately every meter in order to stabilize the measurement of the current velocity.

During the profile measurements, the vessel drifted and with it, the referential of the measured velocity. To minimise this problem, the initial and final position of each station combined with the corresponding elapsed time were used to estimate a mean drift velocity vector which was added to the current profile at each location. Having corrected the current direction from the magnetic declination, the zonal and meridional current components were computed and corrected for the drift of the vessel. To finish the pre-processing, the data was linearly interpolated to 1-dbar steps, starting at the 2 dbar level.

All the vertical distributions of temperature, salinity and along-channel current velocity obtained during the INTAGUS campaigns are represented in Appendix B.

2.2.2 Water level, wind and river discharge data

The water level data (hourly values) for the period of the campaigns was measured by the Hydrographic Institute (IH) of the Portuguese Navy at Cascais and at Terreiro do Paço (see Fig. 2.2(d) for location). These time series were used to calculate the tidal range. During the summer campaigns (INTAGUS07), the tidal range at Terreiro do Paço varied between 1.10 m (neap tide) and 3.60 m (spring tide); during the winter campaigns (INTAGUS08), the tidal range at Cascais varied between 1.60 m (neap tide) and 2.55 m (spring tide). Figs. 2.12(a) and 2.12(b) depict the water level time series during August 2007 and January 2008. In January 2008, the data set has a gap at around day 9. The vertical lines in the figures represent the period of observations during spring tide (dashed lines) and neap tide (dot-dashed lines).

Hourly mean values of wind velocity and direction, obtained at a meteorological station in Lisbon, were provided for the months of August 2007 and January 2008 by the Geophysical Institute Infante Dom Luiz (IGIDL) (see Fig. 2.9 for location). The wind direction had to be converted from meteorological to oceanographic convention, and then the west-east and south-north wind velocity components were computed. Figs. 2.12(c) and 2.12(d) depict the wind data as six vectors per day, which is equivalent to a four-hour time

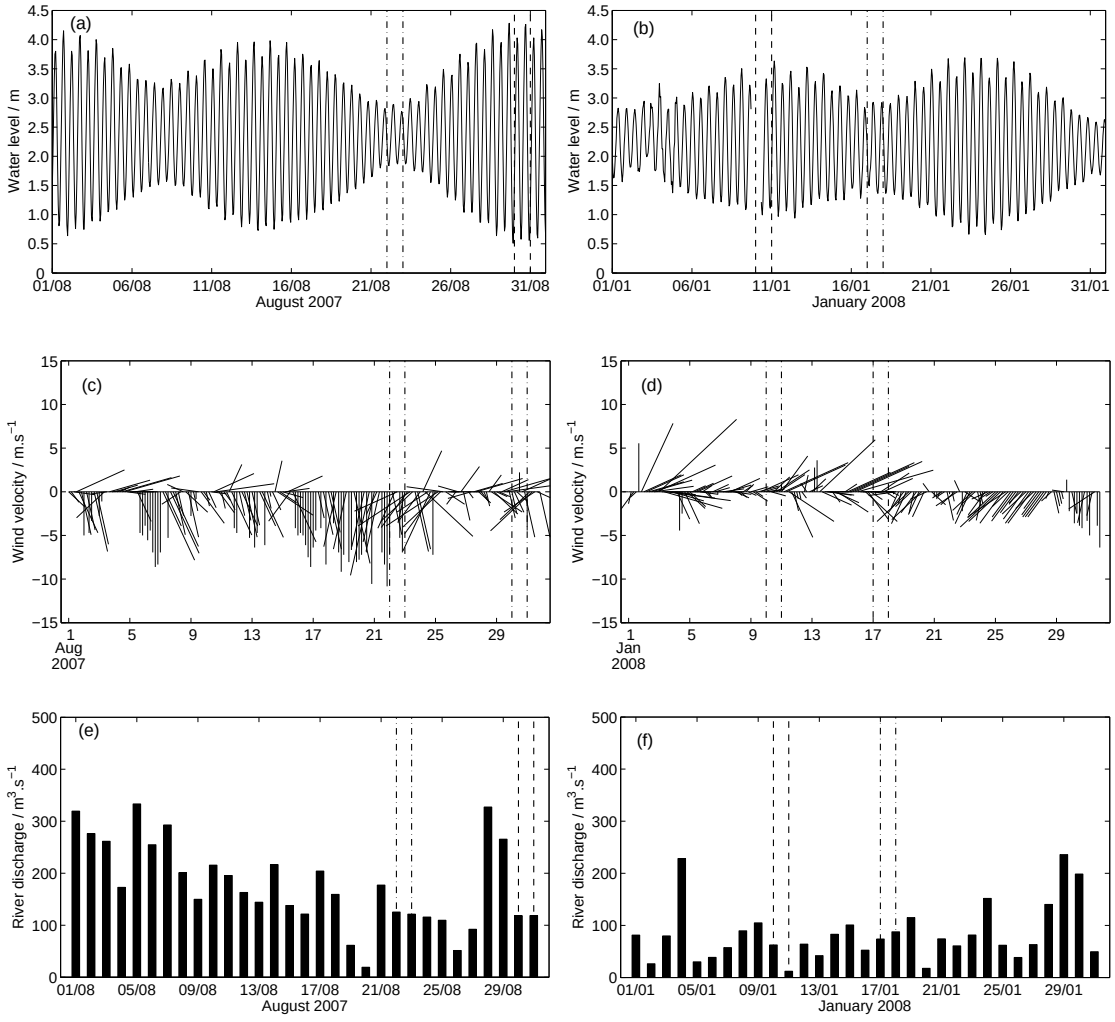

Figure 2.12 – Water level, wind velocity and direction and daily mean values of river flow during (a), (c) and (e) INTAGUS07 and (b), (d) and (f) INTAGUS08 campaigns. The vertical lines mark the period of observations during spring (dashed lines) and neap (dot-dashed lines) tide.

step.

The monthly mean river discharge was 178 m^3 s^{-1} for August 2007 (INTAGUS07) and 84 m^3 s^{-1} for January 2008 (INTAGUS08). These values were calculated from the river discharge time series obtained at the web site http://snirh.pt/ (see Section 2.1.2). The daily

mean values of river discharge during August 2007 and January 2008 are represented in Figs. 2.12(e) and 2.12(f).

Additional information about the water level, wind and river discharge data, namely the start and end dates of the measurements used in this work (contemporary with the observational campaigns) and some characteristics of the sites where the data were collected can be found in Appendix A (Tables A.2 and A.3).

Chapter 3

Tidal propagation within the Tagus Estuary

This chapter is devoted to the description of the tidal propagation within the Tagus Estuary. Water level and current velocity time series are analysed in order to characterise the forcing action of the tide at the estuary's mouth and its evolution inside the estuary. The tidal gauge at Cascais is considered as measuring the oceanic tide forcing at the mouth of the estuary. The analysis of the distortion of the tidal wave within the estuary and the consequent tidal asymmetry, are the main focuses of this chapter.

3.1 Shallow-water tides

The oceanic tide, generated by the gravitational attraction of the moon and the sun, can be represented by the sum of a finite number of sinusoidal or harmonic constituents, grouped into three main species: (*i*) semi-diurnal, with periods of about half day; (*ii*) diurnal, with periods of about one day; and (*iii*) long-period, including all tidal oscillations with periods ranging from 14 days to 19 years.

Given the relatively small dimensions and depths of most estuaries, the direct effect of the gravitational attraction of the moon and the sun on their waters is usually negligible. Therefore, the tide within the estuary is mainly driven by the cooscillation forced by the oceanic tide at its entrance.

While the tidal wave propagates into shallower waters within the estuary, it becomes distorted due to several physical processes, including reflection at the head of the estuary, which is responsible for standing-wave generation and local resonances (Pugh, 1987). Fig. 3.1 depicts the relation between water level and tidal current in the case of a pure standing wave, a pure progressive wave and a system with standing and progressive contributions. In a standing wave system, the tidal elevation and the associated current velocity are 90° out of phase, meaning that slack water (reversal of a tidal current from flood to ebb or vice-versa) will be simultaneous either with high or low water (see Fig. 3.1 (b)). If the energy of the tidal wave is completely dissipated by friction before reflection takes place, then the tidal wave becomes purely progressive (Fig. 3.1 (c)). In this case, tidal elevation and currents are in phase, meaning that maximum flood [ebb] currents occur at high [low] water. In most estuaries, the tidal waves are a mixture of standing and progressive contributions (as in Fig. 3.1 (d)) and the progressive wave contribution can be estimated by the time difference between high or low water and the respective slack water (Dyer, 1997).

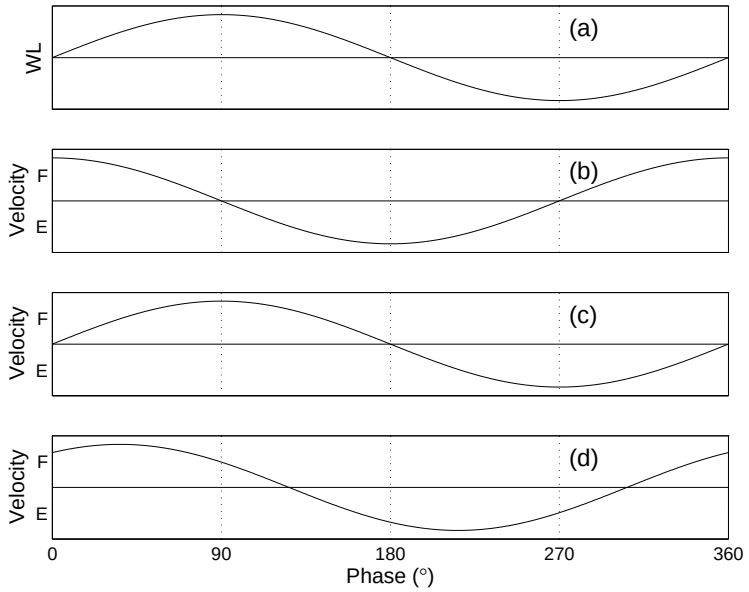

Figure 3.1 – (a) Schematic water level and corresponding velocity variation during one tidal cycle for (b) a pure standing wave, (c) a pure progressive wave and (d) a combination of the two types. F – Flood; E – Ebb.

In estuarine shallow waters, the tidal range frequently becomes a non-negligible fraction of the total water depth and has to be considered for the tidal wave celerity $c = \sqrt{g\,(H + \zeta)}$, where g is the acceleration due to gravity, H is the water column mean depth and ζ is the water surface elevation relative to the mean depth. This means that the wave crest moves faster than the trough, resulting in shorter and more intense flood than ebb currents. Bottom friction is also an important factor that affects tidal wave propagation in shallow waters, delaying the water movement. This is a non-linear process since it depends on the square of the current velocity. Therefore, propagation of the tide in shallow waters develops time asymmetries in the rise and fall of the water surface, as well as in the duration and magnitude of the tidal currents.

These distortions of the normal harmonic variations of tidal levels and currents associated with friction and shallow-water effects, can be represented as harmonic constituents (overtides and compound tides) with angular speeds which are multiples, sums or differences of the astronomical constituents. Overtides are, in fact, higher frequency harmonics of the principal harmonic constituents, e.g. M_4 or M_6, both originated by M_2; or S_4, which is originated by S_2. On the other hand, compound tides are originated by linear combinations of at least two principal harmonic constituents, e.g. M_{sf}, which is the combination of M_2 and S_2; or MK_3, resulting from the combination of M_2 and K_1.

Even [odd] harmonics are those whose frequency is an even [odd] multiple of the original constituent's frequency, e.g. M_4 is an even harmonic of M_2 ($\omega_{M_4} = 2\omega_{M_2}$) and M_6 is an odd harmonic of M_2 ($\omega_{M_6} = 3\omega_{M_2}$). Even harmonics can be primarily generated by the non-linear terms in the equations of momentum (advection) and of continuity, as the response to the increase in the ratio between wave amplitude and total water depth on the celerity of crests and troughs (Parker, 1991). The depth also affects the frictional loss of momentum *per* unit volume of fluid, which is smaller for deeper water columns. In this sense, in shallow waters, crests will tend to travel faster than troughs, leading to the generation of even harmonics. When a mean flow is present (i.e. river flow), the quadratic friction term can cause the delay of the trough relatively to the crest, giving only a small contribution to the generation of even harmonics. Odd harmonics are essentially generated by the quadratic friction term.

Tidal asymmetry is, therefore, the effect of the non-linear growth of overtides and com-

pound tides of the principal harmonic constituents (Dronkers, 1964; Aubrey and Speer, 1985), resulting from finite amplitude effects on the friction and non-linear advection terms. When the tide is distorted, energy is transferred from principal to shallow-water constituents.

Field observations and theoretical work have shown that whenever M_2 is the highest magnitude constituent, it dominates non-linear processes within the estuary (Dronkers, 1964). This author also showed that the interaction between M_2 and its first harmonic, M_4, can explain the general features of tidal asymmetry. Thus, the major part of the tide asymmetry can be represented by the superposition of the constituents M_2 and M_4, both in terms of water level (A) and current velocity (V):

$$\begin{aligned} A &= a_{M_2} \cos(\omega t - \theta_{M_2}) + a_{M_4} \cos(2\omega t - \theta_{M_4}) \\ V &= v_{M_2} \cos(\omega t - \varphi_{M_2}) + v_{M_4} \cos(2\omega t - \varphi_{M_4}) \ , \end{aligned} \tag{3.1}$$

where ω is the M_2 angular frequency and t represents the time; a_{M_2}, a_{M_4} and v_{M_2}, v_{M_4} represent the respective water level amplitudes and current velocity amplitudes; θ_{M_2}, θ_{M_4} and φ_{M_2}, φ_{M_4} represent the respective water level phases and current velocity phases.

Tidal asymmetry can occur with either *flood* or *ebb dominance*. The ratio M_4 to M_2 amplitude, in both water level and current velocity, is used to indicate the magnitude of the tidal asymmetry within the estuary. In addition, both the water level and the current velocity phase of M_4 relative to M_2 (defined as twice the phase of M_2 minus the phase of M_4) are used to identify the type of asymmetry (Aubrey and Speer, 1985; Speer and Aubrey, 1985): flood dominance (0° – 180° for water level and -90° – 90° for current velocity); ebb dominance (180° – 360° for water level and 90° – 270° for current velocity). These relationships are summarised in Fig. 3.2 by the shaded semi-circles and the arrows indicate the relative phases of maximum flood dominance (90° for water level and 360° for current velocity) and ebb dominance (270° for water level and 180° for current velocity) asymmetry. Despite the existence of the shallow-water constituent M_4, the tide can be symmetric for relative phases 180° and 360°, in what respects water level, and 90° and 270°, relative to current velocity.

Usually, in flood dominant estuaries the flood has shorter duration and higher velocity whereas in ebb dominant estuaries the ebb has shorter duration and higher velocity. However some authors (e.g. Blanton and Andrade, 2001; Seim et al., 2006) have reported the

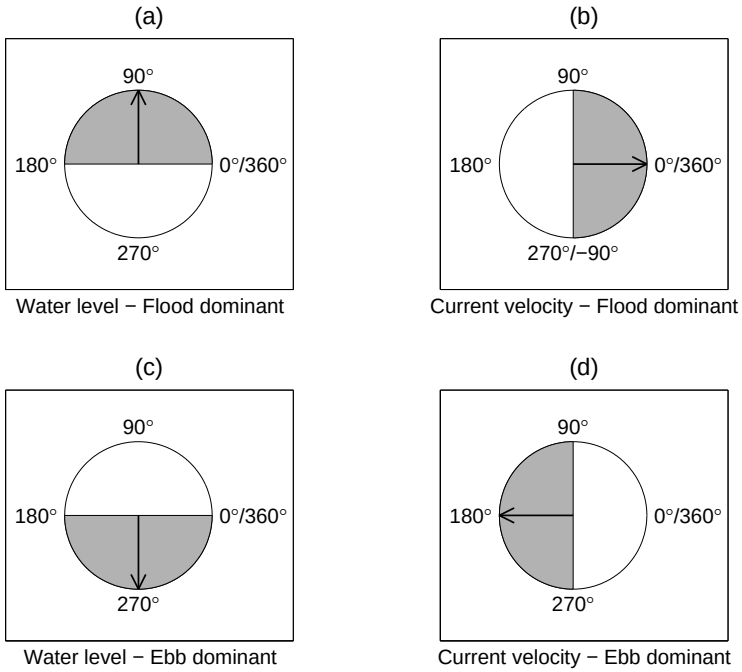

Figure 3.2 – Schematic representation of the linear relationships between relative phase (water level: $2\theta_{M_2} - \theta_{M_4}$; current velocity: $2\varphi_{M_2} - \varphi_{M_4}$) and tidal distortion.

existence of ebb dominant estuarine systems with stronger and longer ebbs, in opposition to the classical concept of stronger but shorter ebbs in ebb dominant systems. Nevertheless, these results are reasonable in estuarine systems where there is enough freshwater inflow to produce a horizontal pressure gradient, acting seaward, making the ebb phase longer than the flood. The harmonic analysis results presented by Seim et al. (2006) for the phase of M_4 relative to M_2 indicated flood dominance in terms of water level ($2\theta_{M_2} - \theta_{M_4} = 121°$) and ebb dominance concerning the vertically integrated current velocity ($2\varphi_{M_2} - \varphi_{M_4} = 136°$).

Tidal asymmetry has important implications for estuarine sediment transport, water contaminants dispersal and, on geological time scales, estuarine stability (Aubrey and Speer, 1985; Speer and Aubrey, 1985; Pugh, 1987). Flood dominant estuaries tend to accumulate coarse sediments in their channels whereas ebb dominant estuaries tend to flush seaward the near-bed sediments.

Friedrichs and Aubrey (1988) combined water level measurements and one-dimensional

numerical modelling to define estuarine characteristics responsible for the different types of tidal asymmetry. They concluded that tidal distortion in shallow estuaries can be the result of two effects: (1) frictional interaction of the tide with the bottom and (2) storage of water on intertidal flats and saltmarshes. These authors concluded that the ratio M_4/M_2 is primarily controlled by the first effect in flood dominant estuaries and by the second effect in ebb dominant estuaries.

3.2 Methodologies

3.2.1 Principal axes

The analysis of vector times series usually starts by deriving the principal axes from the data. In this new coordinate system most of the variance is associated with a major axis and the remaining variance with a minor axis. This is a common technique for improving Empirical Orthogonal Function (EOF) analysis as well as Principal Component Analysis (PCA) (Emery and Thomson, 2001).

Considering the example of a current velocity (speed and direction) time series, the observed velocity vector is given as $\mathbf{u}(t) = \left[\overline{u_1}(t) + u_1'(t) \quad \overline{u_2}(t) + u_2'(t)\right]$, where $\overline{u_1}$ and $\overline{u_2}$ are, respectively, the west-east and south-north mean components and u_1' and u_2' the fluctuations relative to the mean. The problem consists of finding the principal axes of variance, along which the variance of the vector time series, contained in u_1' and u_2', is maximised for a given location. The principal axes are defined in such a way that the velocity components along them are uncorrelated (Emery and Thomson, 2001).

It is then an eigenvalue problem $\mathbf{C}\phi - \lambda\mathbf{I}\phi = 0$, which for a two-dimensional case has the explicit form:

$$\begin{vmatrix} C_{1,1} & C_{1,2} \\ C_{2,1} & C_{2,2} \end{vmatrix} \begin{vmatrix} \phi_1 \\ \phi_2 \end{vmatrix} = \begin{vmatrix} \lambda & 0 \\ 0 & \lambda \end{vmatrix} \begin{vmatrix} \phi_1 \\ \phi_2 \end{vmatrix}, \tag{3.2}$$

where C_{ij} are the components of the covariance matrix $\mathbf{C}$,

$$C_{ii} = \overline{u_i'^2} = \frac{1}{N}\sum_{n=1}^{N}\left[u_i'(t_n)\right]^2$$
$$C_{ij} = \overline{u_i'u_j'} = \frac{1}{N}\sum_{n=1}^{N}\left[u_i'u_j'(t_n)\right] \ ,$$

and (ϕ_1, ϕ_2) are the eigenvectors associated with the two possible eigenvalues λ. The principal axes are computed by setting the determinant of equation (3.2) to zero and the result is the quadratic equation:

$$\left(\overline{u_1'^2} - \lambda\right)\left(\overline{u_2'^2} - \lambda\right) - \overline{u_1'u_2'}^2 = 0 \Leftrightarrow$$
$$\Leftrightarrow \lambda^2 - \left[\overline{u_1'^2} + \overline{u_2'^2}\right]\lambda + \overline{u_1'^2}\,\overline{u_2'^2} - \overline{u_1'u_2'}^2 = 0 \ , \tag{3.3}$$

whose two roots λ_1 and λ_2 ($\lambda_1 > \lambda_2$) are the eigenvalues, corresponding to the variances of the velocity fluctuations along the major and minor principal axes. The principal angle (θ_p), defining the direction along which the variance is maximum (Emery and Thomson, 2001), is given by

$$\theta_p = \frac{1}{2}\arctan\left[\frac{2\overline{u_1'u_2'}}{\overline{u_1'^2} - \overline{u_2'^2}}\right] \ , \tag{3.4}$$

and lies within the range $-\pi/2 \leq \theta_p \leq \pi/2$.

The principal variances (λ_1, λ_2) are obtained from equation (3.3) as:

$$(\lambda_1, \lambda_2) = \frac{1}{2}\left\{\left(\overline{u_1'^2} + \overline{u_2'^2}\right) \pm \left[\left(\overline{u_1'^2} - \overline{u_2'^2}\right)^2 + 4\left(\overline{u_1'u_2'}\right)^2\right]^{1/2}\right\} \ , \tag{3.5}$$

in which the (+) sign is used for λ_1 and the (−) sign is used for λ_2.

The knowledge of the principal axes directions allows to rotate the original vector time series, defining new orthogonal components of the velocity vector along and across the major principal axis direction.

This methodology was applied to the measured current velocity time series in order to find the main direction of the flow in each site within the estuary. Then, the current velocity time series were rotated to the new orthogonal directions, the analysis of the data being focused on the velocity component along the main direction of the flow.

3.2.2 Harmonic analysis

Harmonic analysis is a methodology widely used in the analysis of time series, especially to study tidal surface elevations and currents. It allows to examine specific frequencies and to solve for the harmonic constituents, through the application of least-squares techniques. The tidal signal is thus modelled as the sum of a finite set of sinusoids of specific frequencies. Each one of these frequencies is specified by various combinations of sums and differences of integer multiples of six fundamental frequencies originated by the planetary motions (Godin, 1972) – the *Doodson numbers*. These fundamental frequencies reflect the effects of rotation of the earth (lunar day of 24.8 hours), of the orbital motion of the moon around the earth (lunar month of 27 days) and of the earth around the sun (tropical year), and of periodicities in the location of the lunar perigee (8.85 years), of the lunar orbit tilt (18.6 years), and of the location of the perihelion ($\approx$ 21000 years).

The least-squares harmonic analysis method allows the resolution of several hundred tidal constituents, 45 of which are typically astronomical in origin whereas the remaining include shallow-water constituents, associated with bottom frictional effects and other non-linear terms in the equations of motion (Emery and Thomson, 2001). The length of the time series is the major constraint to determine which constituents should be analysed. A specific tidal constituent should be included in the tidal analysis if the difference between its frequency, f_m, and that of the closest neighbour, f_R, is at least, equal to the fundamental frequency $f_0 = 1/T$ (T represents the total record length). This is expressed by the Rayleigh criterion:

$$|f_m - f_R|\, T \geq R \tag{3.6}$$

where R is typically equal to 1. In fact, the formula means that f_m should be included if f_R is included and the fundamental frequency is less or equal to the frequency separation between those constituents. The choice of f_R is determined by the contribution of this constituent to the tidal potential of the Equilibrium Tide[1]. For example, the major contributor to the Equilibrium Tide in the diurnal band is K_1, whereas in the semi-diurnal band is M_2. The Table 3.1 summarises the required record lengths for inclusion of some of the more important tidal constituents within the respective species (long-period, diurnal, semi-,

[1] Equilibrium tide is the hypothetical tide which would be produced by the lunar and solar tidal forces in the absence of ocean constraints and dynamics.

quarter- and sixth-diurnal).

Long-period		Diurnal		Semi-diurnal		Quarter-diurnal		Sixth-diurnal	
Constituent	RL (h)	Constituent	RL (h)	Constituent	RL (h)	Constituent	RL (h)	Constituent	RL (h)
M_{sf}	355	K_1	24	M_2	13	M_4	25	M_6	26
M_m	764	O_1	328	S_2	355	MS_4	355	$2MS_6$	355
M_f	4383	Q_1	662	N_2	662	MN_4	662	$2MN_6$	662
		P_1	4383	K_2	4383				

Table 3.1 – Required record lengths (RL) to resolve the main tidal constituents in the long-period, diurnal, semi-, quarter- and sixth-diurnal tidal bands.

The aim of the least-squares analysis is to estimate the amplitudes (H_n) and phases (g_n) of the tidal harmonic constituents, providing a compression of the data in the complete time series. It thus allows the comparison of similar data from different locations, in order to understand the characteristics of tidal dynamics. This data reduction can also be used to generate long-term tidal predictions. Tidal variations can therefore be represented by the sum of a finite number of harmonic terms like:

$$H_n \cos(\omega_n t - g_n) \ . \tag{3.7}$$

The least-squares fitting method has several advantages (Pugh, 1987): (*i*) gaps in data are permissible, since fitting is confined to the times when observations were taken; (*ii*) any length of data is admissible, usually complete months or years; (*iii*) transient phenomena are eliminated and (*iv*) several data sampling frequencies are possible, the most common being one hour.

In the present work, harmonic analysis was performed using T_TIDE (Pawlowicz et al., 2002), a package of MATLAB routines. This harmonic analysis package was applied both on scalar (water level, temperature and salinity) and vector (horizontal currents measured by moored current meters) time series. An important feature of this harmonic analysis package is the estimate of the 95% confidence interval associated with each calculated amplitude and phase. Once the confidence interval is estimated, a signal-to-noise power ratio (SNR) is computed based on the square of the ratio of amplitude to amplitude error. Only the constituents whose SNR is above a pre-determined value (usually 1 or 2) are

considered significant. In the present study, only the constituents with SNR > 1 were considered as significant.

Vector time series can be represented as complex numbers $u + iv$, where u is the zonal (west-east) current component and v the meridional (south-north) current component. According to Pawlowicz et al. (2002), the complex form of the currents is based on a physical model of a rotating current vector, which is valid only for linear or nearly linear tidal waves. If that would not be the case, then current time series should be treated as two separate scalar time series (e.g. along and across-channel currents).

The amplitude and phase of each harmonic constituent, determined for each component of the horizontal current (zonal and meridional or along and across-channel), can be used to calculate the parameters of the respective constituent current ellipse, the ellipse traced out by the tip of the velocity vector during one complete tidal cycle (represented by the scheme in Fig. 3.3). In the case of current time series treated as along and across-channel currents, the components of a harmonic constituent are given by:

$$\begin{aligned} U &= \cos(\omega t - g_u) \\ V &= \cos(\omega t - g_v) \ , \end{aligned} \tag{3.8}$$

where U and V are the respective amplitudes and g_u and g_v the respective phase angles.

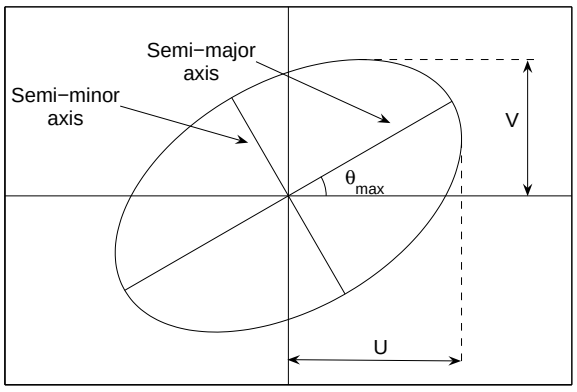

Figure 3.3 – Basic parameters to represent a tidal current ellipse.

Considering the ellipse represented by the scheme in Fig. 3.3, the parameters that allow to describe it can be computed following Pugh (1987). The semi-major (q_{max}) and semi-

minor (q_{min}) axes of the ellipse are given by:

$$\begin{aligned} q_{max} &= \left(\frac{U^2 + V^2 + \alpha^2}{2}\right)^{1/2} \\ q_{min} &= \left(\frac{U^2 + V^2 - \alpha^2}{2}\right)^{1/2} \end{aligned} \quad , \tag{3.9}$$

where

$$\alpha^2 = \left(U^4 + V^4 + 2U^2V^2 \cos 2\left(g_u - g_v\right)\right)^{1/2} \quad . \tag{3.10}$$

The eccentricity of the ellipse may be calculated as:

$$e = \frac{q_{max} - q_{min}}{q_{max} + q_{min}} \, . \tag{3.11}$$

The orientation of the ellipse is given by the direction of the maximum current speed, which is the direction of the semi-major axis:

$$\theta_{max} = \arctan\left[\frac{V \cos\left(g_u - g_v - \delta\right)}{U \cos \delta}\right] \, , \tag{3.12}$$

where

$$\delta = \frac{1}{2} \arctan\left[\frac{V^2 \sin 2\left(g_u - g_v\right)}{U^2 + V^2 \cos 2\left(g_u - g_v\right)}\right] \, . \tag{3.13}$$

The sense of the ellipse vector rotation is given by the following criteria:

$0 < g_v - g_u < \pi$	counter-clockwise
$\pi < g_v - g_u < 2\pi$	clockwise
$g_v - g_u = 0, \pi$	rectilinear flow .

3.2.3 Stage-velocity diagrams

Stage-velocity diagrams, also called hysteresis diagrams (Dyer, 1997), are the representation of the temporal evolution of water level versus current velocity. The stage-velocity diagrams are useful to determine the phase difference between water level and current velocity time series, in order to evaluate the standing or progressive character of a tidal wave. As stated in Section 3.1, in a theoretical standing wave system, slack water occurs simultaneously with high and low waters, whereas for a theoretical progressive wave propagation, slack water occurs midway between high and low water. The stage-velocity diagrams allow to evaluate the progressive character of a tidal wave, through the distance between the

points in the diagram corresponding to the high or low water and those corresponding to the slack water. The time lag between high or low water and the corresponding slack water can then be converted to a phase lag, in degrees.

Stage-velocity diagrams have also been used by some authors (e.g. Blanton et al., 2002) to describe tidal asymmetry by showing the distortion of the diagram caused by adding the shallow-water constituents M_4 and M_6 to the main semi-diurnal constituent M_2.

In order to represent such diagrams, the ideal situation would be to have the combination of water level and tidal current velocity data obtained at the same location, but that was not possible with the available data for this study. It was then assumed that the combinations between current velocity and water level obtained at the closest tidal gauge available would provide a good estimative of the stage-velocity diagrams. During TEJO85 (RCMs A, B and C), water level data were available on tidal gauges Ca, Tp and Cr (see Fig. 2.2 for location), whereas during TEJO88/2 (RCMs D_s, D_b, E_s and E_b) and TEJO89 (RCMs F_m, F_b and G_m), water level data were available on tidal gauges Ca, Pa and Cr. The appropriate pairs of current meter/tidal gauge and the respective periods of simultaneous observations are listed in Table 3.2.

RCM station	Tidal gauge	Simultaneous observations
A	Tp	10/09 – 30/09/85
B	Tp	07/09 – 30/09/85
C	Cr	07/09 – 30/09/85
D_s	Cr	02/08 – 01/09/88
D_b	Cr	02/08 – 07/08/88
E_s	Cr	02/08 – 22/08/88
E_b	Cr	02/08 – 04/08/88
F_m	Pa	06/11 – 11/11/89
F_b	Pa	06/11 – 14/11/89
G_m	Pa	07/11 – 06/12/89

Table 3.2 – Current meter and closest tidal gauge used to represent the *in situ* water level in the respective stage-velocity diagram. Meaning of the subscript letters: *s* – surface; *m* – mid-water; *b* – bottom.

3.3 Data analysis and discussion

3.3.1 Tidal range – space and time variability

The evolution of the tidal range along the estuary during 1972 was analysed using the water level time series from all available tide gauges (see Chapter 2). The beginning and the end of each flood and ebb phase were identified in the tidal gauge records, and the water level variation between the start of each flood and the end of the following ebb was considered as being a single tidal wave. The water level difference between high water and the subsequent low water corresponds to the range of the respective tidal wave. As an example, Fig. 3.4(a) represents the one-year long water level record at Cascais (Ca) and Fig. 3.4(b) the corresponding tidal range, showing a small diurnal inequality, superimposed to the well-defined fortnightly tidal cycle.

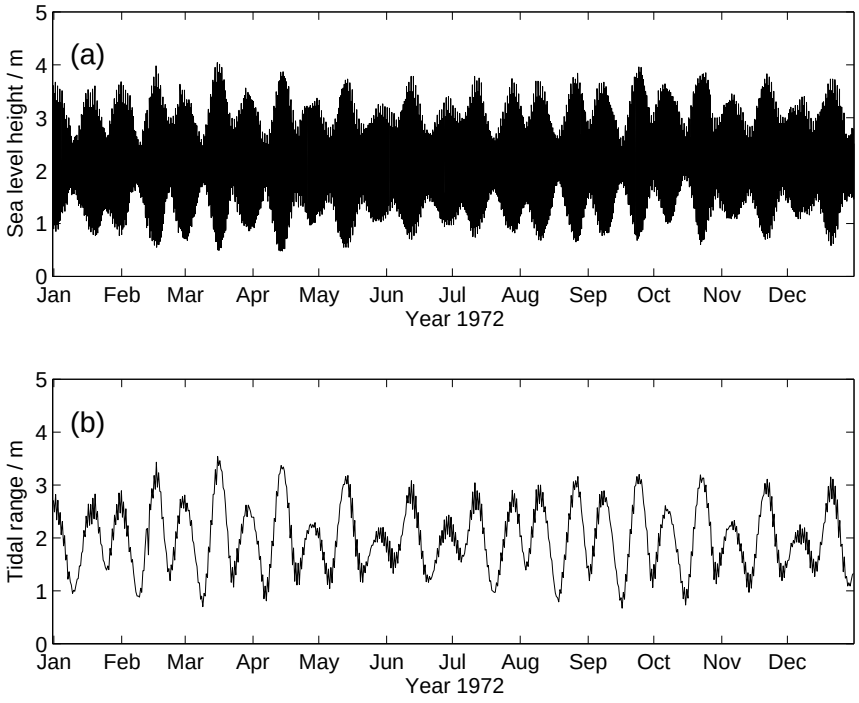

Figure 3.4 – Time series of (a) water level measured at Cascais during 1972 and (b) tidal range calculated from these observations.

Table 3.3 summarises the results of the analysis of the tidal range for all the available

water level records. The minimum range represents the strongest neap tide and the maximum represents the strongest spring tide occurring at each station. Both minimum and maximum ranges increase within the estuary from the mouth to the head, showing that the neaps weaken and the springs strengthen towards the estuary's interior. As the mean water depth decreases from the mouth to the head, this means that, towards the interior, the tidal range is an increasing fraction of the total water depth.

		Neap	Spring	
Survey	Site	Min. (m)	Max. (m)	Mean (m)
1972 (all year)	Ca	0.67	3.54	2.00
	Pa	0.78	3.51	2.10
	Tr	0.74	3.65	2.18
	Pd	0.80	3.78	2.23
	Cc	0.86	3.94	2.40
	Tp	0.82	4.02	2.42
	Sx	0.83	4.03	2.43
	Cr	0.89	4.33	2.58
	Pe	1.00	4.32	2.80
	Vf	1.07	3.68	2.59
Sep. 1985	Ca	0.67	3.38	1.91
	Tp	0.85	3.91	2.42
	Cr	0.93	4.00	2.61
Feb. 1988	Ca	0.80	3.67	2.07
	Tp	0.97	3.95	2.34
	Cr	1.03	4.07	2.35
Aug. 1988	Ca	0.98	3.72	2.21
	Pa	0.85	3.62	2.13
	Cr	1.11	4.27	2.59
Nov. 1989	Ca	1.02	3.18	1.97
	Pa	1.03	3.19	1.98
	Cr	1.32	3.68	2.38

Table 3.3 – Tidal range extrema and mean values (m) obtained from several tidal gauge records along the Tagus Estuary during 1972, September 1985, February and August 1988 and November 1989. Ca: Cascais, Pa: Paço de Arcos, Tr: Trafaria, Pd: Pedrouços, Cc: Cacilhas, Tp: Terreiro do Paço, Sx: Seixal, Cr: Cabo Ruivo, Pe: Ponta da Erva, Vf: Vila Franca de Xira.

The mean tidal range increases along the estuary from the mouth to the estuary's head, at Ponta da Erva (Pe), then decreases towards Vila Franca de Xira (Vf). The mean tidal range values, comprised between ~2.0 and ~2.8 m for all gauges, allow to classify the Tagus Estuary as a mesotidal estuary. The difference in tidal range between neap and spring tide can reach 2.9 m at Cascais (Ca) and 3.3 m at Ponta da Erva (Pe).

Spring and neap tide ranges are variable over the year, as shown by the oscillation of the various relative minima and maxima in Fig. 3.4(b). As a result, the mean tidal range calculated from several one-month long time series, obtained at the same location on different times of the year, shows different values, as evidenced by the different mean tidal range values, both at Ca and Cr, for September 1985, February and August 1988 and November 1989 (see Table 3.3). Several factors can be responsible for this, as the semi-diurnal tidal range is influenced by variations of the distance between the earth and the moon, by variations of the declination of the moon and the sun and also by meteorological disturbances (atmospheric pressure and/or wind) (Pugh, 1987).

Moreover, one can expect that seasonal variations of the river discharge can exert some influence on the intra-annual variability of the tidal range, as Parker (1991) has shown using both *in situ* data and numerical modelling. This author reported a decrease of the tidal range and the modification of the shape of the tidal curve (the time of the low water was delayed), when the river discharge increased significantly.

3.3.2 Main tidal constituents behaviour

Tidal amplitudes (a) and phases (θ) of the main diurnal, semi-diurnal and shallow-water (M_4 and M_6) constituents for each tidal gauge record (see Fig. 2.2(d) for location) were calculated and are given in Table 3.4. These results show that the M_2 constituent, as expected, has the largest amplitude (order of 1.0 m) in all records, followed by S_2 and N_2 constituents. In the deeper part of the estuary (from Cascais (Ca) to Cacilhas (Cc) – see Fig. 2.2(d)), the main diurnal constituents (O_1, K_1) take the third major amplitudes, but in the shallow inner bay (between Terreiro do Paço (Tp) and Vila Franca de Xira (Vf)), the M_4 constituent has higher amplitude than the diurnal. The shallow-water constituent M_6, when significant, has always the lowest amplitude, which can be similar to the M_4, upstream at Vila Franca de Xira (Vf).

		O_1		K_1		N_2		M_2		S_2		M_4		M_6		
Survey	Site	a(m)	θ(°)	a(m)	θ(°)	a(m)	θ(°)	a(m)	θ(°)	a(m)	θ(°)	a(m)	θ(°)	a(m)	θ(°)	F
1972	Ca	0.061	326.2	0.069	69.2	0.212	72.7	0.977	93.5	0.340	121.6	0.012	236.4	0.001	152.0	0.10
	Pa	0.062	331.1	0.066	71.4	0.215	83.1	1.013	100.0	0.353	128.8	0.023	310.6	0.006	301.9	0.09
	Tr	0.062	332.0	0.065	75.3	0.223	88.8	1.053	103.4	0.364	132.5	0.039	311.4	0.008	345.0	0.09
	Pd	0.064	330.9	0.066	72.4	0.225	83.7	1.075	100.6	0.374	129.8	0.048	301.1	0.009	207.8	0.09
	Cc	0.063	332.8	0.068	73.6	0.241	88.0	1.145	103.9	0.398	134.3	0.069	295.1	0.012	333.5	0.08
	Tp	0.062	332.5	0.066	74.4	0.240	88.4	1.156	105.0	0.407	134.9	0.082	298.2	0.012	352.2	0.08
	Sx	0.064	334.4	0.067	75.9	0.242	90.9	1.159	107.4	0.408	137.7	0.087	303.5	0.012	306.0	0.08
	Cr	0.065	331.8	0.068	76.5	0.250	90.9	1.226	107.5	0.430	138.1	0.099	309.3	0.014	320.3	0.08
	Pe	0.065	338.1	0.069	82.8	0.264	101.6	1.298	115.6	0.447	148.8	0.089	334.9	0.033	342.8	0.08
	Vf	0.064	349.0	0.066	94.8	0.226	121.2	1.196	132.5	0.371	169.8	0.038	246.5	0.037	60.9	0.08
Sep. 1985	Ca	0.061	314.2	0.057	61.6	0.204	56.8	0.979	65.6	0.456	90.8	0.010	189.2	0.002	140.7	0.08
	Tp	0.064	335.9	0.057	84.5	0.243	102.9	1.151	107.0	0.524	136.8	0.068	305.7	0.013	0.4	0.07
	Cr	0.063	343.4	0.054	90.5	0.243	113.0	1.215	109.8	0.529	141.7	0.079	319.7	0.017	330.7	0.07
Feb. 1988	Ca	0.062	313.5	0.065	72.4	0.268	46.3	1.018	64.5	0.445	109.9	0.012	199.1	0.004	118.1	0.09
	Tp	0.062	320.4	0.068	76.6	0.281	62.1	1.152	78.7	0.500	123.4	0.071	243.0	0.012	280.1	0.08
	Cr	0.062	324.7	0.067	79.0	0.294	67.9	1.192	83.0	0.497	130.2	0.083	254.0	0.011	258.2	0.08
Aug. 1988	Ca	0.066	312.7	0.074	68.8	0.246	53.2	1.001	64.3	0.411	104.2	0.012	186.1	0.002	113.2	0.10
	Pa	0.063	332.1	0.068	87.0	0.255	81.1	0.984	95.9	0.416	137.7	0.017	285.5	0.007	307.7	0.09
	Cr	0.064	343.2	0.071	96.7	0.301	96.8	1.178	111.2	0.473	155.7	0.084	320.2	0.016	332.1	0.08
Nov. 1989	Ca	0.066	311.5	0.073	40.6	0.254	40.1	1.009	64.3	0.310	70.8	0.012	198.0	***	***	0.11
	Pa	0.060	315.9	0.072	45.0	0.225	46.6	0.987	69.9	0.294	81.2	0.018	219.5	0.007	244.4	0.10
	Cr	0.060	335.6	0.071	49.7	0.271	60.3	1.187	84.6	0.319	100.4	0.070	260.5	0.012	293.3	0.09

Table 3.4 – Amplitudes a(m) and phase angles θ(degrees) of the principal semi-diurnal and diurnal tidal constituents and of the shallow-water constituents M_4 and M_6, given by harmonic analysis of the water level records obtained at several gauges along the Tagus Estuary during 1972, September 1985, February and August 1988 and November 1989. (*** – Constituent not considered significant) Also shown (last column) is the tidal form number (F) at the different sites.

In general, the amplitudes of the semi-diurnal constituents increase from the mouth of the estuary until Ponta da Erva (Pe), and decrease further upstream towards Vila Franca de Xira (Vf). The amplitudes of the diurnal constituents remain practically unchanged along the estuary (Fig. 3.5(a)). M_4 systematically grows from Cascais (Ca) to Cabo Ruivo (Cr), the gradient being higher between Cacilhas (Cc) and Cabo Ruivo (Cr). From this point on, its amplitude decreases upstream towards Vila Franca de Xira (Vf). The M_6 amplitude increases upstream, weakly until Cabo Ruivo (Cr), and then with a stronger gradient (Fig. 3.5(b)). As Cabo Ruivo seems to be a turning point for the shallow-water constituents, this might correspond to changes in the respective generating processes. Fortunato et al. (1999) also reported this fact, stressing the dominance of advective accelerations (responsible for M_4 generation) in the deeper part of the estuary compared with the larger influence of friction (responsible for M_6 generation) in the shallower part of the estuary.

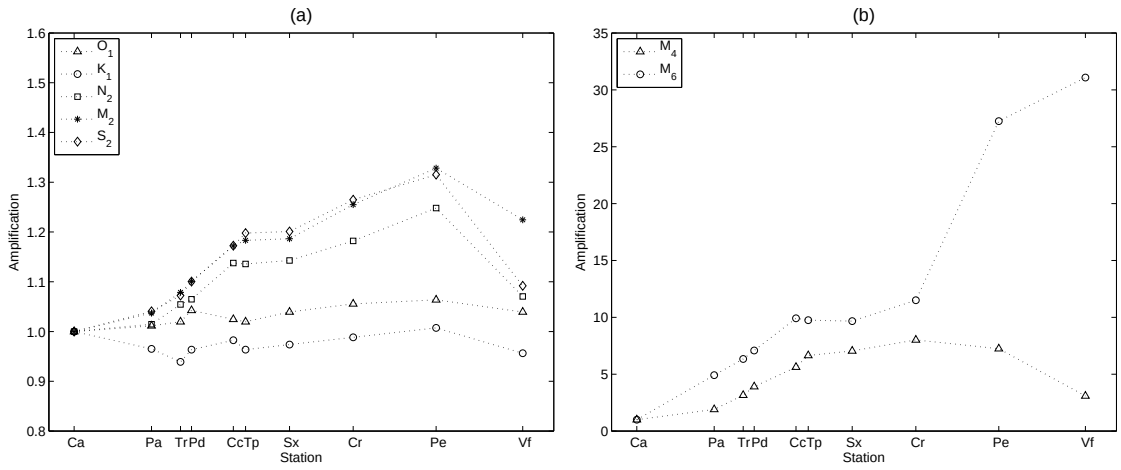

Figure 3.5 – Amplification of the main (a) principal and (b) shallow-water harmonic constituents (amplitude/amplitude at the mouth) over the estuary. The distance between stations in the *x*-axis is scaled by their approximate real distance.

In what concerns the phase difference between the mouth (Cascais) and the head (Vila Franca de Xira) of the estuary for the main diurnal constituents, it is 1h38m for O_1 and 1h42m for K_1 and, for the main semi-diurnal constituents, it is 1h42m for N_2, 1h21m for M_2 and 1h36m for S_2. Therefore, at Vila Franca de Xira, the O_1 and K_1 phase differences

are separated by 4 minutes. The difference between the phases of O_1 and K_1 from Cascais to Vila Franca de Xira is about 255-260°, therefore these constituents are nearly phase-locked along the estuary. On the other hand, the phase difference for M_2 is less 15 minutes than for S_2 and less 21 minutes than for N_2, meaning that the phase of M_2 is experiencing less delay between the mouth and the head of the estuary. Analysing the evolution of the phases of these three semi-diurnal constituents along the estuary, it is observed that N_2 and S_2 are nearly phase-locked, presenting differences between 44 and 49°. As for the pairs N_2 and M_2 and M_2 and S_2, they remain nearly phase-locked until Ponta da Erva (differences of about 14-17° between N_2 and M_2 and 28-30° between M_2 and S_2). Upstream at Vila Franca de Xira, the difference between N_2 and M_2 decrease to 11° and between M_2 and S_2 decrease to 37°. A probable cause for this behaviour can be related to resonance. Since different species of tides (e.g. diurnal and semi-diurnal, as will be seen ahead) can be differently affected by resonance effects (Doodson and Warburg, 1941), distinct constituents within the same tidal species could also present different responses to resonance.

The tidal form number (F), defined as the ratio between the amplitudes of the main diurnal (K_1+O_1) and the main semi-diurnal (M_2+S_2) constituents (Defant, 1961), expresses their relative importance. This non-dimensional number allows the classification of the tide as semi-diurnal dominated ($0 \leq F < 0.25$), mixed but mainly semi-diurnal ($0.25 \leq F < 1.50$), mixed but mainly diurnal ($1.50 \leq F < 3.00$) and diurnal dominated ($F \geq 3.00$).

The values of F computed for the different tide records (Table 3.4) allows to classify the tide in the Tagus Estuary as semi-diurnal dominated. For the 1972 one-year record, the tidal form number was 0.10 at Cascais (Ca), decreasing towards the head of the estuary (0.08 at Ponta da Erva (Pe)). The one-month long water level records, obtained within the period 1985-89, also evidenced a decrease of F from Cascais (Ca) to Cabo Ruivo (Cr). Since the principal diurnal constituents remain practically constant along the estuary, the decrease of F is directly related with the increase of the main semi-diurnal constituents along the estuary (about 33% of increase from Ca to Cr, as shown by Fig. 3.5(a)). In general, as the tidal wave propagates into the estuary, the amplitudes of the principal diurnal and semi-diurnal constituents are expected to decrease, due both to friction and to non-linear transfers of energy (Aubrey and Speer, 1985). Nevertheless, tidal amplification can occur due to the

reflection of the tidal wave at the head of an estuary.

As referred earlier in Section 1.4, Oliveira (1993) reported the existence of resonance in the Tagus Estuary and, having verified this same behaviour in their data set (the 1972 one-year water level data set used in this work), Fortunato et al. (1999) suggested that the behaviour of the semi-diurnal constituents in Tagus Estuary was consistent with the existence of a resonant mode with a period close to twelve hours and showed the presence of a 8-hour period mode, by using a numerical model.

Let us make an estimate of the resonant period (T) for the Tagus Estuary by using Merian's formula (Pugh, 1987) applied to a constant depth (H) rectangular estuary with total length L and one closed end:

$$T = \frac{4L}{\sqrt{gH}} \tag{3.14}$$

Given the shape of the Tagus Estuary, its area was divided in two boxes, as shown in Fig. 3.6. Each box represents a region of the estuary of well defined characteristics: box 1 represents the narrow and relatively deep inlet channel and box 2 represents the wide and shallow inner bay. An approximate characteristic length L was computed as the sum of the characteristic lengths of each region, $L_1 = 11.4$ km for box 1 and $L_2 = 21.1$ km for box 2. The characteristic depth of the estuary, H, was computed from the bathymetric data. The bathymetric soundings were averaged for each box ($h_1 = 21.16$ m for box 1 and $h_2 = 4.43$ m for box 2) and the total characteristic depth was computed as the average of h_1 and h_2, weighted by the number of soundings in each box. Thus, an approximate characteristic length of 32.5 km and an average depth of 7.3 m lead to a resonance period of 4.3 hours, far away from the semi-diurnal period.

Due to the complex shape of the Tagus Estuary and to the fact that, even within each box, the depth is not constant, the Merian's formula can not take into account the continuous reflections of the semi-diurnal wave along the sides and the bottom of the estuary. This is probably the main reason for the difference between the value obtained using this method and both the semi-diurnal tide period and the value reported by Fortunato et al. (1999), referred above. Another possible explanation is related to the fact that the resonance period was estimated disregarding the situations when the intertidal flats are submerged, since tidal wave reflections can still occur and contribute to the resonance effect. This case could not be considered with the simple application of equation (3.14).

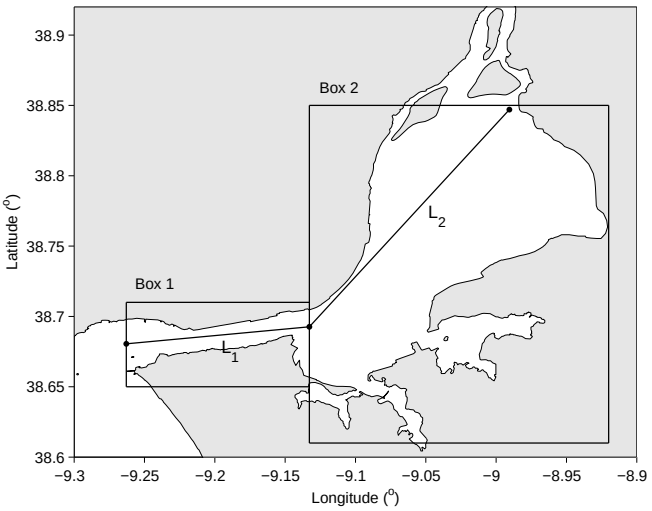

Figure 3.6 – Regions and respective characteristic lengths used to estimate the resonance period of the Tagus Estuary.

3.3.3 Tidal currents

Principal axes

The current velocity data obtained at various depths during the TEJO85, TEJO88/2 and TEJO89 campaigns were analysed in order to characterise the tidal flow within the Tagus Estuary. The main orientation of the flow for each current meter was obtained by calculating the principal axes directions (see Section 3.2.1), thus allowing the current time series to be rotated to a new coordinate system, for which the major principal axis is associated with most of the variance.

Fig. 3.7 depicts the principal axes orientation for all the current meters deployed during the campaigns and then, separately, by regions (inlet channel, mid-estuary and inner bay). The length of the axes are scaled according to their respective standard deviation, i.e., the semi-major and semi-minor axes of the ellipses are given by the square roots of λ_1 and λ_2, respectively (see equations (3.5)). In general, all the major principal axis directions are well aligned with the local bathymetry.

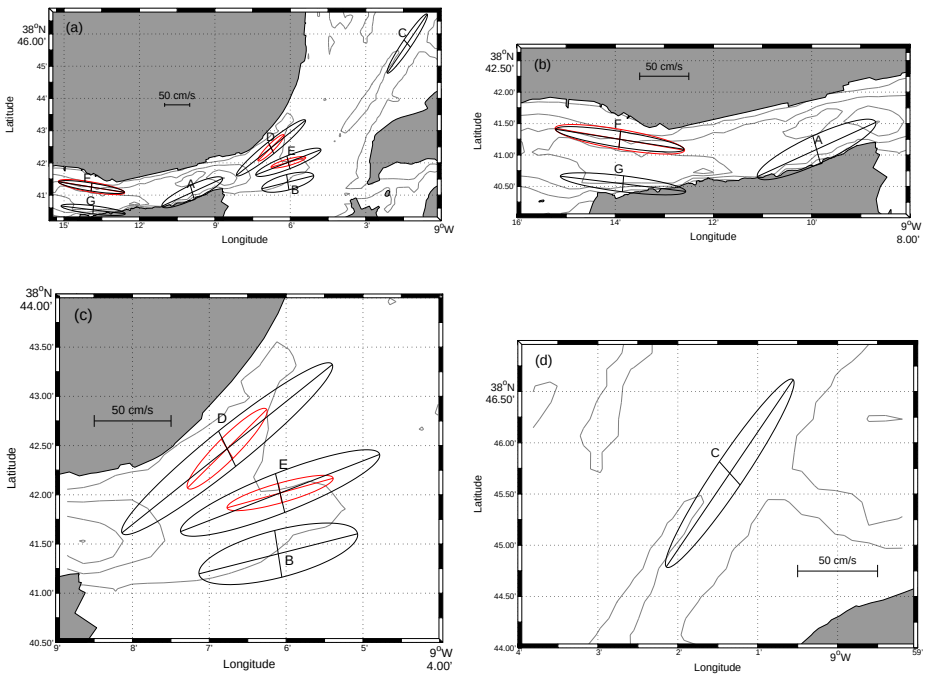

Figure 3.7 – Principal axes directions for (a) all current meters of the observational campaigns TEJO85, TEJO88/2 and TEJO89, (b) the current meters located in the inlet channel, (c) the current meters located in the mid-estuary and (d) the current meter located in the inner bay. The letters identify the mooring site (A, B, C: TEJO85; D, E: TEJO88/2; F, G: TEJO89) and the gray contours show the main features of the bottom topography. Black ellipses refer to near-surface current meters (or mid-water in the case of mooring F) and red ellipses refer to near-bottom current meters.

(i) Inlet channel

At the inlet channel (Fig. 3.7(b)), the principal axes of the mid-water and the near-bottom current at mooring F are practically coincident and show a better alignment with the local bathymetry when compared with mooring G (near the southern margin), mid-water current meter. The major principal axis of the near-surface current at mooring A is also well aligned with the local bathymetry.

(ii) Mid-estuary

In what concerns the mid-estuarine region (Fig. 3.7(c)), all the major principal axes directions align well with the local bathymetry. The near-surface currents in B, D_s and E_s show convergence towards the mouth of the estuary and the consequent divergence in the opposite direction. The angle between the principal directions is higher near the bottom (D_b and E_b, in red in Fig. 3.7(c)) than near the surface (D_s and E_s, in black in Fig. 3.7(c)), suggesting a slightly enhanced convergence/divergence effect of the near-bottom currents when compared with those near the surface. The fact that the sampling period was longer for the near-surface (complete fortnightly cycle) than for the near-bottom (neap tide period) RCMs could account for this difference. To test this hypothesis, principal axes directions were computed for the near-surface current meters, assuming the same sampling period as of those near the bottom. The result showed a small increase of the difference between the near-bottom and near-surface principal axes directions, which is not consistent with the hypothesis of dependence on the sampling period. If that would be the case, the differences between the near-bottom and near-surface principal axes directions would decrease. These differences are therefore, independent of the sampling period, and should be caused by the enhanced friction effects near the bottom.

(iii) Inner bay

As for the inner bay (Fig. 3.7(d)), the major principal axis for the only current meter placed in this region is very well aligned with the local bathymetry and is directed along the axis of the *Cala de Samora*, the local main channel.

Harmonic analysis of current velocity data

All the current velocity time series (TEJO85, TEJO88/2 and TEJO89) were rotated to the new coordinate system defined by the respective principal axes and then harmonic analysis was applied to all of them. The time series were treated as complex series $w(t)$, i.e. $w(t) = u(t) + iv(t)$, where u and v are, respectively, the along and across-channel velocity components and t represents the time. The resulting amplitudes and phases for each current time series, together with those for the correspondent water level time series (see Table 3.2) were then used to calculate stage-velocity diagrams, through equations (3.1) and using

Table 3.4. These diagrams were afterwards compared with the respective observed data, as exemplified for the current meters D_s and G_m in Figs. 3.8(a) and (b) respectively.

The bad correspondence between the calculated stage-velocity diagrams (blue line) and the *in situ* data shown in Fig. 3.8 is much probably the direct consequence of the use of the complex form of the current velocity data in the T_TIDE package. According to Pawlowicz et al. (2002), the representation of the current in the complex form is only valid for linear or nearly linear tidal waves, which is not the case. In order to correct this situation, harmonic analysis was applied on the along and across-channel components of the current velocity time series separately. The result is shown in Fig. 3.8 by the red line.

The scatter of the *in situ* data (dots) around the calculated harmonics (red line) is due to forcing occurring at frequencies lower than M_2, mainly due to the fortnightly tidal cycle (caused by the interaction between M_2 and S_2). Nevertheless, non-tidal factors such as wind or axial pressure gradients due to freshwater discharge can also contribute to that scatter around the harmonics.

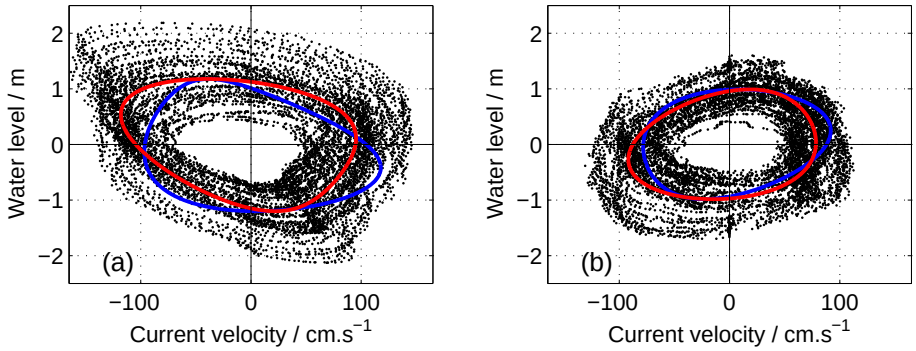

Figure 3.8 – Water level versus current velocity plot of *in situ* data (dots) and calculated harmonics M_2+M_4 through an appropriate (red line) and inadequate (blue line) application of the harmonic analysis package T_TIDE for current meters (a) D_s and (b) G_m. Flood currents are positive and the temporal progression of the water level and current in the diagrams is counter-clockwise.

The harmonic analysis of all the current velocity time series rotated to the principal axes directions provided the amplitudes and phases of the significant tidal constituents (those with SNR >1 – see Section 3.2.2), which were then used to calculate the respective current

velocities. This allowed to analyse the temporal and spatial variations of the maximum tidal current velocity both along and across the principal direction of the flow. The comparison between variance of the tidal current velocity with that of the total current velocity, allowed to quantify the influence of the tide on the total current and the respective spatial and temporal variations. Since spring tide conditions are responsible for higher variance values than neap tide, only the time series covering roughly a complete fortnightly tidal cycle are analysed here, which excludes those obtained with the RCMs D_b (~5 days of observations), E_b (~2 days of observations), F_m (~4 days of observations) and F_b (~8 days of observations) (see Fig. 3.7(a) for location).

The following analysis refers to the tidal current velocity and also to the variance of the total current and its respective tidal contribution. The regions near the mouth/inlet channel (current meters A and G_m), mid-estuary (current meters D_s and E_s) and inner bay (current meter C) are focused separately. The values of variance (σ^2) and its fraction (%) due to tide of both along and across-channel velocity components are presented in Table 3.6.

(i) Inlet channel

In what concerns the maximum tidal current velocity near the surface, the results showed generally stronger currents during the ebb, compared to those during the flood, both in spring and neap tides. An exception is found for the current meter A, located near the southern margin in the inlet channel, where the tidal maximum current velocity is stronger during the flood (140 cm s^{-1}) than during the ebb (125 cm s^{-1}) in spring tide conditions. The tidal currents obtained for RCM G_m, located near the mouth and in mid-water, are similar to those near the surface in the inlet channel (RCM A), except during the flood in spring tide conditions (116 cm s^{-1}), which are lower than that computed for RCM A.

Both current meters A and G_m present similar values for the variance of the along-channel current velocity (~ 4100 cm^2 s^{-2}), as well as similar contributions from the tide. In what concerns the across-channel component, the variance is much lower, between 40 and 131 cm^2 s^{-2}, as well as its contribution from the tide (see Table 3.6).

		O_1				K_1			
Survey	RCM	u_r(cm s^{-1})	φ(°)	v_r(cm s^{-1})	φ(°)	u_r(cm s^{-1})	φ(°)	v_r(cm s^{-1})	φ(°)
Sep. 1985	A	3.05	246.5	0.46	153.5	2.12	344.6	***	***
	B	2.15	279.5	0.83	118.2	2.29	11.2	0.75	144.3
	C	2.69	273.3	1.22	257.2	3.56	19.3	0.87	147.8
Aug. 1988	D_s	3.03	238.0	1.14	222.5	3.38	347.8	0.97	244.4
	D_b	***	***	***	***	***	***	***	***
	E_s	3.39	296.1	***	***	4.62	10.6	1.61	217.5
	E_b	***	***	***	***	***	***	***	***
Nov. 1989	F_m	***	***	***	***	6.48	10.6	***	***
	F_b	***	***	***	***	2.74	349.9	1.25	85.3
	G_m	3.17	236.1	0.31	294.2	2.32	316.3	0.29	4.6
		M_2				S_2			
Survey	RCM	u_r(cm s^{-1})	φ(°)	v_r(cm s^{-1})	φ(°)	u_r(cm s^{-1})	φ(°)	v_r(cm s^{-1})	φ(°)
Sep. 1985	A	77.87	5.5	4.28	93.6	41.42	27.9	2.13	140.2
	B	66.92	18.4	3.56	320.5	34.54	38.9	***	***
	C	76.48	19.8	4.56	107.0	41.10	45.9	1.91	157.0
Aug. 1988	D_s	103.31	6.6	4.24	278.5	38.71	46.9	1.58	5.3
	D_b	42.35	347.6	***	***	***	***	***	***
	E_s	89.52	19.8	6.53	282.2	42.94	61.1	***	***
	E_b	47.28	350.0	***	***	***	***	***	***
Nov. 1989	F_m	91.16	359.0	***	***	***	***	***	***
	F_b	91.18	357.7	2.89	76.7	***	***	***	***
	G_m	84.60	350.7	***	***	22.14	0.1	***	***
		M_4				M_6			
Survey	RCM	u_r(cm s^{-1})	φ(°)	v_r(m)	φ(°)	u_r(m)	φ(°)	v_r(m)	φ(°)
Sep. 1985	A	6.11	93.9	3.71	325.9	***	***	2.32	102.6
	B	7.08	195.8	7.55	35.9	***	***	***	***
	C	7.18	227.9	***	***	***	***	***	***
Aug. 1988	D_s	17.79	148.9	7.05	273.5	3.74	196.7	2.22	176.6
	D_b	11.56	112.6	5.07	33.1	2.98	341.7	2.37	307.9
	E_s	7.97	171.1	3.70	267.4	1.92	29.6	***	***
	E_b	5.44	196.4	5.54	30.3	6.63	323.0	1.02	198.9
Nov. 1989	F_m	8.58	91.3	4.41	10.3	2.45	219.6	2.46	74.3
	F_b	10.04	138.9	***	***	***	***	***	***
	G_m	8.19	194.4	***	***	***	***	***	***

Table 3.5 – Amplitudes (cm s^{-1}) and phase angles φ(degrees) of the main diurnal and semi-diurnal constituents and of the principal quarter and sixth-diurnal shallow-water constituents, given by harmonic analysis of the current velocity records obtained at moorings along the Tagus Estuary during September 1985, August 1988 and November 1989. (*** – Constituent not considered significant or not used in the analysis)

(ii) Mid-estuary

In the mid-estuarine region, during the ebb in spring tide, the tidal current velocity near the surface reached values of about 180 cm s^{-1} (RCM D_s – see Fig. 3.7(a) for location) whereas in neap tide, it reached values of about 70 cm s^{-1} (also obtained for RCM D_s). Comparatively, the maximum surface tidal current is weaker in station E, both during spring (flood: 128 cm s^{-1}; ebb: 148 cm s^{-1}) and neap tide (flood $\approx$ ebb: 42 cm s^{-1}). The tidal current velocity at RCM B, farther from the northern margin, is weaker than in stations D and E during spring tide (flood: 96 cm s^{-1}; ebb: 132 cm s^{-1}) but similar to those stations during neap tide (flood $\approx$ ebb: 45 cm s^{-1}).

The along-channel current variance decreases from the northern margin (D_s) to the southern margin (B). Moreover, there is a considerable difference between RCMs E_s and B (4586 cm^2 s^{-2} and 2768 cm^2 s^{-2}, respectively). These large spatial differences may be caused by a stronger tidal flow over the two local main channels where the RCMs D_s and E_s are located. As for the RCM B, although not very far from the RCM E_s, it does not seem to be located on the main flow path.

In the across-channel direction, the current variance is similar for the RCMs D_s and E_s, around 100 cm^2 s^{-2}, where as for the RCM B attains the highest value of the mid-estuarine current meters, $\sim$ 150 cm^2 s^{-2}. The tidal fraction of this variance is also the highest for the RCM B, much probably because of its location in the connection with the southernmost part of the estuary, where a significant part of the tidal flow acts on the direction perpendicular to that of the inlet channel axis, covering and uncovering the extensive intertidal flats of this region.

(iii) Inner bay

Near the southern margin (RCM C), the maximum tidal current velocity obtained during spring tide was 125 cm s^{-1} for flood and 147 cm s^{-1} for ebb. During neap tide, 41 cm s^{-1} was obtained for flood and 47 cm s^{-1} for ebb. These values are lower than those obtained closer to the northern margin, for RCM D_s, but comparable to those obtained for RCM E_s (although located in mid-estuary, these RCMs were the only ones available closer to the northern margin).

In what concerns the along-channel current variance, the current meter C presents the

lowest values of all the analysed current meter, excluding RCM B. The RCM C was located on the southernmost of the main channels of the inner bay. An important part of the flow is expected to be along this channel, which is probably the reason why the variance for RCM C, although very low, is higher than for RCM B.

The across-channel variance for RCM C is one of the lowest of the current meters analysed, as well as the corresponding tidal fraction. The most probable cause is the constraints on the tidal flow imposed by the bottom topography in this location (see the principal axes direction for this RCM in Fig. 3.7(d) and compare it with the bathymetry contour).

	Along-channel current		Across-channel current	
RCM	σ^2 (cm^2 s^{-2})	Tidal contribution (%)	σ^2 (cm^2 s^{-2})	Tidal contribution (%)
A	4101.7	95.9	131.1	34.2
B	2768.3	96.8	146.6	63.2
C	3662.5	96.3	74.4	25.9
D_s	6519.1	98.0	111.7	55.6
E_s	4586.3	92.2	106.4	37.0
G_m	4114.4	94.8	40.6	5.3

Table 3.6 – Total current variance and the respective tidal contribution for the along and across-channel current components for the near-surface and mid-water (only G_m) current meters.

In summary, the variance of the along-channel current component presents an evident spatial variability, as well as a relatively high tidal contribution (always above 92%). Together with the maximum tidal current velocity, this allows to identify the regions where the tidal flow in the along-channel direction is expected to be stronger. The maximum tidal current velocity showed an increase from the mouth to the mid-estuarine region, especially near the northern margin, where both the variance of the along-channel current and its tidal fraction present the highest values of the current meter set. In the mid-estuarine region, the along-channel tidal flow is more concentrated near the northern margin and the across-channel tidal flow seems to gain importance closer to the southernmost intertidal flat area of the estuary.

Tidal current ellipses

The harmonic analysis of the current allows to calculate the tidal current ellipses of the significant main and shallow-water harmonic constituents (see Section 3.2.2). Figs. 3.9, 3.10 and 3.11 depict the tidal current ellipses of the main principal diurnal, semi-diurnal and shallow-water constituents obtained for each current meter. The axes correspond to the west-east and south-north directions, respectively, and the direction of rotation of the ellipses is indicated by the thickness of the line. When a constituent was not considered significant for one of the current velocity components, the corresponding ellipsis is represented in red.

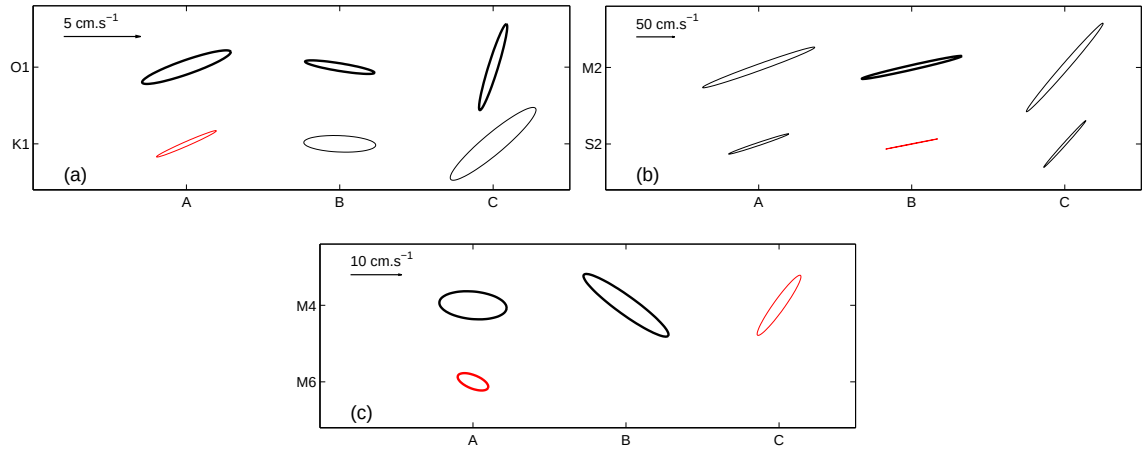

Figure 3.9 – Tidal current ellipses of the main (a) principal diurnal, (b) principal semi-diurnal and (c) shallow-water harmonic constituents for the TEJO85 RCM stations (A, B, C in the *x*-axis). Thin lines indicate counter-clockwise rotation and thick lines indicate clockwise rotation. Red ellipses indicate a constituent not considered significant for one of the velocity components.

In general, all the ellipses have high eccentricity, which means that the tidal currents are essentially rectilinear and the sense of rotation of the ellipses should not be significant. This is most probably due to the constraints imposed by the local bottom topography. The highest eccentricity ellipses (values above 0.90) correspond to the semi-diurnal constituents S_2 and M_2 (Figs. 3.9(b), 3.10(b) and 3.11(b)). The M_2 ellipses have higher eccentricity near

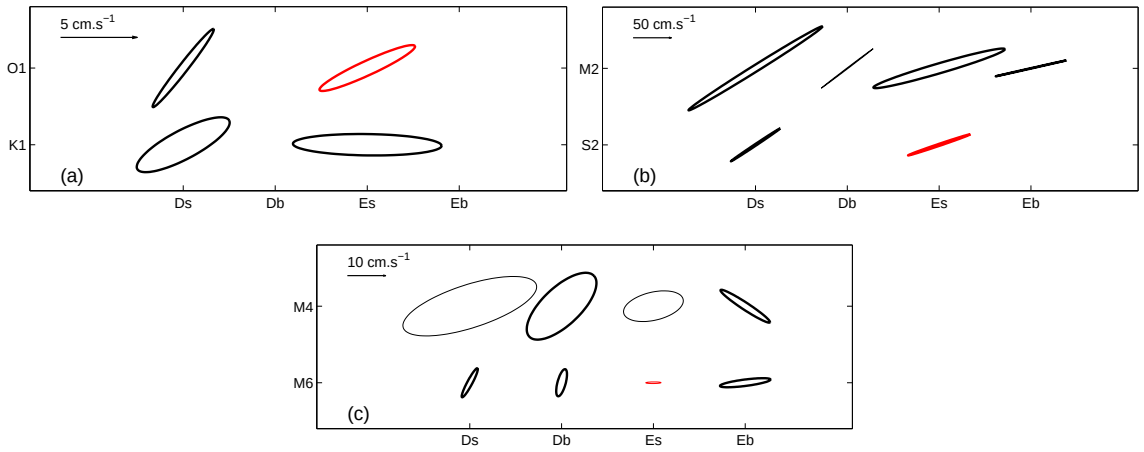

Figure 3.10 – Tidal current ellipses of the main (a) principal diurnal, (b) principal semi-diurnal and (c) shallow-water harmonic constituents for the TEJO88/2 RCM stations (D, E in the *x*-axis). Thin lines indicate counter-clockwise rotation and thick lines indicate clockwise rotation. Red ellipses indicate a constituent not considered significant for one of the velocity components.

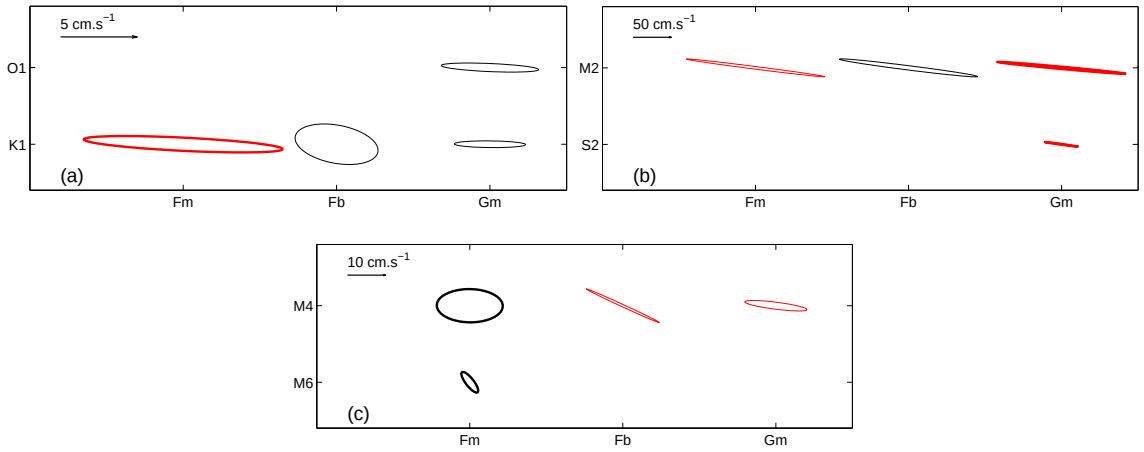

Figure 3.11 – Tidal current ellipses of the main (a) principal diurnal, (b) principal semi-diurnal and (c) shallow-water harmonic constituents for the TEJO89 RCM stations (F, G in the *x*-axis). Thin lines indicate counter-clockwise rotation and thick lines indicate clockwise rotation. Red ellipses indicate a constituent not considered significant for one of the velocity components.

the bottom, which is expected since the local bathymetry imposes a more rectilinear flow. The shallow-water constituents are associated with the lowest eccentricity values.

Comparing Fig. 3.7 with Figs. 3.9 to 3.11 it is possible to observe that the directions of K_1, M_2 and S_2 tidal current ellipses are similar to the local major principal axis direction. On the other hand, the largest deviations from the major principal axis direction are shown mainly by ellipses of M_4 and M_6 constituents, thus appearing to be less influenced by the local bathymetry.

The near-surface tidal ellipses for the mid-estuarine region (current meters B, D_s and E_s) are presented with more detail in Fig. 3.12. This figure evidences that divergence occurs during the flood and convergence during the ebb in this region of the estuary. This result can be extended in depth, as can be seen by comparing the ellipses of the near-surface (D_s and E_s) and the near-bottom (D_b and E_b) current meters on Figs. 3.10(b) and 3.10(c). These figures show that the orientation of the tidal ellipses for the semi-diurnal and shallow-water (except the M_4 ellipse for RCM E_s) constituents is generally constant with depth.

Stage-velocity diagrams

In this section, stage-velocity diagrams are used to illustrate the evolution of the standing/progressive contribution to the tidal wave along the Tagus Estuary. The stage-velocity diagrams were calculated for all current meters deployed during the TEJO85, TEJO88/2 and TEJO89 campaigns. For each current meter, the closest tidal gauge with available data was chosen, resulting in the combinations listed in Table 3.2 (Section 3.2.3).

The M_2 harmonic has always the highest amplitude and explains more than 75% of the variance of the water level and velocity time series obtained during the campaigns. The progressive character of the tide within the Tagus Estuary is thus investigated through the analysis of stage-velocity diagrams (Fig. 3.13) computed using the amplitudes and phases of the main semi-diurnal harmonic constituent, M_2. The following equations have been used:

$$\begin{aligned} A &= \mathrm{a}_{\mathrm{M}_2} \cos\left(\omega t - \theta_{\mathrm{M}_2}\right) \\ V &= \mathrm{v}_{\mathrm{M}_2} \cos\left(\omega t - \varphi_{\mathrm{M}_2}\right) \ , \end{aligned} \tag{3.15}$$

where ω is the M_2 angular frequency and t the time; $\mathrm{a}_{\mathrm{M}_2}$ and $\mathrm{v}_{\mathrm{M}_2}$ represent the corresponding water level and current velocity amplitudes and θ_{M_2} and φ_{M_2} the respective phases.

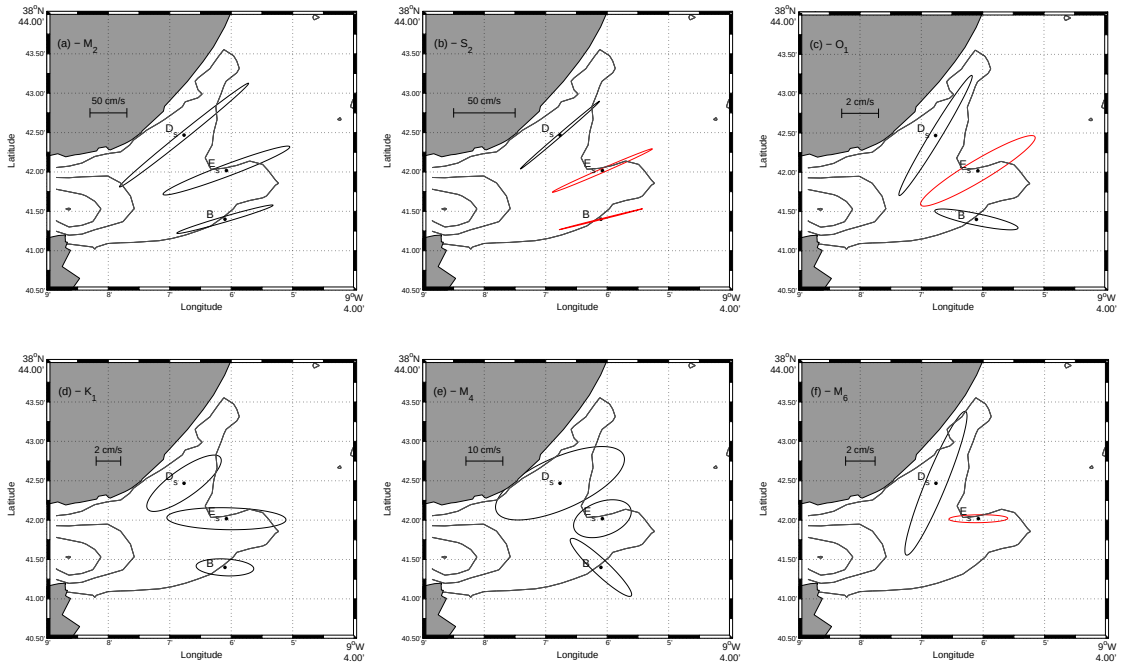

Figure 3.12 – Tidal current ellipses of the (a) M_2, (b) S_2, (c) O_1, (d) K_1, (e) M_4 and (f) M_6 constituents calculated for the current meters located in the transition region between the inlet channel and the inner bay (B, D_s and E_s).

The time elapsed between high water (HW) and high-water slack (HWS – reversal of the tidal current from flood to ebb) and between low water (LW) and low-water slack (LWS – reversal of the tidal current from ebb to flood) allows to estimate the progressive wave contribution of M_2, since it reflects the deviation relative to a purely standing wave system (see Section 3.1). The time differences were computed from the data used for the stage-velocity diagrams of Fig. 3.13.

(i) Inlet channel

The stage-velocity diagrams for the inlet channel are represented in Figs. 3.13(a) (RCM A) and 3.13(c) (RCMs F_b, F_m and G_m). For the RCM A (TEJO85), the HW [LW] occurs about 23 minutes after the HWS [LWS]. For the current meters in moorings F and G (TEJO89), the stage-velocity diagrams show a clockwise rotation of their elliptical form

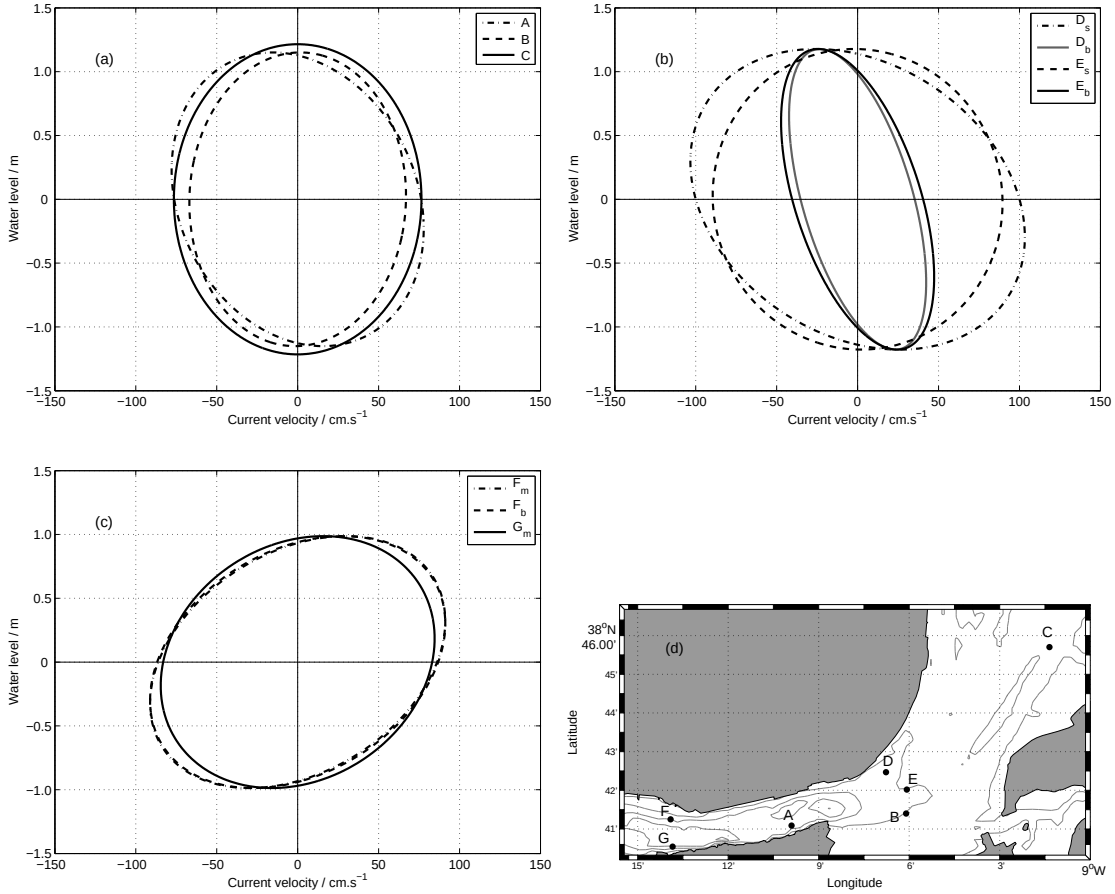

Figure 3.13 – Water level versus current velocity for the M_2 harmonic on the current meters during the (a) TEJO85 (A, B, C), (b) TEJO88/2 (D, E) and (c) TEJO89 (F, G) campaigns and (d) the location of the moorings. Flood currents are positive and the temporal progression of water level and current in the diagrams is counter-clockwise.

relatively to the one for RCM A in such a way that HWS [LWS] occurs after HW [LW] (40 minutes for both mid-water and near-bottom RCMs in mooring F; 23 minutes for mid-water RCM in mooring G). This is only verified for these two moorings F and G, from the entire set analysed in this work.

(ii) Mid-estuary

The stage-velocity diagrams for the near-surface current meters moored in the mid-estuarine region (see Fig. 3.13(b) for the diagrams and 3.13(d) for current meter location) show that HW [LW] occurs about 30 minutes after the HWS [LWS] near the northern margin (current meter D_s) whereas further away from the margin (current meter E_s and B), HW [LW] and HWS [LWS] occur almost simultaneously, showing a much smaller progressive wave contribution. This shows that, within this region, the progressive character of the semi-diurnal tide decreases from the northern to the southern margin.

(iii) Inner bay

In what concerns the current meter located in the inner bay, close to the southern margin (RCM C - TEJO85), the HWS and LWS are almost simultaneous with, respectively, HW and LW, as shown by the respective stage-velocity diagram in Fig. 3.13(a).

In summary, the stage-velocity diagrams of all three campaigns show, for the M_2 wave, an upstream decrease of the progressive contribution, meaning that the interaction between the wave travelling upstream and the reflected wave increases towards the head of the estuary. For the mid-estuary, it is also evident the difference of the progressive character of the semi-diurnal tidal wave between margins. In this sense, the stage-velocity diagrams show a practically standing semi-diurnal tidal wave near the southern margin.

Moorings F and G, placed during a period characterised by an event of strong river discharge, showed a shift in the order of occurrence of HW [LW] and HWS [LWS], when compared with all the other current meters moored within the estuary. The period during which data from mooring F was considered valid ended before the strong increase of the river discharge, whereas the data obtained with RCM G covered also the high river discharge period. However, the phase-velocity diagrams for both moorings (RCMs F_m, F_b and G_m) still evidence HW [LW] occurring prior to HWS [LWS] – see Fig. 3.13(c). Thus, the shift of the order of occurrence of the HW [LW] and HWS [LWS] does not seem to be related to river discharge variability. No observations were available in that region during a low river discharge regime, so a more accurate evaluation of the impact of different freshwater regimes on the phase relations between water level and current velocity is not

possible.

Still concerning the propagation of the M_2 wave, the existence of vertical phase lags (e.g. between D_s and D_b) or horizontal phase lags (e.g. between D_s and E_s), is suggested by the different HWS-HW or LWS-LW time lags. According to Fortunato et al. (1997), the increase of friction leads to the increase of the phase lag between current velocity and water elevation. Therefore, these vertical phase lags can be explained by the increasing friction effects with depth. As for the horizontal phase lags, higher friction is expected nearer the margin, so this can also explain the increased horizontal phase lag near the margin.

For the TEJO88/2 current meters (see location in Fig. 3.13(d)), the results of the harmonic analysis (Table 3.4) show that near-bottom current reverses between 40 and 60 minutes before the near-surface current. Near the surface, the current close to the northern margin reverses before current farther from the margin, whereas near the bottom, the phase lag is equivalent to the current meter's sampling interval (~5 minutes) and can be considered negligible.

3.3.4 Tidal asymmetry

The asymmetric behaviour of the tide in the Tagus Estuary, with ebb tides shorter than flood tides, was shown by computing ebb and flood durations for all the available tide gauge records. This behaviour had already been reported by other authors, e.g. Dias (1993) and Fortunato et al. (1999). The tidal asymmetry grows as the tidal wave propagates upstream, as shown by the difference between ebb and flood duration, increasing from the mouth (~30 minutes at Paço de Arcos) to the interior (~1 hour at Cabo Ruivo).

The former discussion of the harmonic analysis of the current velocity data has already shown ebb currents generally stronger than flood currents, which is also a characteristic of the asymmetric behaviour of the tide. In order to quantify the contributions of the main shallow-water constituents for the tidal asymmetry, the results of the harmonic analysis for all water level and current time series were used to compute amplitude ratios between M_4 and M_2 and between M_6 and M_2, as well as the respective relative phase differences, both for water level and for along-channel current velocity. The influence of the M_6 constituent is evaluated through an analytical test for the whole range of phase difference relative to M_2. This will allow to understand possible changes in the water level and in the current

velocity in regions with relative importance of M_6.

Amplitude ratio and relative phase difference: M_4

The harmonic analysis results allowed to compute the amplitude ratios a_{M_4}/a_{M_2} and v_{M_4}/v_{M_2}, as well as the relative phase differences $2\theta_{M_2}-\theta_{M_4}$ and $2\varphi_{M_2}-\varphi_{M_4}$. The amplitude ratios measure the intensity of the asymmetry and the relative phase provides its sense, i.e. if the tide is flood or ebb dominant (see Section 3.1). The results for the 1972 one-year long water level time series are represented in Fig. 3.14(a), whereas the results for the one-month long water level and current velocity time series are presented, respectively, in Fig. 3.15(a) and in Table 3.7. Since the results in Fig. 3.15 are similar for each gauge site, the campaigns are not specified in the graph.

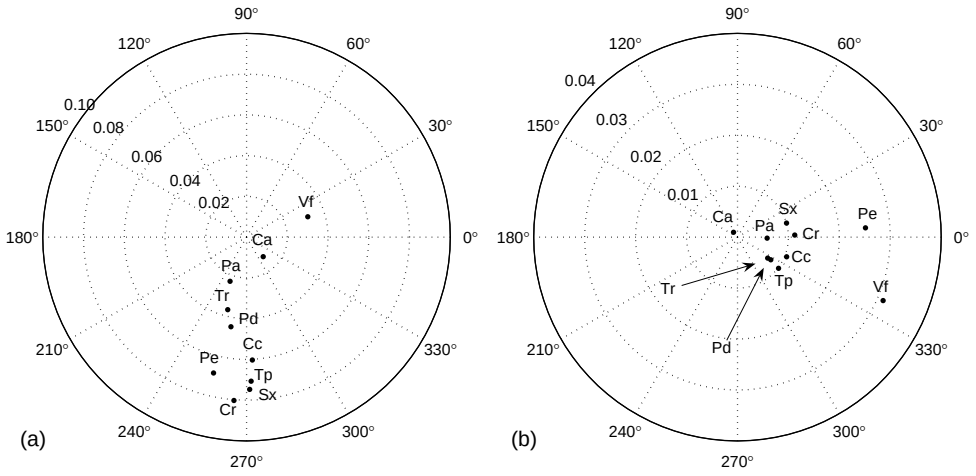

Figure 3.14 – Polar representation of (a) a_{M_4}/a_{M_2} and $2\theta_{M_2}-\theta_{M_4}$ and (b) a_{M_6}/a_{M_2} and $3\theta_{M_2}-\theta_{M_6}$ for the 1972 one-year long water level time series. The amplitude ratios are represented by the distance from the centre to each point and the relative phases by the angle, measured counter-clockwise from the x-axis.

Water level

For the one-year long time series, the water level amplitude ratio a_{M_4}/a_{M_2} grows from about 0.01 at the mouth to about 0.07 at Cabo Ruivo (Cr). Upstream of Cr, i.e. in Pe and Vf, the ratio a_{M_4}/a_{M_2} decreases (see Fig. 3.14(a)), indicating the decreasing asymmetry of

the tide. Also for the one-month long water level time series (see Fig. 3.15(a)), the ratio a_{M_4}/a_{M_2} increases from about 0.01 at the mouth (Ca) to about 0.07 at the estuary's interior (Cr).

The water level relative phase $2\theta_{M_2} - \theta_{M_4}$ for the one-year long series shows almost all values comprised in the interval between 250° and 311°, indicating a tendency for ebb dominance (compare with Fig. 3.2(c)). The exception is for the tidal record obtained at Vf (relative phase of about 18°), which indicates a tendency for flood dominance. The relative phase values for the tidal gauges Cc, Tp and Sx are about 272°, indicating a maximum distortion on water level variation towards ebb dominance in the mid-estuarine region (the transition between the inlet channel and the inner bay).

The one-month long water level time series present relative phase values comprised between 260° and 302°, typical of ebb dominance.

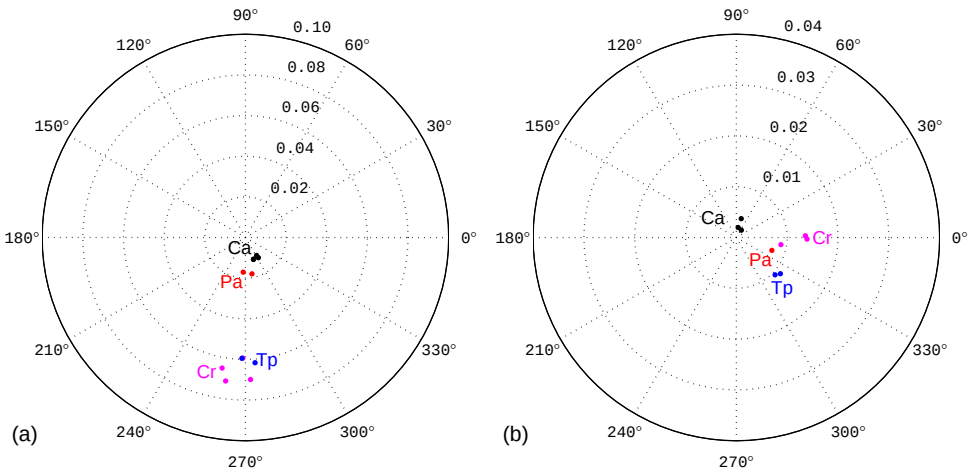

Figure 3.15 – Polar representation of (a) a_{M_4}/a_{M_2} and $2\theta_{M_2} - \theta_{M_4}$ and (b) a_{M_6}/a_{M_2} and $3\theta_{M_2} - \theta_{M_6}$ for the one-month long water level time series. The amplitude ratios are represented by the distance from the centre to each point and the relative phases by the angle, measured counter-clockwise from the x-axis.

Current velocity

In what concerns the amplitude ratio in the case of the current velocities (v_{M_4}/v_{M_2}), it is always different from zero, indicating an asymmetric behaviour of the tidal currents. As for the current velocity relative phase $2\varphi_{M_2} - \varphi_{M_4}$, most of its values are comprised between 90° and 270°, also indicating a tendency for ebb dominance (see Fig. 3.2(c)). The exception is current meter A, moored at the inlet channel, with a relative phase of about 277°, thus indicating a weak tendency for flood dominance. This is consistent with the result presented before for that location, flood stronger than ebb.

In general, for both water level and current, the amplitude ratios and relative phases between M_4 and M_2 point out to the existence of the typical ebb dominance – ebbs with shorter duration and stronger currents.

Survey	Site	v_{M_4}/v_{M_2}	$2\varphi_{M_2} - \varphi_{M_4}$	v_{M_6}/v_{M_2}	$3\varphi_{M_2} - \varphi_{M_6}$
TEJO85	A	0.078	277.2	***	***
	B	0.106	201.0	***	***
	C	0.094	171.8	***	***
TEJO88/2	D_s	0.172	224.4	0.036	183.2
	D_b	0.273	222.6	0.070	341.1
	E_s	0.089	228.5	0.021	29.7
	E_b	0.115	143.7	0.140	7.2
TEJO89	F_m	0.094	266.6	0.027	137.3
	F_b	0.110	216.5	***	***
	G_m	0.097	147.0	***	***

Table 3.7 – Amplitude ratios v_{M_4}/v_{M_2} and v_{M_6}/v_{M_2} and relative phases $2\varphi_{M_2} - \varphi_{M_4}$ and $3\varphi_{M_2} - \varphi_{M_6}$ for the current velocity time series. *** – Constituent not considered significant.

Amplitude ratio and relative phase difference: M_6

Most studies on tidal asymmetry focus the effect of M_4 on the distortion of water level and tidal currents from a sinusoidal form and not much attention has been paid to the contribution of M_6 to tidal asymmetry. In the present work, amplitude ratios a_{M_6}/a_{M_2} and

v_{M_6}/v_{M_2} and relative phases $3\theta_{M_2} - \theta_{M_6}$ and $3\varphi_{M_2} - \varphi_{M_6}$ have been computed based on the harmonic analysis results, in order to identify a possible relation between these parameters and the intensity and sense of the asymmetry. The results for the one-year long water level time series are shown in Fig. 3.14(b) and for the one-month long water level and current velocity time series, are summarised in Fig. 3.15(b) and in Table 3.7, respectively.

Water level

In what concerns the one-year long water level records, the amplitude ratio a_{M_6}/a_{M_2} is comprised between 0.001 at Ca and about 0.011 at Cr (see Fig. 3.14(b)). From Cr to Pe, the amplitude ratio doubles its value and continues increasing further upstream (about 0.031 at Vf). The strong increase of the ratio a_{M_6}/a_{M_2} upstream of Cr indicates the growth of the relative importance of friction, which results in the delay of the low water (Parker, 1991), contributing to the shortening of the time between low and high water. Thus, the behaviour of the ratio a_{M_6}/a_{M_2} upstream of Cr can be probably related to the tendency for flood dominance, earlier indicated by the water level relative phase $2\theta_{M_2} - \theta_{M_4}$ at Vf (see Fig. 3.14(a)).

The one-month long water level time series presented values for amplitude ratio range from 0.002 at Ca to 0.014 at Cr (see Fig. 3.15(b)), which are consistent with those obtained for the one-year long time series in the same estuarine region.

Values of relative phase $3\theta_{M_2} - \theta_{M_6}$ obtained for the one-year long water level time series are comprised between $-37°$ and $16°$ and the values obtained for the one-month long time series are comprised between $-44°$ and $1°$. Thus, according to these results, the phase lag of M_6 relative to M_2 seems to be locked within the interval $]-45°\ 16°]$. Only the tidal gauge closer to the mouth (Ca) shows relative phase values outside of these intervals: $128°$ in the case of the one-year long time series and between $56°$ and $80°$ in the case of one-month long time series.

Current velocity

Concerning the current velocity, only the current meters of TEJO88/2, located in mid-estuary, allowed to determine a few significant (i.e. signal-to-noise ratio greater than 1 – see Section 3.2.2) amplitudes and phases. As a consequence, the amplitude ratio v_{M_6}/v_{M_2}

was essentially computed for these current meters and so they are valid for a very restricted region of the estuary. They show higher values for the near-bottom currents when compared to near-surface currents. This is consistent with the fact that M_6 is originated mainly by bottom friction (see Section 3.1).

As for current velocity time series, the few significant M_6 phases determined by harmonic analysis did not allow to establish a relation with M_2 phases.

Relative effects of M_4 and M_6

The addition of the constituents M_2 and M_4 provides a good description of the tide within the Tagus Estuary, as shown by the comparison between the stage-velocity diagrams for the measured data and the ones obtained with those harmonic constituents (see examples in Fig. 3.8). The effect of the M_6 constituent on water level and current velocity within Tagus Estuary can be demonstrated by adding this constituent to M_2 and also by adding it to the result of M_2 + M_4.

Analytical test

An analytical test was performed in order to evaluate the behaviour of the tidal wave, both in terms of water level and current velocity, according to the phase of M_6 relative to M_2, $3\theta_{M_2} - \theta_{M_6}$ and $3\varphi_{M_2} - \varphi_{M_6}$, respectively. This test was also performed to allow a better interpretation of the M_2 and M_6 relative phases computed from the observational data for water level and to complement that information with the corresponding relative phases for current velocity.

The effects of adding M_6 to M_2 alone or to the combination of M_2 and M_4 were analysed considering maximum flood and maximum ebb dominance conditions, which correspond to different phase relations between M_2 and M_4 (see Fig. 3.2). Two distinct configurations were used, based on the amplitude values from Tables 3.4 and 3.5, representing low and high relative importance of M_6: (A) $a_{M_6}/a_{M_2} = 0.01$ and $v_{M_6}/v_{M_2} = 0.03$; (B) $a_{M_6}/a_{M_2} = 0.03$ and $v_{M_6}/v_{M_2} = 0.10$. The amplitudes of water level and current velocity obtained for M_2, M_4 and M_6 at Terreiro do Paço (Tp) and at Vila Franca de Xira (Vf) were used in equations (3.1), adding the M_6 terms for water level and current velocity: $a_{M_6} \cos(3\omega t - \theta_{M_6})$ and $v_{M_6} \cos(3\omega t - \varphi_{M_6})$.

The results of this experience are presented in terms of water height difference for high and low water along the $3\theta_{M_2} - \theta_{M_6}$ range 0 – 360° and in terms of the difference of maximum flood and ebb currents along the $3\varphi_{M_2} - \varphi_{M_6}$ range 0 – 360°.

When only the constituents M_2 and M_6 were considered, the different conditions of maximum flood dominance or maximum ebb dominance became irrelevant, reinforcing the fact that M_4 is the constituent responsible for the distortion of the tidal wave. In this sense, no differences were noticed between water height in high and low water or between maximum flood and ebb currents for the entire tested range of relative phase difference. Both the high and low water heights and the maximum flood and ebb currents attain a minimum for a relative phase difference of 180° and a maximum for 0/360° (not shown).

Adding the constituent M_6 to the combination of M_2+M_4, differences become evident in both water level and current velocity when considering the cases of (*i*) maximum flood dominance (Figs. 3.16(a) and 3.16(b)) or (*ii*) maximum ebb dominance (Figs. 3.16(c) and 3.16(d)).

Starting with the configuration (A), for maximum flood dominance conditions, the amplitude of the tidal wave in high water is higher than in low water for a relative phase between 0 and 180°; the opposite is verified for a relative phase between 180 and 360°. In what concerns current velocity, maximum flood current is always higher than maximum ebb current, as expected. Both maximum flood and ebb currents attain a maximum for a relative phase of 180°. Considering maximum ebb dominance conditions, the results are essentially the opposite of those for flood dominance. The amplitude of the tidal wave in high water is lower than in low water for a relative phase between 0 and 180° and higher than in low water for a relative phase between 180 and 360°. Concerning current velocity (maximum ebb current is always higher than maximum flood current), both maximum flood and ebb currents attain a minimum for a relative phase of 180°.

Regarding the configuration (B), with both ratios between M_6 and M_2 higher than in the former configuration, the results are not much different (Fig. 3.17), besides the increased differences between the amplitudes in high and low water and between maximum flood and ebb currents. It is also evident in Fig. 3.17 the shift, relative to configuration (A), of the phase values ($3\theta_{M_2} - \theta_{M_6}$ and $3\varphi_{M_2} - \varphi_{M_6}$) corresponding to minimum and maximum differences.

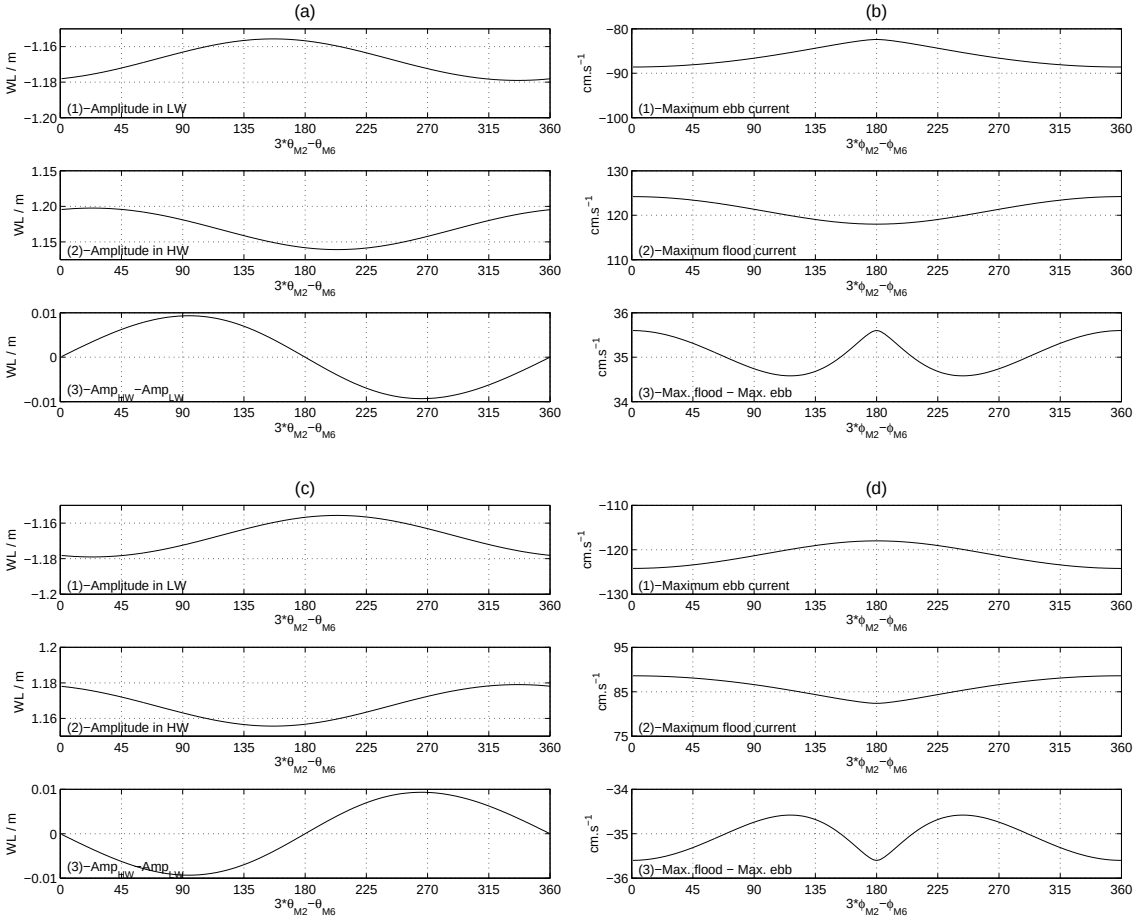

Figure 3.16 – Results of the analytical test of the influence of M_6 on M_2+M_4 with configuration (A) (see text) for (a) water level and (b) current velocity in maximum flood dominance conditions and for (c) water level and (d) current velocity in maximum ebb dominance conditions.

Current meter data

The current meters D_s and F_m were chosen to exemplify the results of adding these shallow-water constituents (Fig. 3.18), since they were the few with significant M_6 amplitude and phase. The distortion caused by M_4 and M_6 is assessed through the comparison of ebb and flood durations and of the relative strength of ebb and flood currents.

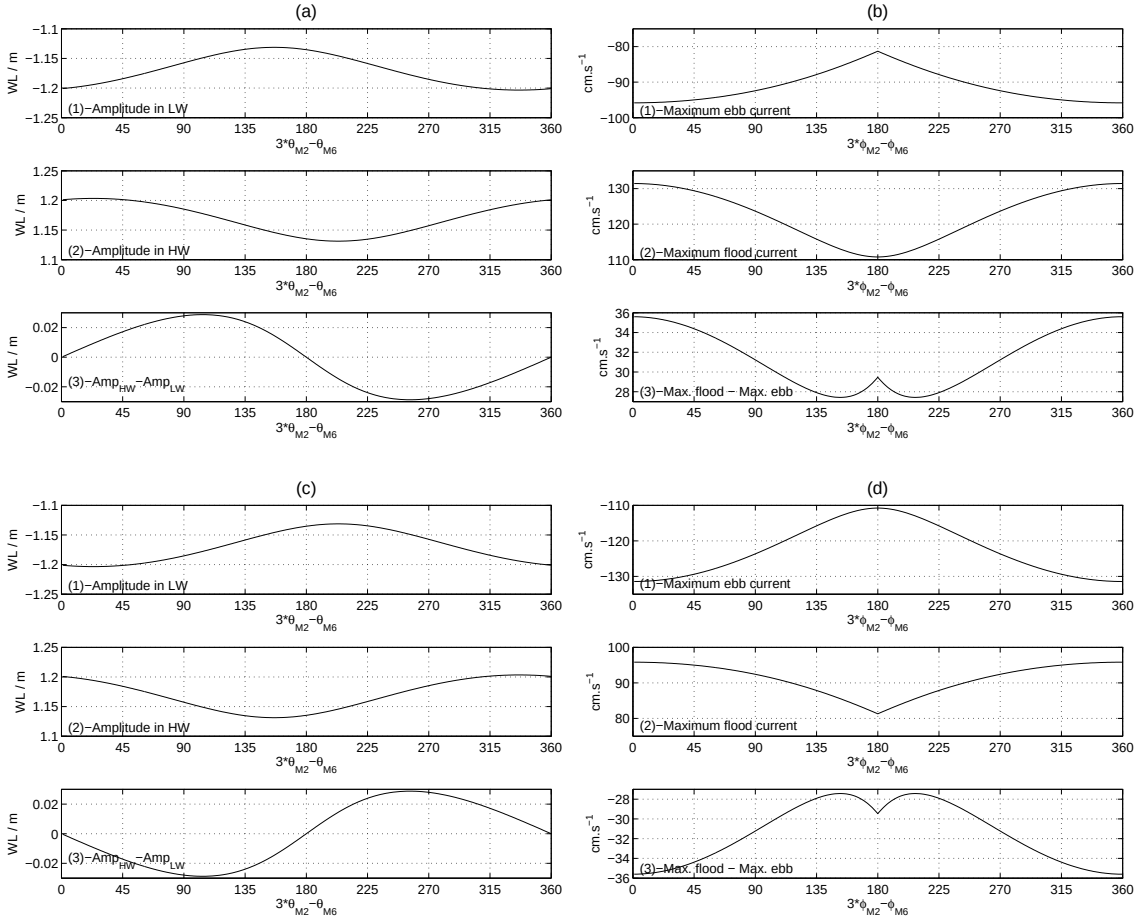

Figure 3.17 – Results of the analytical test of the influence of M_6 on M_2+M_4 with configuration (B) (see text) for (a) water level and (b) current velocity in maximum flood dominance conditions and for (c) water level and (d) current velocity in maximum ebb dominance conditions.

The addition of M_4 to M_2 increases the flood duration and decreases the ebb duration; in general, ebb currents are intensified whereas flood currents decrease their magnitude. The deformation of the stage-velocity diagram in Fig. 3.18 (solid gray line) is well evident when compared with M_2. Adding M_6 to M_2 affects neither ebb and flood durations nor the relative magnitude of the currents (black dash-dotted lines in Fig. 3.18). The addition of M_6 to the result of M_2+M_4 (gray dash-dotted line in Fig. 3.18) affects equally the magnitude of

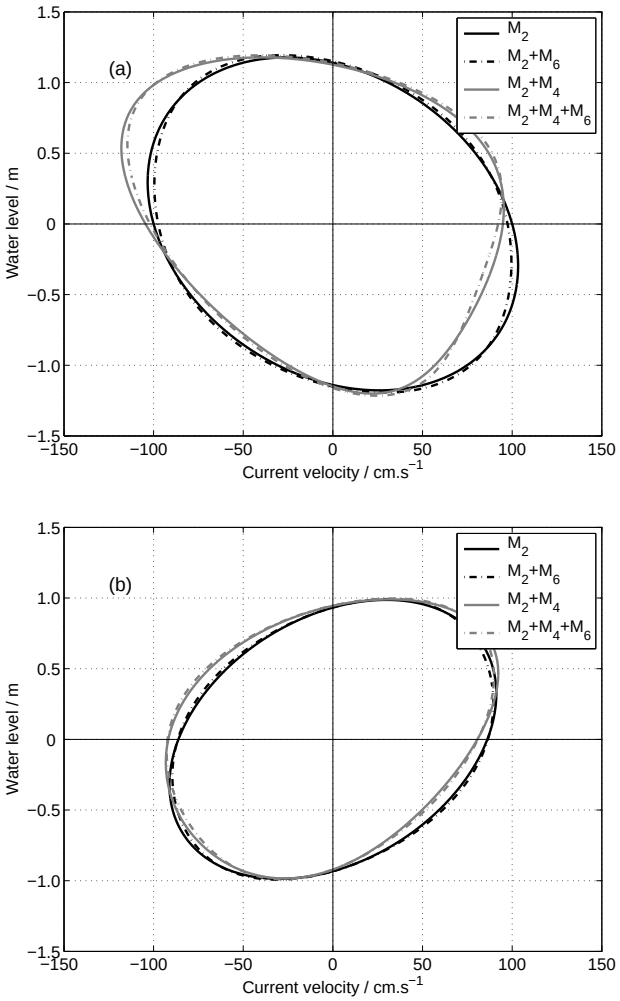

Figure 3.18 – Water level versus current velocity using various combinations of M_2 and its higher frequency harmonics M_4 and M_6 for current meters (a) D_s and (b) F_m. Flood currents are positive and the temporal progression of water level and current in the diagrams is counter-clockwise.

both ebb and flood currents and does not enhance the deformation caused by the addition of M_4, which probably is due to the relatively low importance of the sixth-diurnal constituent in this region of the Tagus Estuary. A similar result was also reported by Blanton et al. (2002) for the Satilla River estuary. On the other hand, the analytical test presented above showed exactly the opposite, since the differences between the amplitudes on high and low

water and between the maximum flood and ebb currents are always different from zero, except when $3\theta_{M_2} - \theta_{M_6}$ equals to 0 or 180°. These results are complemented by Aldridge (1997), who showed, with a simple analytical test, that the addition of the M_6 constituent could reverse the sense of the asymmetry.

In summary, the observational data showed that M_6 has a small effect on the tidal wave distortion within the channel and mid-estuarine regions of Tagus Estuary, generally causing only a slight increase of both ebb and flood current magnitudes.

3.4 Summary of results

Based on the water level data, the Tagus Estuary can be classified as a mesotidal estuary and its tide as essentially semi-diurnal. The tidal range within the estuary is strongly influenced by the fortnightly cycle, the difference between neap and spring tide reaching up to 3 m. The tidal range increases within the estuary from Cascais to Ponta da Erva, as well as the semi-diurnal harmonic constituents. Despite losing energy to the shallow-water constituents within the estuary, the semi-diurnal tide keeps growing as it evolves from the mouth until Ponta da Erva, decreasing further upstream at Vila Franca de Xira. This suggests that a fraction of the tidal energy is reflected somewhere between Ponta da Erva and Vila Franca de Xira. The existence of a resonant mode with a period close to that of the semi-diurnal constituents is consistent with these observations. The Merian's formula was used to estimate the resonance period of the Tagus Estuary, but it proved to be an oversimplification in terms of the morphological characteristics of the estuary. This method does not account for the continuous reflections of the semi-diurnal wave along the margins and on the bottom of the estuary. The resultant resonance period was, therefore, too far from the semi-diurnal period and also from the estimative reported by Fortunato et al. (1999), using a numerical model.

Both shallow-water constituents M_4 and M_6 increase their amplitudes within the estuary, from the mouth to the head. The M_4 constituent grows from Cascais to Cabo Ruivo, whereas M_6 grows softly from the mouth to Cabo Ruivo, and with a steeper gradient upstream of that location. Given that the M_4 generation is primarily attributed to the nonlinear effects of advection and the M_6 is essentially generated by bottom friction, these

observations suggest that the advective accelerations are important within the estuary from the mouth to Cabo Ruivo whereas bottom friction assumes a greater importance upstream of that point.

The tide is the main responsible for the variability of the current intensity, whereas bottom topography acts as a major constraint to the current direction, as shown by the diurnal and semi-diurnal tidal ellipses. Currents generated by the shallow-water constituents M_4 and M_6 are more rotary and less influenced by the local bathymetry. The intensity of tidal currents seems to be stronger in the mid-estuarine and interior regions, as compared with the intensity near the mouth and, in general, ebbs are stronger than floods. In the mid-estuarine region, tidal flow is more concentrated near the northern margin. Also in this region, a higher progressive wave character of the semi-diurnal tidal wave M_2 near the northern margin is evidenced, when compared with the opposite margin.

The decrease of the time lag between HW [LW] and HWS [LWS] within the estuary indicates that the progressive wave contribution of M_2 is reduced from the mouth to the interior and the semi-diurnal tide behaves essentially like a standing wave in the mid-estuary and in the inner bay.

The existence of asymmetry in the tide within the Tagus Estuary is evidenced by ebbs being shorter than floods, with the time difference increasing from the mouth to the interior. The amplitude ratios of M_4 relative to M_2 and the phase of M_4 relative to M_2, both for water level and for current velocity, indicate ebb dominance, consistent with shorter and stronger ebbs.

A strong amplification of the amplitude ratio of M_6 relative to M_2 is evidenced by the water level data upstream of Cabo Ruivo. In addition, the phase of M_4 relative to M_2 at Vila Franca de Xira indicates flood dominance conditions. These results suggest a possible relation between the increasing importance of the M_6 constituent and the shift in the sense of the tidal asymmetry (from ebb to flood dominance) in this region of the estuary.

The separated effects of adding M_4 and M_6 to M_2 were then investigated in order to examine the influence of each one of these shallow-water constituents in the tidal asymmetry. The addition of M_4 increases flood duration and decreases ebb duration, whereas ebb currents are intensified and flood currents decrease their magnitude. In general, adding M_6 to M_2 causes the magnitude of both ebb and flood currents to increase and does not affect

ebb or flood durations, these results being valid to the inlet channel and mid-estuarine regions of the Tagus Estuary. No data were available to investigate the effects of M_6 in the region where this shallow-water constituent seems to gain importance relative to M_4, the inner bay.

Nevertheless, an analytical test considering two different configurations in terms of the importance of M_6 relative to M_2 has shown that the difference between the amplitude of the tidal wave in high and low water is generally different from zero, except when the phase of M_6 relative to M_2 equals 0 or 180°, and that the relative magnitude of maximum flood and ebb currents also changes according to the phase of M_6 relative to M_2. So, it can be concluded that the M_6 constituent can play an important role in the tidal asymmetry.

Chapter 4

Thermohaline and circulation patterns

The main objectives of this chapter are to characterise the horizontal and vertical structures of the thermohaline and dynamical fields of the Tagus Estuary and to investigate the role and the effects of the principal forcing mechanisms (tide, wind and river discharge) on the estuarine dynamics.

The thermohaline conditions within the estuary during the observational campaigns described in Chapter 2 are presented. The data are analysed in order to classify the Tagus Estuary using quantitative methods (Prandle, 1985; Hansen and Rattray, 1966) and in order to establish relations between the principal forcing mechanisms and the observed thermohaline tidal and subtidal variability. Finally, the direct influence of the adjacent coastal ocean on the Tagus Estuary's dynamics is studied.

4.1 Hydrology and classification of the Tagus Estuary

4.1.1 Hydrology conditions

CTD data

Temperature and salinity data collected during the campaigns are presented in the form of Temperature-Salinity (T/S) diagrams in Fig. 4.1, where density anomaly[1] contours are

[1]Density anomaly: defined as $\gamma_t = \rho(S,T,0) - 1000$ (kg m^{-3}), where ρ represents the density of a sample at the atmospheric pressure with salinity S and temperature T.

also shown.

The T/S values with higher density anomalies correspond to stronger presence of seawater, thus representing the near-bottom layers, and those with lower density anomalies are more influenced by the freshwater of the near-surface layer.

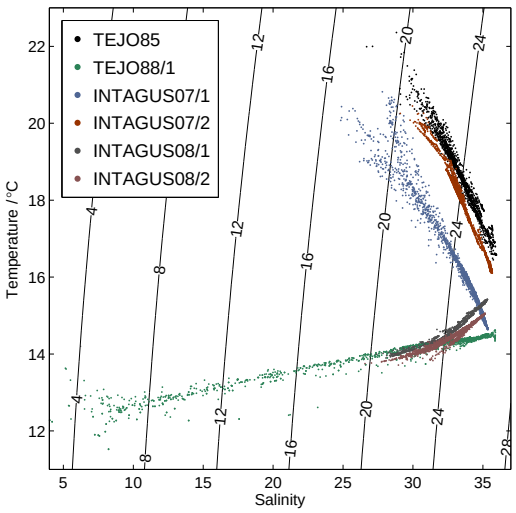

Figure 4.1 – Multiple T/S diagrams for all CTD stations during TEJO85, TEJO88/1 and INTAGUS campaigns, superimposed on the density anomaly γ_t (kg m^{-3}) contours.

The salinity range is similar for all campaigns (TEJO85 and INTAGUS), except for TEJO88/1 campaign (winter), which has a much larger range than the others. This can be the result of a larger river discharge: 1201 m^3 s^{-1} (TEJO88/1) as compared to 184 m^3 s^{-1} (TEJO85), 178 m^3 s^{-1} (INTAGUS07) and 84 m^3 s^{-1} (INTAGUS08). It should be noticed that the winter campaign INTAGUS08 was performed during a river discharge regime typical of a dry season, and this is the most probable cause for the salinity range being similar to those measured during the summer campaigns.

During summer, seawater is colder than river water within the estuary and the reverse occurs in winter, but with a smaller contrast, as evidenced by the T/S diagrams of the CTD campaigns in Fig. 4.1.

The temperature difference between summer and winter is much larger for river water than for seawater. In what concerns river water, the low discharge (meaning that surface water has higher residence time) combined with longer insolation period during summer is

the most probable cause for that large temperature difference. As for seawater, the small temperature difference between summer and winter can be due to the coastal water cooling associated with upwelling events in summer, which influence the near-bottom temperature within the estuary. This can be shown through the CTD data for the INTAGUS campaigns. Analysing the corresponding T/S diagrams in more detail (Fig. 4.2), the set of T/S diagrams for the summer INTAGUS campaign (22 and 23 August 2007, neap tide) shows a near-bottom temperature (~14.6°C) lower than the INTAGUS winter campaign (15 – 15.5°C). This feature is further analysed ahead in Section 4.4. As for salinity, no significant differences are observed.

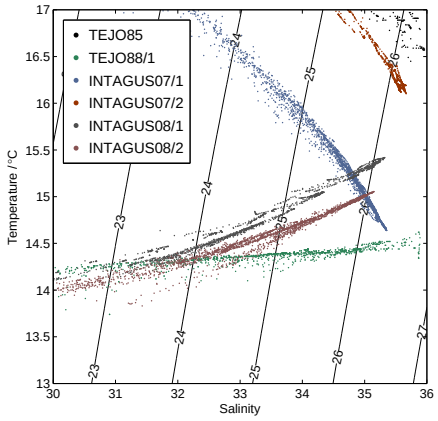

Figure 4.2 – Detailed view for the salinity range 30 – 36 and temperature range 13 – 17°C of the multiple T/S diagrams presented in Fig. 4.1, superimposed on the density anomaly γ_t (kg m^{-3}) contours.

RCM data

The temperature and salinity extrema, mean and standard deviation values, calculated from the RCMs time series (see Fig. 4.3 for location), are presented in Table 4.1 and show some characteristics of the thermohaline structure of the Tagus Estuary. TEJO85 (RCMs A, B and C) evidences an increase of the mean temperature and a decrease of the mean salinity between the channel and the interior of the estuary. The consequent longitudinal density gradient is a main characteristic of many estuaries and drives the gravitational circulation.

In the inner bay, the near-surface temperature and salinity mean values of TEJO88/2 (summer) evidence a stronger presence of seawater closer to the northern margin (D_s), whereas the near-bottom (D_b and E_b) mean values do not show significant differences between the two sites.

In the inlet channel, TEJO89 campaign (winter), both the mid-water and the near-bottom levels show temperature and salinity mean values with stronger influence of river water near the northern margin (F_m and F_b).

		Temperature (°C)					Salinity				
Survey	RCM	N. obs.	Min.	Max.	Mean	Std. dev.	N. obs.	Min.	Max.	Mean	Std. dev.
TEJO85	A	4165	16.5	21.5	19.2	0.9	4165	24.3	34.9	32.0	1.6
	B	4610	16.6	23.0	19.5	1.0	4610	23.3	34.1	30.8	1.9
	C	4610	17.4	22.7	20.5	0.8	4610	19.8	33.0	28.2	2.0
TEJO88/2	D_s	8614	15.5	24.1	18.9	1.2	8614	19.6	34.8	30.5	2.1
	D_b	8618	15.1	19.8	17.5	1.0	8618	26.8	34.7	32.2	1.5
	E_s	6045	17.4	24.3	19.4	1.1	6046	20.7	33.6	29.8	2.3
	E_b	8647	15.4	20.4	17.6	0.9	4719	28.8	34.6	32.6	1.1
TEJO89	F_m	8627	15.6	18.4	16.6	0.7	8627	23.5	35.9	32.7	2.5
	F_b	8627	16.2	18.7	17.0	0.6	8627	25.6	35.7	33.0	2.0
	G_m	8329	16.1	18.6	17.1	0.5	8329	28.1	35.9	33.7	1.5
	G_b	8329	16.3	18.5	17.1	0.5	8329	29.9	35.9	34.1	1.1

Table 4.1 – Basic statistics concerning the temperature and salinity time series obtained during all RCM campaigns in Tagus Estuary (TEJO85, TEJO88/2 and TEJO89).

4.1.2 Quantitative classification of the Tagus Estuary

Quantitative methods

As referred before (Chapter 1), the Stratification-Circulation diagram, developed by Hansen and Rattray (1966), is one of the most widely used quantitative classification schemes for estuaries. This scheme is based on two dimensionless parameters: a stratification parameter ($\delta s/\langle s \rangle$) and a circulation parameter (u_s/u_f), both defined in Section 1.2.2.

These parameters are based respectively on time-averages over a complete semi-diurnal tidal cycle (net values) of salinity and current velocity. The methodology presented here follows Kjerfve (1979). The net value of the generic quantity Y, at a given non-dimensional depth η_j, is

$$\left\langle Y\left(\eta_j\right)\right\rangle = \frac{1}{n}\left\{\frac{1}{2}Y\left(\eta_j, t_0\right) + \sum_{k=1}^{n-1} Y\left(\eta_j, t_k\right) + \frac{1}{2}Y\left(\eta_j, t_n\right)\right\} , \tag{4.1}$$

where $j = 0, 1, \ldots, m; \eta_0, \eta_1, \ldots, \eta_m$ represent non-dimensional depths defined as $\eta = z/\mathrm{d}(t)$ (z represents the depth and $\mathrm{d}(t)$ is the total water depth at a given station and time); t_0 is the starting time; t_n is the time at the end of the tidal cycle; and

$$t_k = t_0 + k\Delta t , \tag{4.2}$$

for $k = 1, 2, \ldots, n-1$. Departing from equation (4.1), the net velocity and salinity profiles can be computed.

The depth-average of a net quantity $\langle Y\rangle$ can be computed in the following way:

$$\overline{\langle Y\rangle} = \frac{1}{m}\left\{\frac{1}{2}\langle Y\left(\eta_0\right)\rangle + \sum_{j=1}^{m-1}\left\langle Y\left(\eta_j\right)\right\rangle + \frac{1}{2}\langle Y\left(\eta_m\right)\rangle\right\} . \tag{4.3}$$

The circulation parameter is defined as the ratio between the net surface velocity and the depth-averaged net velocity and the stratification parameter is defined as the ratio between the difference bottom minus surface net salinities and the depth-averaged net salinity. Using the notation of Kjerfve (1979), it thus follows:

$$\begin{aligned} \text{Circulation parameter} &= \frac{\langle V\left(\eta_0\right)\rangle}{\overline{\langle V\rangle}} \\ \text{Stratification parameter} &= \frac{\langle S\left(\eta_m\right)\rangle - \langle S\left(\eta_0\right)\rangle}{\overline{\langle S\rangle}} . \end{aligned} \tag{4.4}$$

When both the stratification and circulation parameters were available, the Stratification-Circulation Diagram (Hansen and Rattray, 1966) has been used. However, when only the stratification parameter could be computed, the criterion established by Prandle (1985) was used to classify the estuary. Comparatively to the Stratification-Circulation Diagram, this scheme is not so accurate since different types of circulation, described by different circulation parameter values, may change the estuary's classification, despite keeping the stratification parameter constant.

Prandle (1985) showed that the water column is considered *well mixed* for $\delta s/\langle s \rangle < 0.15$, *partially mixed* for $0.15 < \delta s/\langle s \rangle < 0.32$ and *stratified* for $\delta s/\langle s \rangle > 0.32$ (δs is defined as the surface to bottom difference in salinity; $\langle s \rangle$ is defined as the average vertical or cross-sectional salinity).

Three different regions were defined within Tagus Estuary according to their morphological characteristics: (*i*) the Mouth of the estuary; (*ii*) the Inlet Channel; and (*iii*) the Bay (constituted by the mid-estuary and the inner bay). Each one of these three main regions, depicted in Fig. 4.3, was classified according to the stratification and circulation (when available) parameters.

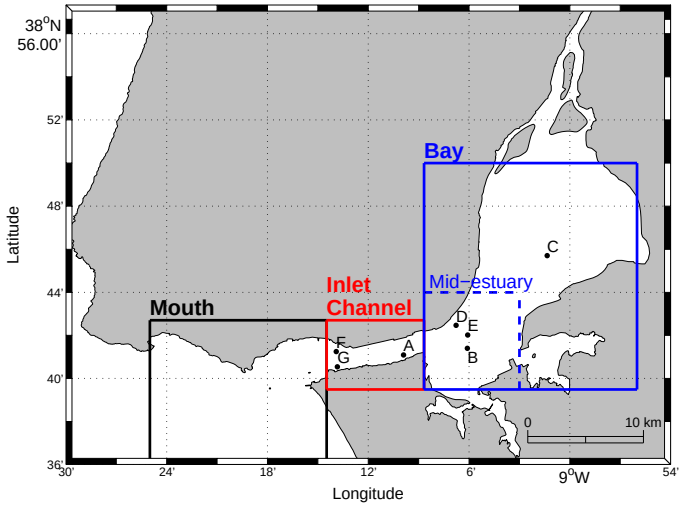

Figure 4.3 – Regions within Tagus Estuary according to which the circulation and stratification parameters were calculated and analysed. Black: Mouth; Red: Inlet channel; Blue: Bay (Mid-estuary and Inner bay). The positions of the current meters of campaigns TEJO85 (A, B, C), TEJO88/2 (D, E) and TEJO89 (F, G) are also indicated.

The CTD profiles obtained during the campaigns TEJO85 and TEJO88/1 were used to estimate the stratification parameter in different regions of the estuary during spring and neap tide conditions, respectively. As the measured profiles covered different phases of several semi-diurnal tidal cycles, it was assumed that the use of all profiles would provide an estimate of the net salinity over a complete semi-diurnal tidal cycle. The stratification parameter for each region was thus computed by averaging all the salinity values at each

level.

In what concerns the INTAGUS campaigns, although current velocity profiles are available, only the stratification parameter was computed, using the repeated salinity profiles along two cross-sections in the Tagus Estuary. The measurements were not carried out over a complete semi-diurnal tidal cycle (as shown by Fig. 2.11), meaning that the influence of the tide was not completely eliminated from the averaged values.

The analysis of the propagation of the tidal wave within the Tagus Estuary (see Chapter 3), based on the time series obtained during the TEJO85 and TEJO88/2 campaigns, showed that the current velocity is about 90° out of phase with water height in the mid-estuary, whereas the phase difference between salinity and water height is relatively small and can be neglected. This means that, given the time coverage of the semi-diurnal tidal cycle for the INTAGUS observations, one can roughly estimate the salinity range but not the current velocity range. Thus, only the stratification parameter could be reasonably estimated but not the circulation parameter, and so the INTAGUS data were only classified according to the stratification.

From all the available RCM hydrographic and current velocity time series, only those obtained during the TEJO88/2 campaign could be used to calculate both parameters through equations (4.4), since in the TEJO85, only near-surface time series were obtained and, in TEJO89, none of the near-surface current meters were retrieved (only near-bottom hydrographic and current velocity time series were available from this campaign). Thus, one semi-diurnal tidal cycle in spring and in neap tide peaks were selected from the TEJO88/2 data and the corresponding temperature, salinity and longitudinal current velocity data were extracted from the records in order to calculate the parameters. Depth-averaged salinity and current velocity were computed using only near-surface and near-bottom values. The results would probably be somewhat different if the whole vertical profile had been measured.

Classification results

The stratification and circulation parameters were computed and the corresponding results, grouped by the estuarine regions defined in Fig. 4.3, are summarised in Tables 4.2 to 4.4.

According to the criterion defined by Prandle (1985), based on the stratification parameter, the results for TEJO85 and TEJO88/1 show that, independently of the regions defined earlier (see Fig. 4.3), the water column in the Tagus Estuary was well mixed ($\delta s/\langle s\rangle < 0.15$) for the combination of summer with spring tide conditions and stratified ($\delta s/\langle s\rangle > 0.32$) for the combination of winter with neap tide conditions (Table 4.2). During summer, the typical low river discharge is responsible for a weak vertical density gradient when compared to that in winter, due to a higher river discharge regime. When compared to neap tides, spring tides are characterised by stronger currents, promoting stronger vertical mixing.

In both cases, spring tide in summer and neap tide in winter, the stratification parameter increases from the mouth to the interior of the estuary, which is expected since the decrease of the tidal currents to the interior is responsible for the decrease of the vertical mixing efficiency along the water column.

Survey	Mouth	Inlet channel	Bay
TEJO85 (Summer, spring)	0.02	0.04	0.05
TEJO88/1 (Winter, neap)	0.42	0.74	0.95

Table 4.2 – Stratification ($\delta s/\langle s\rangle$) parameter calculated for three different regions within the Tagus Estuary from CTD data obtained during TEJO85 and TEJO88/1 campaigns.

TEJO88/2 (Summer, Bay)		
	Stratification	Circulation
Spring tide	0.06	5.67
Neap tide	0.17	8.11

Table 4.3 – Stratification ($\delta s/\langle s\rangle$) and circulation ($u_s/u_f$) parameters calculated from the RCM data obtained during TEJO88/2 campaign.

The stratification parameter computed for the mooring located at the Bay during sum-

mer (TEJO88/2) indicates well mixed water column, both during spring and neap tide (see Table 4.3). Nevertheless, the water column presents some degree of stratification in neap tide conditions, as would be expected, since tidal currents and, consequently, vertical mixing are weaker than during spring tide (see Section 1.3.1).

A circulation parameter lower than 1 does not fit in the Stratification-Circulation diagram (see Fig. 1.3), since this value corresponds to the upper limit of the diffusive fraction of the total upstream salt transfer (ν), when the upper estuary salt flux is entirely due to diffusion. However, for the data of mooring D, during TEJO88/2, the circulation parameter was, in fact, lower than 1. The problem must have been the use of only near-surface and near-bottom net values to compute the depth-averages. This can be overcome by computing the mean cross-sectional velocity (u_f) as the ratio between the river flow and the area of the considered cross-section. In this sense, the monthly mean river flow for August 1988 (255 $m^3\ s^{-1}$) and the area of the cross-section passing through the moorings of TEJO88/2 (436.5 dam^2) were used to compute the circulation parameter. The results, presented in Table 4.3 allow to classify this region of the estuary as Type *2a* [*2b*] in spring [neap] tide, by using the Stratification-Circulation diagram (see Fig. 1.3). This means that this region is classified as partially mixed, with a higher degree of stratification in neap tide. The net flow is expected to reverse at depth and both advection and diffusion have important contributions to the total upstream salt flux.

In what concerns the INTAGUS campaigns (Table 4.4), the stratification parameter indicates well mixed conditions ($\delta s/\langle s\rangle < 0.15$) both in the Inlet channel and in the Bay (see Fig. 4.7), except during INTAGUS07/1 campaign (summer, neap tide), for which the parameter indicates partially mixed conditions ($0.15 < \delta s/\langle s\rangle < 0.32$) in both cross-sections. In the Inlet channel cross-section, the stratification parameter presents a decreasing trend towards the southern margin.

Considering the stratification parameter, the Tagus Estuary is generally a well mixed estuary, although some stratification can arise during typical winter river discharge or in neap tide conditions. When these two factors combine, stratification intensifies within the estuary and the water column can be considered as stratified. The use of the Stratification-Circulation diagram for the TEJO88/2 data indicated partially mixed conditions whereas the stratification parameter alone has indicated well mixed conditions.

Station	Inlet channel			
	INTAGUS07/1 (Summer, neap)	INTAGUS07/2 (Summer, spring)	INTAGUS08/1 (Winter, spring)	INTAGUS08/2 (Winter, neap)
A	0.17	0.02	0.05	0.10
B	0.17	0.02	0.05	0.09
C	0.17	0.02	0.04	0.09
D	0.17	0.02	0.03	0.08
E	0.16	0.01	0.02	0.05
Station	Bay			
	INTAGUS07/1 (Summer, neap)	INTAGUS07/2 (Summer, spring)	INTAGUS08/1 (Winter, spring)	INTAGUS08/2 (Winter, neap)
F	0.23	—	0.02	0.08
G	0.23	—	0.01	0.06
H	0.16	—	0.00	0.03
I	0.21	—	0.01	0.09
J	0.19	—	0.03	0.10
K	0.17	—	0.03	0.06
L	0.12	—	—	—

Table 4.4 – Stratification ($\delta s/\langle s \rangle$) parameter calculated for stations located at the Inlet channel and at the Bay from CTD data obtained during INTAGUS07/1, INTAGUS07/2, INTAGUS08/1 and INTAGUS08/2 campaigns.

4.2 Variability on tidal frequencies

Dynamically, the Tagus Estuary is strongly influenced by the tide, as shown by the analysis of water level and current velocity time series in the previous chapter. This analysis has put into evidence the importance of the principal semi-diurnal and shallow-water harmonic constituents on the dynamics of the Tagus Estuary. In this section, the main objective is to analyse the variability of both the dynamical and thermohaline structures on tidal frequencies using fixed point time series, measured by RCMs, and vertical distributions along longitudinal and transverse sections, obtained with CTD.

4.2.1 Fixed point time series

The strong variability associated with the semi-diurnal tide period (~12.4 h) is clearly evidenced in the time series of both water level and longitudinal (along the major principal axis) current velocity within the estuary. As an example, Figs. 4.4(a) and 4.4(c) represent the time series of, respectively, the water level at Terreiro do Paço and the along-channel component of the current measured in the inlet channel (site A in Fig. 4.3) during the TEJO85 campaign. The corresponding power spectral density plots (Figs. 4.4(b) and 4.4(d)) show the variance peaks associated with the diurnal, semi-, quarter-, sixth- and eighth-diurnal frequencies; in both cases the highest peak is associated with the M_2 frequency.

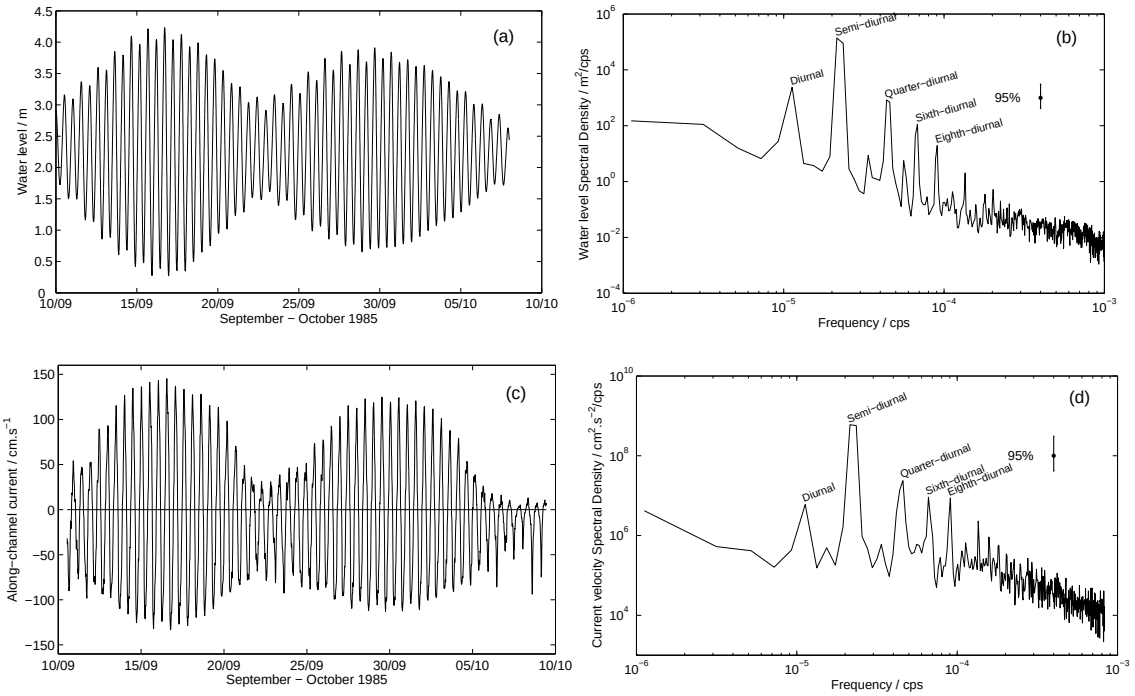

Figure 4.4 – (a) Water level time series at Terreiro do Paço and (b) respective spectral density; (c) Along-channel current time series measured at RCM mooring A (TEJO85) and (d) respective spectral density. Positive (negative) currents indicate flood (ebb). The peaks corresponding to diurnal, semi-, fourth-, sixth- and eighth-diurnal frequencies are identified by the respective labels.

These figures also show the modulation due to the fortnightly tidal cycle. In the water level time series (Fig. 4.4(a)), this is evidenced by the higher tidal range (surface level difference between consecutive high and low water) during spring tide and lower tidal range during neap tide. In what concerns the along-channel current velocity (Fig. 4.4(c)), stronger flood (positive) and ebb (negative) currents occur during spring tide, contrasting with weaker flood and ebb currents occurring during neap tide.

Salinity and temperature within the Tagus Estuary are also strongly influenced by the semi-diurnal tidal cycle, as exemplified in the time series and in the corresponding power spectral density plots (Fig. 4.5). The highest variance peak is always associated to semi-diurnal frequencies, but there is also a significant amount of variance associated with diurnal and also with higher frequencies.

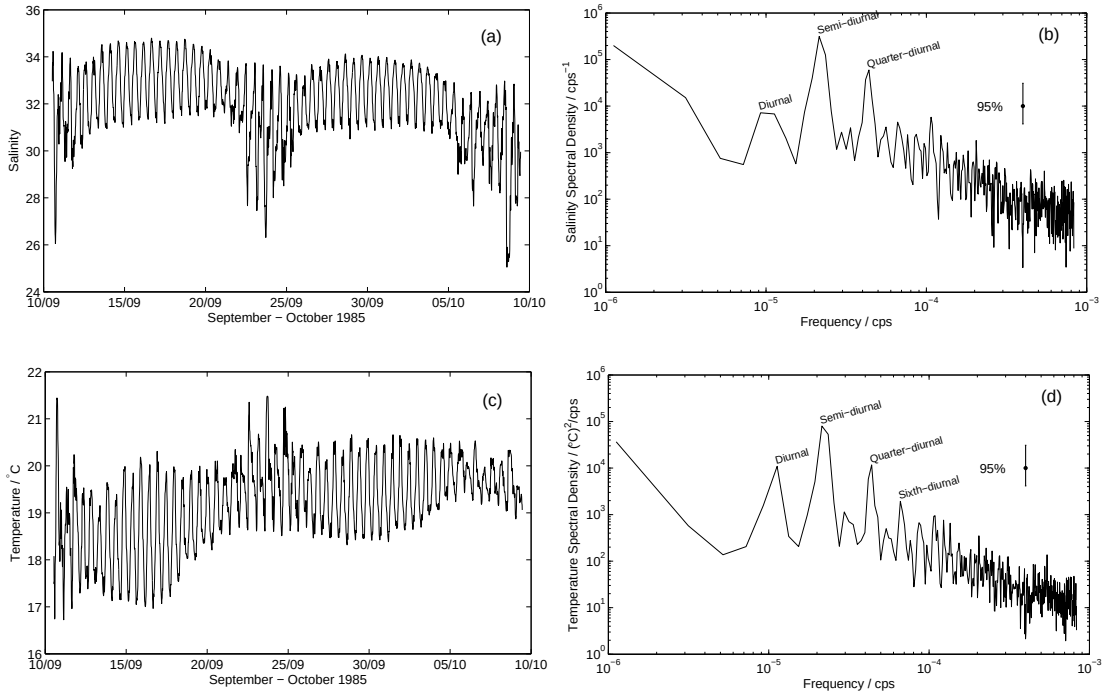

Figure 4.5 – (a) Salinity time series and (b) respective spectral density; (c) Temperature time series and (d) respective spectral density, both measured at RCM mooring A (TEJO85). The peaks corresponding to diurnal, semi-, fourth- and sixth-diurnal frequencies are identified by the respective labels.

As observed for the current velocity, the fortnightly modulation is also evident in the hydrology time series, as Figs. 4.5(a) and 4.5(c) demonstrate, mainly showing an increase of variability during the neap tide periods due to the decrease of the vertical mixing. The spring-neap cycle is evident in the salinity (both the maximum and minimum salinity are higher in spring tide than in neap tide) and in temperature (both the maximum and minimum temperature are lower in spring tide than in neap tide).

4.2.2 Longitudinal sections

Longitudinal sections (along the axis of the estuary) of the inlet channel and of the mid-estuarine/inner bay region performed during TEJO85 and TEJO88/1 campaigns (spring and neap tide conditions, respectively) are analysed by comparing the vertical distributions of temperature and salinity at high water (HW) and low water (LW). In the following analysis, the sections are considered to be synoptic, an audacious assumption, since these sections were completed in between 2h50m and 3h52m, the equivalent to about one quarter of a complete semi-diurnal tidal cycle. In what concerns the location of the sections, those of TEJO85 are not exactly coincident for high and low water. During TEJO88/1, the region near the mouth and the inner bay were surveyed on different days and the corresponding salinity sections are presented separately in Fig. 4.6.

The salinity sections corresponding to spring tide conditions (performed during summer) are represented in Figs. 4.6(a) (high water) and 4.6(b) (low water), whereas those corresponding to neap tide conditions (performed during winter) are represented in Figs. 4.6(c) (high water) and 4.6(d) (low water) for the inlet channel and inner bay and in Figs. 4.6(e) (high water) and 4.6(f) (low water) for the region near the mouth. Vertical distributions of temperature are not shown here since the observed patterns are similar to those observed in vertical distributions of salinity. Since the salinity range reached in summer is much smaller than that in winter (see Fig. 4.1), the colour bar limits and the contour spacing used in Fig. 4.6 differ in accordance with the respective salinity range.

For spring tide conditions, in summer (Figs. 4.6(a) and 4.6(b)), the vertical distributions show a relatively well mixed water column near the mouth and a slight upstream increase in the stratification. The well mixed conditions result from the intense vertical mixing that characterises the spring tide and from the small salinity differences between surface and

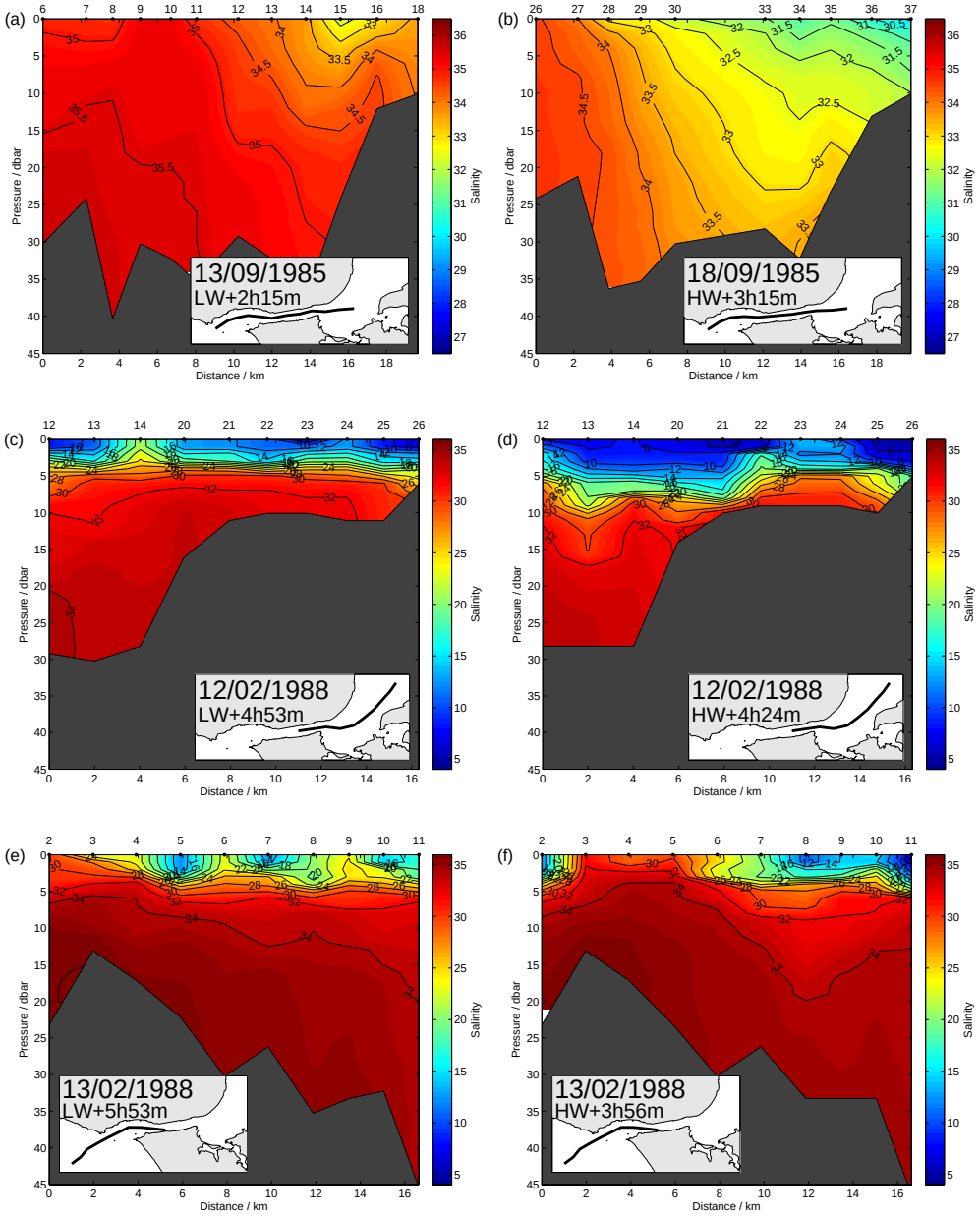

Figure 4.6 – Vertical salinity distributions along longitudinal sections (see insets for location) during (a) summer/spring tide/high water, (b) summer/spring tide/low water, (c) and (e) winter/neap tide/high water and (d) and (f) winter/neap tide/low water. The numbers in the top horizontal axis identify the stations and the interior of the estuary is on the right of the figure.

bottom layers, a consequence of the low river discharge.

In addition, the vertical stratification and the horizontal salinity gradient strengthen from flood to ebb. The harmonic analysis results on the RCM data from TEJO88/2 (Table 3.5) show stronger tidal currents (e.g. for M_2) near the surface than near the bottom, so the variation of stratification during the tide is much probably caused by tidal straining. Thus, during the ebb, the shear in the velocity profile promotes a higher velocity of the fresher water in the surface layer relative to the saltier water near the bottom. Therefore, salinity near the surface tends to decrease faster than near the bottom, increasing the surface-to-bottom salinity difference and, consequently, stratification. During the flood, the differential movement of the water acts to diminish the stratification.

In neap tide conditions, during winter (Figs. 4.6(c) and 4.6(d)), a relatively strong stratification was evidenced by the practically horizontal isohalines. In the inlet channel and inner bay, the maximum vertical salinity gradient was located in the first 5 meters depth along the section in high water (Fig. 4.6(c)), and between 5 and 10 m in low water (Fig. 4.6(d)). Near the mouth (Figs. 4.6(e) and 4.6(f)), stratification was comparatively weaker and the maximum salinity gradient was in the upper 5 m. The stratified water column observed during TEJO88/1 results from the combination of weak vertical mixing (due to neap tide) and significant salinity differences between surface and bottom layers (due to high river discharge).

4.2.3 Transverse sections

Let us now consider transverse (perpendicular to the axis of the estuary) sections of hydrology and along-channel current. The evolution of the thermohaline and dynamical structures in the transverse direction within the inlet channel and the inner bay is analysed using data from the INTAGUS campaigns. The location of the respective cross-sections (Channel and Bay) is depicted in Fig. 4.7, together with their bottom topography profiles. The complete set of vertical distributions of hydrology and along-channel current velocity are presented in the Appendix B (see Section B.5).

Like the longitudinal sections, the transverse sections were also considered to be synoptic, as they were completed in about 30-60 minutes. In this case, it can be considered as a more realistic assumption than in the case of the longitudinal sections. The data are

presented as their temporal evolution on given non-dimensional levels, (η), obtained by the ratio of the actual and the total water column depths. The resultant figures should allow a more correct synoptic interpretation of the analysed quantity. Temperature is not shown here since the patterns are similar to those observed for salinity.

Besides the temperature differences in freshwater, as previously mentioned in Section 4.1.1, no other significant differences were observed in the thermohaline structure between summer and winter and the same happens with the dynamical structure across the section due to the fact that the winter campaigns were actually performed during summer-like river discharge conditions.

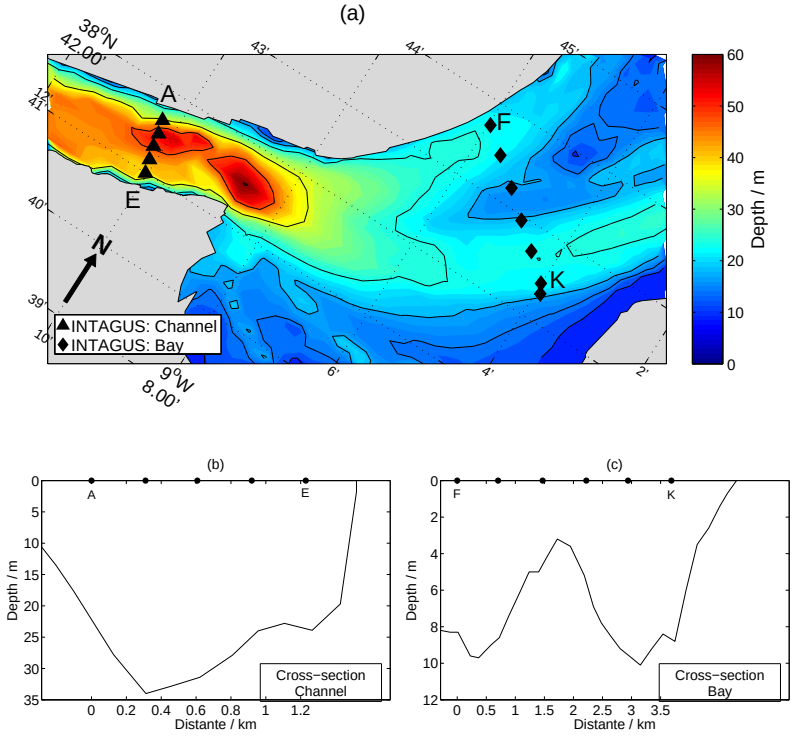

Figure 4.7 – (a) Location of the transversal sections carried out in the Tagus Estuary in the frame of the project INTAGUS, superimposed on the bottom topography. Bathymetric contours are drawn for 0 m, 2 m and 5 m and then for every 10 m. Bottom topography profiles at sections Channel (b) and Bay (c), with the respective station labels.

Inlet channel

The time evolution of salinity and of longitudinal current velocity along several non-dimensional levels (η) on a cross-section in the inlet channel (section Channel in Fig. 4.7) is shown in Figs. 4.8 and 4.9 for neap tide conditions and Figs. 4.10 and 4.11 for spring tide conditions.

They showed, generally, a typical standing wave behaviour: highest [lowest] salinity values and high-water slack (HWS) [low-water slack (LWS)] occurring almost simultaneously with HW [LW], especially in spring tides (see Figs. 4.10 and 4.11). The small time lag between HWS [LWS] and HW [LW] is more noticeable in neap tide conditions. This seems to point out to a reinforcement of the standing wave character of the tide associated to spring tide conditions. The analysis presented in Section 3.3.3 showed that the semi-diurnal wave behaves essentially as a standing wave, especially in the mid-estuarine and interior regions of the Tagus Estuary. Nevertheless, those results did not take into account a possible influence of the fortnightly tidal cycle. The results in this Section indicate that the fortnightly tidal cycle can exert some influence in the balance between the standing and progressive wave characters of the tidal wave, but not enough to change its essential behaviour.

Closer to the southern margin, LWS is gradually anticipated towards the bottom, thus the ebb duration decreases with depth in this part of the cross-section (compare Figs. 4.8(a) and (d) with Figs. 4.8(c) and (f), respectively). As the southern end of the cross-section is relatively closer to the margin than the northern end (see Fig. 4.7(b)), the lateral friction and the weaker currents near the southern margin can contribute to shorten the ebb phase there relatively to the northern end. Although the flood does not seem to be affected in the same way (see Figs. 4.10), it is important to refer that the flood and ebb were partly covered in, respectively, spring and neap tide conditions.

At each level, the salinity range between HW and LW is larger in neap tide than in spring tide conditions. Lateral salinity gradients are also more evident during neap tide, with the highest values close to the southern margin and the lowest values close to the opposite margin. As depth increases, these lateral gradients gradually become weaker or vanish. In spring tide conditions, the lateral gradients are much less evident, due to the stronger vertical mixing associated with stronger currents. In consequence, the whole

cross-section becomes more homogeneous in spring tide.

As expected, salinity increases and current velocity decreases towards the bottom. The low current velocities near the bottom should be the cause of the relatively small variability of the thermohaline structure at deeper levels, especially in neap tide conditions, as shown by Figs. 4.9(c) and 4.9(f). In what concerns temperature, it decreases with depth in summer but increases in winter.

Maximum flood and ebb currents were observed near the surface, close to the northern margin or in the northern half of the cross-section, both in neap and spring tide conditions (Figs. 4.8 and 4.10). This is as expected, since the southern end of the cross-section is closer to the margin than the opposite side, thus the lateral friction effects being stronger at the southern end.

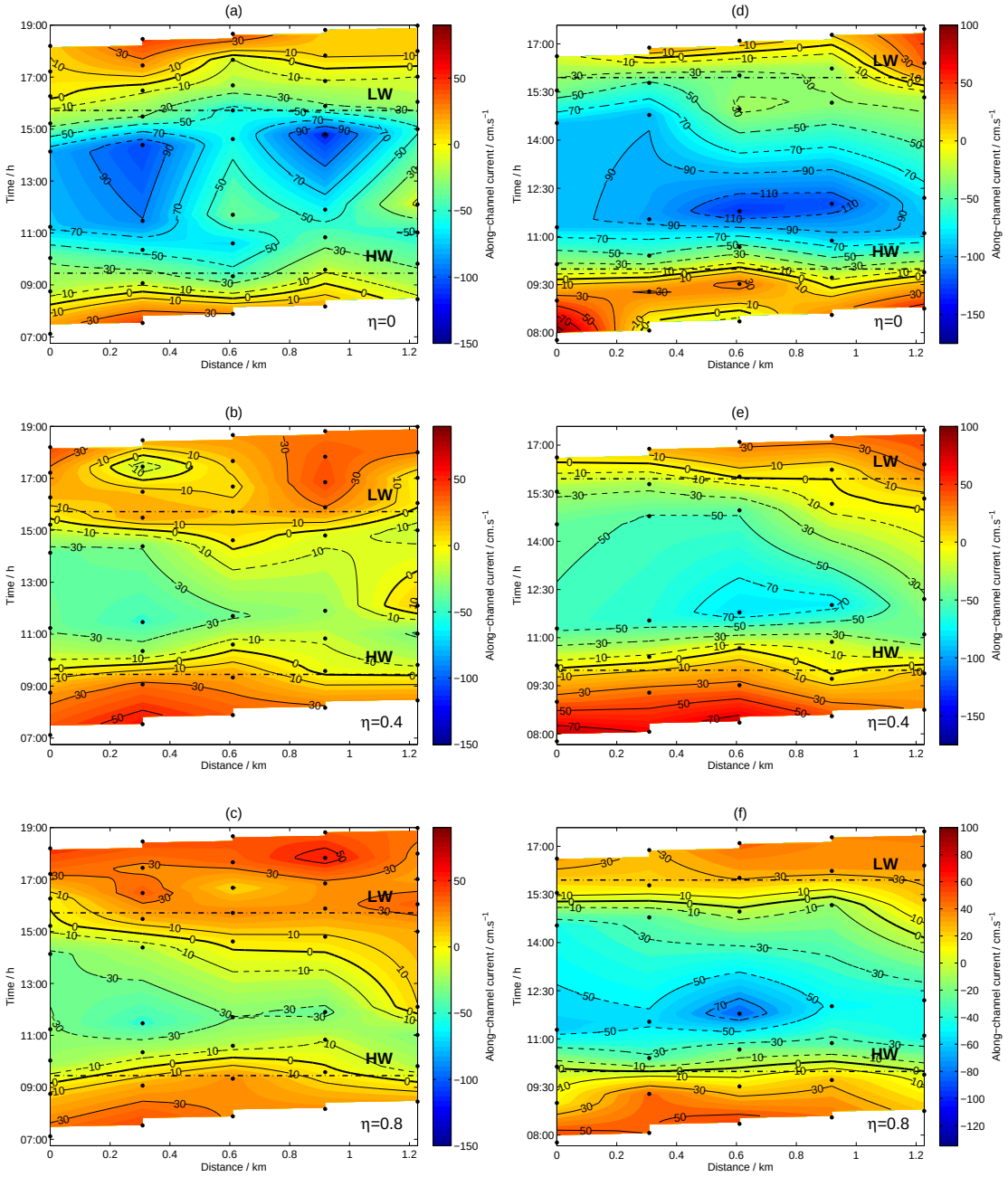

Figure 4.8 – Cross-section temporal evolution of the along-channel current velocity (cm s^{-1}) at the inlet channel during summer (left column) and during winter (right column) in neap tide conditions on the non-dimensional levels (a) and (d) $\eta = 0$, (b) and (e) $\eta = 0.4$ and (c) and (f) $\eta = 0.8$. Positive [negative] values indicate flood [ebb] current. The cross-section is oriented from north (distance=0 km) to south, the two dash-dotted lines represent the times of HW and LW and the dots indicate the time of each profile.

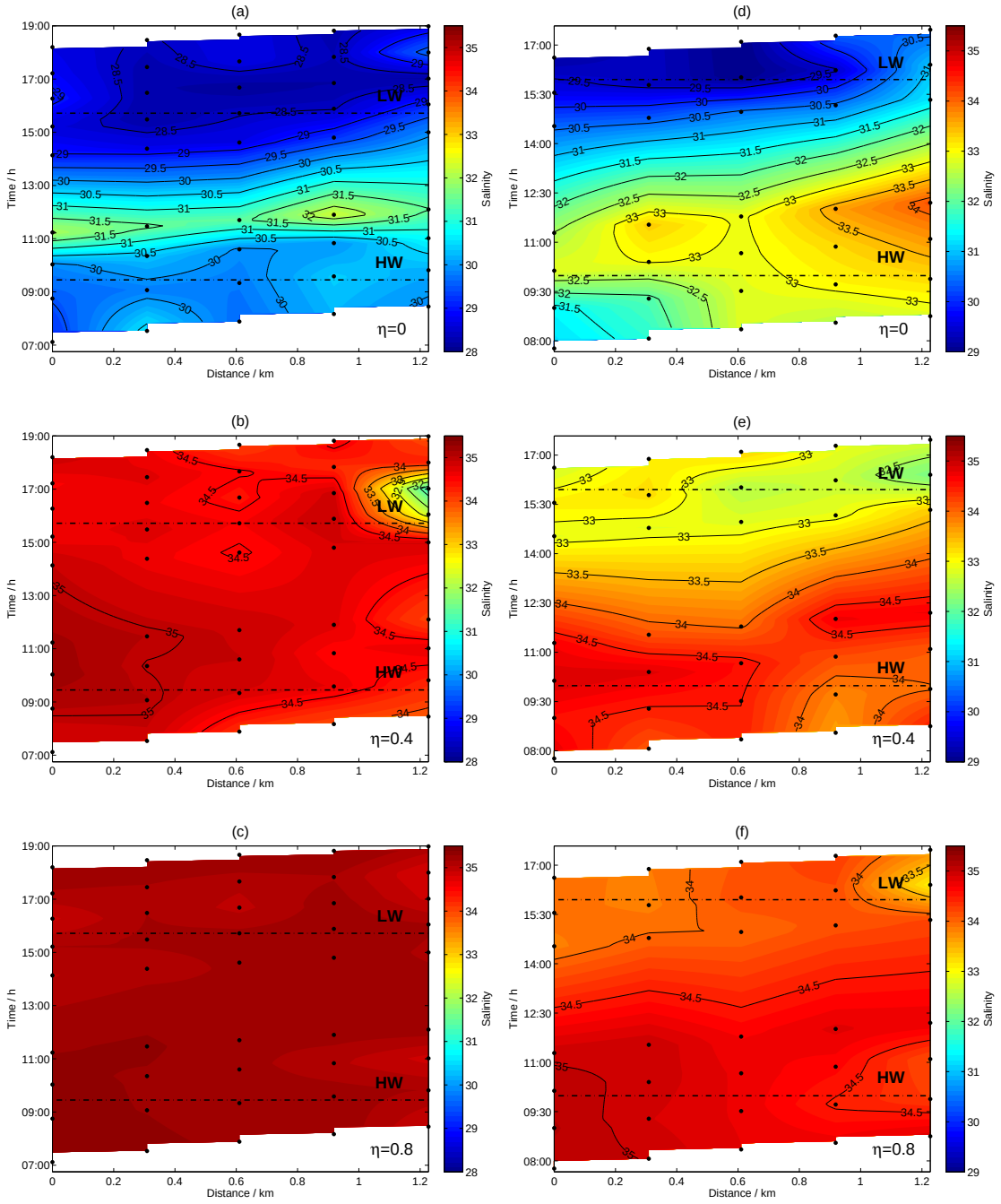

Figure 4.9 – Cross-section temporal evolution of the salinity at the inlet channel during summer (left column) and during winter (right column) in neap tide conditions on along the non-dimensional levels (a) and (d) $\eta = 0$, (b) and (e) $\eta = 0.4$ and (c) and (f) $\eta = 0.8$. The cross-section is oriented from north (distance=0 km) to south, the two dash-dotted lines represent the times of HW and LW and the dots indicate the time of each profile.

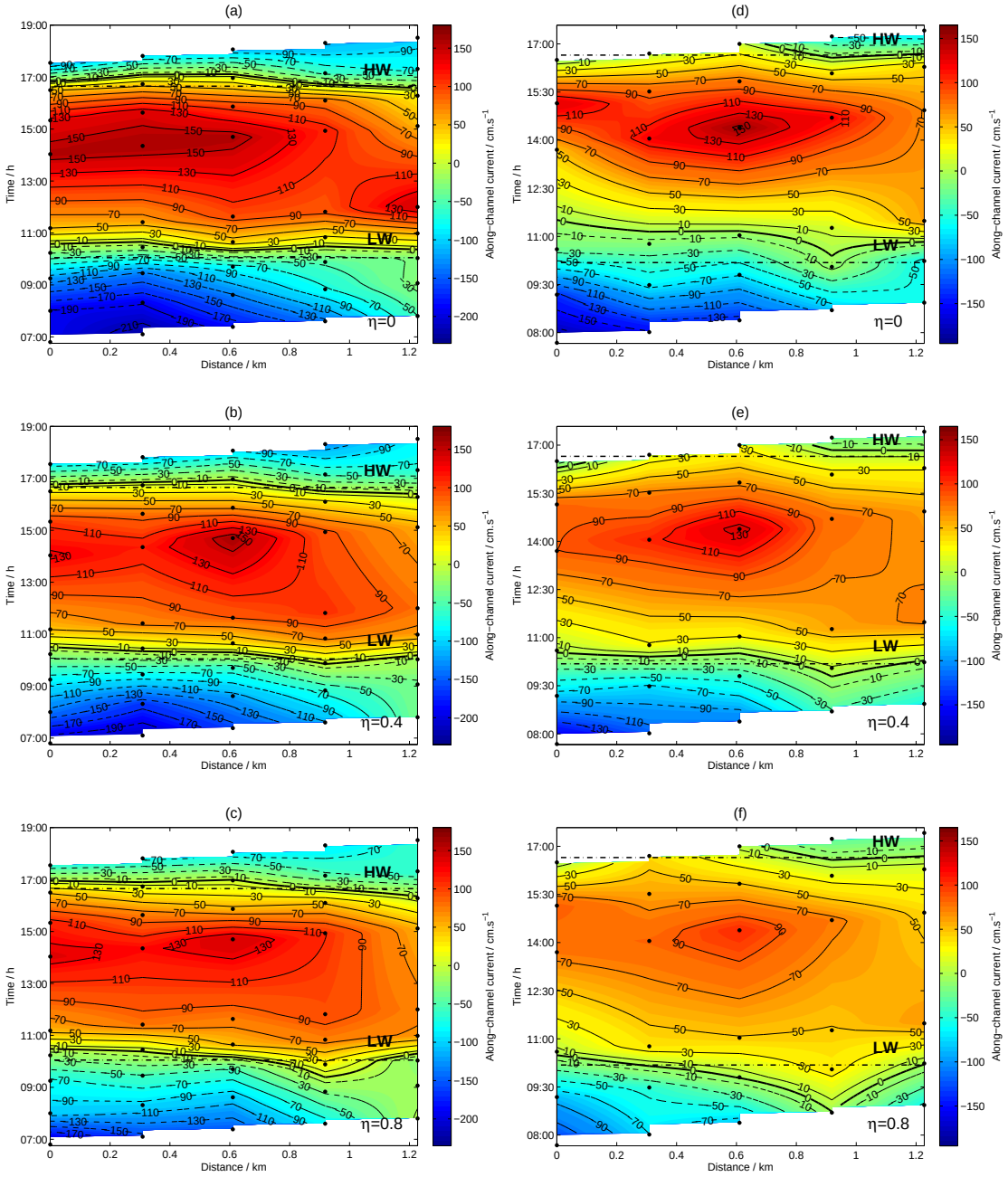

Figure 4.10 – Cross-section temporal evolution of the along-channel current velocity (cm s^{-1}) at the inlet channel during summer (left column) and during winter (right column) in spring tide conditions on the non-dimensional levels (a) and (d) $\eta = 0$, (b) and (e) $\eta = 0.4$ and (c) and (f) $\eta = 0.8$. Positive [negative] values indicate flood [ebb] current. The cross-section is oriented from north (distance=0 km) to south, the two dash-dotted lines represent the times of HW and LW and the dots indicate the time of each profile.

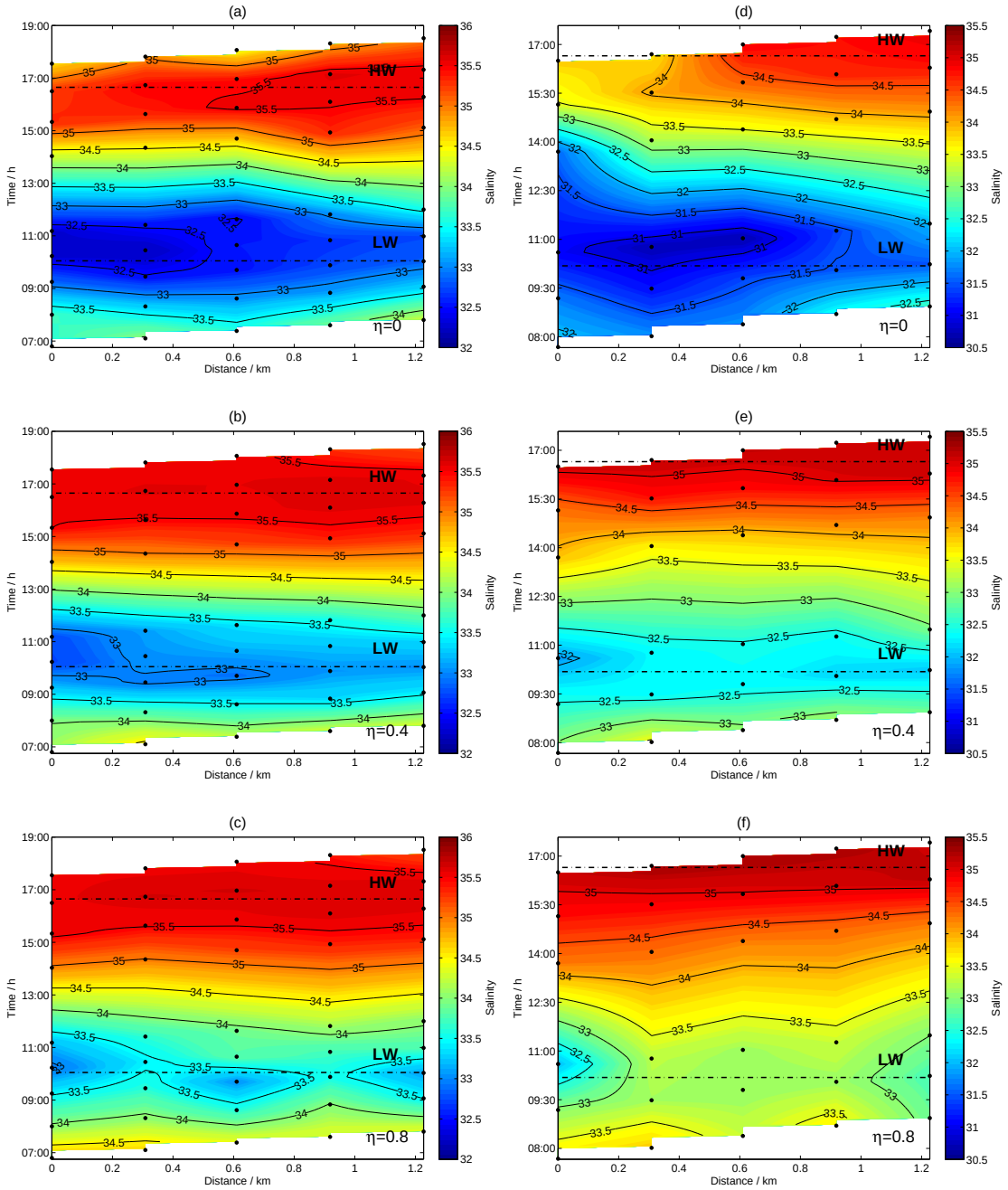

Figure 4.11 – Cross-section temporal evolution of the salinity at the inlet channel during summer (left column) and during winter (right column) in spring tide conditions on the non-dimensional levels (a) and (d) $\eta = 0$, (b) and (e) $\eta = 0.4$ and (c) and (f) $\eta = 0.8$. The cross-section is oriented from north (distance=0 km) to south, the two dash-dotted lines represent the times of HW and LW and the dots indicate the time of each profile.

Inner bay

The time evolution along several non-dimensional levels (η) of the hydrology and current velocity data obtained at a cross-section in the inner bay (section Bay in Fig. 4.7) is shown in Figs. 4.12 and 4.13 for neap tide conditions and Figs. 4.14 and 4.15 for spring tide conditions.

The analysis showed a generalized standing wave behaviour, both in spring and neap tide conditions, evidenced by the occurrence of the highest current velocities (flood and ebb) half-way between HW and LW (or LW and HW), as shown by the Figs. 4.12 and 4.14. The predominance of the standing wave character was also evidenced by the salinity (Figs. 4.13 and 4.15), the lowest [highest] salinity values occurring close to LW [HW], especially in the northern end of the cross-section. This is consistent with what was found for the inlet channel and corroborate the results presented in Section 3.3.3, for the M_2 wave, which pointed out to a relative reinforcement of the standing wave character towards the estuary's interior.

In neap tide conditions, the highest velocities were observed closer to the northern margin or in the northern half of the cross-section, coinciding with the main channel of the inner bay bathymetry (see Fig. 4.7(c)). As for spring tide conditions, the highest currents were essentially associated with the two main topography channels (compare Figs. 4.12 and 4.14).

In the INTAGUS07/2 campaign (summer, neap tide), the HWS seems to be delayed with depth close to the southern margin, indicating a possible shortening of the ebb (see Figs. 4.12(a) to (c)). The thermohaline structure evidences an increasing predominance of saltier water near the southern end of the cross-section, which could be a consequence of the reduced ebb duration. Nevertheless, nothing similar was observed in winter during neap tide, especially in the along-channel current.

Another interesting case is shown by the figures of the INTAGUS08/1 campaign (winter, spring tide), Figs. 4.14(d) to (f). In this case and again closer to the southern end of the cross-section, the LWS was delayed, independently of the water level. This seems to indicate a possible shortening of the flood, which is just a hypothesis since the HWS was not sampled. The delay of the LWS is probably the reason for the slope of the isohalines towards the northern end of the cross-section, observed between LW and HW,

consequence of lowest salinity values near the southern margin than near the opposite margin (see Figs. 4.15(d) to (f)). Nothing similar is observed in summer, during spring tide conditions.

The river discharge regime was found to be summer-typical for both summer (INTAGUS07) and winter (INTAGUS08) campaigns, thus it is very unlikely to be a probable cause for the features described above. In what concerns the wind conditions, it was mainly northeasterly in INTAGUS07/2 and southwesterly in INTAGUS08/1, which means that the wind was perpendicular to the cross-section orientation in both cases. Depths are lower close to the southern end of the cross-section, meaning that the effects of the local wind on the whole water column would be more effective there than close to the northern end. Assuming that the ebb was in fact shortened in INTAGUS07/2, as well as the flood in INTAGUS08/1, it becomes evident that the predominant wind direction was favouring the shortened phase. The remaining question is: why is this observed only during neap tide in summer and during spring tide in winter? It seems that a combination between the fortnightly cycle phase and the predominant wind direction could explain the observations.

As referred earlier in the case of the inlet channel, the lateral gradients in neap tide conditions were stronger than in spring tide, for the same reasons already stated.

In neap tide conditions, the highest salinity values were found essentially on the two main topography channels (one near the northern end of the cross-section and the other near its southern end). Closer to the northern margin, the salinity in the surface layer follows the oscillatory pattern imposed by the semi-diurnal tide, but gradually vanishing towards the bottom (compare $\eta = 0$ with $\eta = 0.8$ in both summer and winter in Fig. 4.13), whereas close to the opposite margin the oscillatory pattern of the salinity is not so evident, being absent near the bottom. This should be due to the stronger presence of freshwater near the surface close to the northern margin of the Tagus Estuary. Thus, the data evidenced a clear lateral variability, especially near the surface. Lateral gradients were weaker in spring tide conditions, as shown by the observation of the highest [lowest] salinity values at HW [LW] along the entire cross-section length in Fig. 4.15.

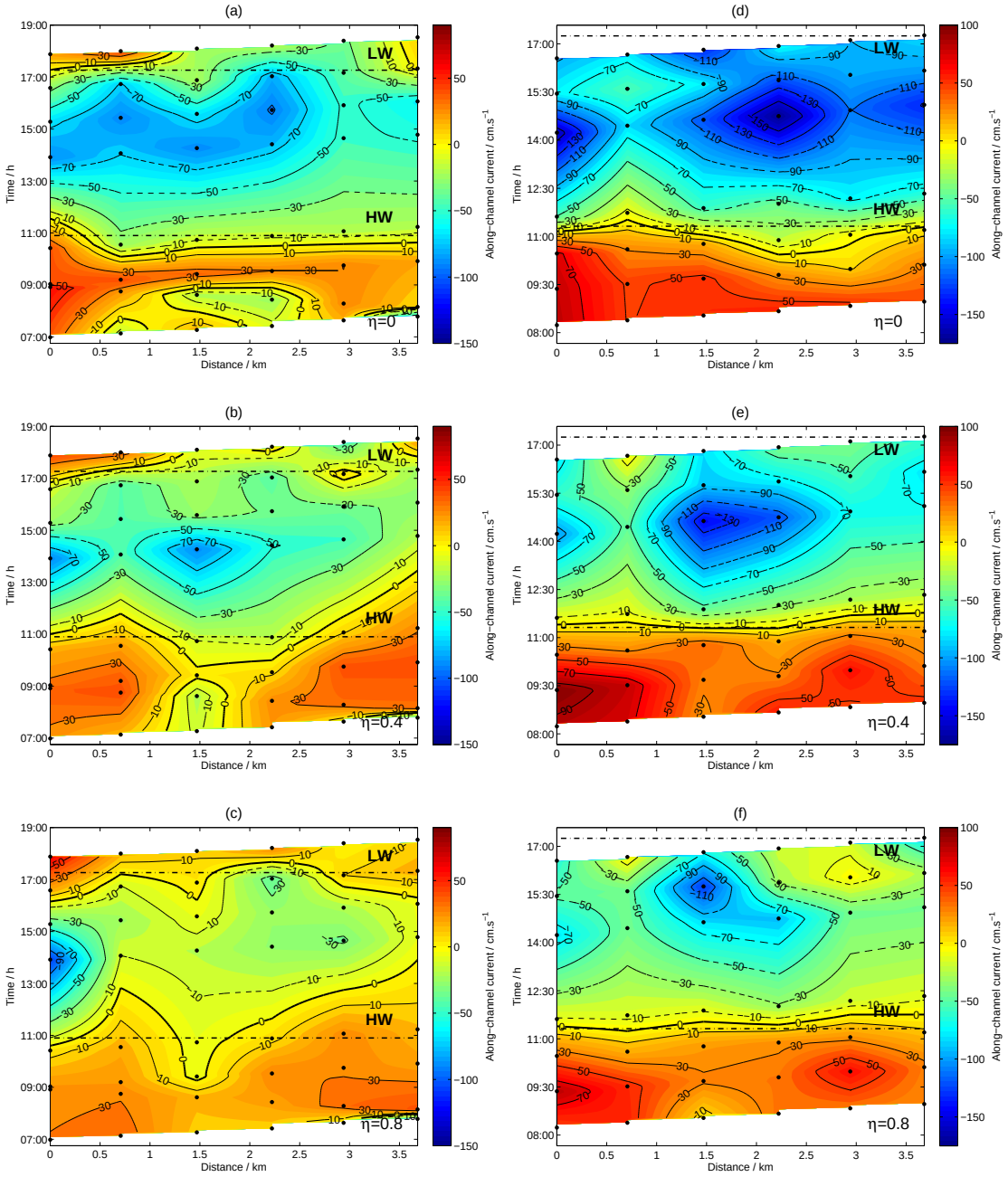

Figure 4.12 – Cross-section temporal evolution of the along-channel current velocity (cm s^{-1}) at the inner bay during summer (left column) and during winter (right column) in neap tide conditions on the non-dimensional levels (a) and (d) $\eta = 0$, (b) and (e) $\eta = 0.4$ and (c) and (f) $\eta = 0.8$. Positive [negative] values indicate flood [ebb] current. The cross-section is oriented from north (distance=0 km) to south, the two dash-dotted lines represent the times of HW and LW and the dots indicate the time of each profile.

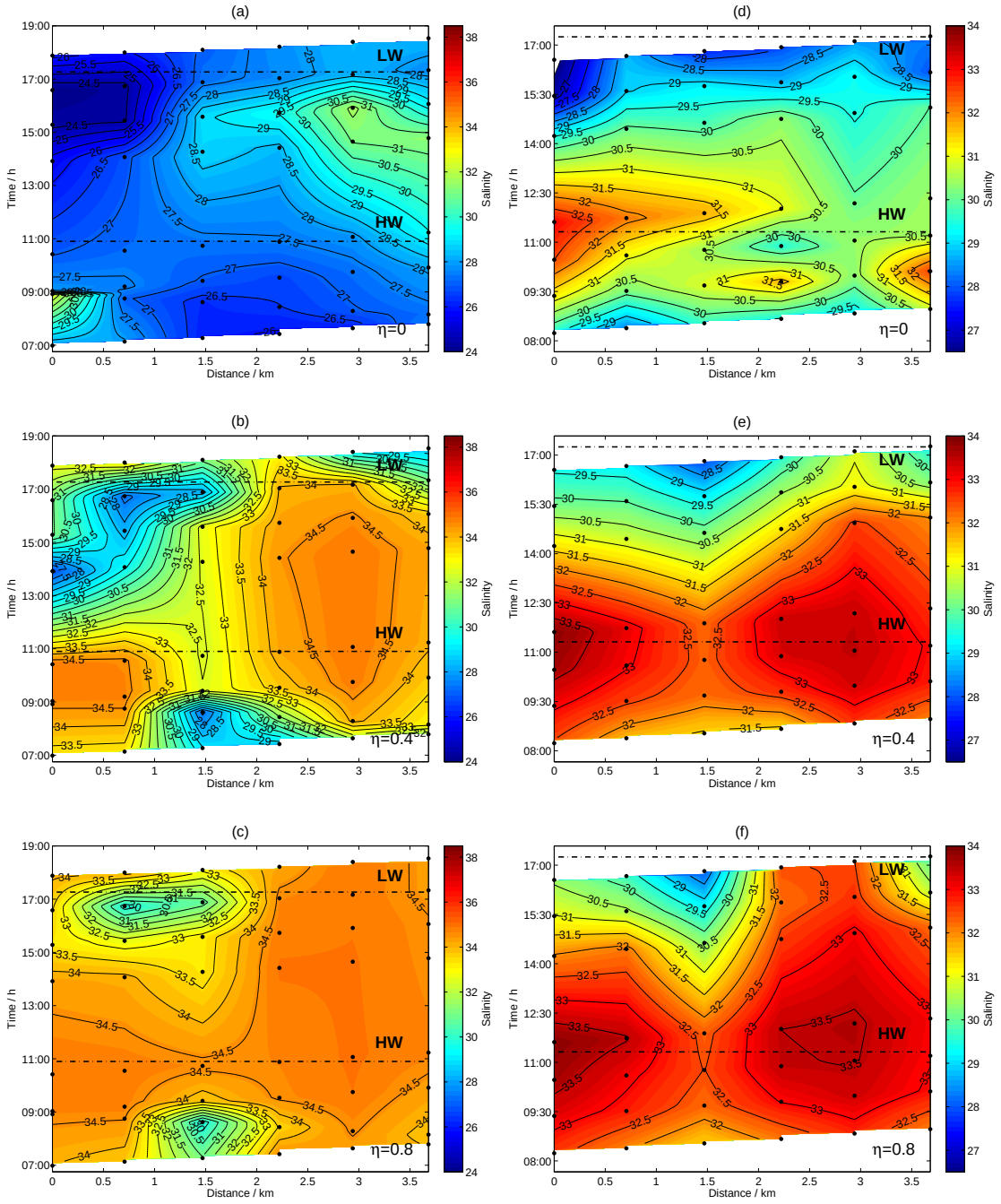

Figure 4.13 – Cross-section temporal evolution of the salinity at the inner bay during summer (left column) and during winter (right column) in neap tide conditions on the non-dimensional levels (a) and (d) $\eta = 0$, (b) and (e) $\eta = 0.4$ and (c) and (f) $\eta = 0.8$. The cross-section is oriented from north (distance=0 km) to south, the two dash-dotted lines represent the times of HW and LW and the dots indicate the time of each profile.

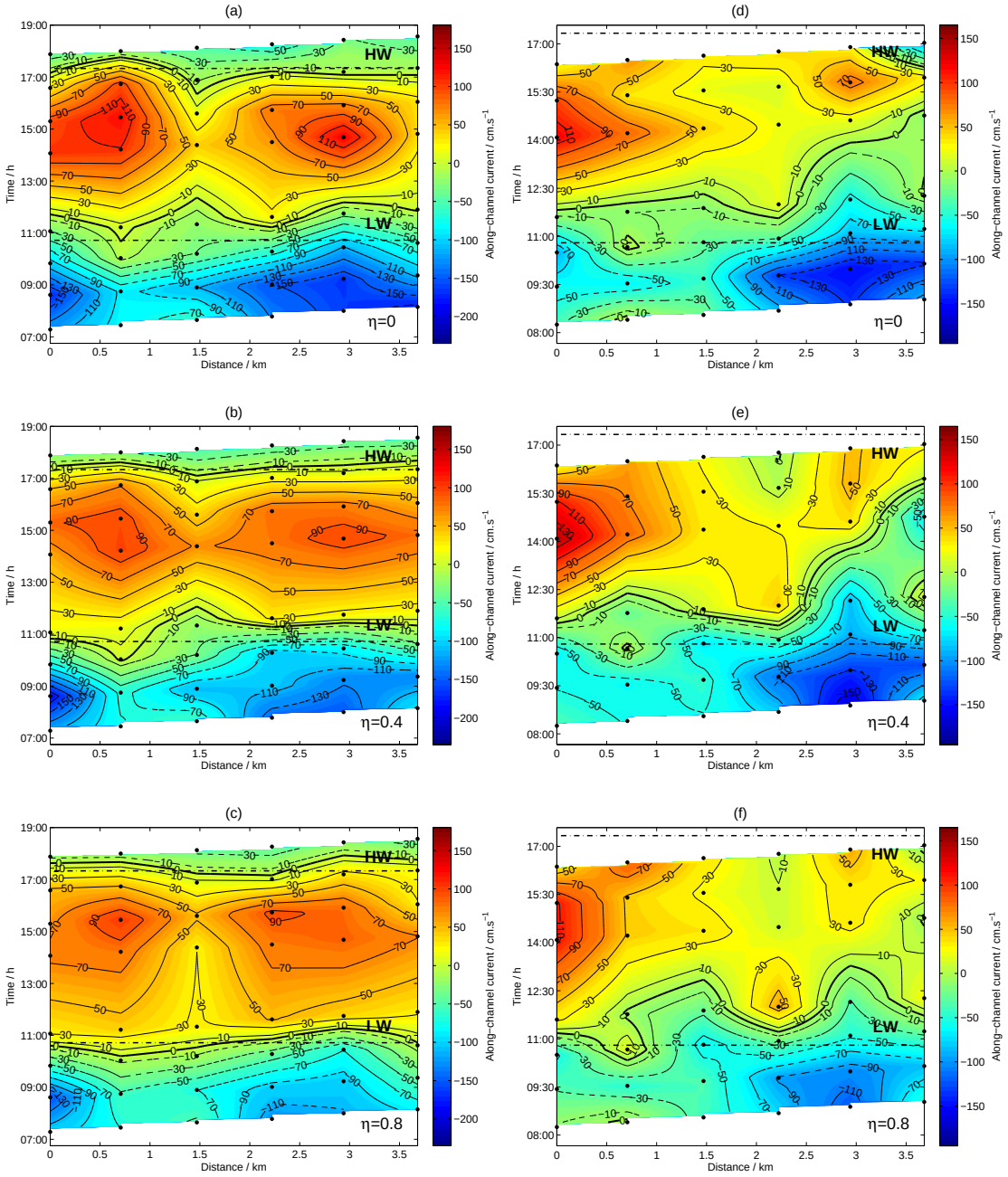

Figure 4.14 – Cross-section temporal evolution of the along-channel current velocity (cm s^{-1}) at the inner bay during summer (left column) and during winter (right column) in spring tide conditions on the non-dimensional levels (a) and (d) $\eta = 0$, (b) and (e) $\eta = 0.4$ and (c) and (f) $\eta = 0.8$. Positive [negative] values indicate flood [ebb] current. The cross-section is oriented from north (distance=0 km) to south, the two dash-dotted lines represent the times of HW and LW and the dots indicate the time of each profile.

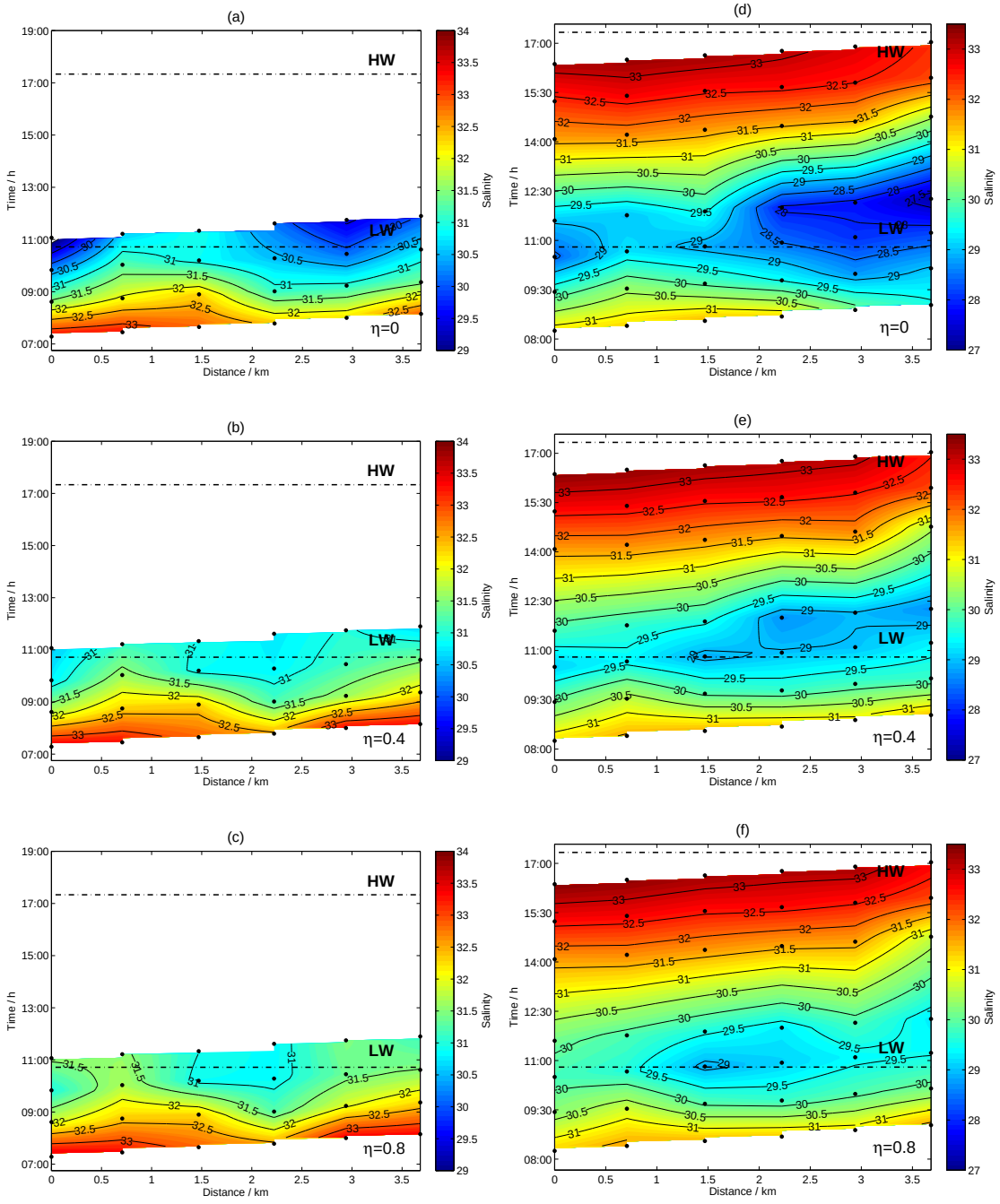

Figure 4.15 – Cross-section temporal evolution of the salinity at the inner bay during summer (left column) and during winter (right column) in spring tide conditions on the non-dimensional levels (a) and (d) $\eta = 0$, (b) and (e) $\eta = 0.4$ and (c) and (f) $\eta = 0.8$. The cross-section is oriented from north (distance=0 km) to south, the two dash-dotted lines represent the times of HW and LW and the dots indicate the time of each profile.

4.3 Subtidal variability

The study of the subtidal variability within the Tagus Estuary is based on the temperature, salinity and along-channel current velocity time series. These series were low-pass filtered, using a two-way Butterworth digital filter (Emery and Thomson, 2001). A third order Butterworth filter with a cut-off frequency equivalent to 40 hours was used, in order to remove all the tidal oscillations as well as other high-frequency effects.

After applying the low-pass filter, but before further analysis, a percentage of the end values of the series had to be neglected due to ringing effects linked to the discontinuities at the ends of the input series (measured data). It is often assumed that about 10% of output data at each end of the filtered series should be neglected, but each case is different and Emery and Thomson (2001) recommend the elimination to be based on a trial and error approach using visual inspection.

In the present case, depending on the length of the measured time series, between 5 and 15% of the output data at each end of the filtered series was eliminated, which corresponded to approximately 3 semi-diurnal tidal cycles.

4.3.1 Dynamical and thermohaline fields

This section presents the analysis of the low-pass filtered time series for the along-channel current velocity and thermohaline fields obtained in the Tagus Estuary with the moored current meters in the different campaigns. The objective is to better understand the subtidal circulation and thermohaline structure of the estuary and its possible relations to the forcing mechanisms. The subtidal circulation may be driven by density gradients, wind stress or tidal movements.

In this sense, the low-pass filtered time series of water level, wind, river discharge, sea-level pressure and air temperature were analysed in order to try to relate them to the behaviour of the subtidal dynamical and thermohaline fields.

As already referred in this work, both the dynamical and thermohaline fields are strongly affected by the fortnightly tidal cycle, so it is necessary to know the spring and neap tide peaks during the period of the observations when investigating its importance.

The contribution of the shallow-water constituent M_{sf}, which has the same period as

the fortnightly cycle (14.77 days), was estimated for the periods of observations of the campaigns TEJO85, TEJO88/2 and TEJO89, by using harmonic analysis on the respective water level series obtained at Cascais. The results showed that this component was not significant, since its signal-to-noise ratio was always lower than 1. By combining the amplitudes and phases of the constituents M_2 and S_2, it was verified that these are the main contributors for the fortnightly modulation of the tide. Thus, the spring and neap tide peaks are here referred to the dates obtained from the analysis of the tidal range (spring [neap] tide peak corresponds to a relative maximum [minimum] of the tidal range) and are reported in Table 4.5.

Survey	Spring tide	Neap tide
TEJO85	16 and 29/09 1985	23/09 and 9/10 1985
TEJO88/2	1, 14 and 29/08 1988	7 and 22/08 1988
TEJO89	14 and 30/11 1989	7 and 21/11 and 7/12 1989

Table 4.5 – Dates of spring and neap tide peaks during the observational campaigns, as determined from the measured tidal range at Cascais.

TEJO85

During this campaign, the wind was characterised by a relatively small meridional component, with one significant northerly wind event lasting about three days. The zonal component was mainly westerly during the period of observations, except between a small period of about four days.

The river discharge was relatively steady for the considered period, thus it should not have been determinant on the fluctuations of the subtidal dynamical and thermohaline fields during the TEJO85 campaigns.

The subtidal water level at Cabo Ruivo (Cr) and at Terreiro do Paço (Tp) was higher than at Cascais (Ca), as shown in Fig. 4.16(a), with the consequent barotropic pressure gradient force directed seaward. A higher coherency was noticed between Ca and Tp than between Ca and Cr, suggesting that the subtidal water level at Cr and Tp could be differently affected by the forcing mechanisms. From those mechanisms should be excluded the

sea-level pressure, since it affects the entire estuary in the same way. As for the wind, its orthogonal components did not show an evident relation to the water level differences between Cr and Tp. However, no other projections of the wind were computed and compared with the subtidal water level, therefore there is still the possibility that the observed water level differences could have been caused by the wind.

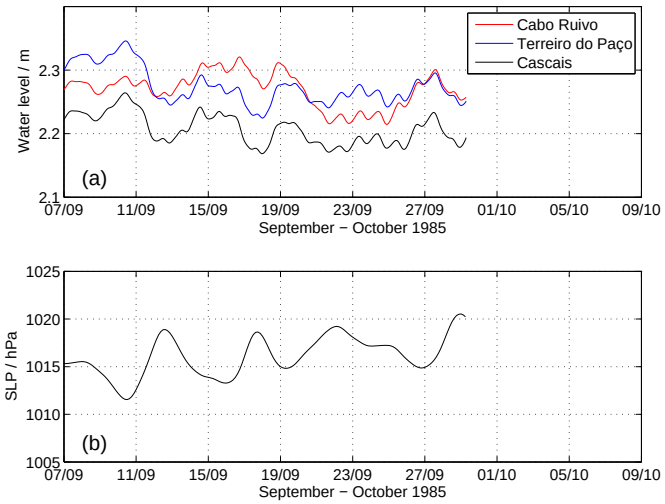

Figure 4.16 – Low-pass filtered (40 h) (a) water level time series measured at Cabo Ruivo (red), Terreiro do Paço (blue) and Cascais (black) and (b) sea-level pressure measured at Montijo during the TEJO85 campaign.

The sea-level pressure during the TEJO85 (see Fig. 4.16(b)) was characterised by a succession of relative maxima and minima with a period varying between 3 and 7 days. Variations on the low-pass filtered water level can be associated with the patterns shown by the sea-level pressure (Fig. 4.16(a)), evidencing the inverse barometer effect.

The subtidal along-channel current velocity obtained for the current meters deployed during TEJO85 (see Fig. 4.3 for location) is shown in Fig. 4.17. These current meters were suspended near the surface and located in three different places within the estuary: inlet channel (A), mid-estuarine region (B) and inner bay (C). For current meters A and B, the strong influence of the fortnightly tidal cycle is well evidenced, whereas for current meter C there is no clear relation with the spring-neap cycle.

Considering the current meters from the mouth to the estuary's interior, it is observed

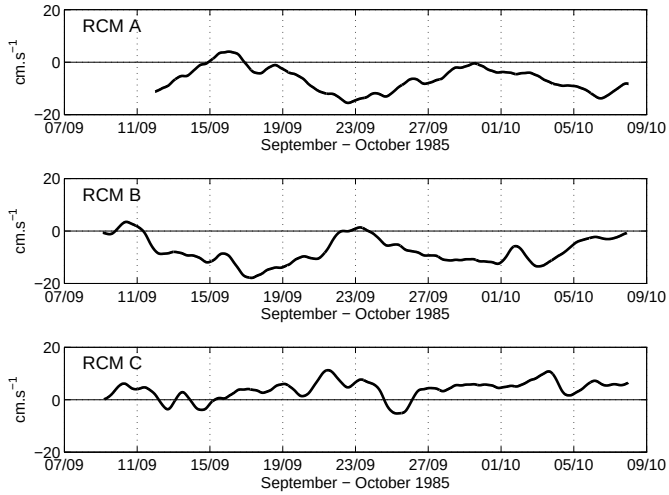

Figure 4.17 – Low-pass filtered (40 h) along-channel current velocity time series from the TEJO85 current meters. Positive (negative) values mean landward (seaward) current.

the expected salinity decrease and temperature increase (see Fig. 4.18), as a consequence of the horizontal density gradient. There is also evidence of a positive trend in all the subtidal temperature time series as well as a negative trend in the salinity time series, although not so intense. As previously referred in the beginning of Section 4.1.1, September generally marks the end of the coastal upwelling season off Portugal, and the positive trend observed in the temperature time series within the estuary is probably a consequence of that.

The subtidal along-channel current near the surface was mainly seaward, both for RCMs A and B, but their behaviours relative to the spring-neap cycle were different.

For current meter A, the subtidal current reached a maximum seaward during neap tide ($\sim$15 cm s^{-1}) while during spring tide, it was near zero or even changed direction, becoming landward ($\sim$5 cm s^{-1}). Assuming the Tagus Estuary as a partially mixed estuary (see Section 4.1.2), the typical two-layer circulation structure is expected (seaward directed current near the surface and landward directed near the bottom). In the presence of stratification, the baroclinic and barotropic components of the horizontal pressure gradient act on the same direction on the flood, but in opposite directions on the ebb. This generates an upstream near-bottom flow, with a compensating near-surface outflow (Jay and Smith, 1988). During the transition to spring tide, the increase of tidal current velocities and the

consequent increase of the vertical mixing, as well as the decrease of the horizontal density gradients, are responsible for changes on the two-layered residual circulation structure (Dyer, 1997). This explains the behaviour of the subtidal current on RCM A.

In what concerns the subtidal salinity and temperature time series (Fig. 4.18), only the RCM A (inlet channel) undoubtedly evidences the influence of the fortnightly tidal cycle: salinity increase and temperature decrease during spring tide (16 and 29 September) and the opposite during neap tide (23 September and 8 October). Thus, as expected, the seawater (colder, saltier) influence in the thermohaline characteristics of the inlet channel surface layer, during a summer-typical river flow regime, is stronger during spring tide due to a stronger vertical mixing.

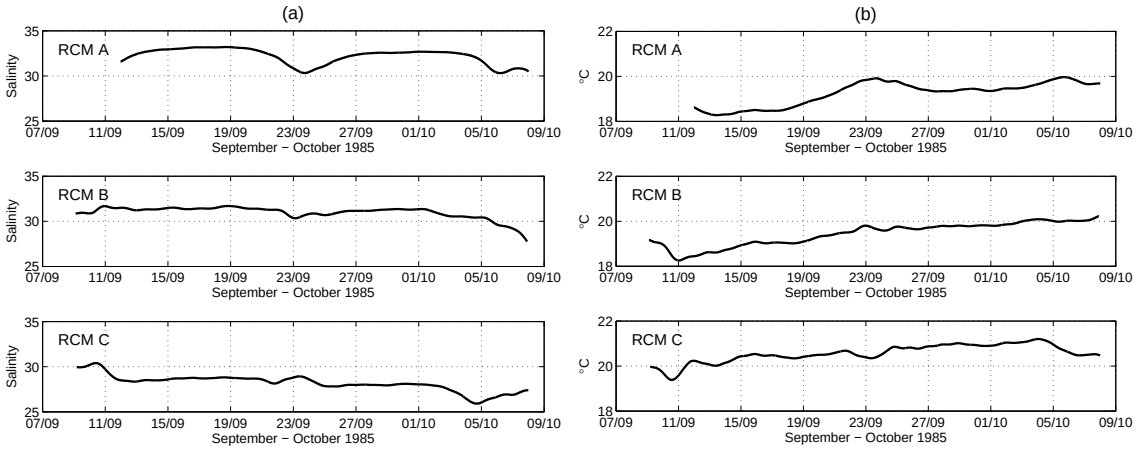

Figure 4.18 – Low-pass filtered (40 h) time series of (a) salinity and (b) temperature, from the TEJO85 current meters.

As for the current meter B, the subtidal current reached a maximum seaward during spring tide (~18 cm s^{-1}) and during neap tide peaks it was near zero or became landward (<5 cm s^{-1}). This current meter was approximately located on the seaward branch of a clockwise eddy suggested by Dias (1993), based on the results of a 4-days numerical simulation for spring tide conditions, originated mainly due to bottom topography constraints. This clockwise eddy allows to explain the subtidal current behaviour at RCM B during spring tide conditions. As for neap tide conditions, the weaker tidal currents could have

changed the location of the clockwise eddy or even prevented its formation, thus changing the subtidal current behaviour in RCM B.

For current meter C, the subtidal along-channel current was mainly landward, reaching a maximum of $\sim$10 cm s^{-1}, and was only seaward during two short periods (between 12 and 15 September and between 25 and 26 September), so a partially-mixed typical two-layered structure could not be assumed for this inner bay location, unlike the suggested by Fiadeiro (1987). The fact that the subtidal current at site C does not seem to be directly related to the fortnightly cycle could indicate that other forcing mechanisms, such as the wind or the river discharge, play an important role in this case. However, the river discharge did not show any relevant variation during the observations and, in what concerns the wind, none of its components evidences a clear relation to the subtidal current direction at site C. Based on the same results of the 4-days numerical simulation for spring tide conditions referred above, Dias (1993) have suggested the existence of a clockwise eddy closer to the southern margin in the inner bay, originated by bottom topography constraints, whose landward branch corresponds to the location of the RCM C. This allow to explain the observed residual current direction at site C.

The spring-neap cycle influence in the thermohaline field was more subtle in the mid-estuarine and inner bay current meters (B and C, respectively), where only a small variation of the salinity and temperature was noticed during neap tide. This could be either due to the decrease of the seawater influence as the distance from the mouth grows and/or due to a less efficient vertical mixing. In the case of the RCM B, since its subtidal current is affected by the fortnightly cycle, the low seawater influence due to the distance from the mouth seems to be the cause for the weak correlation between the subtidal thermohaline series and the spring-neap cycle. As for the RCM C, located upstream of RCM B, the current was not affected by the fortnightly cycle, thus the low correlation between this cycle and the subtidal thermohaline series could be explained by a weak vertical mixing combined with a low seawater influence.

TEJO88/2

The wind was characterised by a meridional component predominantly from the north during the entire period of observations, an expected behaviour during summer in the Por-

tuguese west coast. The maximum northerly wind intensity occurred around 20-21 August (10 m s^{-1}). The zonal component was mainly westerly during the period of observations and always below 5 m s^{-1}.

The river discharge was relatively steady for the considered period and should not have been determinant on the evolution of the subtidal dynamical and thermohaline fields during this campaign.

The subtidal water level decreased towards the interior, from Cascais (Ca) to Cabo Ruivo (Cr), causing a barotropic pressure gradient force in that direction. The strong negative water level trend evidenced by the Cr data (see Fig. 4.19(a)) could have been caused by problems in the tidal gauge, lasting until about 23 August, when the record becomes similar to those at Paço de Arcos (Pa) and Cascais.

The main features shown by the water level series can be associated with the sea-level pressure during the TEJO88/2 (see Fig. 4.19(b)), evidencing the inverse barometer effect.

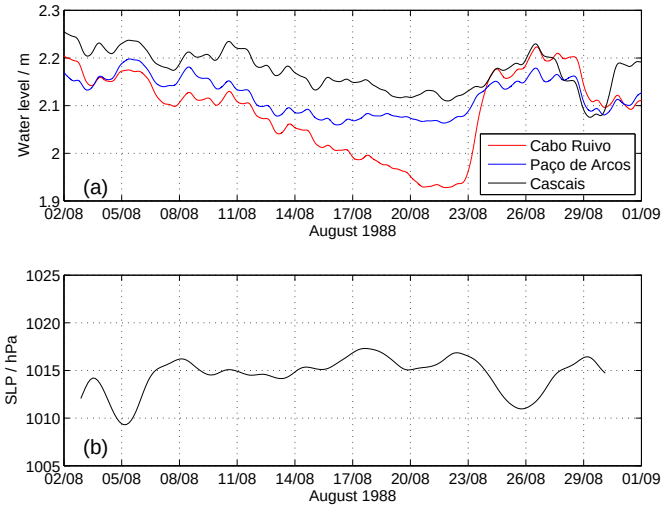

Figure 4.19 – Low-pass filtered (40 h) (a) water level time series measured at Cabo Ruivo (red), Paço de Arcos (blue) and Cascais (black) and (b) sea-level pressure measured at Montijo during the TEJO88/2 campaign.

Fig. 4.20 presents the subtidal along-channel current for the near-surface current meters of the TEJO88/2 campaign. The near-bottom valid records were too short to compute the subtidal series.

The subtidal along-channel current is mainly landward in the current meter D_s (closer to the northern margin) and mainly seaward in the current meter E_s. This evidences the existence of a horizontal shear in this region of the estuary during the TEJO88/2 observational campaign, characterised by typical summer river discharge and wind. The subtidal current is close to zero around the neap tide peak (7 August), both in current meters D_s and E_s. After the neap tide, the intensity of the current increases reaching about 10 cm s^{-1} in spring tide for RCM E_s (seaward) and 8 cm s^{-1} for RCM D_s (landward).

The subtidal current behaviour showed by RCM E_s is similar to that described earlier for RCM B (TEJO85). The two current meters are relatively close (see Fig. 2.2(c) for location) and the river discharge regime is similar in the two campaigns. The wind regime, on the other hand, was different when comparing the campaigns TEJO85 and TEJO88/2 (see Figs. 2.6(a) and 2.6(c)), but this seemed to have no direct influence on the circulation pattern.

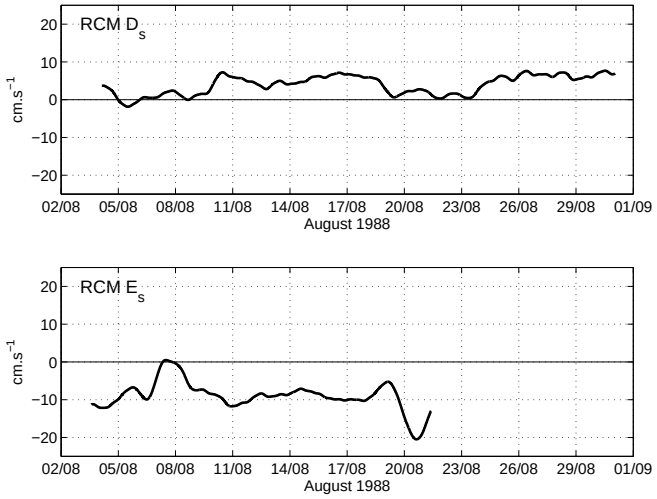

Figure 4.20 – Low-pass filtered (40 h) along-channel current velocity time series from the TEJO88/2 near-surface current meters. Positive (negative) values mean landward (seaward) current.

The thermohaline subtidal time series obtained for the near-surface (D_s and E_s) and near-bottom current meters (D_b and E_b) show a clear influence of the fortnightly tidal cycle (Fig. 4.21) with similar behaviour in both sites, in spite of the subtidal along-channel

current direction in RCM D_s being essentially opposite to that in RCM E_s. The effects of a vertical mixing during spring tides stronger than during neap tides is shown by the decrease of the vertical salinity and temperature gradients during spring tide and their increase during neap tide.

Both the near-surface and near-bottom subtidal temperature series in the two moorings show a marked decrease which occurred around 20 August. This seems to be directly related to the strong increase of the northerly wind intensity and will be analysed with more detail in Section 4.4.

An anomalous behaviour of the salinity for mooring D can be noticed in the last 5 days of the time series (spring tide period), when the near-bottom values decreased below the near-surface values (Fig. 4.21(a), top panel) while the near-bottom and near-surface temperatures show a normal behaviour. The most likely explanation for that strange behaviour in salinity is the failure of the conductivity cell of the near-bottom current meter, since the near-surface salinity series is apparently normal.

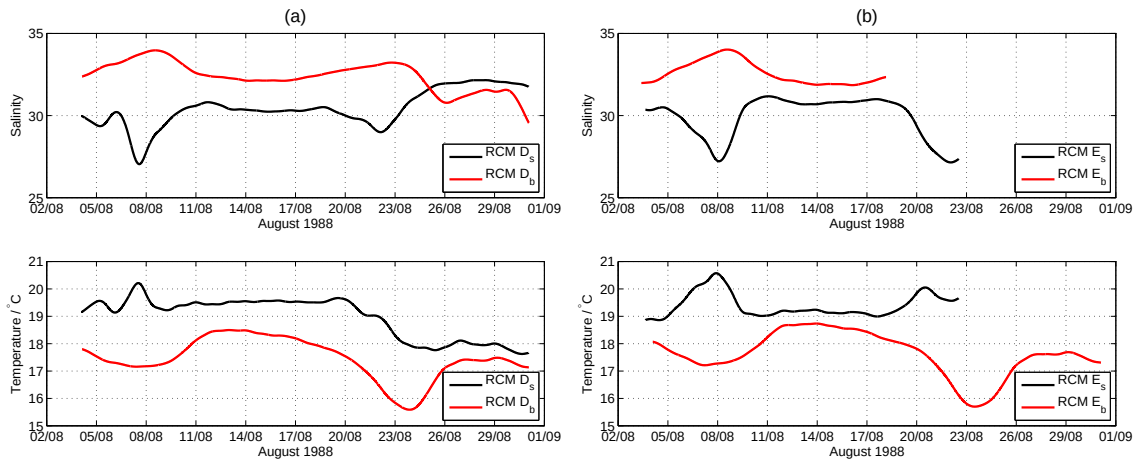

Figure 4.21 – Low-pass filtered (40 h) time series of (top) salinity and (bottom) temperature from the TEJO88/2 moorings (a) D and (b) E. Black line: near-surface current meters; Red line: near-bottom current meters.

TEJO89

The meridional wind component was predominantly from the north in the initial period of the campaign, becoming mainly from the south afterwards. As for the zonal component, it shows a short easterly wind period (about four days), changing to westerly for about 11 days and then becoming essentially easterly until the end of the observational period.

The river discharge was relatively low and steady until 18 November, showing then a sudden increase and peaking in 23 November.

The subtidal water level increased towards the interior, from Cascais (Ca) to Cabo Ruivo (Cr) (Fig. 4.22(a)), resulting in a barotropic pressure gradient force directed seaward during the entire period of observations. All three tidal stations along the estuary showed similar patterns of the water level fluctuations.

The sea-level pressure showed a negative trend until late November, then began to increase until it reached a maximum in early December. Again, the correlation between the sea-level pressure and the water level is consistent with the inverse barometer effect.

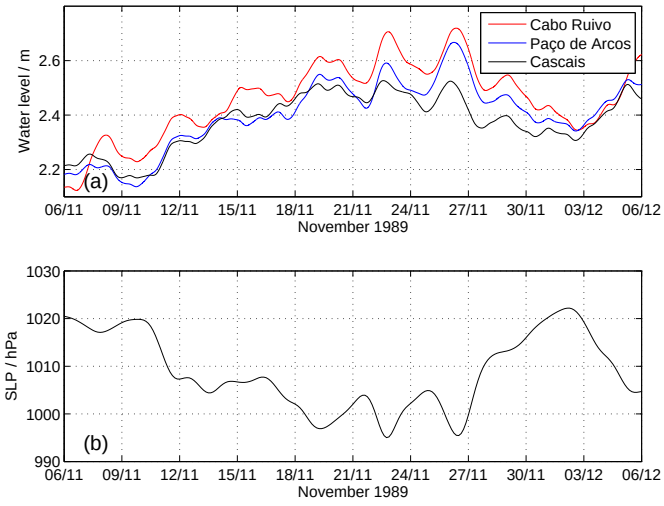

Figure 4.22 – Low-pass filtered (40 h) (a) water level time series measured at Cabo Ruivo (red), Paço de Arcos (blue) and Cascais (black) and (b) sea-level pressure measured at Montijo during the TEJO89 campaign.

The subtidal along-channel current velocity during the TEJO89 campaign was mea-

sured by RCMs F and G (Fig. 4.23), which were moored in the inlet channel (see Fig. 4.3). The record length at mooring F was relatively short and did not allow to extract any relevant information about the influence of the forcing mechanisms on the subtidal current.

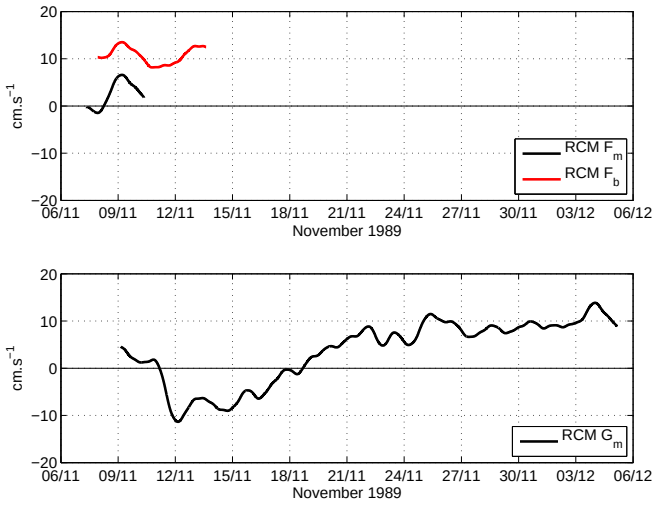

Figure 4.23 – Low-pass filtered (40 h) along-channel current velocity time series from the TEJO89 mid-water (black line) and near-bottom (red line) current meters. Positive (negative) values mean landward (seaward) current.

For mooring G, near the southern margin, only the mid-water current (lower panel of Fig. 4.23) was possible to obtain. It presented a landward direction during most part of the record (reaching a maximum of $\sim$ 15 cm s^{-1} near the end of the campaign), except from around 11 to 19 November, when it was seaward (reaching a maximum of $\sim$ 10 cm s^{-1}).

On a simulation of the depth-averaged eulerian residual velocities in the mouth of the Tagus Estuary, Fortunato et al. (1997) showed the existence of a clockwise eddy near the mouth of the estuary, even for the case of a strong river flow (4000 m^3 s^{-1}) and the RCM G was approximately located in its downstream branch, which provides a plausible explanation for the seaward current direction observed in Fig. 4.23. The landward current direction which occurred afterwards seemed to be associated with a sudden increase of the river flow (see Fig. 2.8(d)), although this is not expectable.

Another possibility of explanation for the change of direction could be related to the wind. Results of a bidimensional model of circulation in the Tagus Estuary (Ambar and

Backhaus, 1983) show landward residual current near the mouth, close to the southern margin, in the presence of southwestern wind, independently of the fortnightly cycle and of the river discharge regime. In this perspective, the analysis of the wind record during November 1989 (see Fig. 2.6(d)) shows a period of about a week of relatively strong southerly wind, starting around 17-18 November, which could have caused the landward current episode.

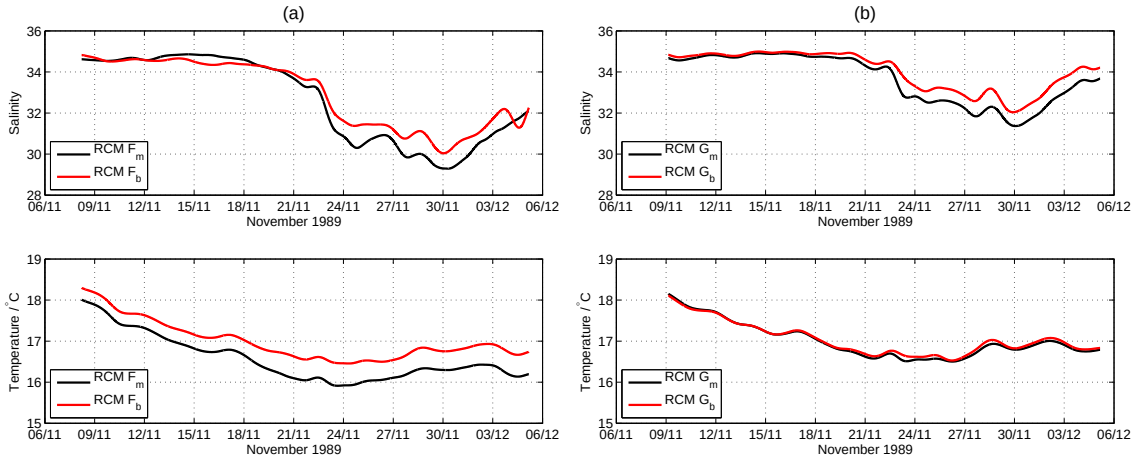

Figure 4.24 – Low-pass filtered (40 h) time series of (top) salinity and (bottom) temperature from the TEJO89 moorings (a) F and (b) G. Black line: mid-water current meters; Red line: near-bottom current meters.

In what concerns the thermohaline time series, presented in Fig. 4.24, they did not seem to be affected by the fortnightly cycle in the sense that no changes evidencing the vertical mixing variability associated to the cycle spring-neap tide are observed in the records. Around 22 November, the subtidal salinity decreased from about 34.5 (nearly constant since the beginning of the record) to about 30.0 in mooring F and 32 in mooring G, around 30 November. The sudden increase of the river discharge around 19 November, already referred above, is the most probable cause for the salinity decrease, the water column near the northern margin being more influenced by the presence of freshwater (compare the top panels of Figs. 4.24(a) and 4.24(b)).

As for the temperature, a negative trend is evidenced since the beginning of the record

until attaining a minimum around 24 November. The wind record (see Fig. 2.6(d)) showed the predominance of northerly wind between 1 and 18 November, which could have caused coastal upwelling, and consequently decreased the temperature of the seawater layers within the estuary. The positive trend in the temperature after 24 November could be therefore related to the end of the upwelling event, associated with the veering of the wind from northerly to southerly around 18 November.

4.4 Remote wind forcing effects - coastal upwelling

As referred earlier in Section 4.3.1, a sudden decrease of the whole water column temperature observed within the estuary during summer (TEJO88/2) could have been caused by an upwelling event in the adjacent coastal ocean. To confirm this hypothesis, the contemporary wind data obtained at the meteorological station of Montijo (see Fig. 2.2(d) for location) were analysed as follows.

Also referred earlier in Section 4.1.1, during the INTAGUS campaigns the near-bottom water was colder in summer than in winter. The association of this interesting feature to the occurrence of upwelling is also analysed in this section through the inspection of contemporary wind data and satellite sea surface temperature (SST).

4.4.1 Wind stress components

The pre-processing of wind data contemporary with TEJO88/2 – August 1988 – is described in Section 2.1.2, therefore, this section only describes the method to calculate the zonal and meridional wind stress components, which are important to evaluate the existence of wind favourable to the occurrence of upwelling.

As a result of experimental observations, the magnitude of the wind stress on the sea surface is approximately proportional to the wind speed squared and acts in the direction of the wind. Thus, the zonal (τ_x) and meridional (τ_y) wind stress components (N m^{-2}) are computed as:

$$\begin{aligned} \tau_x &= \rho_{air} C_d u_w \left(u_w^2 + v_w^2\right)^{1/2} \\ \tau_y &= \rho_{air} C_d v_w \left(u_w^2 + v_w^2\right)^{1/2} \end{aligned} \quad , \tag{4.5}$$

where ρ_{air} is the air density (assumed to be 1.28 kg m^{-3}), u_w and v_w are the zonal and meridional wind velocity components (m s^{-1}), respectively. C_d is the dimensionless drag coefficient, which, according to Large and Pond (1981), can be parameterised in the following way:

$$C_d = \begin{cases} 1.2 & , 4 \leq U_w \leq 11 \text{ m s}^{-1} \\ 0.49 + 0.065U_w & , 11 \leq U_w \leq 25 \text{ m s}^{-1} \end{cases} \tag{4.6}$$

where $U_w = \left(u_w^2 + v_w^2\right)^{1/2}$ is the wind velocity.

Since the wind velocity during August 1988 was seldom higher than 11 m s^{-1}, according to the parameterisation 4.6, the drag coefficient was assumed to be constant, $C_d = 1.2$.

4.4.2 Water column cooling events within the estuary

TEJO88/2

The temperature time series obtained near the surface and near the bottom off Sta. Apolónia (Fig. 4.25) during the TEJO88/2 campaign show an anomalous temperature decrease around 20 August. Near the surface, the mean temperature, which remained fairly constant (~19°C) until 20 August, decreased by about 1°C between 20 and 24 August. Near the bottom, the mean temperature also showed a decrease, even stronger (1.5°C), during the period 20 to 24 August.

The occurrence of this cooling event throughout the whole water column is also shown in the temperature time series recorded by the thermistor sensors moored at the same site. Fig. 4.26 represents the low-pass filtered temperature (T_{cut}=40 h) for the thermistor chain of mooring D (see Fig. 4.3 for location), showing values during the neap tide of 24 August about 1.5°C lower than at comparable depths during the neap tide of 7 August. The fact that this cooling is more intense near the bottom discards the hypothesis of it being due to a decrease of the air temperature and seems to indicate an input of colder water arising from the sea.

This cooling event turned out to be more evident due to the fact that it has occurred during neap tide and so the small vertical mixing could not mask the water cooling in the bottom layer.

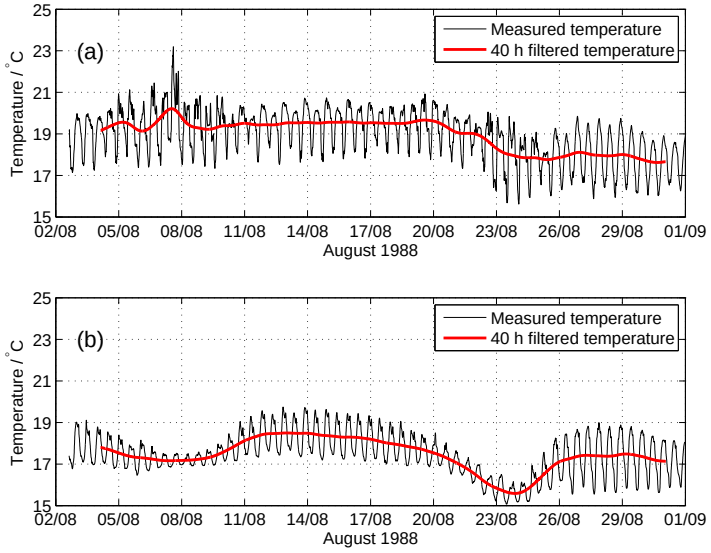

Figure 4.25 – Temperature time series measured by current meters during TEJO88/2 (a) near the surface and (b) near the bottom. The thick red line is the corresponding low-pass filtered time series (Butterworth digital filter with cut-off frequency equivalent to 40 h).

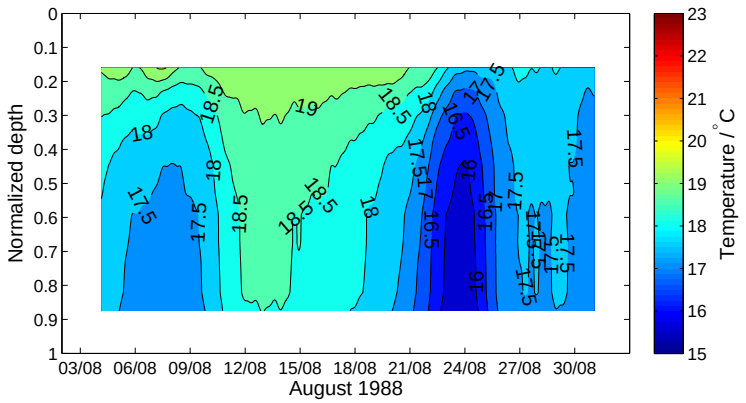

Figure 4.26 – Low-pass filtered (Butterworth digital filter with cut-off frequency equivalent to 40 h) temperature measured with a thermistor chain at mooring D during TEJO88/2. The normalised depth was calculated by dividing each thermistor's nominal depth by the total water column depth.

In order to verify the possible occurrence of a coastal upwelling event, the contemporaneous wind records obtained at the meteorological station of Montijo were analysed (see Fig. 2.2(d) for location). The north-south orientation of the Portuguese west coast means that coastal upwelling is closely related to the behaviour of the meridional wind stress component.

The wind velocity stick diagram for August 1988 (Fig. 4.27(a)) shows the occurrence of northerly wind during most part of the month, with an intensification becoming evident at around 17 August. The corresponding meridional wind stress (Fig. 4.27(b)) showed to be southward (favourable to coastal upwelling), peaking around 20-21 August. The temperature of the water column within the estuary then begins to decrease as earlier described, an evidence of the influence of the adjacent coastal ocean upwelled waters.

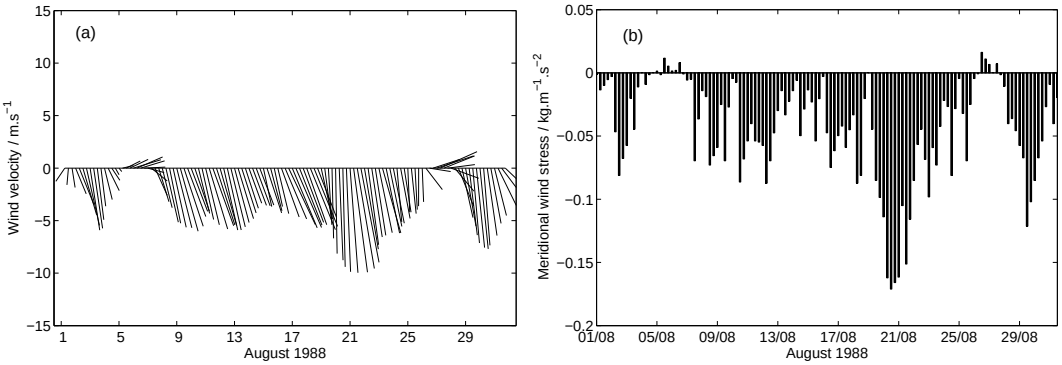

Figure 4.27 – (a) Stick diagram of the wind measured during TEJO88/2 campaign in August 1988 and (b) respective meridional wind stress component (kg m^{-1} s^{-2}).

INTAGUS

In what concerns the near-bottom water temperature feature observed during the INTAGUS campaigns (August 2007 for summer and January 2008 for winter), described earlier in Section 4.1.1, the wind velocity stick diagram for summer (Fig. 4.28(a)) shows the regular occurrence of northerly wind during the whole month. Nevertheless, a stronger and more persistent event occurred from about 16 to 22 August, after which the wind intensity decreased. The corresponding meridional wind stress (Fig. 4.28(b)) shows southward

direction (negative values) during most part of the month, increasing as expected during each strong north wind event.

The occurrence of upwelling was confirmed by the analysis of the sea surface temperature (SST) of the coastal ocean in the vicinity of the mouth of the estuary, as exemplified in Fig. 4.29 by a contemporary satellite SST image, and can then be associated to the near-bottom temperature measured within the estuary in summer being lower than in winter.

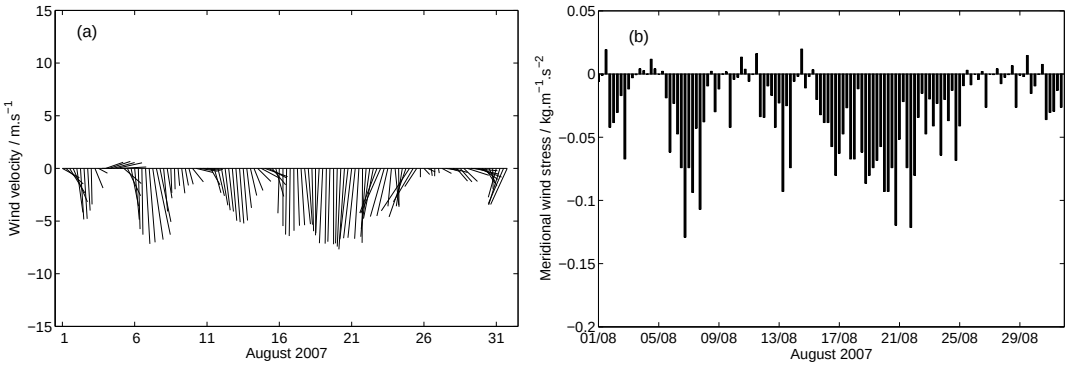

Figure 4.28 – (a) Stick diagram of the wind measured during INTAGUS07/1 campaign in August 2007 and (b) respective meridional wind stress component (kg m^{-1} s^{-2}).

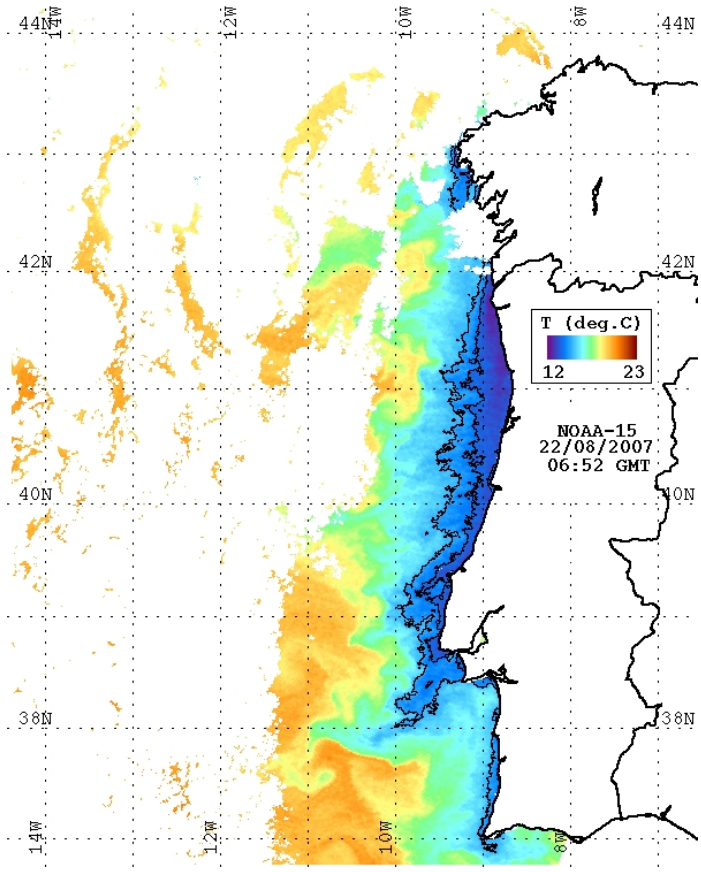

Figure 4.29 – Sea surface temperature (SST) image from NOAA-15 at 06:52 Greenwich Mean Time (GMT), 22 August 2007, with the representation of the 14 and 15 °C isotherms.

4.5 Summary of results

The Tagus Estuary is characterised by a complex bottom topography and margin morphology, so three different regions were defined within the estuary according to their morphological characteristics: the mouth, the inlet channel and the inner bay (containing the mid-estuarine region). Two quantitative methods of estuarine classification based on stratification and circulation parameters were applied separately to each region. It should be here referred that the spatial distribution of the stations where observations were performed may not be representative of each region of the estuary.

A quantitative method of classification based on the stratification parameter, of Prandle (1985), was used to classify the Tagus Estuary. On a typical summer river discharge regime, the Tagus Estuary is generally well mixed, especially during spring tides, whereas stratification is enhanced in neap tide conditions or on typical winter river discharge regime. When these two last conditions combine, stratification intensifies further and the estuary can be classified as stratified.

When classifying the estuary by means of the Stratification-Circulation diagram, used only for summer, both during spring and neap tide conditions and at the mid-estuarine region, the results are type *2a* during spring tide and *2b* during neap tide. This means that this region of the Tagus Estuary can be considered as partially mixed, with a higher degree of stratification in neap tide. One can thus expect a two-layered dynamical structure, characterised by seaward directed current in the upper layer and landward directed current in the bottom layer. It is also expected that the upstream salt flux has the important contributions of both advection and diffusion.

The analysis of the thermohaline conditions in the Tagus Estuary shows a large temperature range between summer and winter for river water, evidencing the seasonal atmospheric influence on the estuarine surface waters. As for seawater, the temperature range between summer and winter is much smaller, which could be due to the occurrence of upwelling events in summer, influencing the near-bottom temperature within the estuary.

The repeated cross-sections on the estuary did not show significant differences in both the thermohaline and dynamical structures between summer and winter, this being essentially due to the fact that the winter campaigns took place during “summer typical” river discharge conditions.

During summer, two distinct water temperature events observed within the estuary were related to the occurrence of coastal upwelling, showing a remote wind forcing effect on the estuarine thermohaline structure.

When investigating the subtidal variability of the dynamical and thermohaline structures within the Tagus Estuary and the influence of the principal forcing mechanisms, the inverse barometer effect is generally observed in the joint analysis of water level and sea-level pressure measured in the Tagus Estuary.

The dynamical and thermohaline structures within the estuary are, in general, strongly influenced by the fortnightly cycle. This is shown by the increase (decrease) of variability of the water column thermohaline structure in neap (spring) tide, by the variability of the subtidal current direction at specific locations within the estuary and also evidenced by the differences in the stratification parameter as earlier referred. Although influenced by the spring-neap cycle in some locations, the order of magnitude of the subtidal current was, in general, 10 cm s^{-1}, one order of magnitude below the tidal current.

The fortnightly tidal cycle is important in establishing different thermohaline and dynamical patterns associated with the semi-diurnal tide, especially in what concerns lateral gradients across the inlet channel and the inner bay. This is due to the turbulent mixing variability associated to the spring-neap cycle (stronger mixing during spring tide), caused by the respective current intensity variations.

The subtidal thermohaline series obtained from the RCMs data at the inlet channel showed that the fortnightly cycle influence is much weaker near the mouth than in the mid-estuarine region. This may be explained by the fact that the stratification is much lower near the mouth and so the vertical mixing effect on the thermohaline structure during the spring-neap cycle becomes less important, i.e. the baroclinic effects are not so important near the mouth as in the mid-estuary. In what concerns the dynamical structure at the inlet channel, the periods of observation of the region closer to the mouth and of that in the mid-estuary were distinct, which may explain the observed differences. Near the mouth, during winter, the subtidal current direction presented a change from a seaward to a landward period, which can be related to the veering of the wind. A relatively strong southerly wind event could have caused this change, in accordance to other authors numerical simulations results. Closer to the mid-estuary, during summer, the spring-neap cycle seems to influence

the current direction, being seaward during neap tide and landward (with lower intensity) during spring tide. In this case, assuming a partially-mixed water column in neap tide, which is supported by the classification results obtained with the Stratification-Circulation diagram, the residual flow near the surface was expected to be seaward. But in spring tide, the higher velocity currents could have enhanced the water column vertical mixing and destroyed the two-layered circulation pattern, thus reversing the near-surface flow towards the interior (landward).

In the mid-estuarine region, the thermohaline structure generally evidences a strong influence of vertical mixing variability associated to the fortnightly cycle, thus periodically reducing or strengthening the water column stratification. As for the dynamical structure, the near-surface subtidal current behaviour shows the existence of different paths for the landward and for seaward current. The landward branch was found closer to the northern margin whereas the seaward branch was located farther from that margin. However, this pattern was found during summer typical river discharge and only in spring tide conditions. The wind seemed to have no influence on the establishment of this circulation pattern.

As for the inner bay, the only RCM (C) moored there, close to the southern margin, did not show any influence of the fortnightly cycle, both on the thermohaline and on the dynamical structures. It shows a general landward subtidal current, and no relation with the principal forcing mechanisms was found. Again, the results of the numerical simulation reported by Dias (1993) shows the existence of a clockwise eddy and the location of the RCM C was approximately coincident with its landward branch.

Fixed point time series and vertical distributions of salinity, temperature and along-channel current velocity evidence a strong forcing by the semi-diurnal tide. This strong forcing is especially evident on the variability of tidal currents and on the strengthening of horizontal salinity gradients and vertical stratification from flood to ebb, which is mainly caused by tidal straining.

The joint analysis of the dynamical and thermohaline fields showed that the tide behaves essentially as a standing wave within the Tagus Estuary, confirming the results already presented in Chapter 3 for the M_2 constituent.

Both in the inlet channel and in the mid-estuary, ebb and flood durations were observed to decrease with depth, in the southern end of the cross-section. This was probably a

consequence of the enhanced friction effects due to the proximity of the lateral boundaries close to the southern margin.

As expected, the deepest regions constitute the preferred path for the flow of saltier water, this being especially evident in the mid-estuarine region, along the two main bottom channels. The freshwater, on the other hand, flows near the surface, preferably close to the northern margin.

The results showed and analysed in this Chapter reinforce the semi-diurnal tide as the main forcing mechanism of the Tagus Estuary, driving its dynamics and establishing the main thermohaline patterns. When analysing the subtidal variability, the fortnightly cycle was verified to be the main forcing mechanism for the residual circulation, by setting the water column thermohaline structure. It also became clear that the bottom topography and the coastline morphology play an important role on the estuarine circulation, complementing the fortnightly tide on the establishment of different residual circulation patterns. As for the wind, although its importance as a forcing mechanism, the data only allowed to show its role in terms of its remote forcing effects on the estuary, through the occurrence of coastal upwelling and consequent influence of the temperature of the estuarine waters. The river discharge acts mainly on the setting of the water column stratification, strengthening the stratification during winter-typical river discharge regimes. Although not shown in this study, the river discharge should also be important to establish the estuarine residence time, which should increase when the river discharge decrease and vice-versa.

Chapter 5

Summary of conclusions and future work

5.1 Main conclusions

This chapter presents a brief overview of the main conclusions of the present study and closes with a few suggestions for future research in the Tagus Estuary.

The work presented here was carried out with the main objective of describing some aspects of the physical oceanography of the Tagus Estuary, namely, to better understand the propagation of the tide within the estuary, to establish thermohaline and circulation patterns and to investigate the role of the principal forcing mechanisms (tide, wind and river discharge) on the estuarine dynamics.

With these objectives in mind, a large set of observations collected in different years in the Tagus Estuary, in the frame of several research projects of the group of Physical Oceanography of the Faculty of Sciences of the University of Lisbon, was gathered, re-processed and analysed. The data set is constituted by hydrology and current profiles in several sections along and across the estuary as well as by repeated profiles at fixed positions, and also by time series obtained with self-recording equipment moored at several positions within the estuary. Some of the data were obtained during summer and other during winter, in neap and spring tide conditions, and were complemented by contemporary water level measurements from tidal gauges in the margins of the estuary, wind records in

the vicinity of the estuary and river discharges at about 130 km upstream of the mouth. A set of one-year long water level records along both margins of the estuary during 1972 was also used in this study.

The main morphological characteristics of the Tagus Estuary allow to classify it as a "coastal plain estuary". As for its tidal range, the Tagus Estuary can be classified as "mesotidal". In terms of its water column structure, the results obtained with quantitative methods showed that the estuary can be generally considered "partially mixed", in agreement with other authors. Its stratification is generally enhanced in neap tide conditions and, when these conditions are combined with typical winter river discharge, the Tagus Estuary can then be classified as "stratified", with a two-layer residual circulation (landward near the bottom and seaward near the surface).

In general, the current velocity data collected in the Tagus Estuary have shown consistency with the typical circulation of a partially mixed estuary, which is in accordance with results obtained by other authors. The data analysis also showed features consistent with the existence of several eddies, earlier suggested by other authors' numerical simulations. In particular, these eddies appear in estuarine regions where the morphology presents abrupt changes in the channel breath, bottom depth or margin orientation. The observations suggested that these structures can be affected by the wind or by the spring-neap variability of the water column stratification, either changing their location or even being destroyed.

In what concerns the thermohaline field, salty water occupies the bottom layers, the saltiest water being found in the deepest sites, as shown in the main channels of the inner bay. At the inlet channel, saltier bottom water is found generally close to the southern margin, whereas fresher surface water is found close to the northern margin, not only in the inlet channel but also in the inner bay. These preferred paths for the seawater and for the river water are compatible with the Coriolis force veering if we assume the residual current to be landward near the bottom and seaward near the surface.

The bottom topography and the margin morphology of the Tagus estuarine system can be considered as "static" forcing mechanisms, because of their important role conditioning the spatial variability of the observed circulation patterns and the boundary friction effects. In particular, considering the semi-diurnal time scale, the bottom topography was found to be the principal constraint to the direction of the tidal currents.

In what concerns the "dynamical" forcing mechanisms in the estuary, their relative importance depends on the considered time scales.

As the tide is known to be the main forcing mechanism in most estuaries, an attempt was made to better characterise its propagation within the Tagus Estuary. The semi-diurnal frequency was shown to be the main source of energy for the estuarine dynamics and for forcing the main thermohaline patterns. The tidal wave propagates in the estuary as a mixed progressive/standing wave. Its standing character, progressively increases towards the interior, suggesting an upstream increase of the interaction between incident and reflected waves. This seems to be related with a resonant mode within the estuary, whose period is close to that of the semi-diurnal tide. An asymmetric behaviour of the tide is revealed with the ebbs being generally shorter and stronger than floods. This ebb dominance intensifies towards the interior, much probably due to the extensive intertidal flat area in this region. The asymmetry is mainly caused by the quarter-diurnal harmonic constituent M_4, since its growing amplitude towards the estuary's interior is coincident with the intensification of the ebb dominance. Upstream of Cabo Ruivo the amplitude of the sixth-diurnal constituent M_6 started to increase and the sense of the asymmetry shifted from ebb to flood dominance. Tidal currents are of the order of 10^2 cm s^{-1} and are stronger in the mid-estuary and in the inner bay, when compared to the inlet channel, this being consistent with the increase of the tidal range from the mouth to the interior of the estuary. As for residual (subtidal) currents, they are one order of magnitude below the tidal currents (10 cm s^{-1}), this being the usual relation found in most estuarine systems.

The fortnightly tidal cycle, in general, influences strongly the dynamical and thermohaline structures within the Tagus Estuary. Current intensity variations during the spring-neap cycle are the main cause for the turbulent mixing variability which, in turn, leads to modifications in the water column stratification, and is responsible for changes in the circulation patterns within the estuary.

The action of the river discharge as a forcing mechanism was mainly on a seasonal time scale, by influencing the salinity of the surface layer and, consequently, enhancing the stratification of the water column for typical winter river discharge. The modulation of the river discharge fluctuations caused by the numerous dams along the Tagus River may be the reason for the small variability of the river flow during the periods of observation.

However, a sudden variation of the river discharge which was not completely attenuated seemed to be associated with modifications on the circulation patterns, due to changes of the water column stratification.

In what concerns the atmospheric forcing, the effect of the wind, air temperature and atmospheric pressure have been evaluated in the present work.

The observations only have clearly shown the wind's remote forcing effects, by the intensification of coastal upwelling off Portugal during summer which, in turn, caused the estuarine water temperature to decrease. Nevertheless, the data also gave some hints about its local forcing effects. These were mainly due to changes on the subtidal circulation which could be related to the wind veering. Given the different wind regimes affecting the Portuguese coastal region in summer (mainly northerly) and in winter (mainly southwesterly), differences in the circulation patterns of the Tagus Estuary are to be expected between summer and winter. It is thus apparent that the wind influences the Tagus Estuary's dynamics mainly on a seasonal time scale but also on smaller time scales.

The effects of the air temperature proved to be mainly seasonal, strongly influencing the surface temperature conditions, as the result of conductive and convective heat transfer. Concerning the atmospheric pressure, the joint analysis of the corresponding series and of the water level series showed that its main influence is through the inverse barometer effect, which affects the barotropic component of the residual circulation.

This study has contributed to increase the understanding of some aspects of the dynamics of the Tagus Estuary, grounded on direct observations. Some of the observed features are well in accordance with the results obtained by other authors using numerical models. Although the propagation of the tide has been previously studied, this work helps to clarify some aspects of its asymmetric behaviour. Namely the tide gauge and current meter data allowed to quantify the spatial evolution of the tidal asymmetry within the estuary, in terms of the relative ratio and phase difference between the constituents M_2 and M_4, and also helped to clarify the role and importance of the constituent M_6 for the asymmetry. Contributions were also given to the links between different thermohaline and circulation patterns and the corresponding forcing mechanisms. A new-found result worth mentioning is the remote effect of the coastal wind on the estuarine water temperature, causing its decrease due to the influence of colder upwelled waters from the adjacent coastal region.

5.2 Future work

During the present study, some limitations in the data were identified, suggesting specific aspects to be taken into consideration in the planning of future observational campaigns. The most important limitations found were:

- The observational campaigns did not cover some of the important combinations of forcing conditions, e.g. the spring tide conditions and typical winter river discharge regime;

- The loss of some moored equipment (current meters and thermistor chains) or marine fouling problems affecting some of their sensors (e.g. conductivity sensor, current meter rotor) shortened the time series (configured to last one month) and prevented the completion of the fortnightly tidal cycle;

- Due to logistic difficulties, it was not possible to repeat the CTD profiles across the two sections of the estuary over a complete semi-diurnal cycle in the INTAGUS campaigns.

Better spatial and temporal coverages are thus desirable in order to improve the monitoring programmes in the Tagus Estuary. The complex shape and bottom topography of this estuary requires a spatial coverage which would allow a significant representation of the several estuarine regions. In addition, longer time series would allow the study of the effects of the forcing mechanisms on a wider range of time scales than those focused in the present work (e.g. the effects of mean sea-level changes on the estuarine dynamics). Taking the past experience in consideration, a future observational strategy for the Tagus Estuary could include the use of the existing moored navigation buoys as platforms for oceanographic and meteorological equipment, and also the use, as ships-of-opportunity, of the numerous ferry-boats that daily cross the estuary in different routes. This would allow to surpass the limitations encountered by observational surveys in heavy traffic regions and to obtain long-term oceanographic and meteorological series.

The direct wind influence on the dynamics of the Tagus Estuary is an important issue as the wind was identified in this study as the most probable cause for some of the changes occurred in the subtidal circulation. Several studies (e.g. Weisberg, 1976; Elliott, 1978;

Wang, 1979) have shown how wind-driven circulation often dominates the subtidal circulation of estuaries, demonstrating that the wind can control the salinity structure and the residence time within an estuary. The investigation of the wind-driven circulation in the Tagus Estuary's would be important and useful in what concerns the improvement of its residence time estimates.

The turbulent vertical mixing is the main physical process responsible for the setting of the stratification and essential when determining the estuarine momentum and salt balances (Peters, 1997). In this sense, the investigation of the magnitude and variability patterns of turbulent mixing would be a valuable contribution for the increasing of the realism of numerical models, by the attempt to improve their parameterization of turbulent mixing.

Appendix A

Observational campaigns: dates and duration

This appendix contains detailed information about the dates and duration of each observational campaign in the Tagus Estuary, as well as the type of data that was sampled. It also provides details about the site location, periods of observations used in the present study and sample rate of tidal, meteorological and river discharge data.

Survey	Data type	Period of observations
TEJO85	CTD profiles	12/09 – 19/09/1985
	RCM series	07/09 – 09/10/1985
TEJO88/1	CTD profiles	11/02 – 13/02/1988
TEJO88/2	RCM and TR series	02/08 – 01/09/1988
TEJO89	RCM series	06/11 – 06/12/1988
INTAGUS07/1	CTD and DCS profiles	22/08 – 23/08/2007
INTAGUS07/2		30/08 – 31/08/2007
INTAGUS08/1	CTD and DCS profiles	10/01 – 11/01/2008
INTAGUS08/2		17/01 – 18/01/2008

Table A.1 – Dates of the observational campaigns performed in the Tagus Estuary and the corresponding type of data collected. CTD – *Conductivity-Temperature-Depth*; RCM – *Recording Current Meter*; TR – *Temperature Recorder*; DCS – *Doppler Current Sensor*.

Gauge site	Latitude (N)	Longitude (W)	Period of observations	Sample rate (min)
Cascais (Ca)	38° 41.50'	9° 25.00'	01/01/1972 – 31/12/1972	60
			01/09/1985 – 09/10/1985	60
			01/02/1988 – 29/02/1988	60
			28/07/1988 – 03/09/1988	60
			01/11/1989 – 07/12/1989	60
			01/01/2008 – 31/01/2008	60
Paço de Arcos (Pa)	38° 41.40'	9° 17.50'	26/01/1972 – 27/01/1973	60
			27/07/1988 – 05/09/1988	5
			01/11/1989 – 12/12/1989	5
Trafaria (Tr)	38° 40.40'	9° 13.80'	01/01/1972 – 31/12/1972	60
Pedrouços (Pd)	38° 41.50'	9° 13.40'	01/01/1972 – 31/12/1972	60
Cacilhas (Cc)	38° 41.20'	9° 8.80'	01/01/1972 – 31/12/1972	60
Terreiro do Paço (Tp)	38° 42.30'	9° 7.90'	01/01/1972 – 31/12/1972	60
			28/08/1985 – 30/09/1985	5
			27/01/1988 – 07/03/1988	5
			01/08/2007 – 31/08/2007	60
Seixal (Sx)	38° 38.90'	9° 4.50'	01/01/1972 – 31/12/1972	60
Cabo Ruivo (Cr)	38° 45.30'	9° 5.40'	01/01/1972 – 31/12/1972	60
			28/08/1985 – 30/09/1985	5
			27/01/1988 – 29/02/1988	5
			27/07/1988 – 05/09/1988	5
			01/11/1989 – 11/12/1989	5
Ponta da Erva (Pe)	38° 49.90'	8° 57.90'	01/01/1972 – 31/12/1972	60
V. Franca de Xira (Vf)	38° 57.00'	8° 59.30'	01/01/1972 – 31/12/1972	60

Table A.2 – Periods of tidal observations used in the present study, location and sample rate of each gauge in the Tagus Estuary.

Data type	Station	Latitude (N)	Longitude (W)	Period of observations	Sample rate
Meteorological data (*)	Montijo	38° 42.00’	9° 3.00’	04/09/1985 – 30/09/1985 01/02/1988 – 29/02/1988 01/08/1988 – 31/08/1988 01/11/1989 – 31/12/1989	Synoptic observations (6, 9, 12, 15 and 18 h GMT)
Wind	Lisboa	38° 43.00’	9° 9.00’	01/08/2007 – 31/08/2007 01/01/2008 – 31/01/2008	Hourly
River discharge	Almourol	39° 27.60’	8° 22.80’	02/10/1973 – 18/07/2008	Daily

Table A.3 – Periods of observations of meteorological data (* includes wind speed and direction, sea level atmospheric pressure and sea level air temperature) and river discharge, and location of the respective stations.

Appendix B

Thermohaline and current time series and vertical distributions

This appendix presents all the *in situ* data obtained in the frame of the observational campaigns described in Chapter 2. The data are grouped in time series measured by the moorings and in vertical distributions of thermohaline and current velocity data measured by multiparameter probes and CTDs.

Detailed informations about the moorings deployed in the Tagus Estuary are presented in tables and the corresponding thermohaline and current time series are shown. The longitudinal and transversal vertical distributions of salinity, temperature and along-channel current velocity are also represented, together with their respective location within the estuary.

B.1 TEJO85: moorings

Mooring A	Latitude (N)	Longitude (W)	Sample rate	Site depth (m)	Deployment	Recovery
	38° 41.09’	9° 9.90’	10 min	24.2	10/09/1985	09/10/1985

RCM A		Installed sensors				
		Temperature	Conductivity	Pressure	Direction	Speed
	First good record	10/09 – 12h55m	10/09 – 12h55m	—	10/09 – 12h55m	10/09 – 12h55m
	Last good record	09/10 – 10h55m	09/10 – 10h55m	—	09/10 – 10h55m	09/10 – 10h55m

Table B.1 – Deployment informations about mooring A (TEJO85) and respective current meter details.

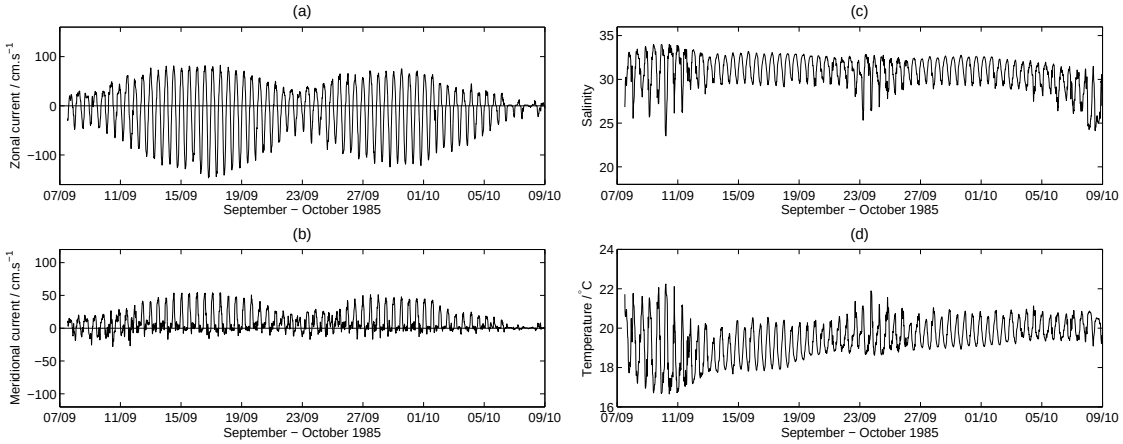

Figure B.1 – Time series of (a) zonal and (b) meridional current velocity components, (c) salinity and (d) temperature measured by the current meter A (TEJO85).

Mooring B	Latitude (N)	Longitude (W)	Sample rate	Site depth (m)	Deployment	Recovery
	38° 41.40'	9° 6.10'	10 min	9.2	07/09/1985	09/10/1985
RCM B		Installed sensors				
		Temperature	Conductivity	Pressure	Direction	Speed
	First good record	07/09 – 12h15m	07/09 – 12h15m	07/09 – 12h15m	07/09 – 12h15m	07/09 – 12h15m
	Last good record	09/10 – 12h25m	09/10 – 12h25m	09/10 – 12h25m	09/10 – 12h25m	09/10 – 12h25m

Table B.2 – Deployment informations about mooring B (TEJO85) and respective current meter details.

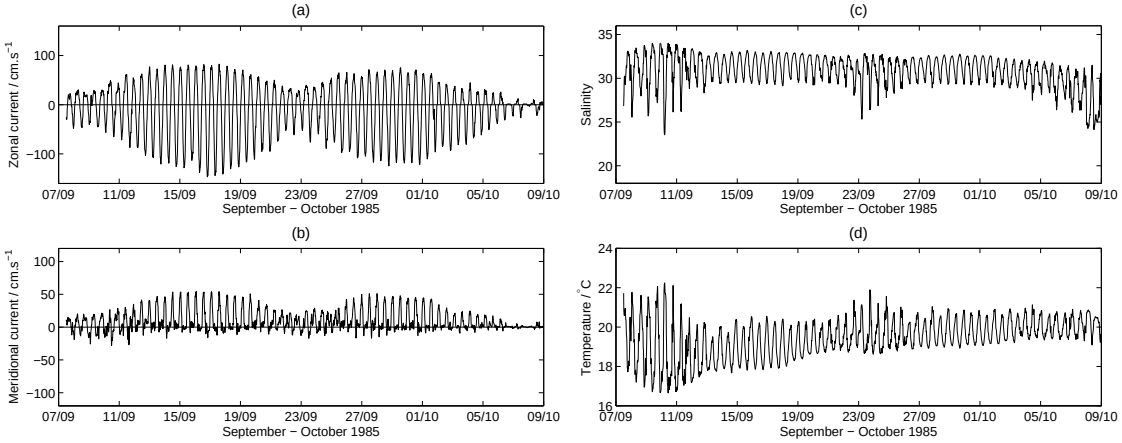

Figure B.2 – Time series of (a) zonal and (b) meridional current velocity components, (c) salinity and (d) temperature measured by the current meter B (TEJO85).

Mooring C	Latitude (N)	Longitude (W)	Sample rate	Site depth (m)	Deployment	Recovery
	38° 45.70’	9° 1.35’	10 min	9.3	07/09/1985	09/10/1985

RCM C		Installed sensors				
		Temperature	Conductivity	Pressure	Direction	Speed
	First good record	07/09 – 14h05m	07/09 – 14h05m	—	07/09 – 14h05m	07/09 – 14h05m
	Last good record	09/10 – 14h15m	09/10 – 14h15m	—	09/10 – 14h15m	09/10 – 14h15m

Table B.3 – Deployment informations about mooring C (TEJO85) and respective current meter details.

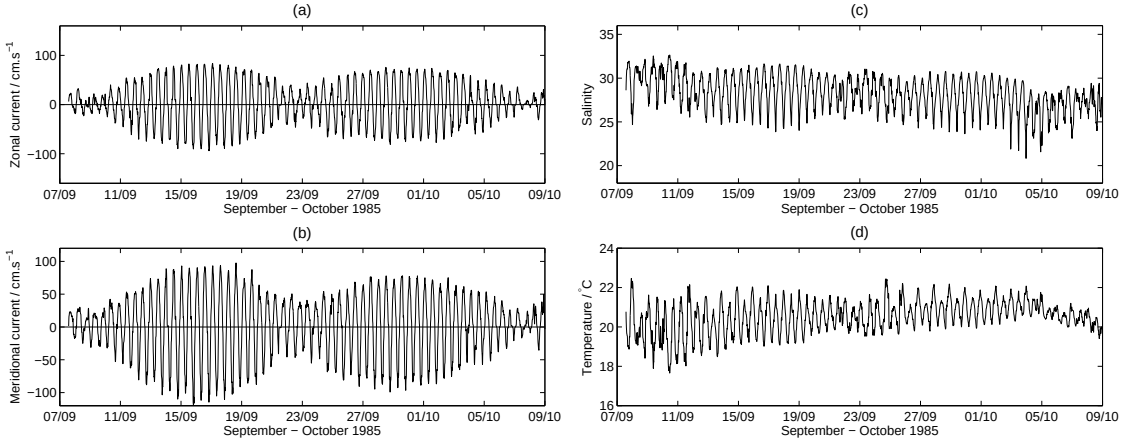

Figure B.3 – Time series of (a) zonal and (b) meridional current velocity components, (c) salinity and (d) temperature measured by the current meter C (TEJO85).

B.2 TEJO88/2: moorings

Mooring D	Latitude (N)	Longitude (W)	Sample rate	Site depth (m)	Deployment	Recovery
	38° 42.47'	9° 6.77'	5 min (RCM)	12.8	02/08/1988	01/09/1988
RCM D_s		Installed sensors				
		Temperature	Conductivity	Pressure	Direction	Speed
	First good record	02/08 – 15h30m	02/08 – 15h30m	02/08 – 15h30m	02/08 – 15h30m	02/08 – 15h30m
	Last good record	01/09 – 13h15m	01/09 – 13h15m	01/09 – 13h15m	01/09 – 13h15m	01/09 – 13h15m
RCM D_b		Installed sensors				
		Temperature	Conductivity	Pressure	Direction	Speed
	First good record	02/08 – 15h20m	02/08 – 15h20m	02/08 – 15h20m	02/08 – 15h20m	02/08 – 15h20m
	Last good record	01/09 – 13h25m	01/09 – 13h25m	01/09 – 13h25m	07/08 – 16h05m	18/08 – 16h25m
TR D	First good record	Last good record	Thermistors	Chain length	D. between therm.	Sample rate
	02/08 – 15h50m	01/09 – 13h40m	11	~30 m	~1.5 m	10 min

Table B.4 – Deployment informations about mooring D (TEJO88/2) and respective current meters and thermistor chain details. D_s – near-surface RCM; D_b – near-bottom RCM.

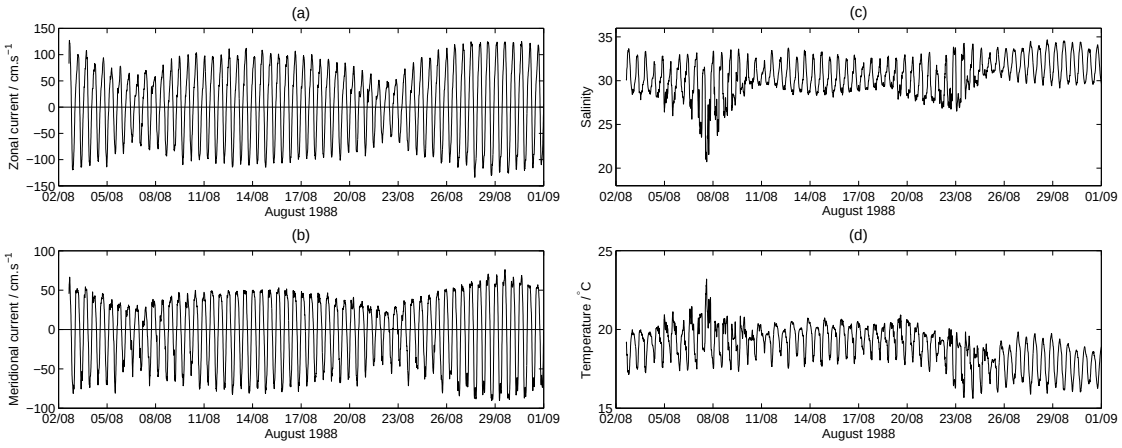

Figure B.4 – Time series of (a) zonal and (b) meridional current velocity components, (c) salinity and (d) temperature measured by the near-surface current meter D_s (TEJO88/2).

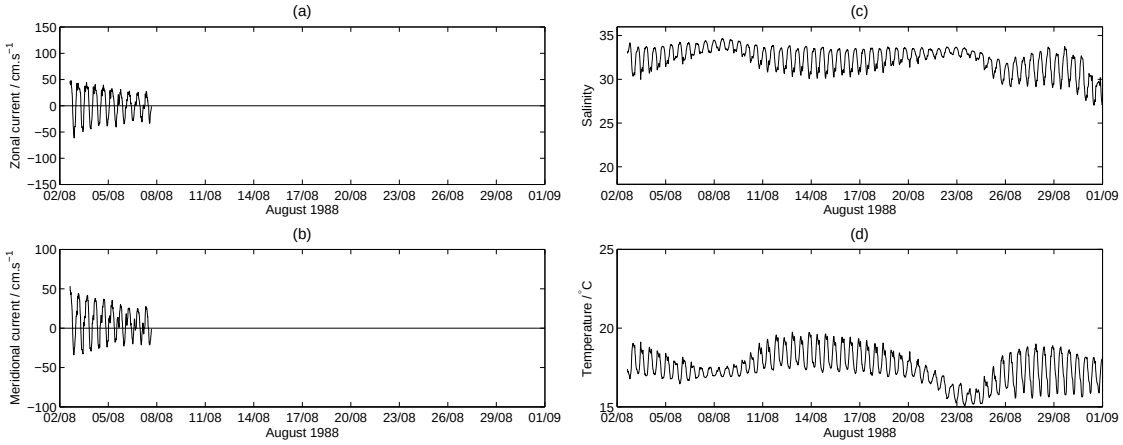

Figure B.5 – Time series of (a) zonal and (b) meridional current velocity components, (c) salinity and (d) temperature measured by the near-bottom current meter D_b (TEJO88/2).

Mooring E	Latitude (N)	Longitude (W)	Sample rate	Site depth (m)	Deployment	Recovery
	38° 42.02'	9° 6.08'	5 min (RCM)	10.5	02/08/1988	01/09/1998
RCM E_s		Installed sensors				
		Temperature	Conductivity	Pressure	Direction	Speed
	First good record	02/08 – 14h20m	02/08 – 14h20m	02/08 – 14h20m	02/08 – 14h20m	02/08 – 14h20m
	Last good record	23/08 – 14h00m	23/08 – 14h05m	23/08 – 14h05m	22/08 – 09h15m	22/08 – 19h05m
RCM E_b		Installed sensors				
		Temperature	Conductivity	Pressure	Direction	Speed
	First good record	02/08 – 14h05m	02/08 – 14h05m	02/08 – 14h05m	02/08 – 14h05m	02/08 – 14h05m
	Last good record	01/09 – 14h35m	18/08 – 23h15m	01/09 – 14h35m	07/08 – 04h35m	04/08 – 05h25m
TR E	First good record	Last good record	Thermistors	Chain length	D. between therm.	Sample rate
	02/08 – 14h50m	01/09 – 14h40m	11	~30 m	~1.5 m	10 min

Table B.5 – Deployment informations about mooring E (TEJO88/2) and respective current meters and thermistor chain details. E_s – near-surface RCM; E_b – near-bottom RCM.

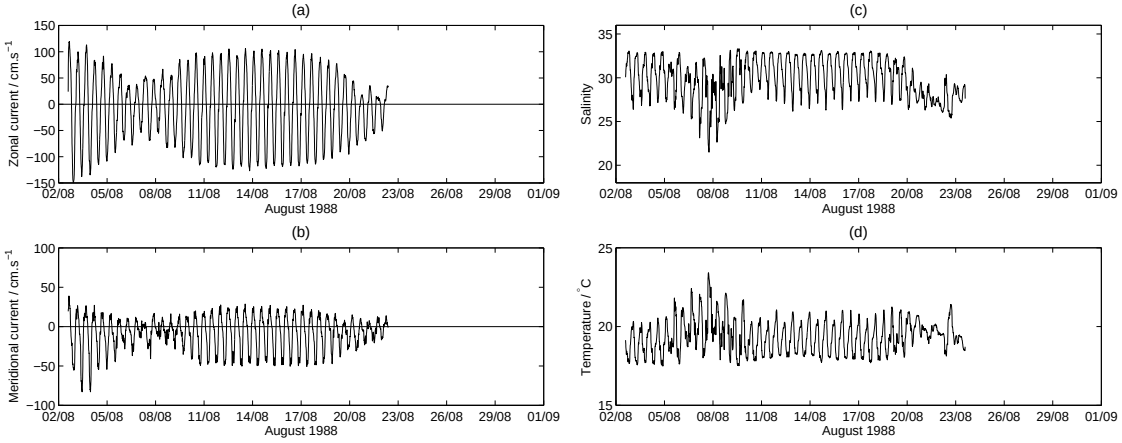

Figure B.6 – Time series of (a) zonal and (b) meridional current velocity components, (c) salinity and (d) temperature measured by the near-surface current meter E_s (TEJO88/2).

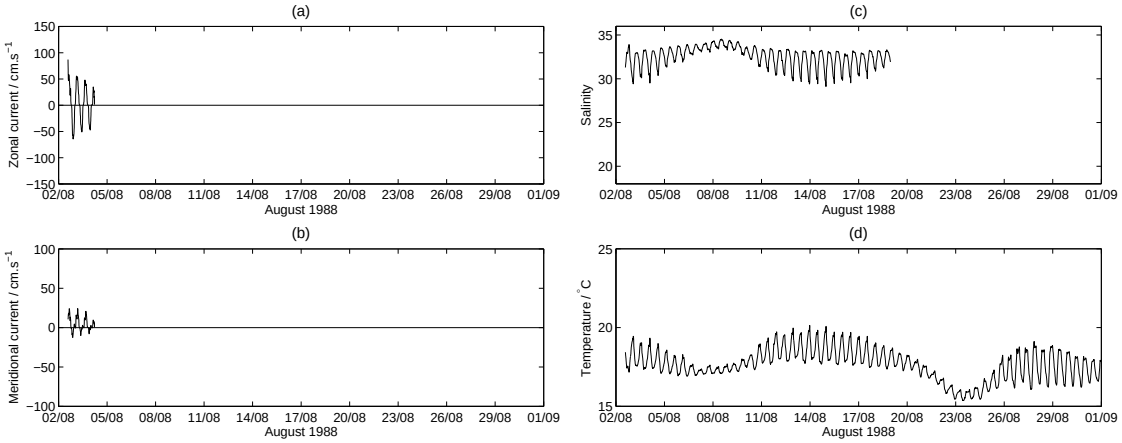

Figure B.7 – Time series of (a) zonal and (b) meridional current velocity components, (c) salinity and (d) temperature measured by the near-bottom current meter E_b (TEJO88/2).

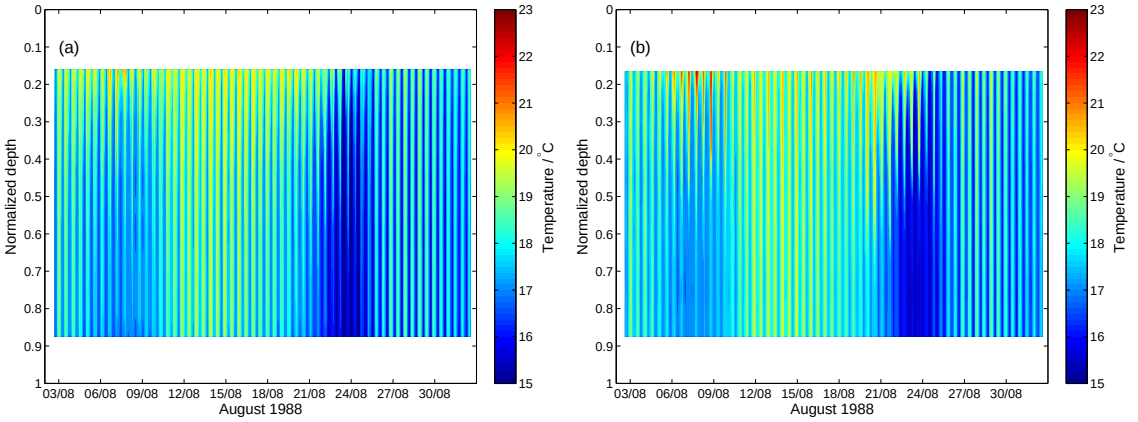

Figure B.8 – Time series of vertical distributions of temperature measured by the thermistor chains included in moorings (a) D and (b) E (TEJO88/2).

B.3 TEJO89: moorings

Mooring F	Latitude (N)	Longitude (W)	Sample rate	Site depth (m)	Deployment	Recovery
	38° 41.25'	9° 13.91'	5 min	19.3	06/11/1989	06/12/1989
RCM F_m		Installed sensors				
		Temperature	Conductivity	Pressure	Direction	Speed
	First good record	06/11 – 17h15m	06/11 – 17h15m	06/11 – 17h15m	06/11 – 17h15m	06/11 – 17h15m
	Last good record	06/12 – 16h05m	06/12 – 16h05m	06/12 – 16h05m	11/11 – 00h05m	11/11 – 00h05m
RCM F_b		Installed sensors				
		Temperature	Conductivity	Pressure	Direction	Speed
	First good record	06/11 – 17h15m	06/11 – 17h15m	06/11 – 17h15m	06/11 – 17h15m	06/11 – 17h15m
	Last good record	06/12 – 16h05m	06/12 – 16h05m	06/12 – 16h05m	14/11 – 19h55m	14/11 – 19h55m

Table B.6 – Deployment informations about mooring F (TEJO89) and respective current meters details. F_m – middle-water RCM; F_b – near-bottom RCM.

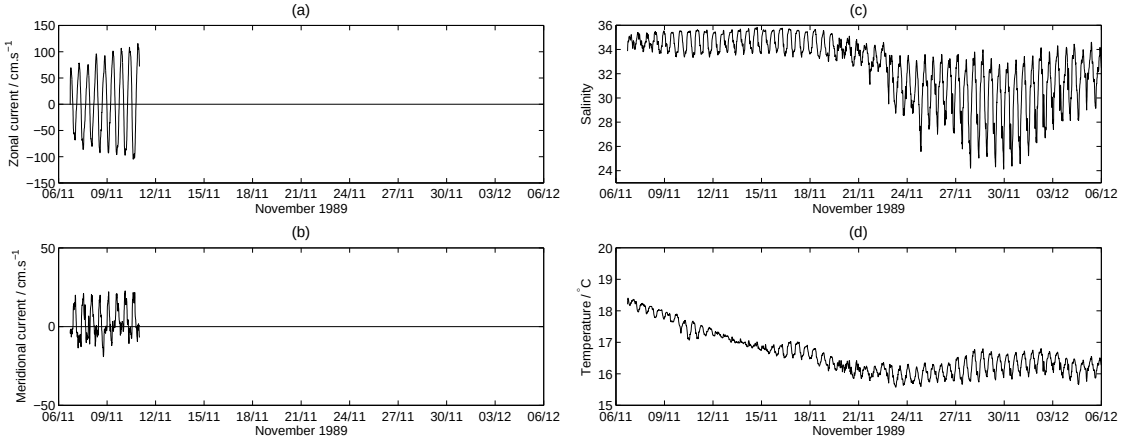

Figure B.9 – Time series of (a) zonal and (b) meridional current velocity components, (c) salinity and (d) temperature measured by the mid-water current meter F_m (TEJO89).

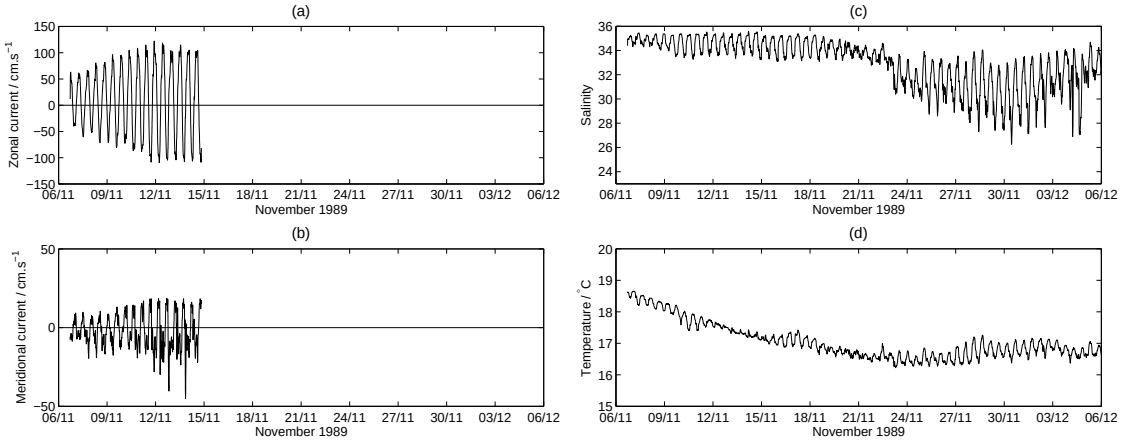

Figure B.10 – Time series of (a) zonal and (b) meridional current velocity components, (c) salinity and (d) temperature measured by the near-bottom current meter F_b (TEJO89).

Mooring G	Latitude (N)	Longitude (W)	Sample rate	Site depth (m)	Deployment	Recovery
	38° 40.54'	9° 13.84'	5 min	29.3	07/11/1989	06/12/1989
RCM G_m		Installed sensors				
		Temperature	Conductivity	Pressure	Direction	Speed
	First good record	07/11 – 16h35m	07/11 – 16h35m	07/11 – 16h35m	07/11 – 16h35m	07/11 – 16h35m
	Last good record	06/12 – 14h35m	06/12 – 14h35m	06/12 – 14h35m	06/12 – 14h35m	06/12 – 14h35m
RCM G_b		Installed sensors				
		Temperature	Conductivity	Pressure	Direction	Speed
	First good record	07/11 – 16h35m	07/11 – 16h35m	07/11 – 16h35m	N. A.	07/11 – 16h35m
	Last good record	06/12 – 14h35m	06/12 – 14h35m	06/12 – 14h35m	N. A.	18/11 – 19h10m

Table B.7 – Deployment informations about mooring G (TEJO89) and respective current meters details. G_m – middle-water RCM; G_b – near-bottom RCM. N. A. – good quality data not available.

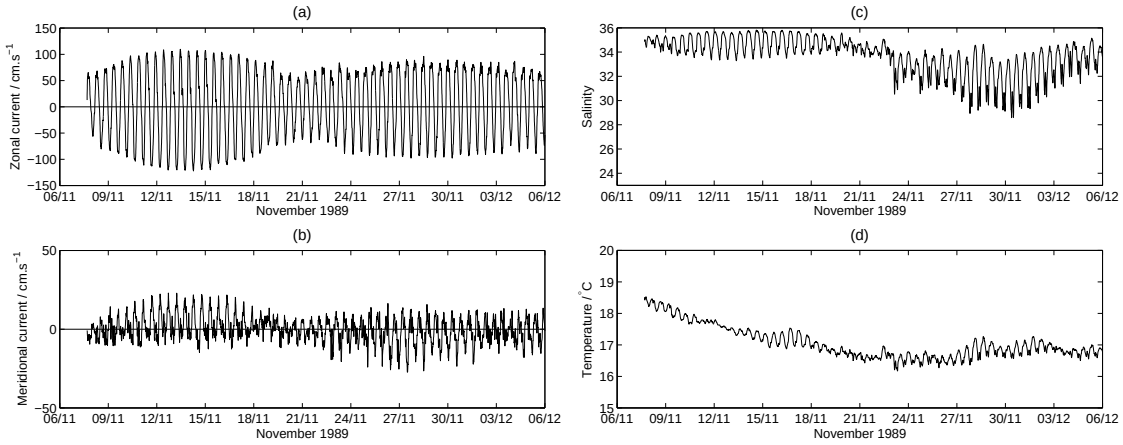

Figure B.11 – Time series of (a) zonal and (b) meridional current velocity components, (c) salinity and (d) temperature measured by the mid-water current meter G_m (TEJO89).

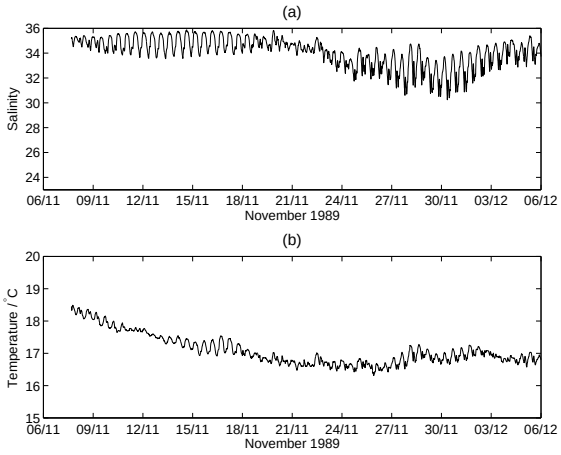

Figure B.12 – Time series of (a) salinity and (b) temperature measured by the near-bottom current meter G_b (TEJO89).

B.4 Thermohaline vertical distributions

This section presents the salinity and temperature vertical distributions along the several sections performed during the observational campaigns TEJO85 and TEJO88/1. The vertical distributions are grouped by longitudinal, transversal and fixed sections.

B.4.1 TEJO85 longitudinal sections

The locations of the longitudinal sections are given in an inset on the figures. The date and start time of each section, relative to the former tidal peak, are also presented. The numbers in the top horizontal axis identify the stations and the interior of the estuary is on the right side of the figure.

Salinity

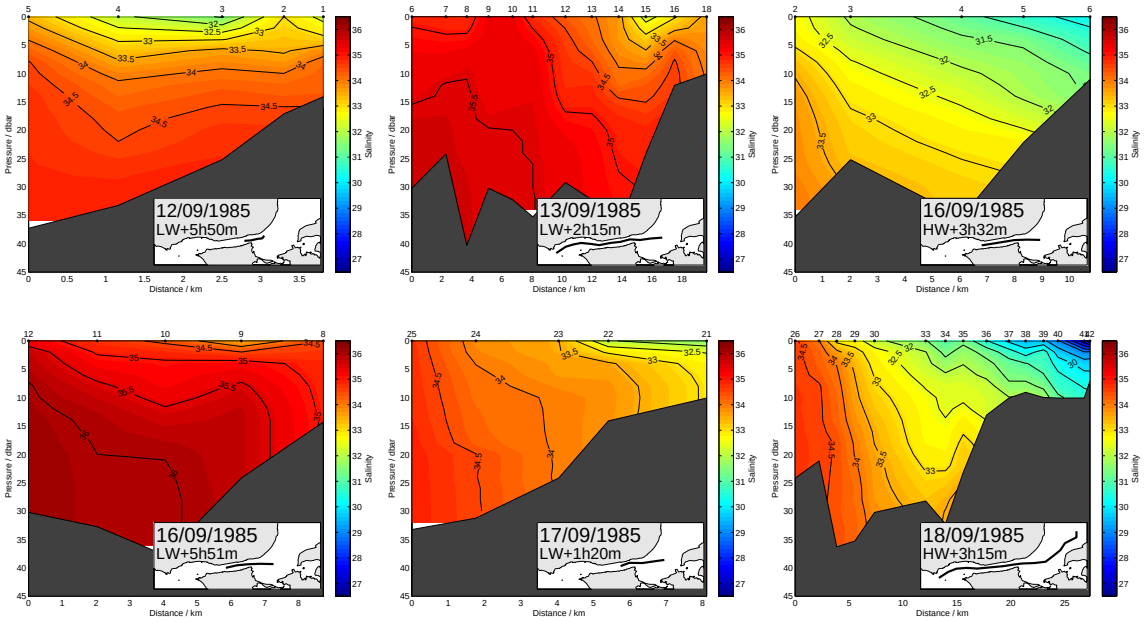

Figure B.13 – Longitudinal sections of salinity obtained during the TEJO85 campaign.

Temperature

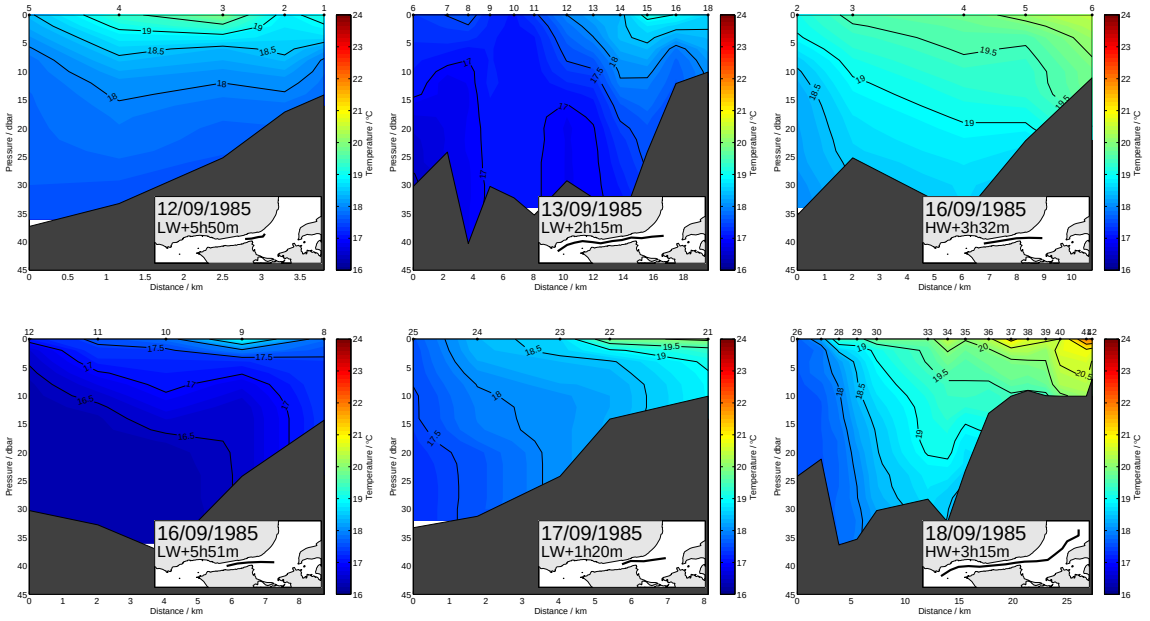

Figure B.14 – Longitudinal sections of temperature obtained during the TEJO85 campaign.

B.4.2 TEJO85 transversal sections

During TEJO85, two transversal sections were carried out: one in the inner bay (sp19tr) inlet channel, with 6 repetitions, and one in the inlet channel (vo19tr), with 5 repetitions. The location of these transversal sections is represented in Fig. B.15.

The vertical distributions of salinity and temperature of each repetition of both sections are shown in Figs. B.16 – B.19. The start time of the section, relative to the former tidal peak, is also presented in the figure. The numbers in the top horizontal axis identify the station and the right side of the figure corresponds to the northern margin.

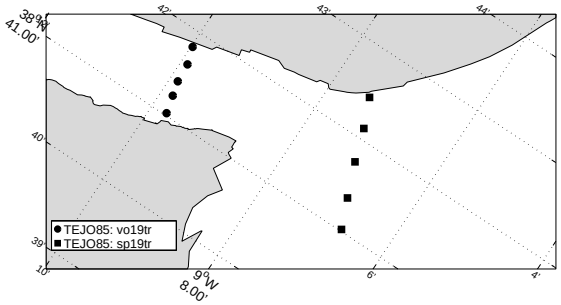

Figure B.15 – Location of the transversal sections carried out during the TEJO85 campaign.

Salinity

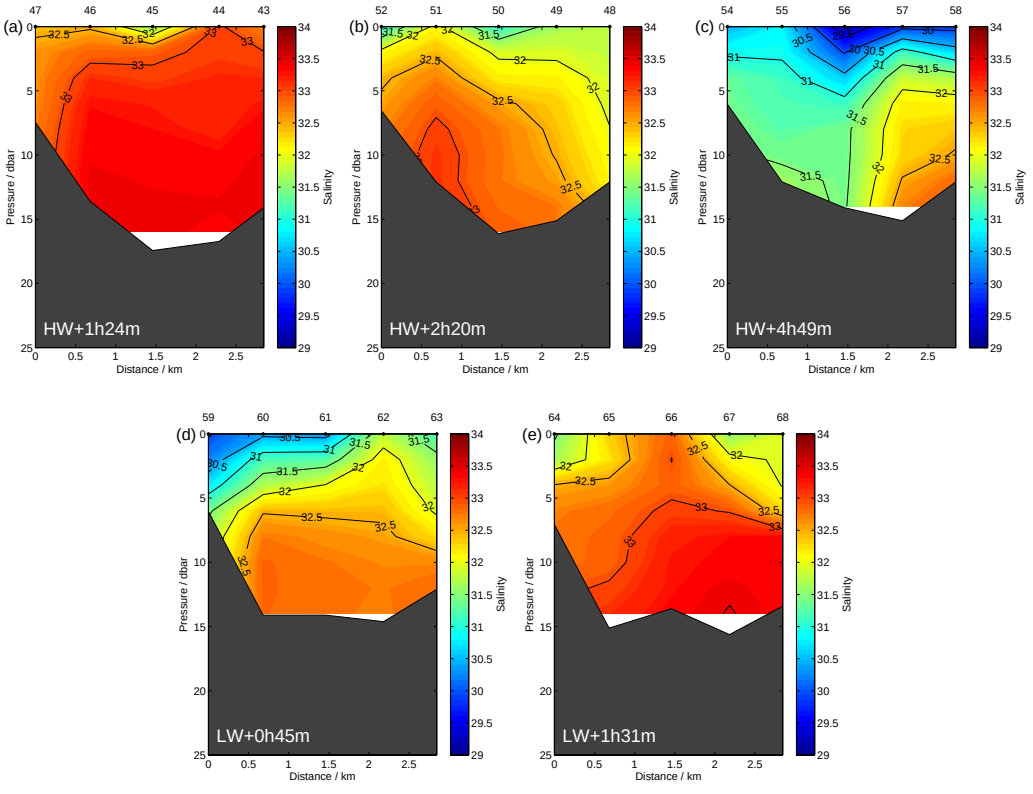

Figure B.16 – Transversal sections of salinity obtained in the inner bay – section ‘sp19tr’.

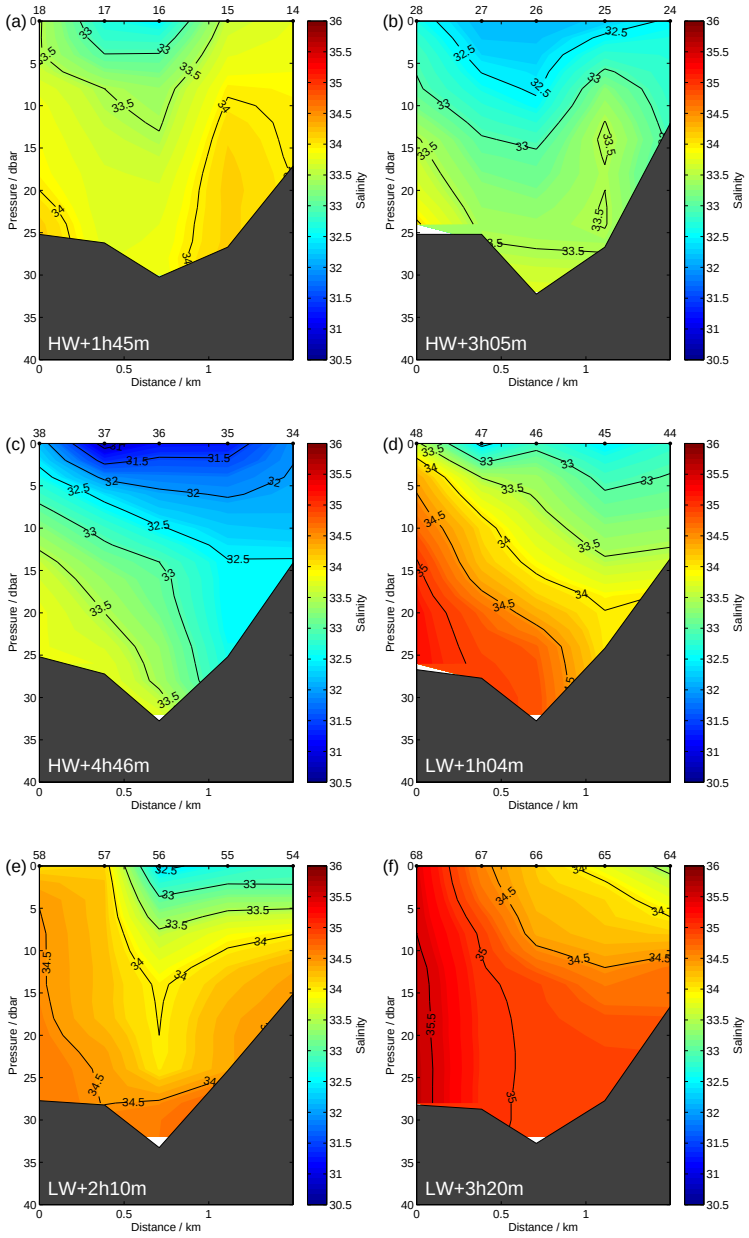

Figure B.17 – Transversal sections of salinity obtained in the inlet channel – section 'vo19tr'.

Temperature

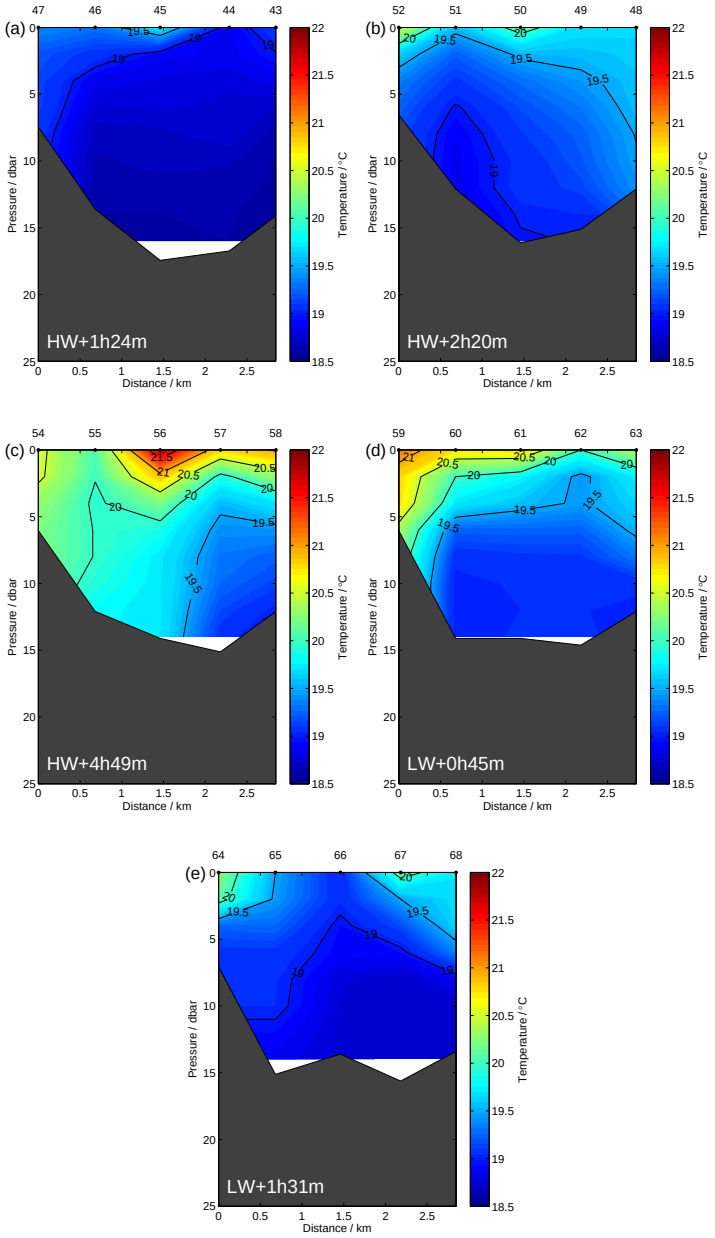

Figure B.18 – Transversal sections of temperature obtained in the inner bay – section ‘sp19tr’.

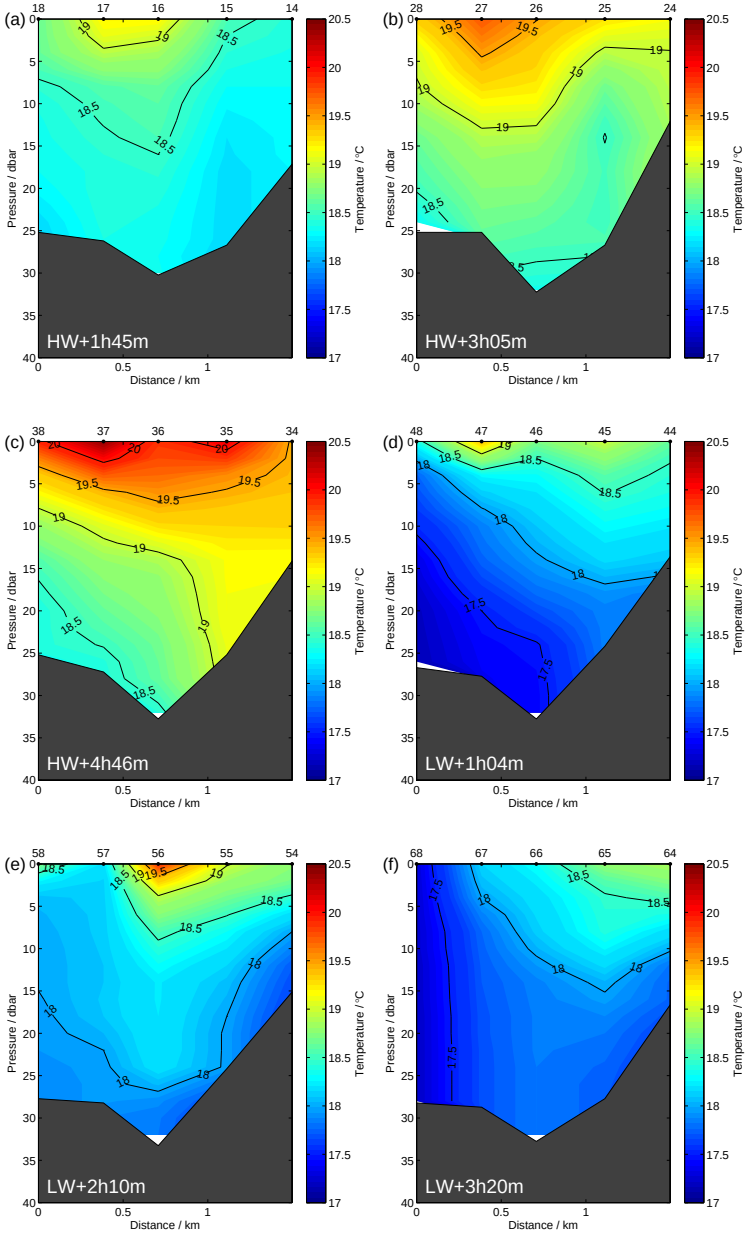

Figure B.19 – Transversal sections of temperature obtained in the inlet channel – section 'vo19tr'.

B.4.3 TEJO85 fixed stations

Fixed stations consisted in several repetitions of salinity and temperature profiles, which are represented as temporal vertical distributions. The locations of the stations are given in an inset on the figures. The date and start time of each station, relative to the former tidal peak, are also presented.

Salinity

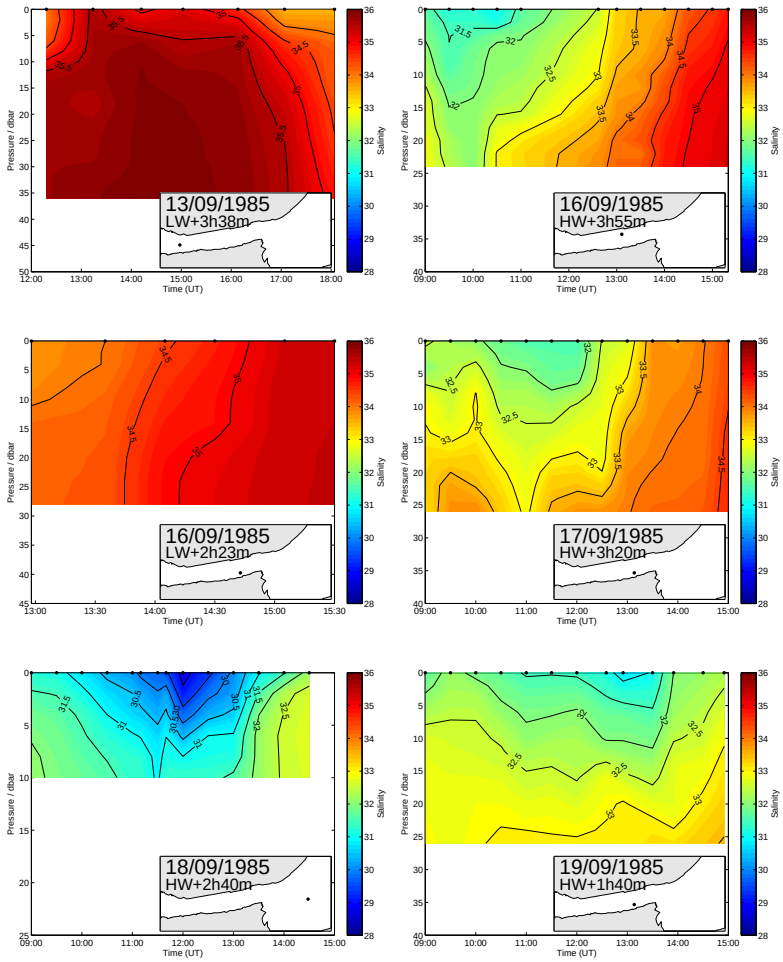

Figure B.20 – Time sections of salinity obtained during the TEJO85 campaign.

Temperature

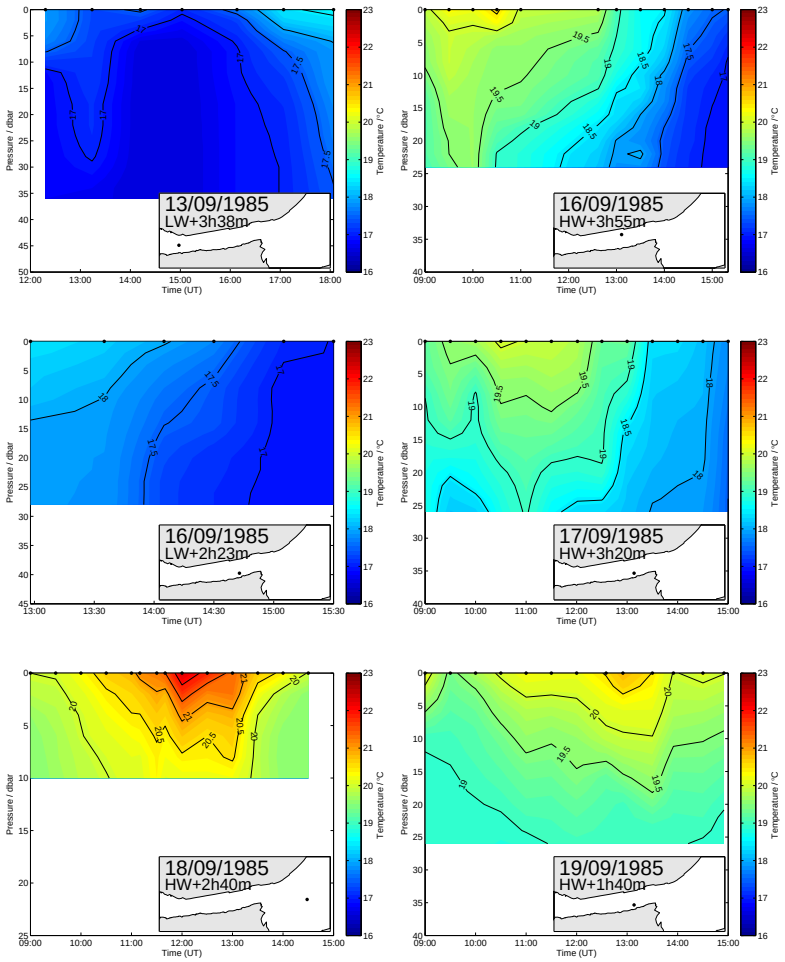

Figure B.21 – Time sections of temperature obtained during the TEJO85 campaign.

B.4.4 TEJO88/1 longitudinal sections

The locations of the longitudinal sections are given in an inset on the figures. The date and start time of each section, relative to the former tidal peak, are also presented. The numbers in the top horizontal axis identify the stations and the interior of the estuary is on the right side of the figure.

Salinity

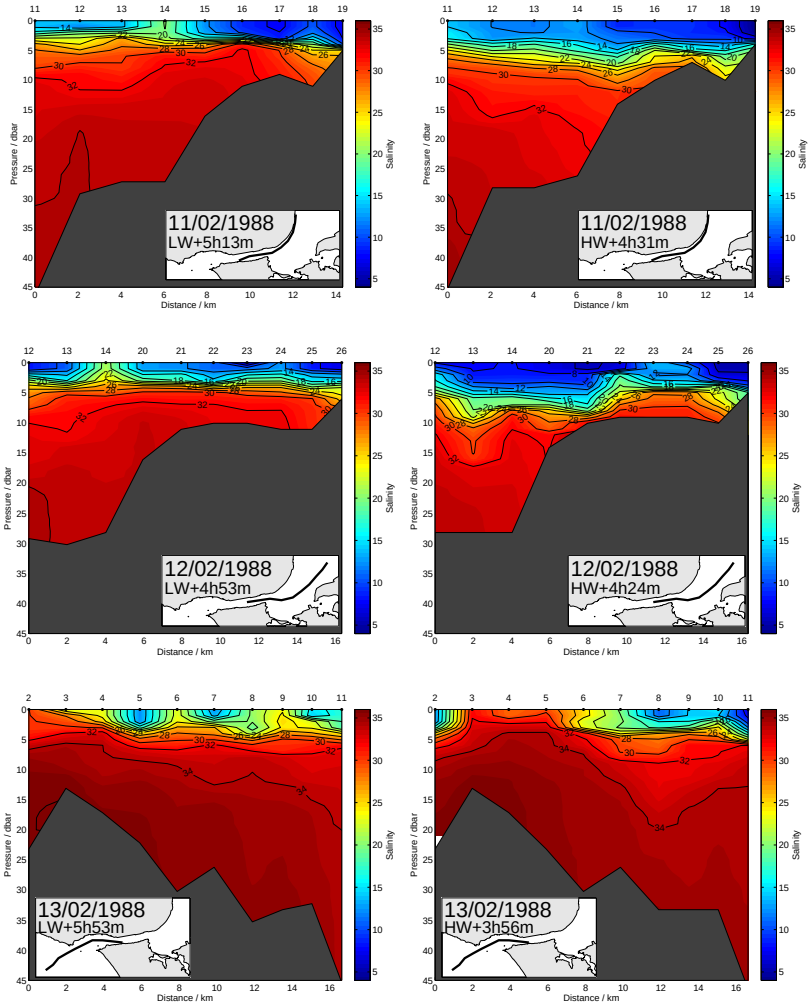

Figure B.22 – Longitudinal sections of salinity obtained during the TEJO88/1 campaign.

Temperature

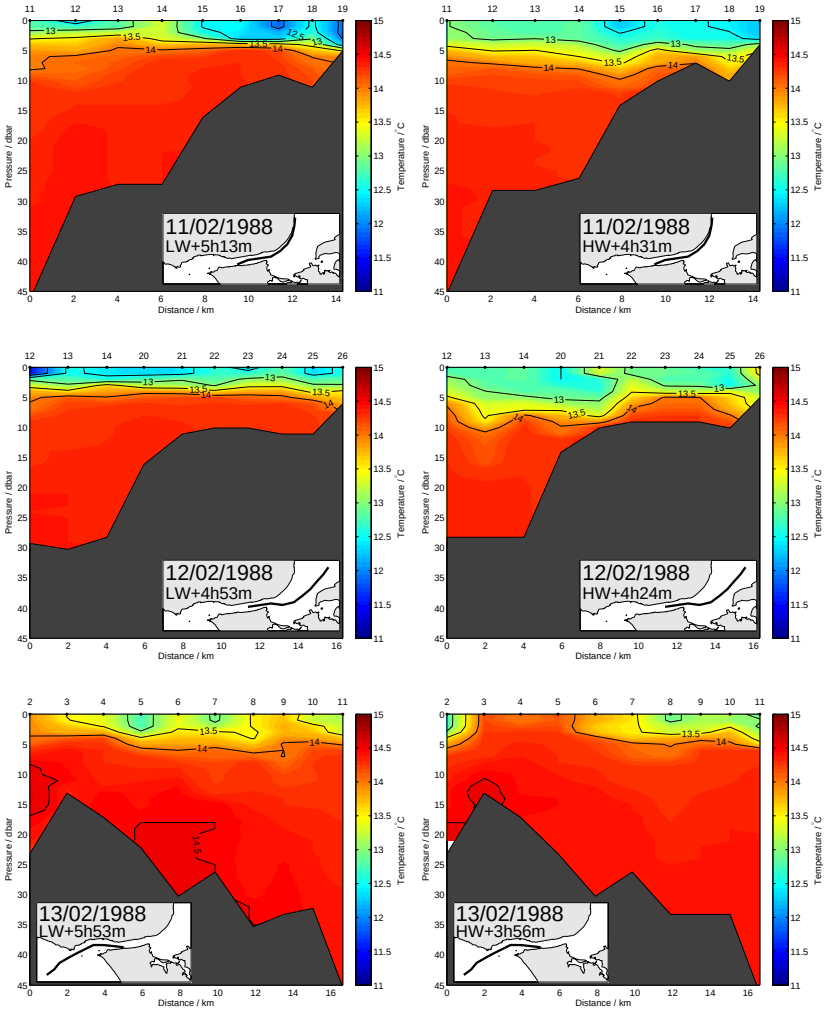

Figure B.23 – Longitudinal sections of temperature obtained during the TEJO88/1 campaign.

B.4.5 TEJO88/1 fixed stations

Fixed stations consisted in several repetitions of salinity and temperature profiles, which are represented as temporal vertical distributions. The locations of the stations are given in an inset on the figures. The date and start time of each station, relative to the former tidal peak, are also presented.

Salinity

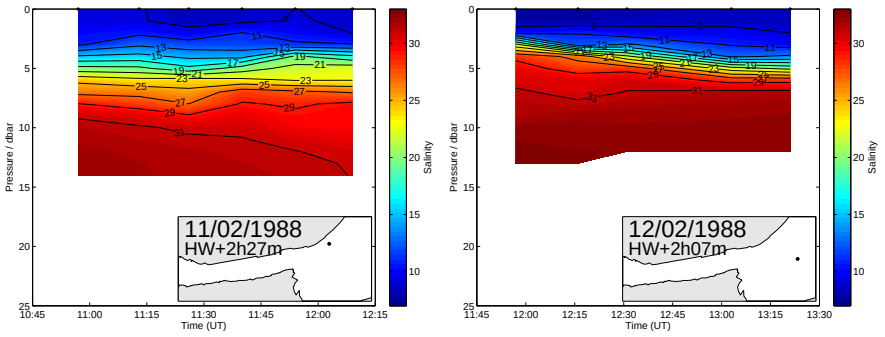

Figure B.24 – Time sections of salinity obtained during the TEJO88/1 campaign.

Temperature

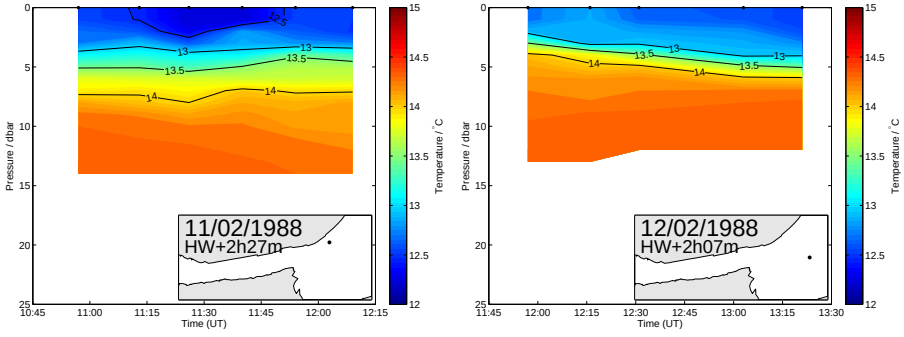

Figure B.25 – Time sections of temperature obtained during the TEJO88/1 campaign.

B.5 Thermohaline and current velocity sections

This section presents the vertical distributions of salinity, temperature and along-channel current velocity along the two transversal sections performed during the observational campaigns INTAGUS. The locations of the sections are represented in Fig. B.26.

Sections are grouped by campaign: INTAGUS07/1, INTAGUS07/2, INTAGUS08/1 and INTAGUS08/2. The start time of each section, relative to the former tidal peak, is presented in the corresponding figure. In the top horizontal axis, the subscript number in each station letter indicates the repetition number of that station and the right side of the figure corresponds to the northern margin.

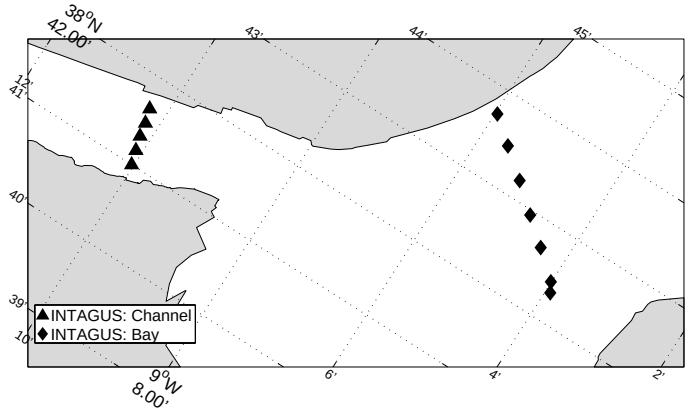

Figure B.26 – Location of the transversal sections carried out during the INTAGUS campaigns.

B.5.1 INTAGUS07/1 sections

Salinity

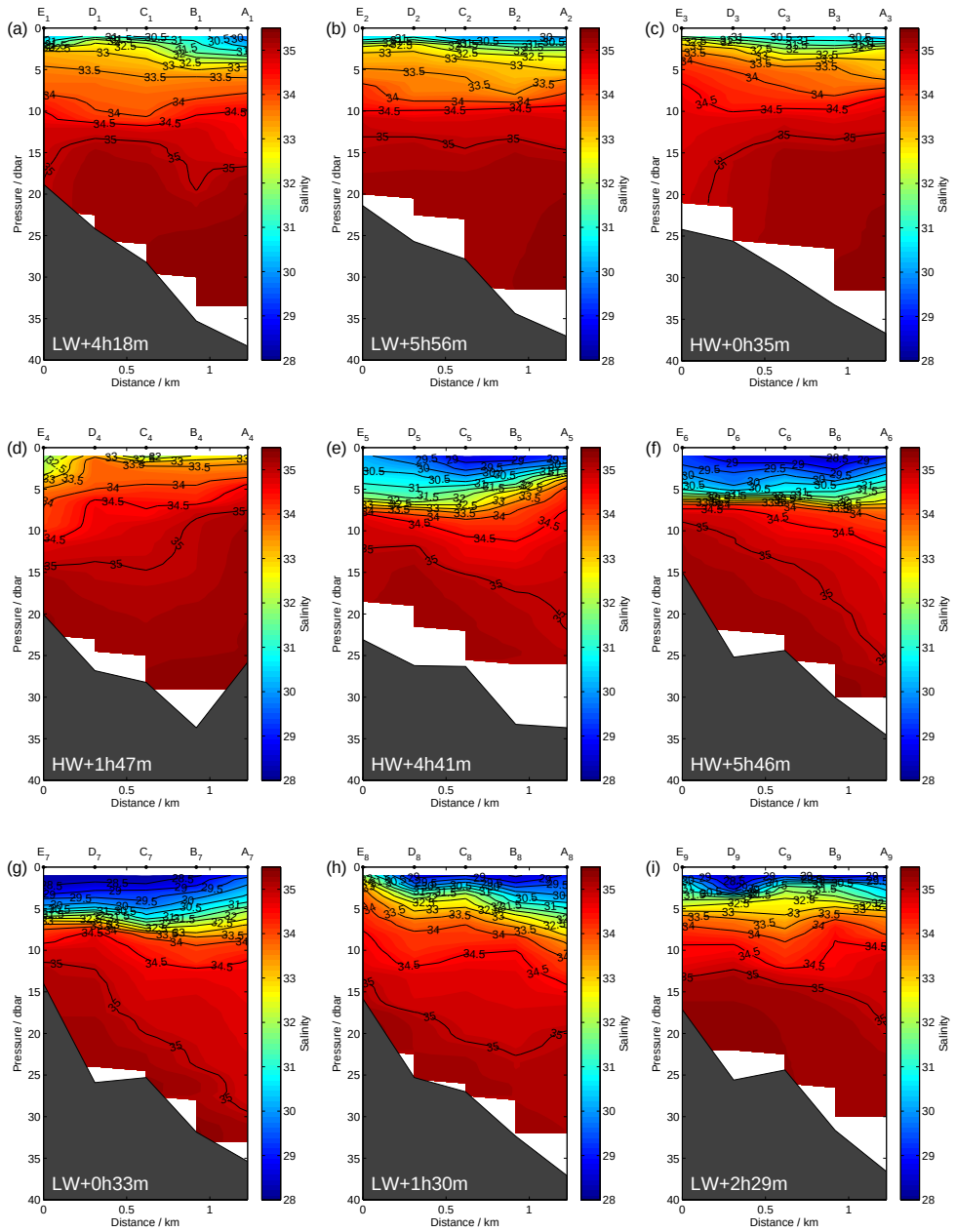

Figure B.27 – Transversal sections of salinity obtained in the inlet channel.

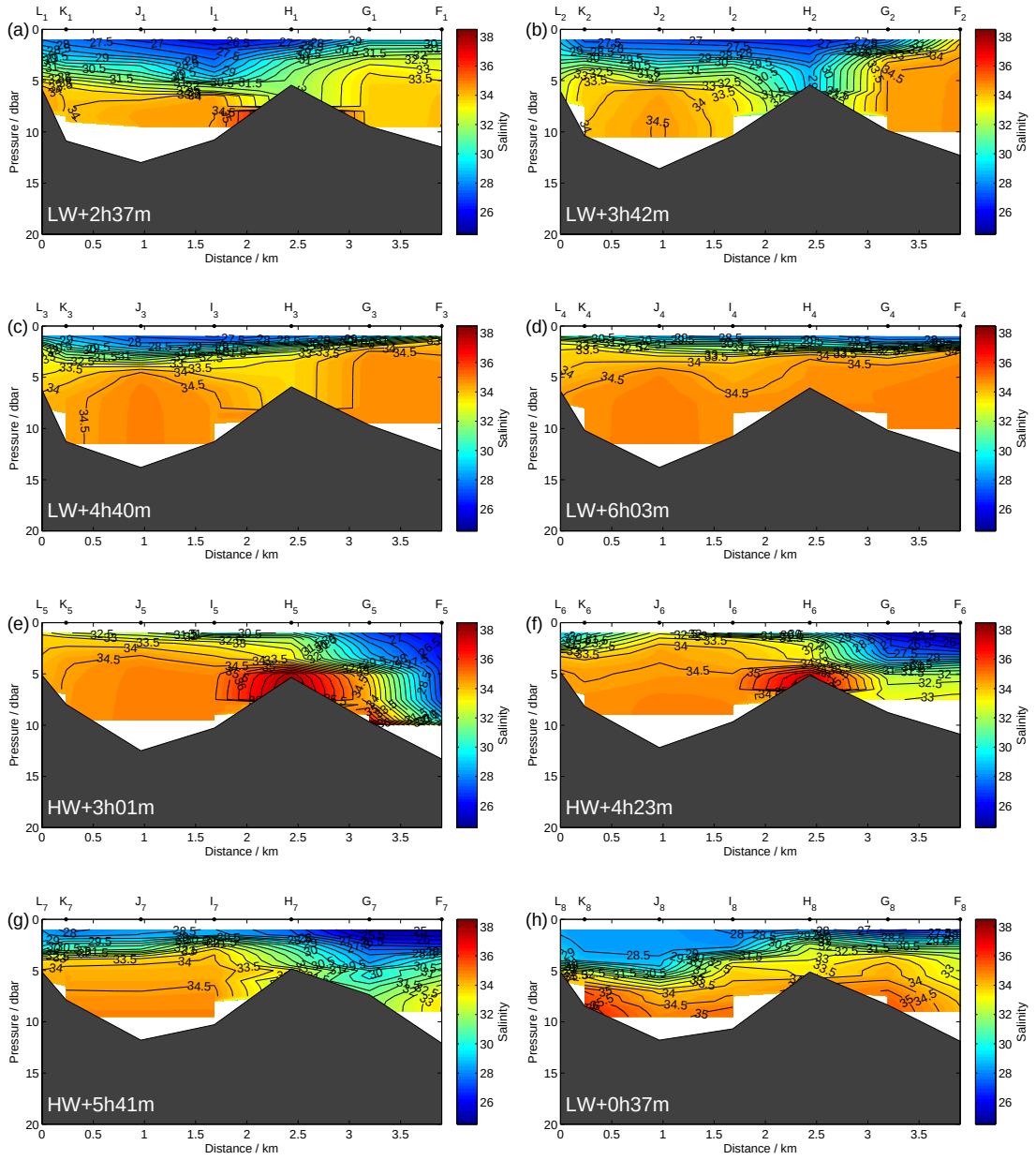

Figure B.28 – Transversal sections of salinity obtained in the inner bay.

Temperature

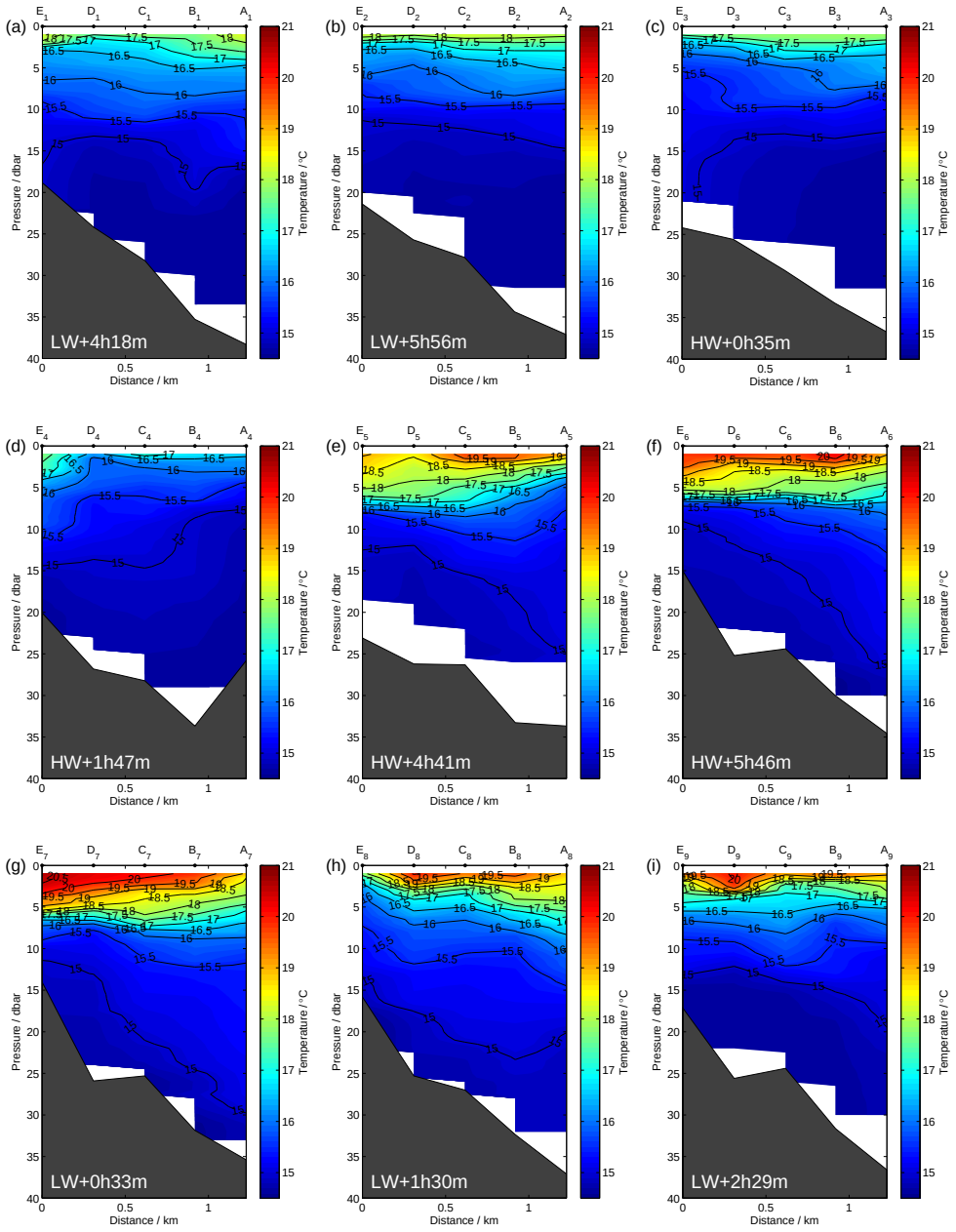

Figure B.29 – Transversal sections of temperature obtained in the inlet channel.

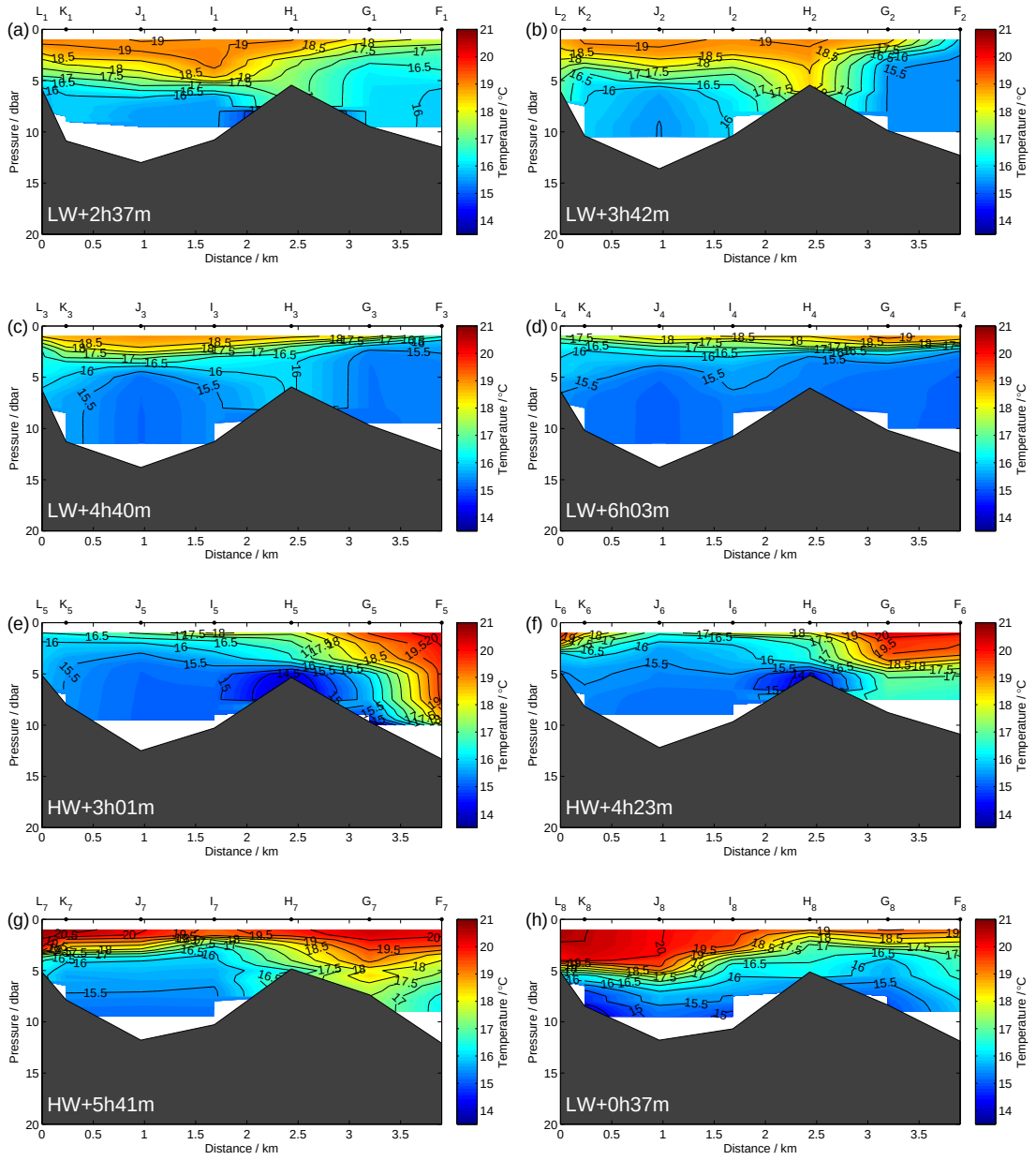

Figure B.30 – Transversal sections of temperature obtained in the inner bay.

Along-channel current velocity

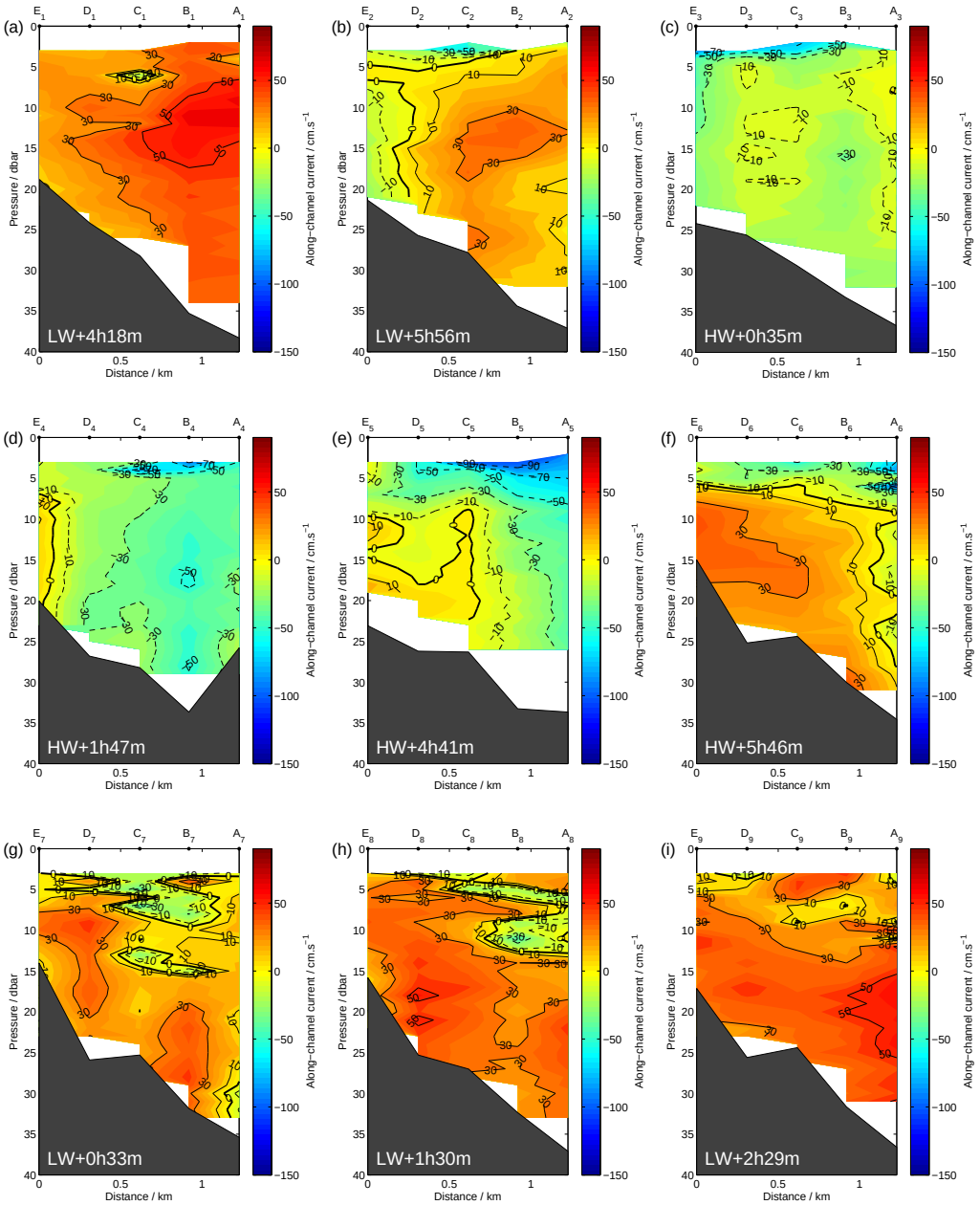

Figure B.31 – Transversal sections of along-channel current velocity obtained in the inlet channel.

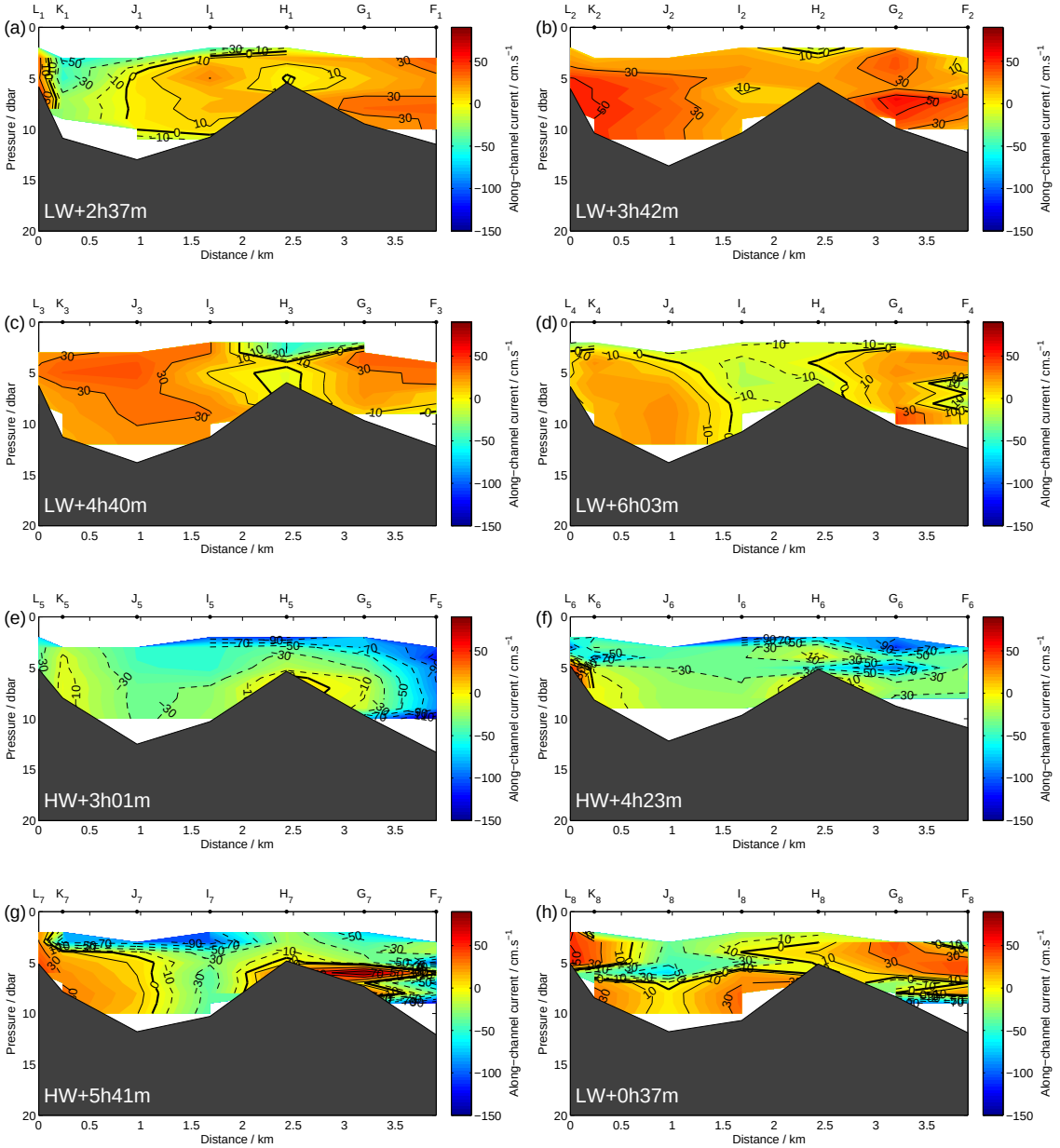

Figure B.32 – Transversal sections of along-channel current velocity obtained in the inner bay.

B.5.2 INTAGUS07/2 sections

Salinity

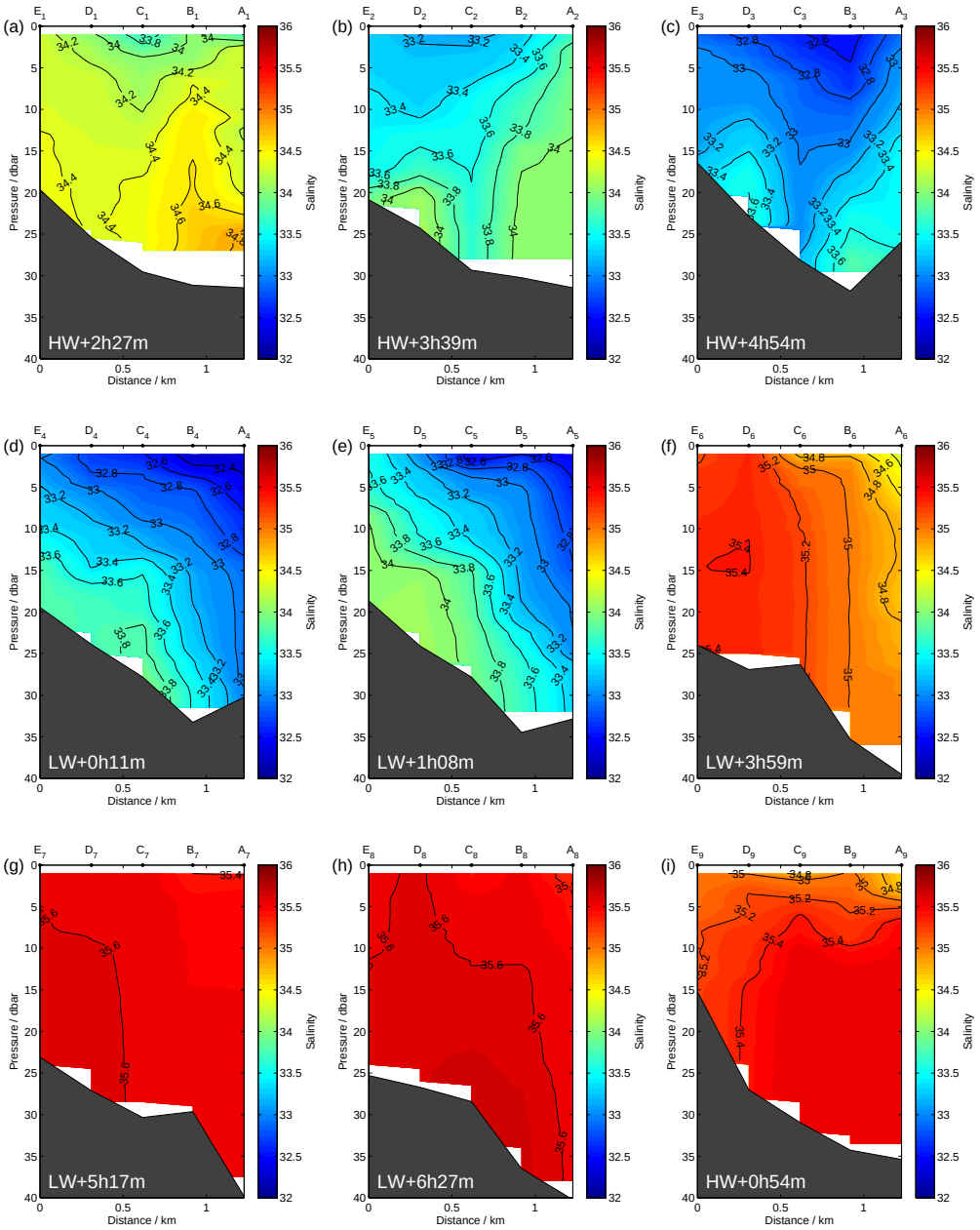

Figure B.33 – Transversal sections of salinity obtained in the inlet channel.

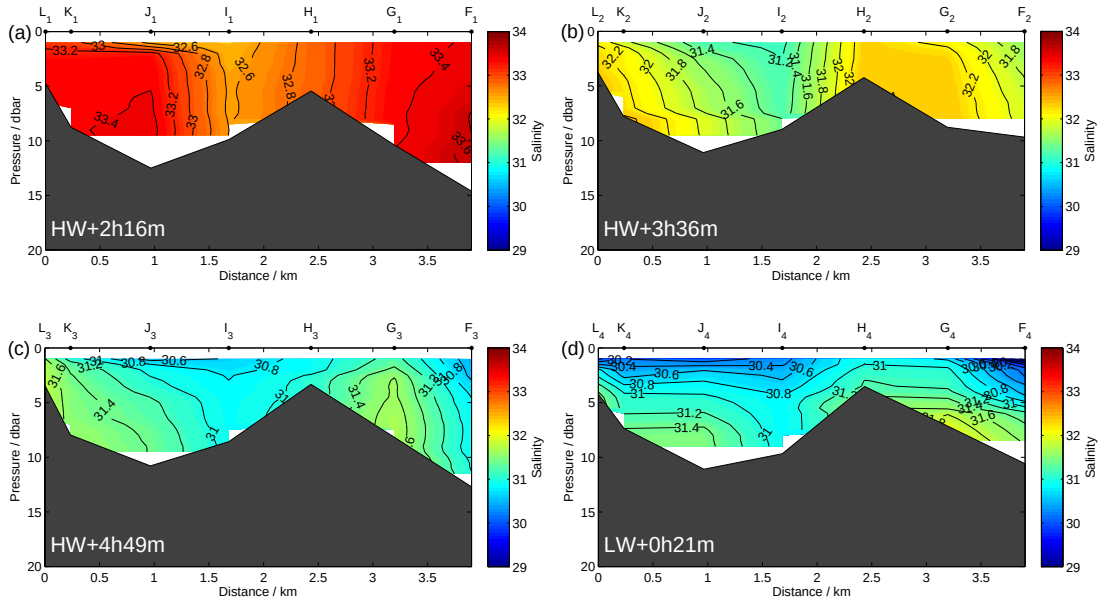

Figure B.34 – Transversal sections of salinity obtained in the inner bay.

Temperature

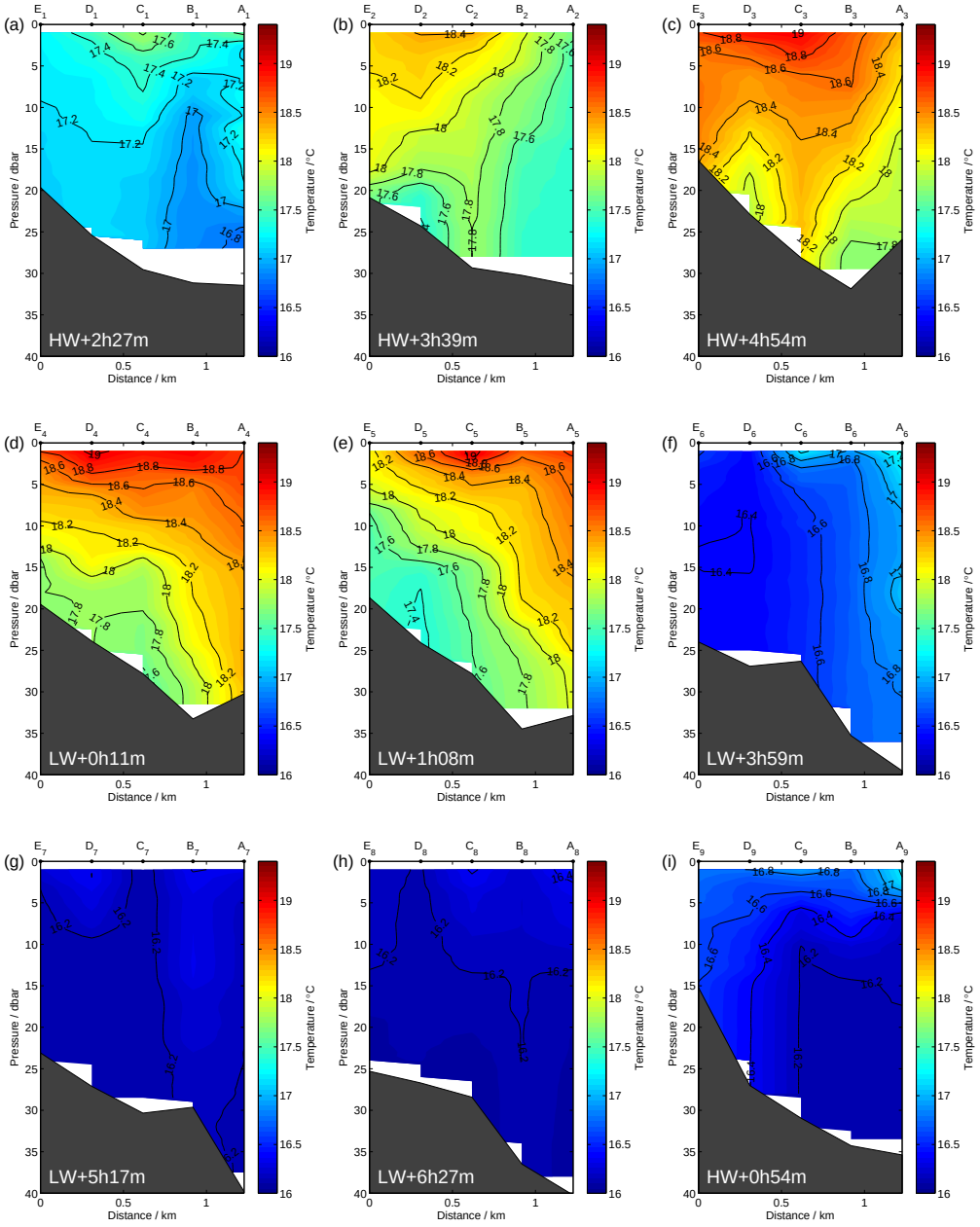

Figure B.35 – Transversal sections of temperature obtained in the inlet channel.

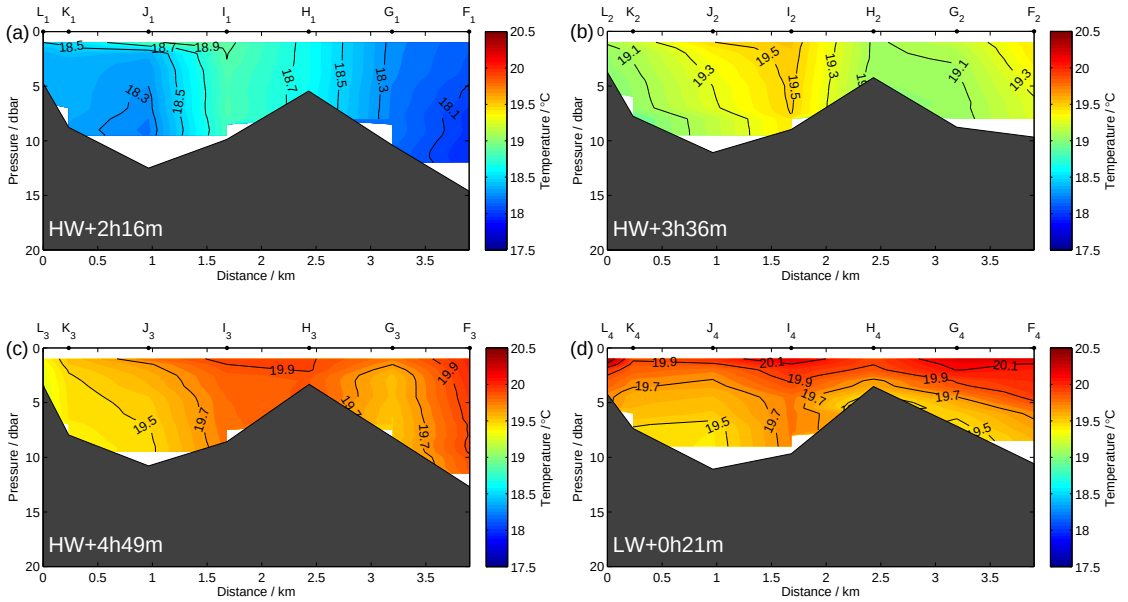

Figure B.36 – Transversal sections of temperature obtained in the inner bay.

Along-channel current velocity

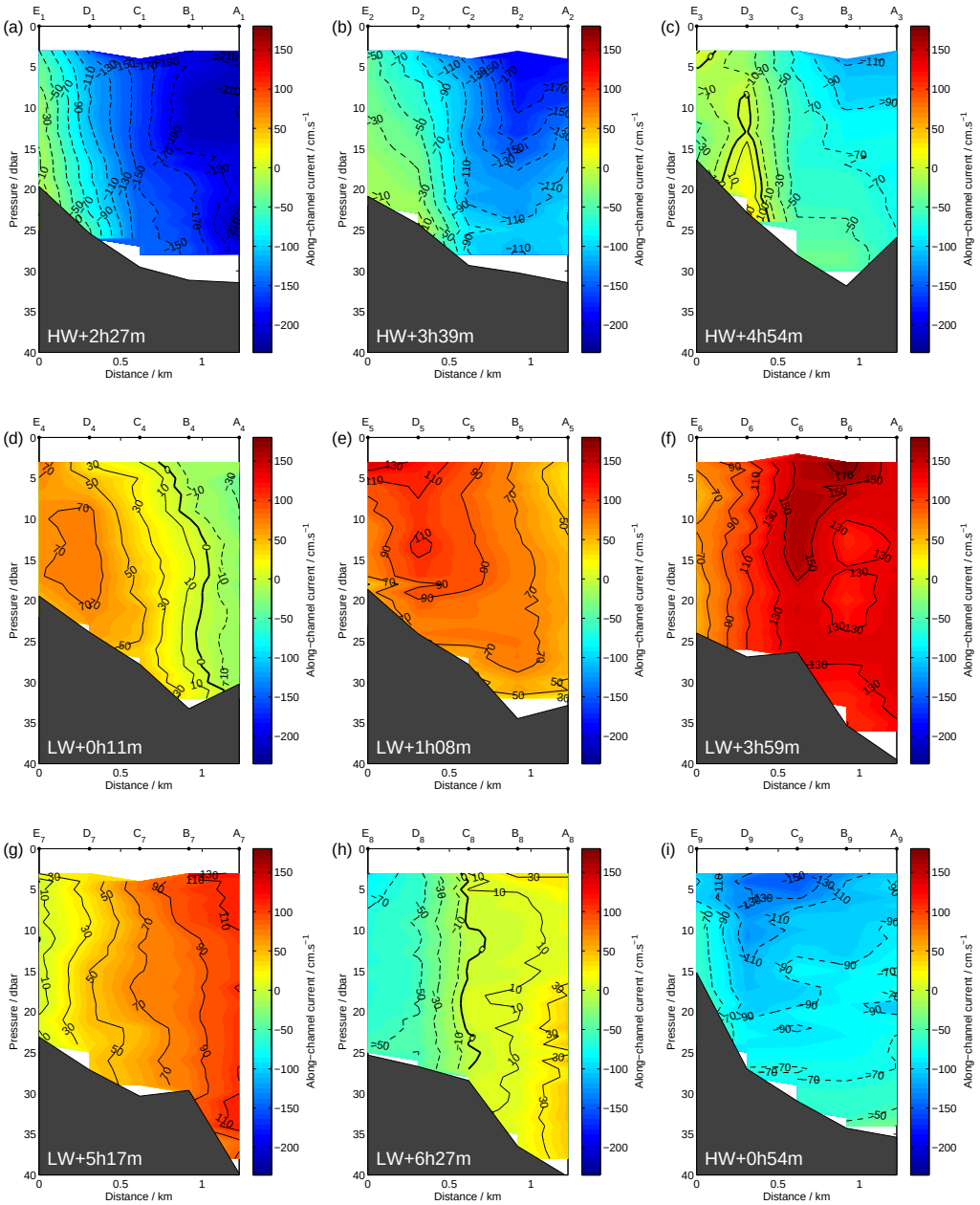

Figure B.37 – Transversal sections of along-channel current velocity obtained in the inlet channel.

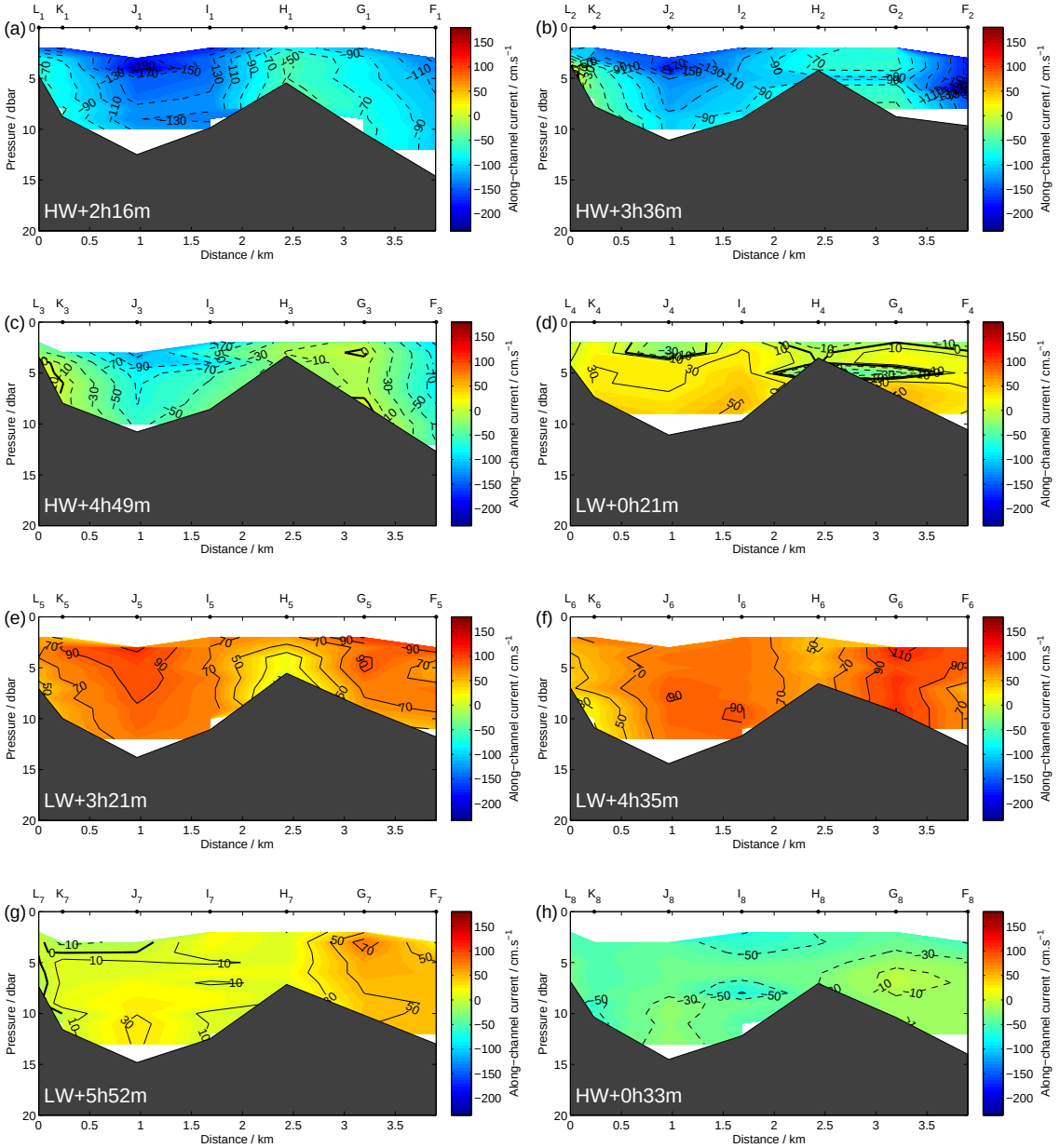

Figure B.38 – Transversal sections of along-channel current velocity obtained in the inner bay.

B.5.3 INTAGUS08/1 sections

Salinity

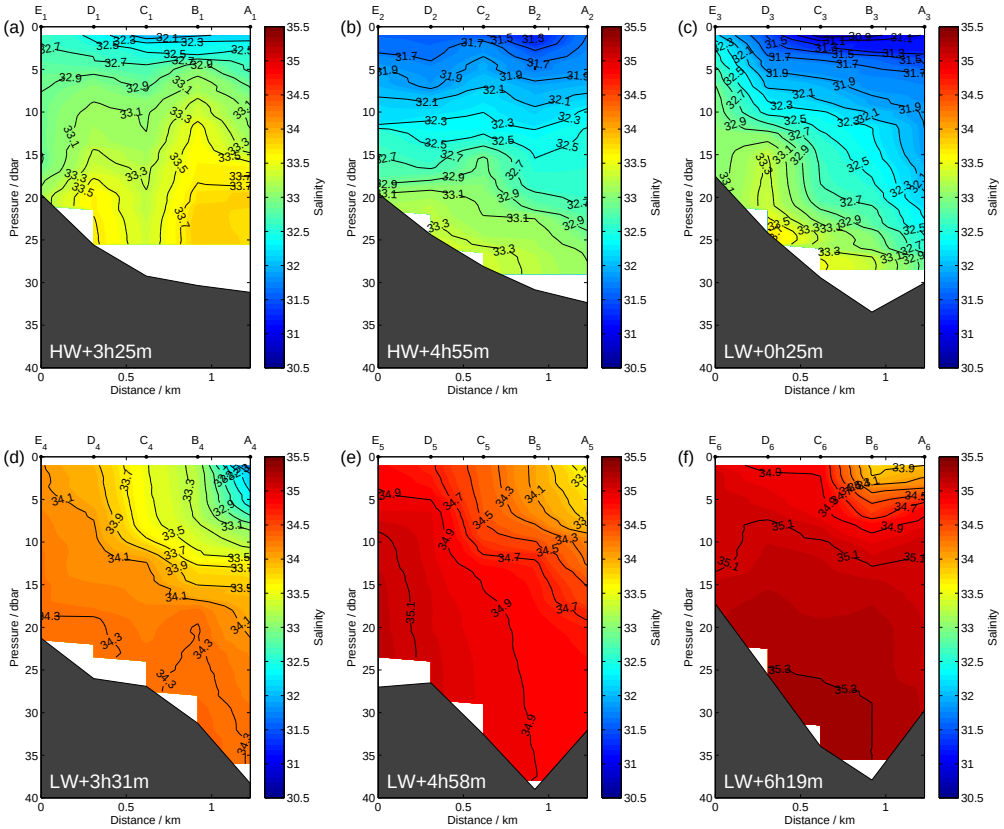

Figure B.39 – Transversal sections of salinity obtained in the inlet channel.

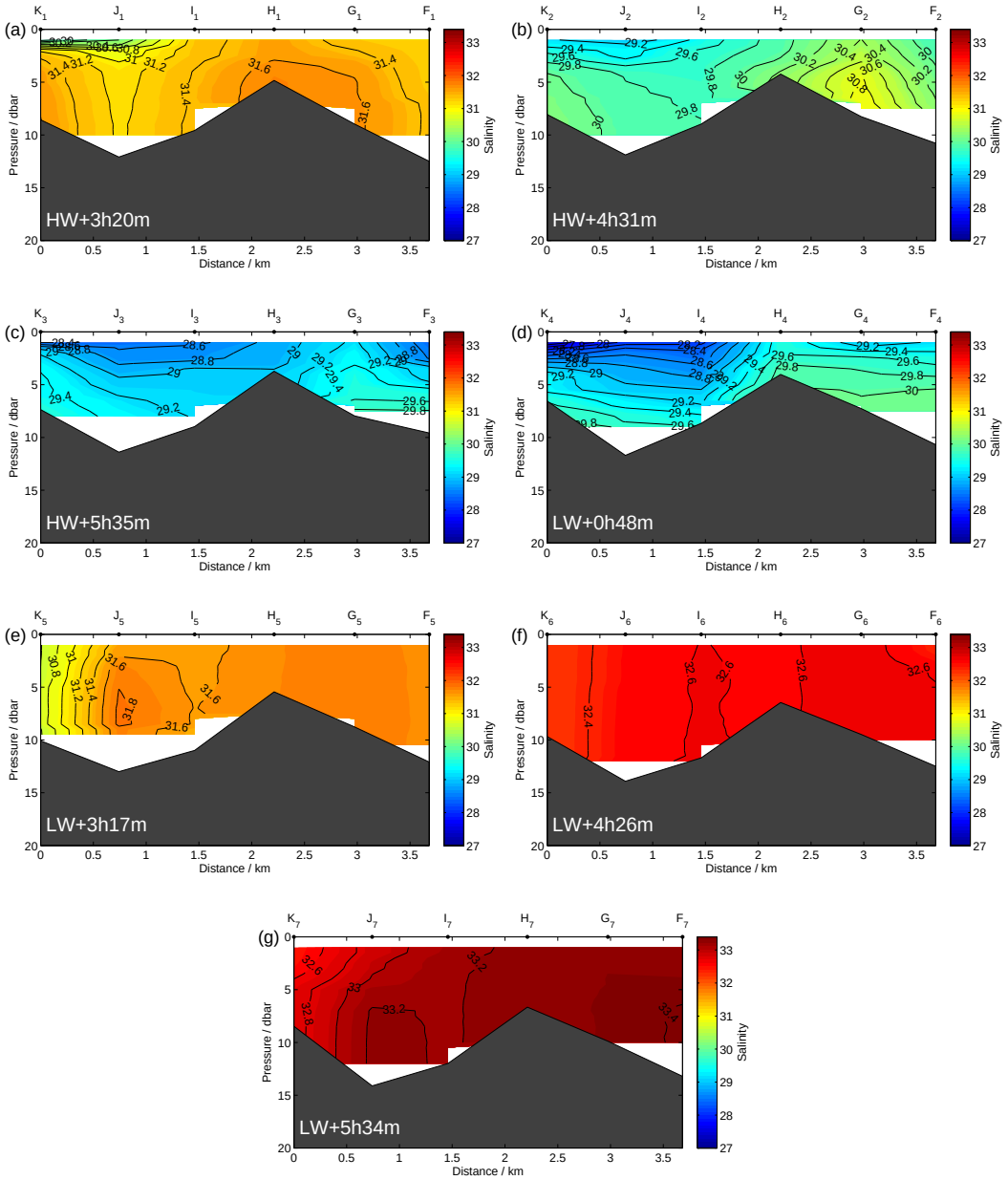

Figure B.40 – Transversal sections of salinity obtained in the inner bay.

Temperature

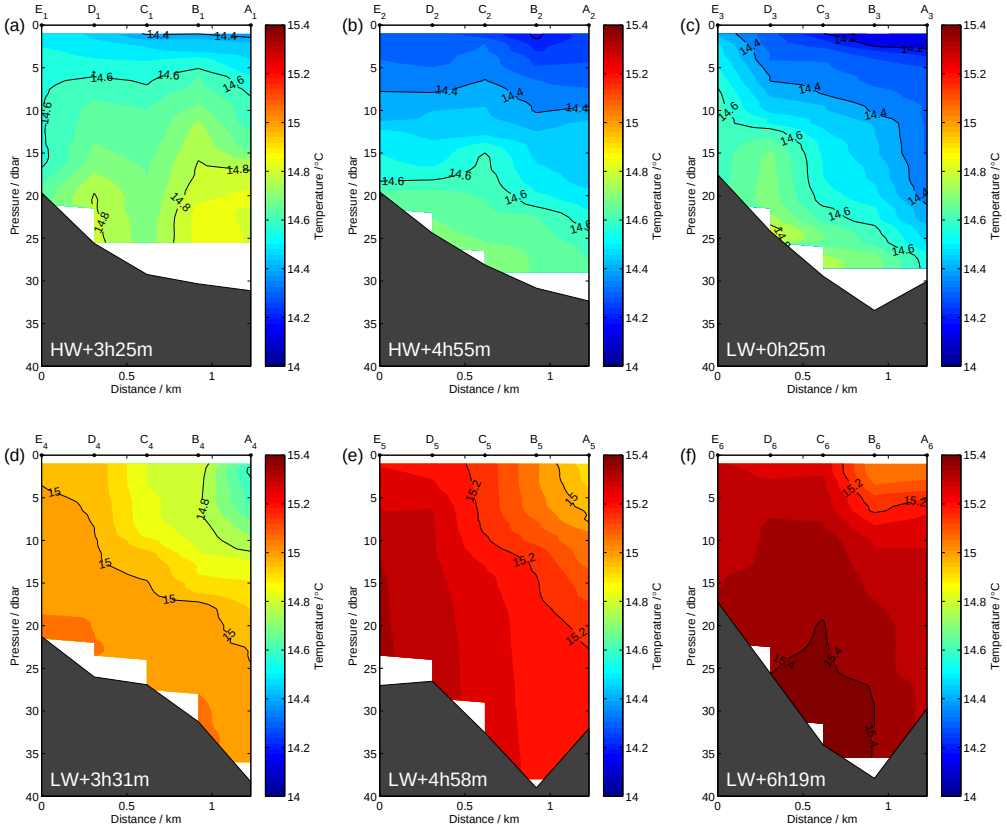

Figure B.41 – Transversal sections of temperature obtained in the inlet channel.

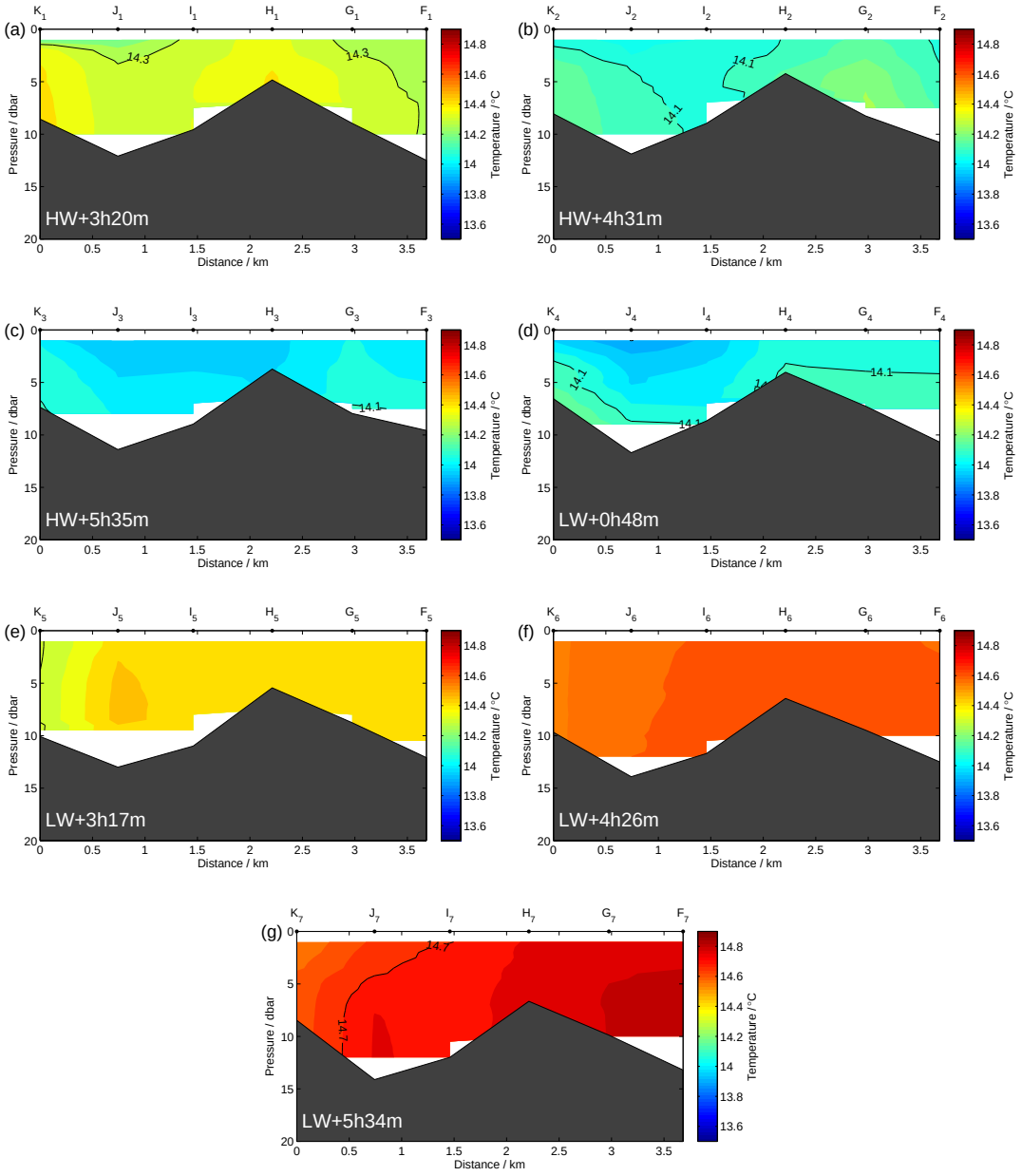

Figure B.42 – Transversal sections of temperature obtained in the inner bay.

Along-channel current velocity

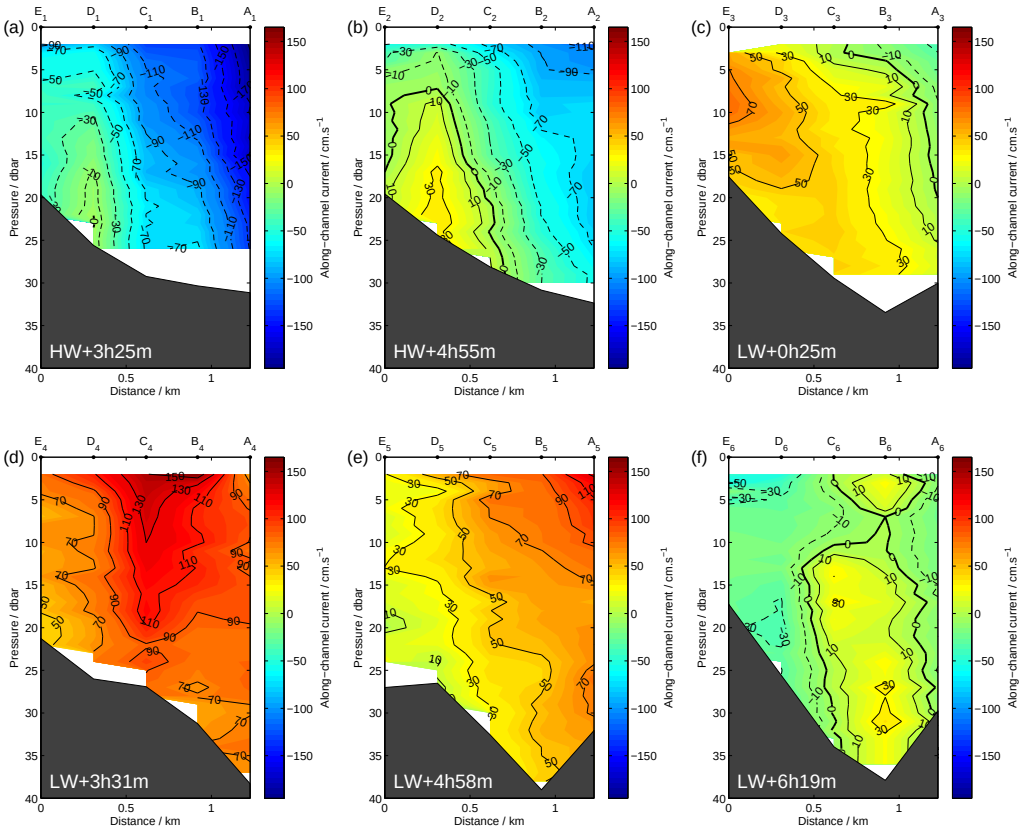

Figure B.43 – Transversal sections of along-channel current velocity obtained in the inlet channel.

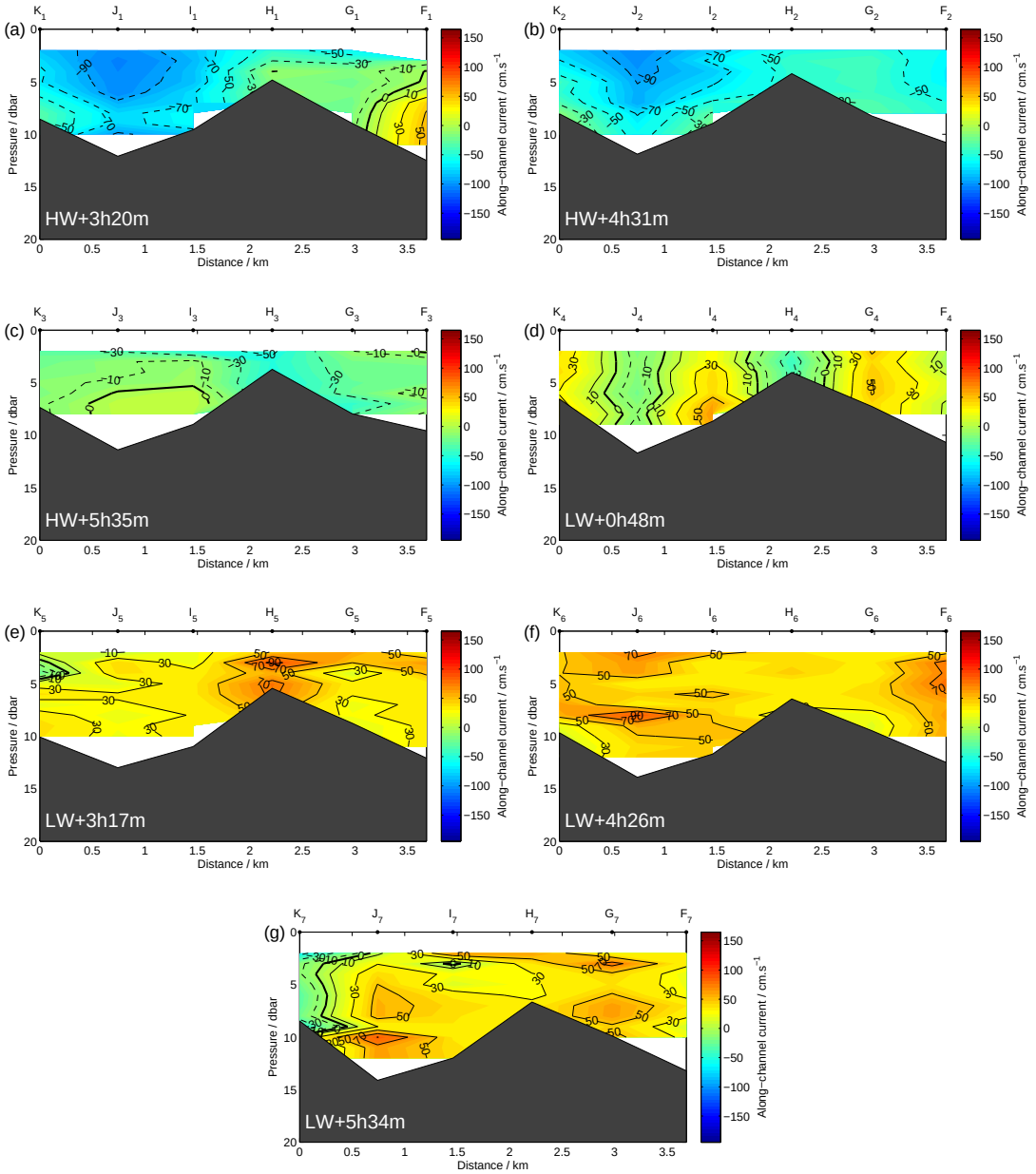

Figure B.44 – Transversal sections of along-channel current velocity obtained in the inner bay.

B.5.4 INTAGUS08/2 sections

Salinity

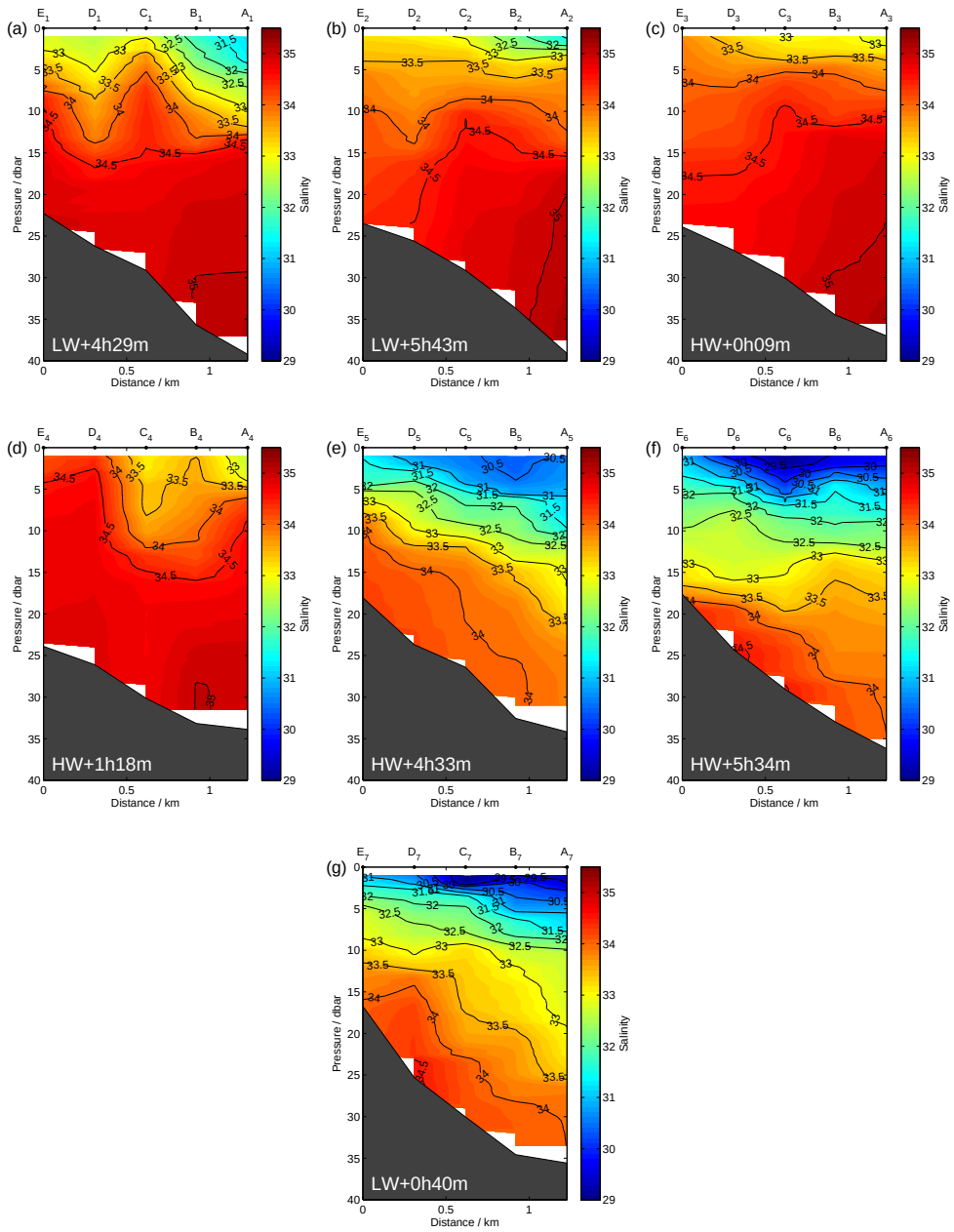

Figure B.45 – Transversal sections of salinity obtained in the inlet channel.

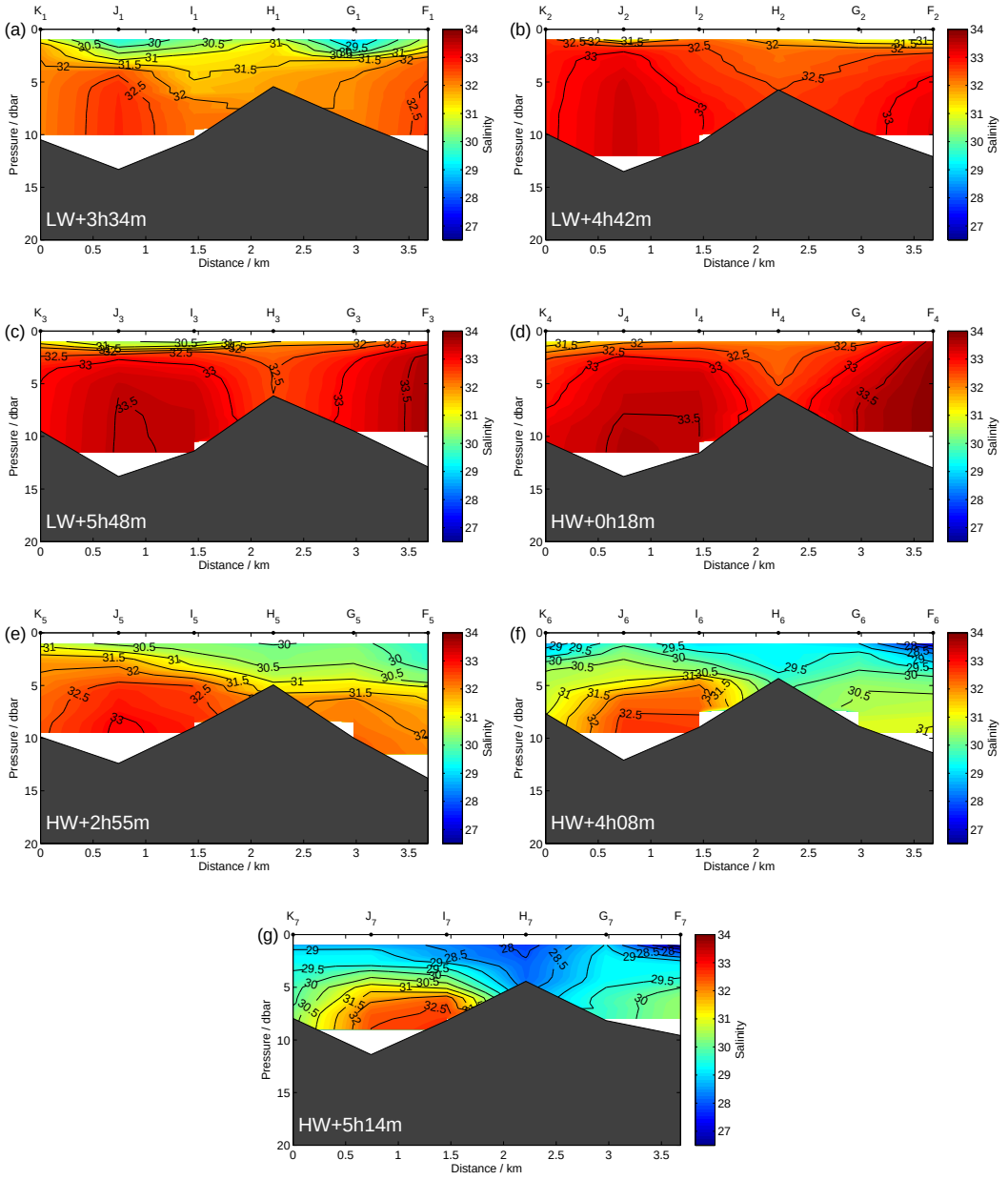

Figure B.46 – Transversal sections of salinity obtained in the inner bay.

Temperature

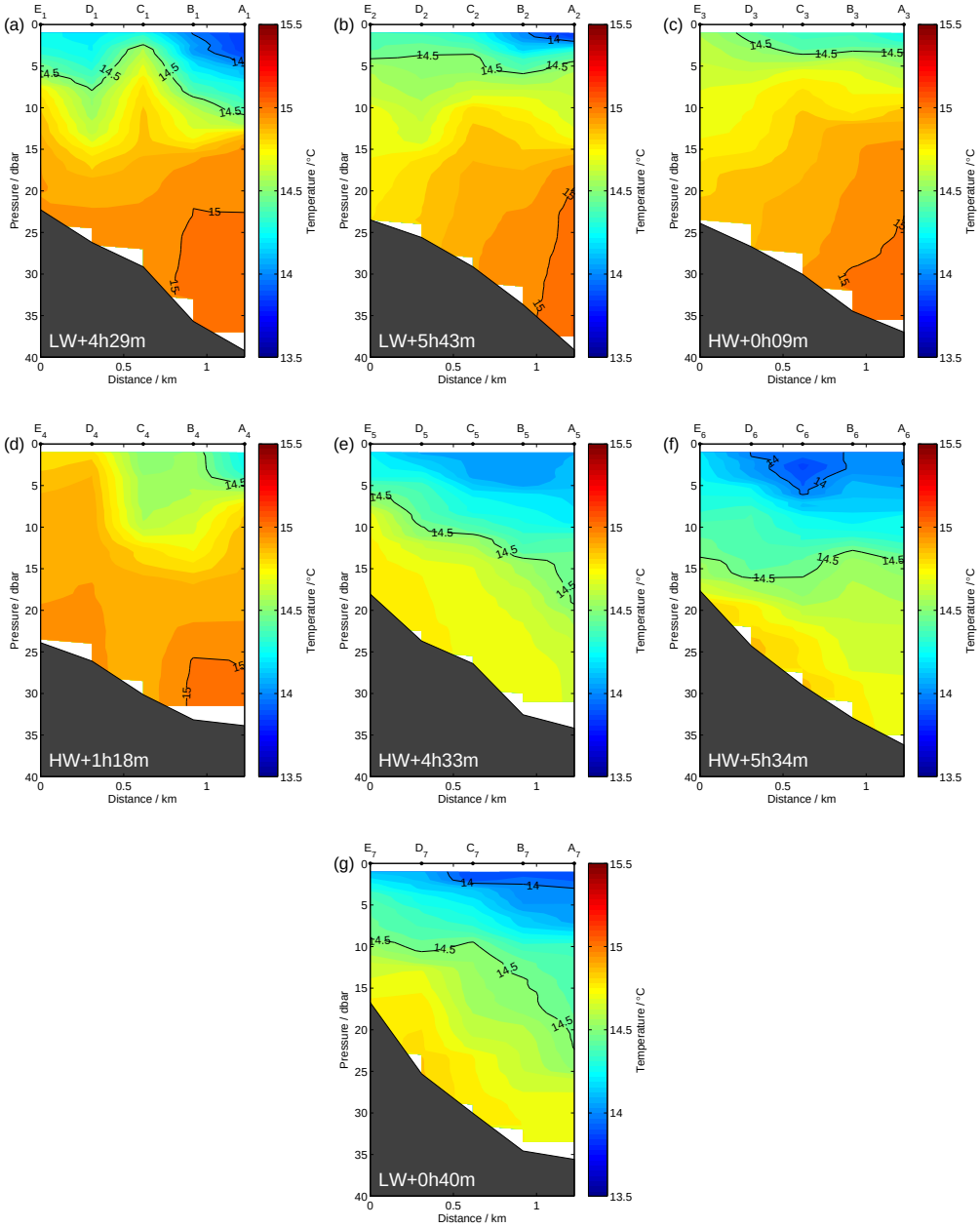

Figure B.47 – Transversal sections of temperature obtained in the inlet channel.

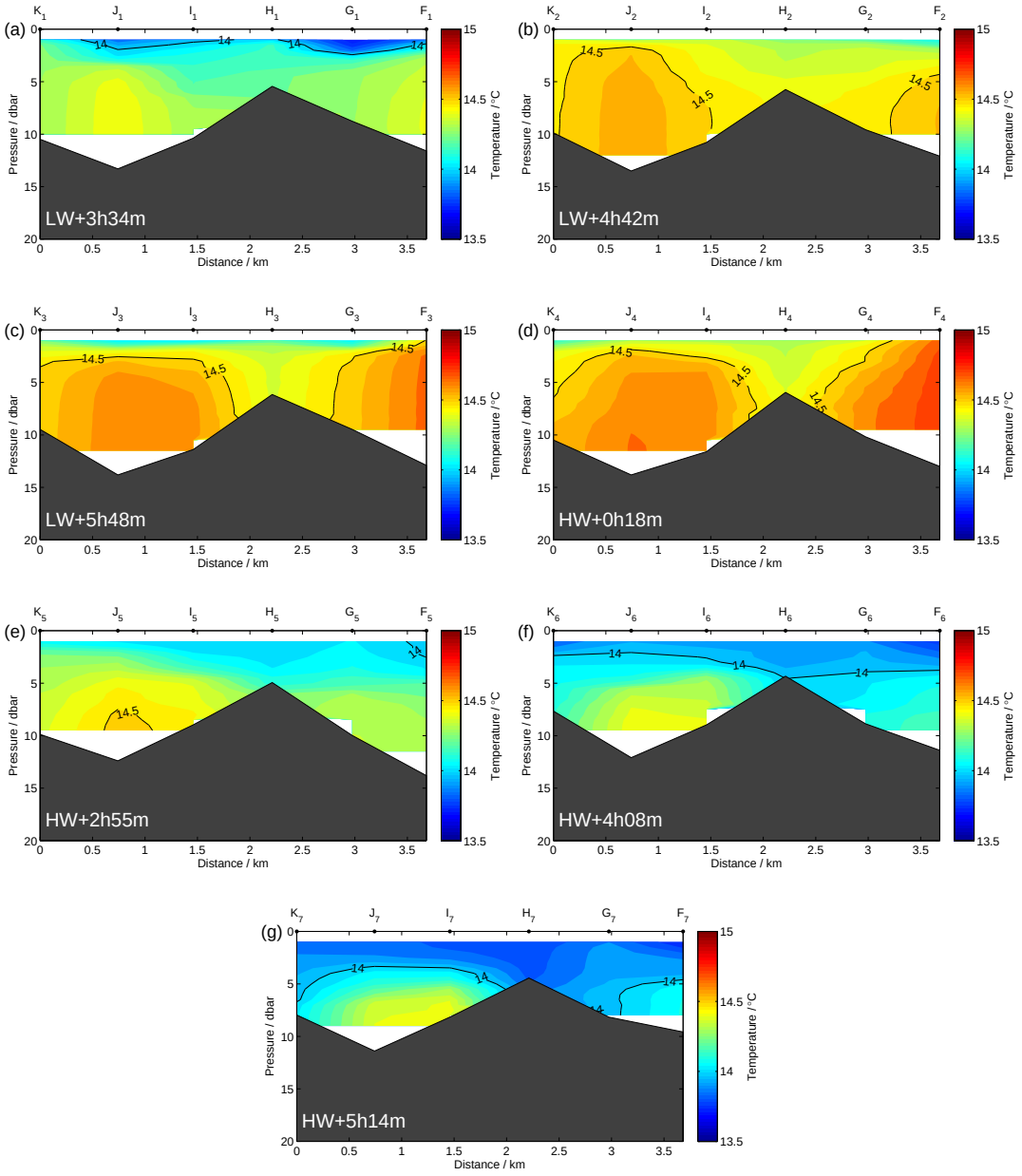

Figure B.48 – Transversal sections of temperature obtained in the inner bay.

Along-channel current velocity

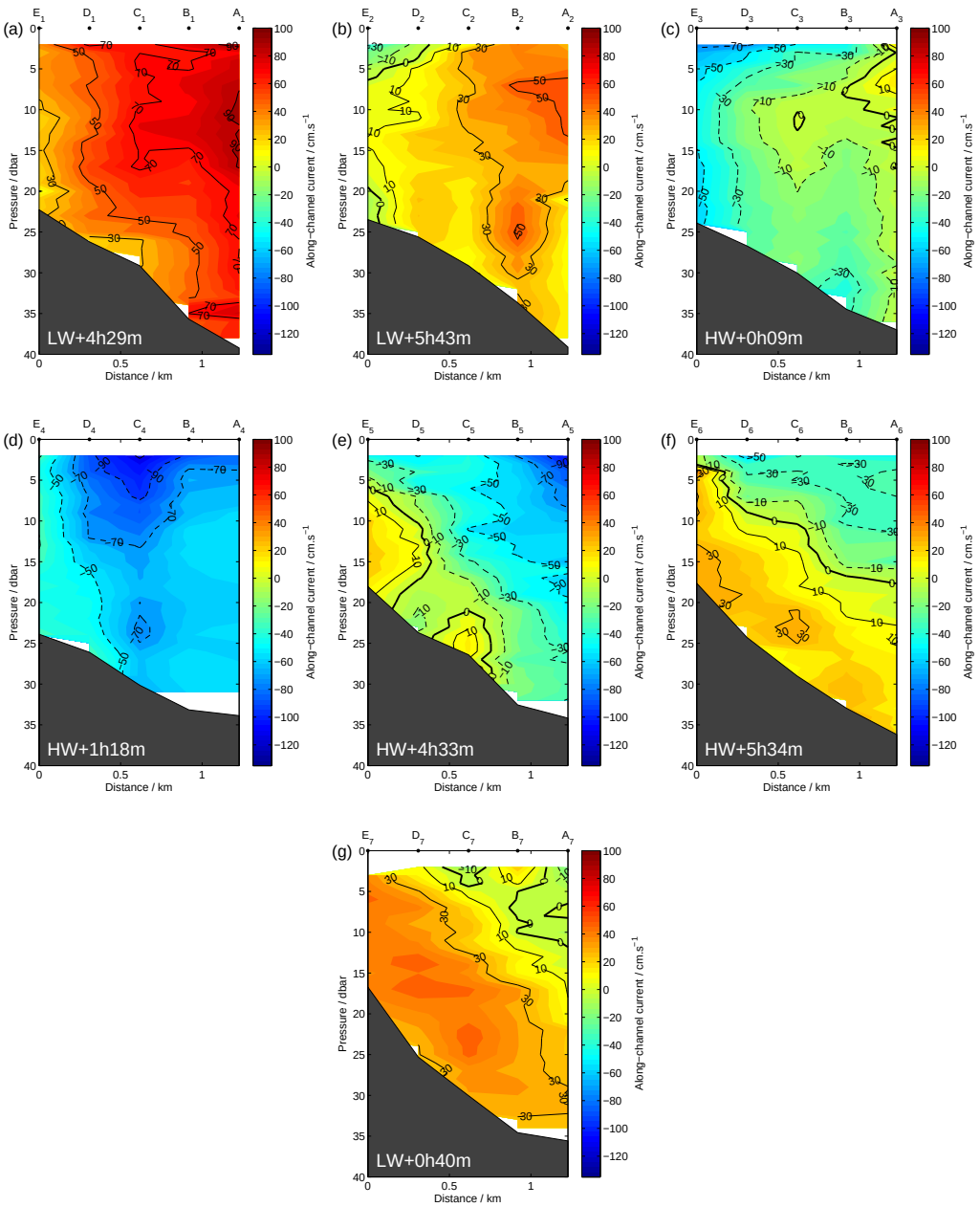

Figure B.49 – Transversal sections of along-channel current velocity obtained in the inlet channel.

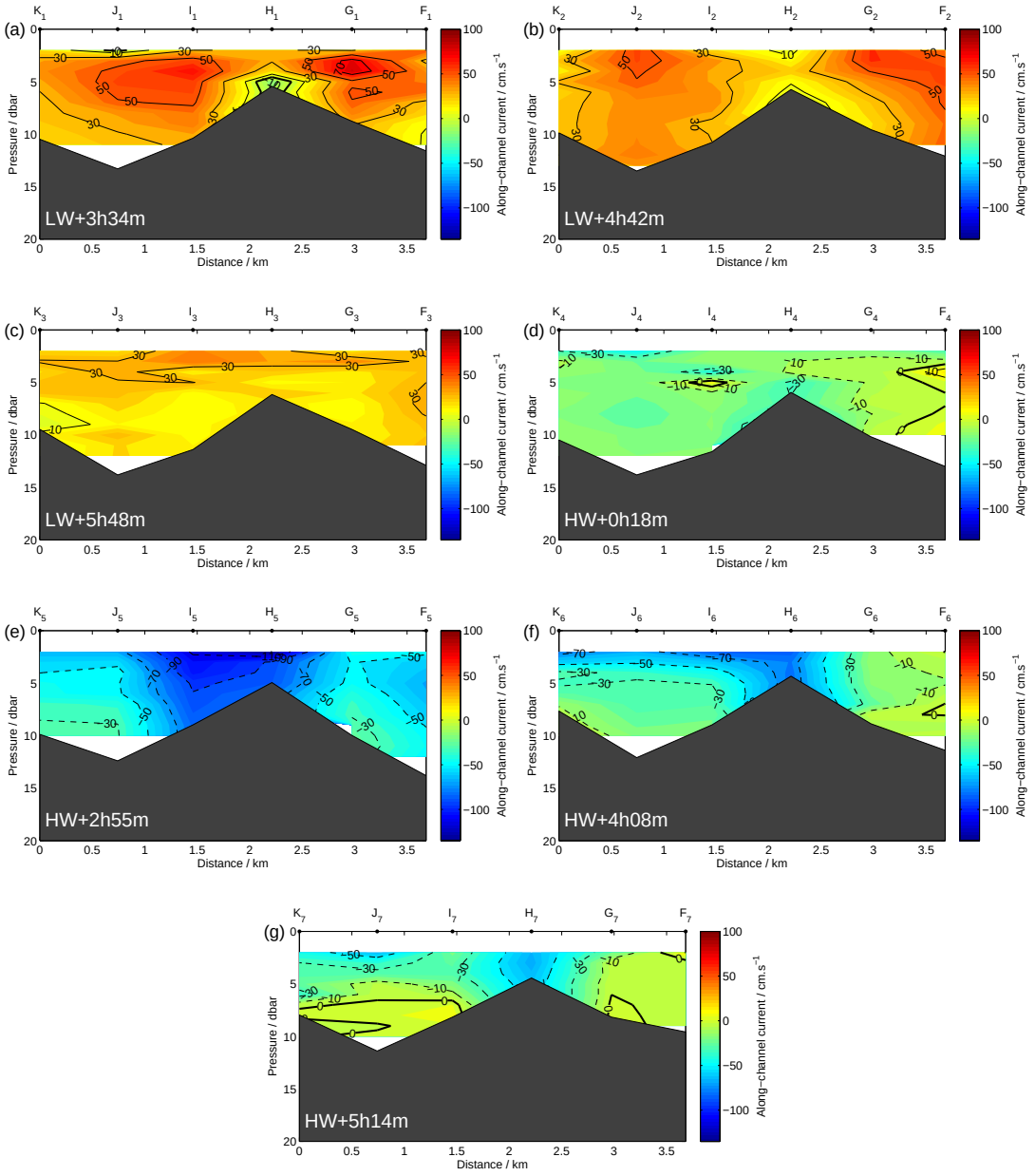

Figure B.50 – Transversal sections of along-channel current velocity obtained in the inner bay.

Appendix C

Tidal chart records

This appendix presents the tidal charts, produced by the analogue gauges located at Cabo Ruivo, Terreiro do Paço and Paço de Arcos. The charts contain the water level evolution for several days. Each chart produced at the Cabo Ruivo gauge contains up to seven days of water level evolution, whereas those produced at the Terreiro do Paço and Paço de Arcos gauges contain up to 14 days of water level records each.

The tables present the period of observations corresponding to each chart, which is identified by its origin site initials (e.g. **cr** for Cabo Ruivo), the year of the observations (**85** for September 1985, **881** for February 1988, **882** for August 1988 and **89** for November 1989) and the number of the chart. The figures show the charts that have been digitalised.

	Tidal chart	Period of observations		Tidal chart	Period of observations
Sep1985	cr85_1	27/08 – 03/09/1985	Feb1988	cr881_1	26/01 – 02/02/1988
	cr85_2	03/09 – 11/09/1985		cr881_2	02/02 – 09/02/1988
	cr85_3	11/09 – 17/09/1985		cr881_3	09/02 – 15/02/1988
	cr85_4	17/09 – 25/09/1985		cr881_4	15/02 – 23/02/1988
	cr85_5	25/09 – 01/10/1985		cr881_5	23/02 – 01/03/1988
Aug1988	cr882_1	26/07 – 02/08/1988	Nov1989	cr89_1	31/10 – 07/11/1989
	cr882_2	02/08 – 09/08/1988		cr89_2	07/11 – 14/11/1989
	cr882_3	09/08 – 16/08/1988		cr89_3	14/11 – 21/11/1989
	cr882_4	16/08 – 23/08/1988		cr89_4	21/11 – 28/11/1989
	cr882_5	23/08 – 30/08/1988		cr89_5	28/11 – 05/12/1989
	cr882_6	30/08 – 06/09/1988		cr89_6	05/12 – 12/12/1989

Table C.1 – Time span covered by the charts from the Cabo Ruivo tidal gauge.

	Tidal chart	Period of observations		Tidal chart	Period of observations
Sep1985	tp85_1	27/08 – 11/09/1985	Feb1988	tp881_1	26/01 – 09/02/1988
	tp85_2	11/09 – 25/09/1985		tp881_2	09/02 – 23/02/1988
	tp85_3	25/09 – 08/10/1985		tp881_3	23/02 – 08/03/1988

Table C.2 – Time span covered by the charts from the Terreiro do Paço tidal gauge.

	Tidal chart	Period of observations		Tidal chart	Period of observations
Aug1988	pa882_1	26/07 – 09/08/1988	Nov1989	pa89_1	31/10 – 14/11/1989
	pa882_2	09/08 – 23/08/1988		pa89_2	14/11 – 28/11/1989
	pa882_3	23/08 – 06/09/1988		pa89_3	28/11 – 13/12/1989

Table C.3 – Time span covered by the charts from the Paço de Arcos tidal gauge.

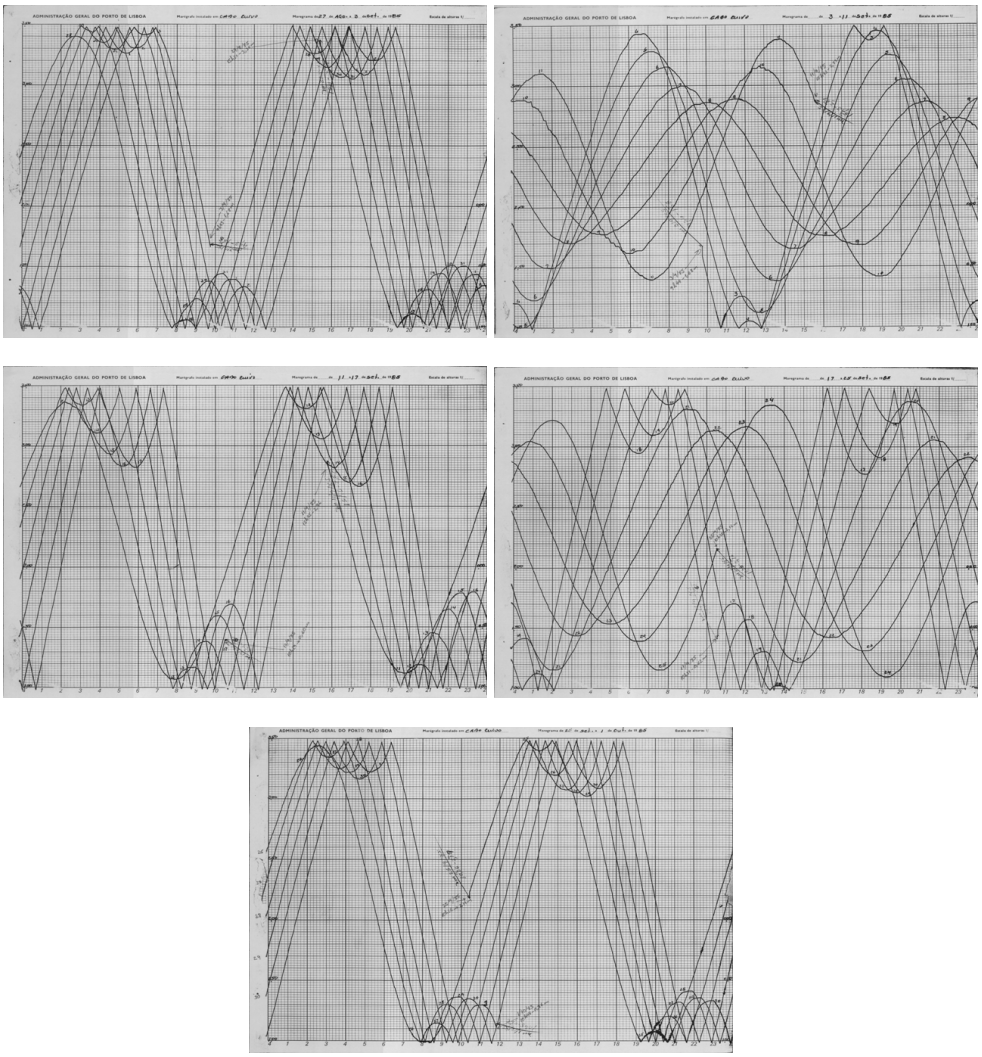

Figure C.1 – Charts from the Cabo Ruivo tidal gauge during September 1985.

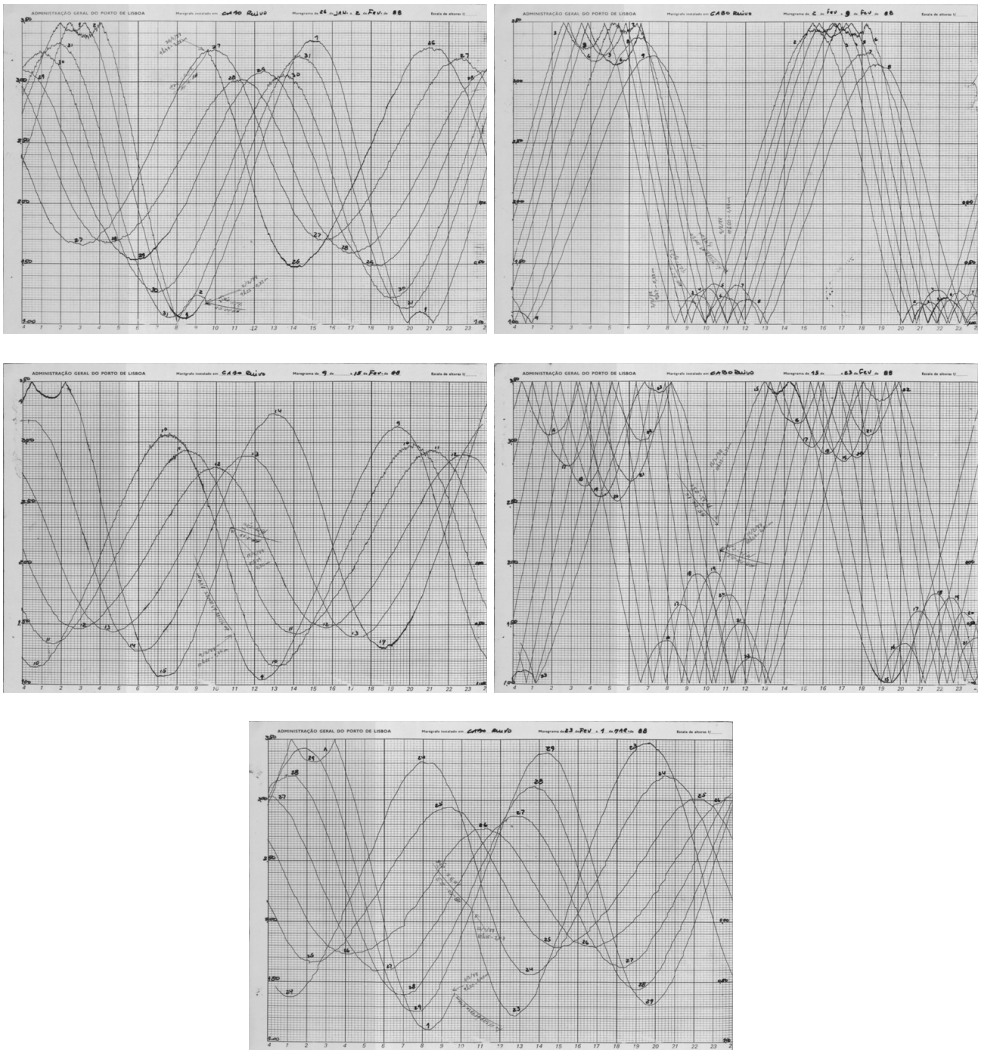

Figure C.2 – Charts from the Cabo Ruivo tidal gauge during February 1988.

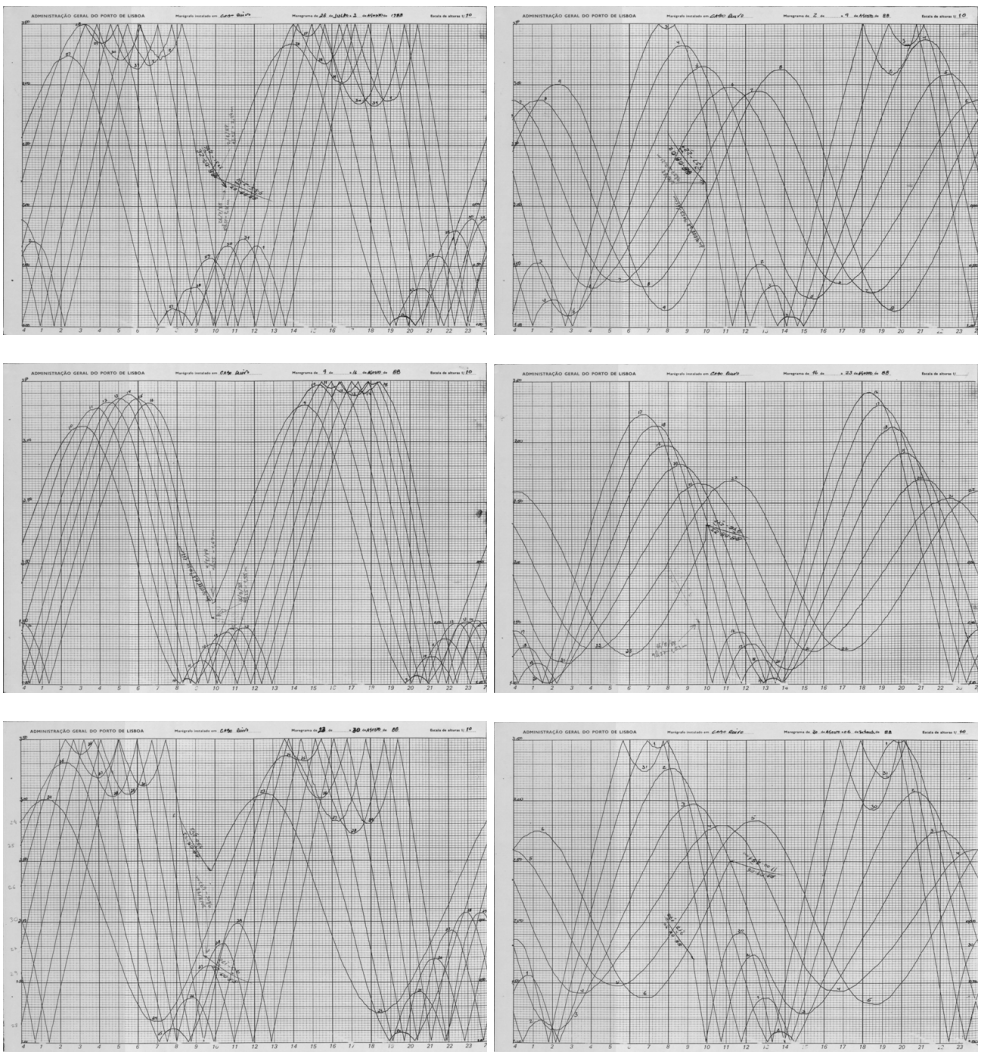

Figure C.3 – Charts from the Cabo Ruivo tidal gauge during August 1988.

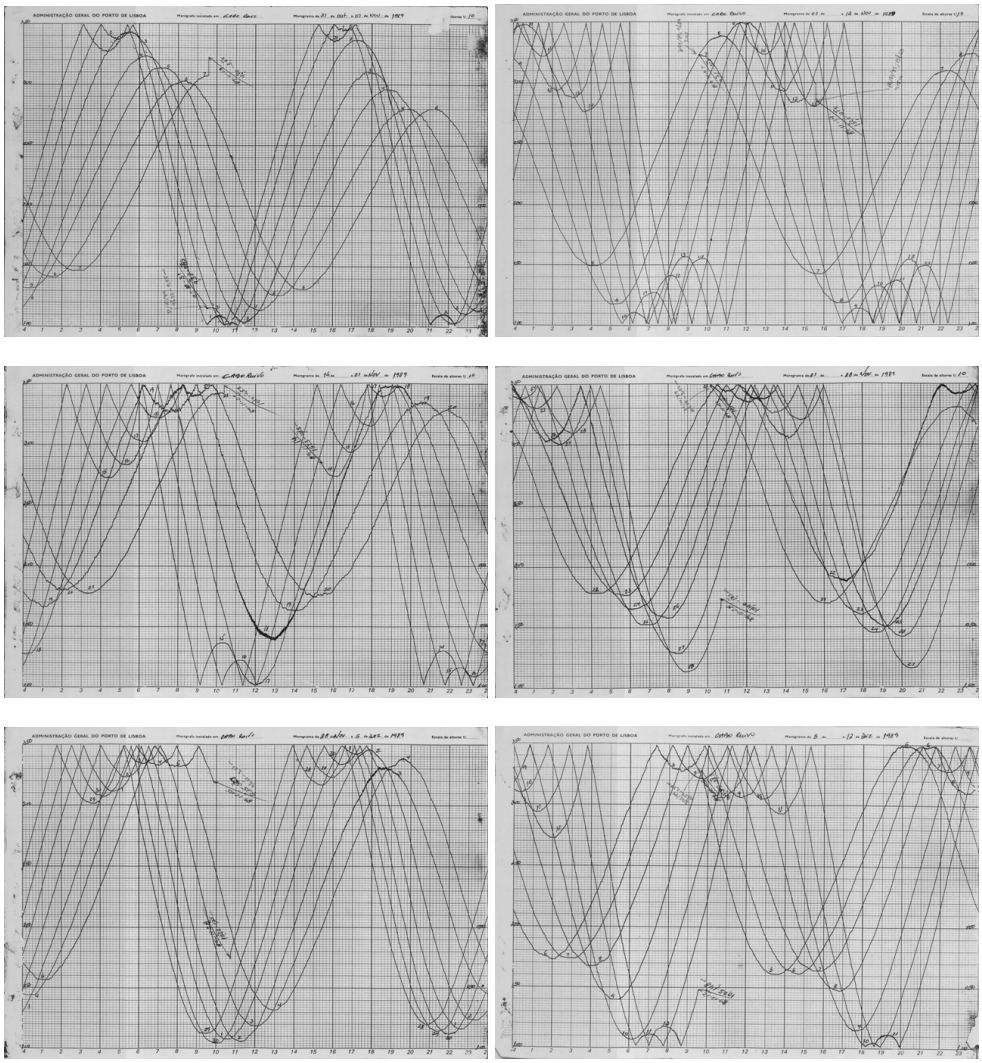

Figure C.4 – Charts from the Cabo Ruivo tidal gauge during November 1989.

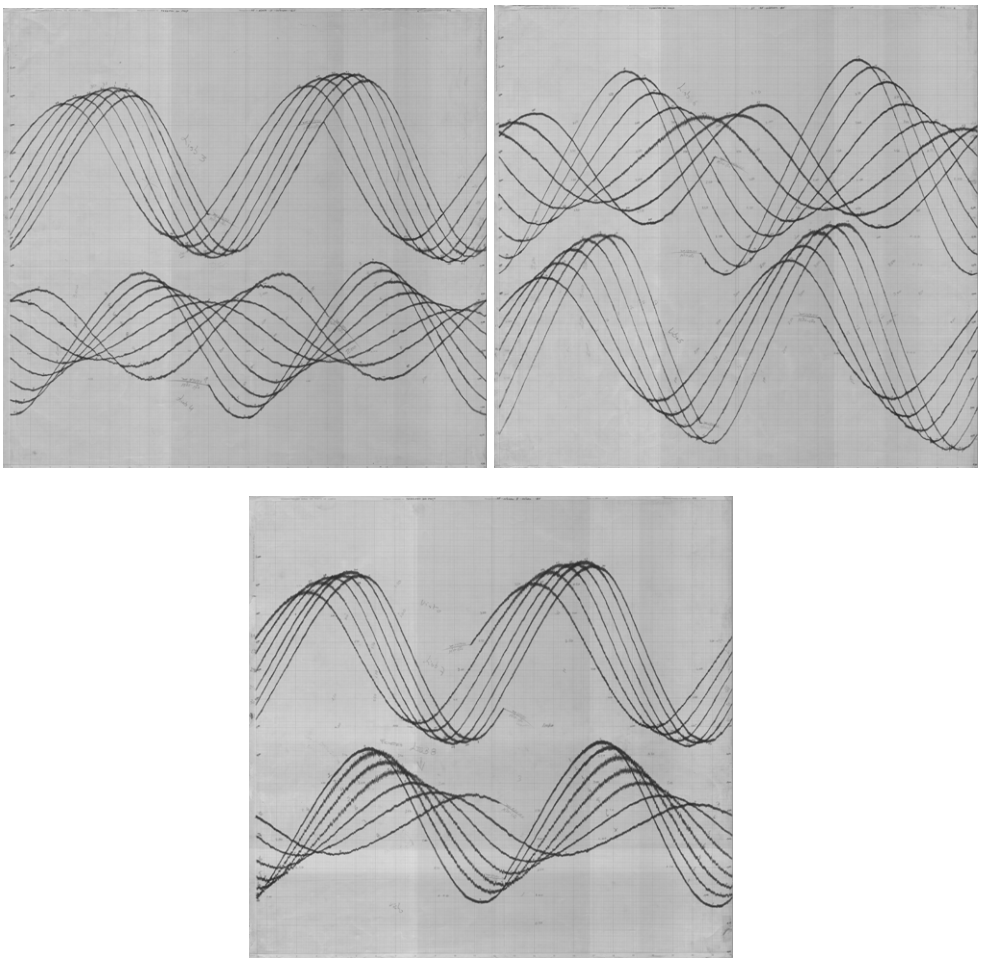

Figure C.5 – Charts from the Terreiro do Paço tidal gauge during September 1985.

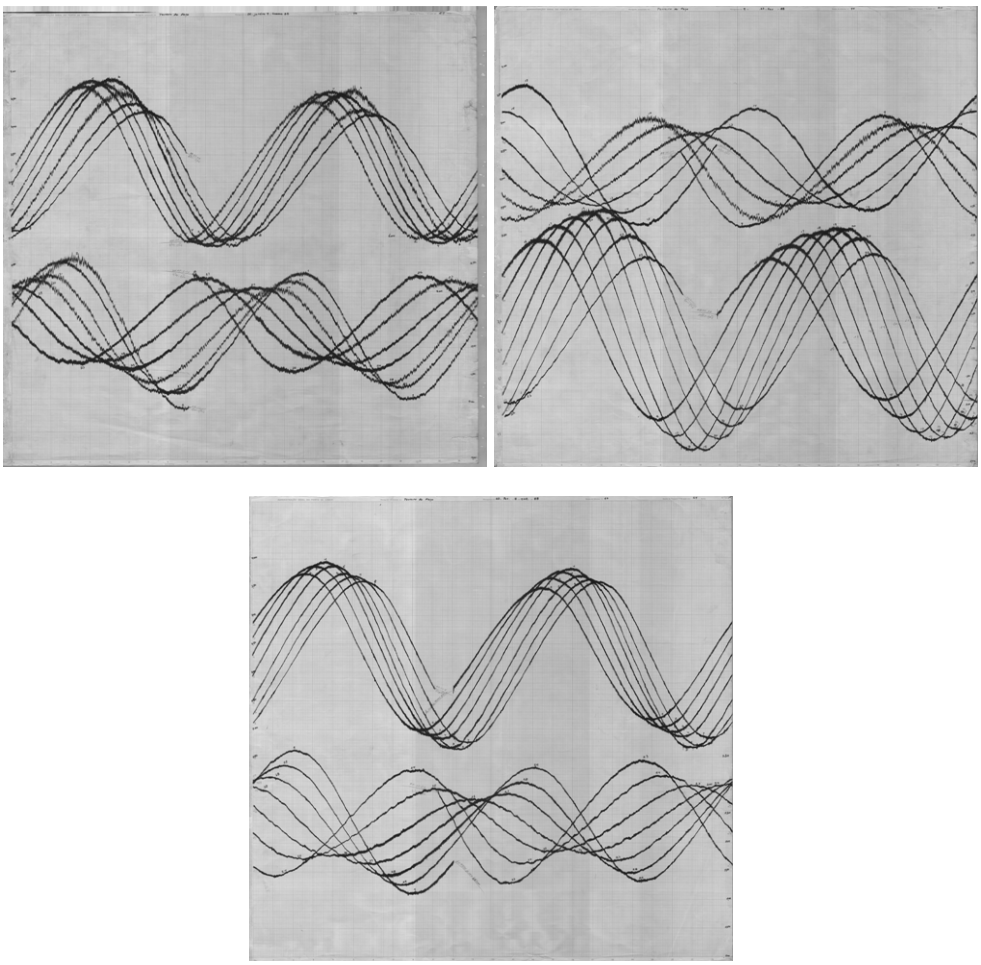

Figure C.6 – Charts from the Terreiro do Paço tidal gauge during February 1988.

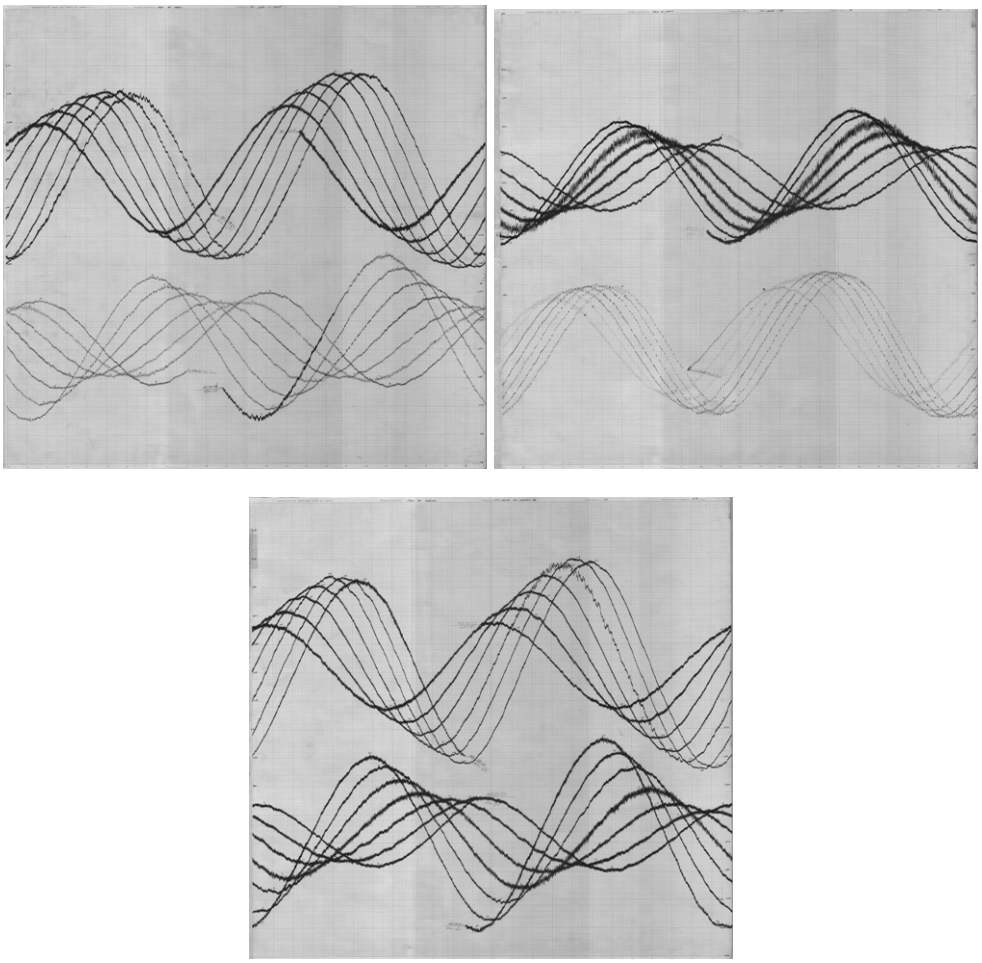

Figure C.7 – Charts from the Paço de Arcos tidal gauge during August 1988.

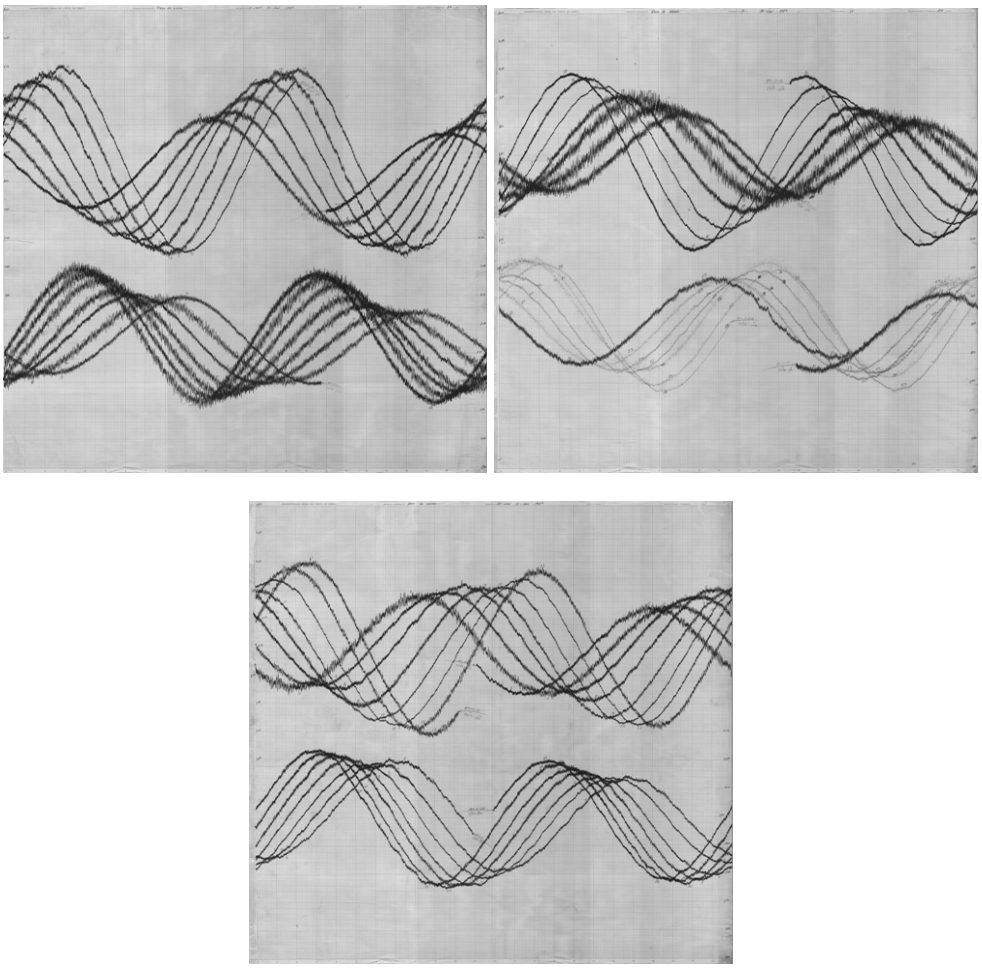

Figure C.8 – Charts from the Paço de Arcos tidal gauge during November 1989.

References

Aldridge, J. N., 1997. Hydrodynamic Model Predictions of Tidal Asymmetry and Observed Sediment Transport Paths in Morecambe Bay. Estuarine, Coastal and Shelf Science 44, 39–56.

Alves, M., 1983. Oceanografia de Estuários. Oceanografia do Estuário do Tejo, Relatório de estágio profissionalizante. Departamento de Física, Faculdade de Ciências da Universidade de Lisboa.

Ambar, I., 1989. Distribuição termohalina ao longo do estuário do Tejo em Fevereiro de 1988 - campanha Tejo88/1, technical report n° 2/89, Grupo de Oceanografia, Departamento de Física, Universidade de Lisboa, unpublished.

Ambar, I., Backhaus, J., 1983. A bidimensional numerical model of circulation in the Tejo Estuary. Comunicação apresentada na Conferência Nacional de Física, Évora.

Ambar, I., Backhaus, J., Fiúza, A., Mahnke, P., Quadfasel, D., 1989. Hydrographic observations in the Tejo-estuary during September 1985, technical report n° 5/89, Institut für Meereskunde der Universität Hamburg, unpublished.

Andreae, M. O., Byrd, J. T., Froellch Jr., P. N., 1983. Arsenic, Antimony, Germanium, and Tin in the Tejo Estuary, Portugal: Modeling a Polluted Estuary. Environmental Science & Technology 17 (12), 731–737.

Anjos, D., Fernandes, R., Lino, S., Pita, G., Neves, R., 2003. Modelação Operacional no Estuário do Tejo – REALTIME (Acoplamento de um Modelo e de um Sistema Automático de Aquisição de Dados). In: VII Congresso Nacional de Engenharia do Ambiente. Lisbon, Portugal.

Arantes e Oliveira, E., 1941. Esgotos de Lisboa – Estudos de Ante Projecto. Trabalho elaborado para a Câmara Municipal de Lisboa.

Aubrey, D. G., Speer, P. E., 1985. A Study of Non-linear Tidal Propagation in Shallow Inlet/Estuarine Systems. Part I: Observations. Estuarine, Coastal and Shelf Science 21, 185–205.

Baldaque da Silva, A., 1893. Estudo histórico-hidrográfico sobre a barra e o porto de Lisboa. Imprensa Nacional.

Blanton, J. O., Andrade, F. A., 2001. Distortion of Tidal Currents and the Lateral Transfer of Salt in a Shallow Coastal Plain Estuary (O Estuário do Mira, Portugal). Estuaries 24 (3), 467–480.

Blanton, J. O., Lin, G., Elston, S. A., 2002. Tidal current asymmetry in shallow estuaries and tidal creeks. Continental Shelf Research 22, 1731–1743.

Braunschweig, F., Martins, F., Chambel, P., Neves, R., 2003. A methodology to estimate renewal time scales in estuaries: the Tagus Estuary case. Ocean Dynamics 53, 137–145.

Cameron, W. M., Pritchard, D. W., 1963. Estuaries. In: Hill, M. N. (Ed.), The Sea. Vol. 2. John Wiley & Sons, New York, pp. 306–324.

Canas, A., Santos, A., Leitão, P., 2009. Effect of large scale atmospheric pressure changes on water level in the Tagus Estuary. Journal of Coastal Research SI 56, 1627–1631.

Costa, M. J., 1986. The Tagus Estuary as a Nursery. In: Estuarine processes: an application to the Tagus Estuary. Direcção-Geral da Qualidade do Ambiente, Lisbon, Portugal, pp. 395–412.

Costa, M. J., Vasconcelos, R., Costa, J. L., Cabral, H. N., 2007. River flow influence on the fish community of the Tagus estuary (Portugal). Hydrobiologia 587 (1), 113–123, doi:10.1007/s10750-007-0690-x.

Davies, J. H., 1964. A morphogenetic approach to world shorelines. Zeitschrift für Geomorphologie 8, 127–142.

Decreto Lei n.° 565/76 de 19 de Julho, 1976. Diário da República n.° 167/76 – I Série. Presidência do Conselho de Ministros.

Defant, A., 1961. Physical Oceanography. Vol. II. Pergamon Press, New York.

DGQA (Ed.), 1986. Estuarine processes: an application to the Tagus Estuary. UNESCO / IOC / CNA, Lisboa, Portugal.

Dias, J. M., 1993. Comparação dos resultados de um modelo numérico bidimensional com observações de correntes no Estuário do Tejo. Master's thesis, Faculdade de Ciências da Universidade de Lisboa.

Doodson, A. T., Warburg, H. D., 1941. Admiralty Manual of Tides. Hydrographic Department, Admiralty, London.

Dronkers, J. J., 1964. Tidal Computations in Rivers and Coastal Waters. North Holland Publishing, Amsterdam.

Dyer, K. R., 1997. Estuaries: A Physical Introduction. John Wiley & Sons, England.

Elias, N. P., 1986. Application of the physical model to the Tejo estuary. In: Estuarine processes: an application to the Tagus Estuary. Direcção-Geral da Qualidade do Ambiente, Lisbon, Portugal, pp. 55–72.

Elliott, A. J., 1978. Observations of the meteorologically induced circulation in the Potomac estuary. Estuarine, Coastal and Marine Science 6, 285–300.

Emery, W. J., Thomson, R., 2001. Data analysis methods in physical oceanography. Elsevier, Amsterdam.

Fanjul, E., Gomez, B., Carretero, J., Arevalo, I., 1998. Tide and surge dynamics along the Iberian Atlantic coast. Oceanologica Acta 21 (2), 131–143.

Fernandes, R., Silva, J., Leitão, P., Braunschweig, F., Neves, R., Domingos, J., 2004. Sistema de Monitorização Operacional para o Estuário do Tejo. In: APRH (Ed.), Proceedings do 7° Congresso da Água. CD-ROM.

Fiadeiro, P., 1987. Estudos sobre a dinâmica e a qualidade da água no Estuário do Tejo. In: Anais do Instituto Hidrográfico. No. 8. Instituto Hidrográfico, pp. 73–83.

Figueres, G., Martin, J. M., Meybeck, M., Seyler, P., 1985. A Comparative Study of Mercury Contamination in the Tagus Estuary (Portugal) and Major French Estuaries (Gironde, Loire, Rhône). Estuarine, Coastal and Shelf Science 20, 183–203.

Fortunato, A. B., Baptista, A. M., Luettich Jr., R. A., 1997. A three-dimensional model of tidal currents in the mouth of the Tagus estuary. Continental Shelf Research 17 (14), 1689–1714.

Fortunato, A. B., Oliveira, A., 2005. Influence of Intertidal Flats on Tidal Asymmetry. Journal of Coastal Research 21 (5), 1062–1067.

Fortunato, A. B., Oliveira, A., Baptista, A. M., 1999. On the effect of tidal flats on the hydrodynamics of the Tagus estuary. Oceanologica Acta 22 (1), 31–44.

Freire, P., Andrade, C., 1999. Wind-induced sand transport in Tagus estuarine beaches. First results. Aquatic Ecology 33, 225–233.

Freire, P., Taborda, R., Andrade, C., 2006. Caracterização das praias estuarinas do Tejo. In: APRH (Ed.), Proceedings do 8° Congresso da Água. Figueira da Foz, CD-ROM.

Friedrichs, C. T., Aubrey, D. G., 1988. Non-linear Tidal Distortion in Shallow Well-mixed Estuaries: a Synthesis. Estuarine, Coastal and Shelf Science 27, 521–545.

Gameiro, C., Cartaxana, P., Brotas, V., 2007. Environmental drivers of phytoplankton distribution and composition in Tagus Estuary, Portugal. Estuarine, Coastal and Shelf Science 75 (1-2), 21–34.

Godin, G., 1972. The Analysis of Tides. University of Toronto Press.

Hansen, D. V., Rattray, M., 1966. New Dimensions in Estuary Classification. Limnology and Oceanography 6 (3), 319–326.

ICNB, 2007. Webpage of the Nature Conservation and Biodiversity Institute. http://portal.icnb.pt/ICNPortal/vPT2007-AP-EstuarioTejo/Homepage+Areas+Protegidas.htm.

Jay, D. A., Smith, J. D., 1988. Residual Circulation in and Classification of Shallow, Stratified Estuaries. In: Dronkers, J., van Leussen, W. (Eds.), Physical Processes in Estuaries. Springer-Verlag, pp. 21–41.

Kiley, K. P., Welch, C. S., 1989. The Response of Estuarine Circulation to Local Wind Events. In: Neilson, B. J., Kuo, A., Brubaker, J. (Eds.), Estuarine Circulation. Humana Press, pp. 97–112.

Kjerfve, B., 1979. Measurement and analysis of water current, temperature, salinity and density. In: Dyer, K. R. (Ed.), Estuarine hydrography and sedimentation. Cambridge University Press, London, pp. 186–226.

Large, W. G., Pond, S., 1981. Open Ocean Momentum Flux Measurements in Moderate to Strong Winds. Journal of Physical Oceanography 11, 324–336.

Lemos, P., 1965. Estuário do Tejo. Tech. rep., Administração-Geral do Porto de Lisboa.

Lima, C., Martin, J. M., Meybeck, M., Figuères, G., Seyler, P., 1986. Mercury in the Tagus Estuary: an acute or obsolete problem? In: Estuarine processes: an application to the Tagus Estuary. Direcção-Geral da Qualidade do Ambiente, Lisbon, Portugal, pp. 413–454.

MacCready, P., 1999. Estuarine Adjustment to Changes in River Flow and Tidal Mixing. Journal of Physical Oceanography 29, 708–726.

Macedo, M. E., 2006. Caracterização de Caudais – Rio Tejo. Tech. rep., Direcção de Serviços de Monitorização Ambiental, Lisboa, CCDR-LVT.

Martins, M., Ferreira, J. G., Calvão, T., Figueiredo, H., 1984. Nutrientes no Estuário do Tejo. Comparação da Situação em Caudais Médios e em Cheia, com Destaque para Alterações na Qualidade da Água. In: APRH (Ed.), I Simpósio Luso-Brasileiro de Engenharia Sanitária e Ambiental. pp. 1–10.

Officer, C. B., 1976. Physical Oceanography of Estuaries (and Associated Coastal Waters). John Wiley & Sons, EUA.

Oliveira, A., Baptista, A. M., 1997. Diagnostic Modeling of Residence Times in Estuaries. Water Resources Research 33 (8), 1935–1946.

Oliveira, F., 2000. Numerical simulation of wave propagation in the entrance of the Tagus estuary. In: Spaulding, M., Butler, H. L. (Eds.), Estuarine and Coastal Modeling VI. ASCE, pp. 510–525.

Oliveira, I. B. M., 1993. Port of Lisbon – Improvement of the Access Conditions Through the Tagus Estuary Entrance. In: Proceedings of the 23^{rd} International Conference of Coastal Engineering. pp. 2745–2757.

Parker, B. B., 1991. The relative importance of the various non-linear mechanisms in a wide range of tidal interactions (Review). In: Parker, B. B. (Ed.), Tidal Hydrodynamics. John Wiley & Sons, New York, pp. 237–268.

Pawlowicz, R., Beardsley, B., Lentz, S., 2002. Classical tidal harmonic analysis including error estimates in MATLAB using T_TIDE. Computers and Geosciences 28, 929–937.

Peters, H., 1997. Observations of Stratified Turbulent Mixing in an Estuary: Neap-to-Spring Variations During High River Flow. ECSS 45, 69–88.

Portela, L., Neves, R., 1994a. Modelling temperature distribution in the shallow Tejo Estuary. In: Tsakiris, G., Santos, M. A. (Eds.), Advances in Water Resources Technology and Management. A. A. Balkema, Rotterdam, pp. 457–463.

Portela, L., Neves, R., 1994b. Numerical modelling of suspended sediment transport in tidal estuaries: a comparison between the Tagus (Portugal) and the Scheldt (Belgium-The Netherlands). Netherlands Journal of Aquatic Ecology 28 (3-4), 329–335.

Portela, L., Neves, R., 1996. Modelação matemática da distribuição da salinidade no Estuário do Tejo. In: Proceedings do 3° Congresso da Água.

Prandle, D., 1985. On salinity regimes and the vertical structure of residual flows in narrow tidal estuaries. Estuarine, Coastal and Shelf Science 20 (5), 615–635.

Pritchard, D. W., 1952. Salinity distribution and circulation in the Chesapeake Bay Estuaries system. Journal of Marine Research 11, 106–123.

Pritchard, D. W., 1955. Estuarine Circulation Patterns. In: Proceedings of the American Society of Civil Engineers. No. 717. pp. 1–11.

Pritchard, D. W., 1967. What is an Estuary: Physical Viewpoint. In: Lauff, G. H. (Ed.), Estuaries. No. 83. American Association for the Advancement of Science, pp. 3–5.

Pritchard, D. W., 1989. Estuarine Classification - A Help or a Hindrance. In: Neilson, B. J., Kuo, A., Brubaker, J. (Eds.), Estuarine Circulation. Humana Press, New Jersey, pp. 1–38.

Pugh, D. T., 1987. Tides, Surges and Mean Sea-Level. John Wiley & Sons.

Ribeiro, C., Waniek, J., Sharples, J., 2004. Observations of the spring-neap modulation of the gravitational circulation in a partially mixed estuary. Ocean Dynamics 54, 299–306.

Rodrigues, D. A., Teles, M., Leendertse, J. J., 1986. Numerical modelling of the Tejo estuary for currents and water quality predictions. In: Estuarine processes: an application to the Tagus Estuary. Direcção-Geral da Qualidade do Ambiente, Lisbon, Portugal, pp. 7–22.

Rodrigues da Silva, M. C., 2003. Instrumentos de Apoio à Gestão de Estuários. Indicadores Ambientais. Ph.D. thesis, Universidade Nova de Lisboa, Faculdade de Ciências e Tecnologia.

Rusu, L., Bernardino, M., Soares, C. G., 2009. Influence of Wind Resolution on the Prediction of Waves Generated in an Estuary. Journal of Coastal Research SI 56, 1419–1423.

Seim, H., Blanton, J., Elston, S., 2006. Tidal circulation and energy dissipation in a shallow, sinuous estuary. Ocean Dynamics 56, 360–375.

Speer, P. E., Aubrey, D. G., 1985. A Study of Non-linear Tidal Propagation in Shallow Inlet/Estuarine Systems. Part II: Theory. Estuarine, Coastal and Shelf Science 21, 207–224.

Unesco, 1983. Algorithms for computation of fundamental properties of seawater. Unesco Technical Papers in Marine Science, No 44, 58 pp.

Unesco, 1988. The acquisition, calibration, and analysis of CTD data. Unesco Technical Papers in Marine Science, No 54, 102 pp.

Vale, C., Sundby, B., 1987. Suspended Sediment Fluctuations in the Tagus Estuary on Semi-Diurnal and Fortnightly Time-Scales. Estuarine, Coastal and Shelf Science 25 (5), 495–508.

Valente, A., da Silva, J., 2009. On the observability of the fortnightly cycle of the Tagus estuary turbid plume using MODIS ocean colour images. Journal of Marine Systems 75, 131–137.

Vaz, N., Fernandes, L., Leitão, P. C., Dias, J. M., Neves, R., 2009. The Tagus Estuarine Plume Induced by Wind and River Runoff: Winter 2007 Case Study. Journal of Coastal Research SI 56, 1090–1094.

Wang, D.-P., 1979. Wind-Driven Circulation in the Chesapeake Bay, Winter 1975. Journal of Physical Oceanography 9, 564–572.

Wang, D. P., Elliott, A. J., 1978. Non-Tidal Variability in the Chesapeake Bay and Potomac River: Evidence for Non-Local Forcing. Journal of Physical Oceanography 6, 225–232.

Weisberg, R. H., 1976. The Non-Tidal Flow in the Providence River of the Naragansett Bay. Journal of Physical Oceanography 6, 721–734.